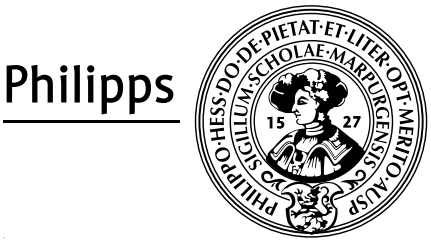

Localized transition states in many-particle systems

Dissertation

zur Erlangung des
Doktorgrades der Naturwissenschaften
(Dr. rer. nat.)

dem

Fachbereich Physik
der Philipps-Universität Marburg

vorgelegt von

Jens Christian Pfeifer

aus
Frankfurt/Main

Marburg/Lahn, 2015

Vom Fachbereich Physik der Philipps-Universität Marburg
als Dissertation angenommen am: 09.10.2015
Tag der mündlichen Prüfung: 12.10.2015

Erstgutachter: Prof. Dr. Bruno Eckhardt — Fachbereich Physik, Philipps-Universität Marburg

Zweitgutachter: Prof. Dr. Holger Waalkens — Faculty of Mathematics, Rijksuniversiteit Groningen

Hochschulkennziffer 1180

Abstract

This thesis addresses the investigation of the transition from order to chaos in two different systems. In this context, both numerical simulations and theoretical considerations are applied. Popular examples of such transitions are, among others, the melting of a crystal or the transition from a laminar flow to turbulence. They have in common that the variation of an external parameter, for example temperature, results in an abrupt change in the properties of the system: The ordered, well-defined structure of a crystal transforms to the unordered, random configuration of a liquid.

In the first part of this thesis, we investigate the influence of a linear, periodic shear on a system of mutually repelling particles. This can be considered as a model for a well known phenomenon, the mixing of a blob of dye in a liquid confined between two concentric cylinders. If the cylinders are rotated back and forth slowly enough so that the flow remains in the laminar regime, a demixing is possible and after one period we retrieve the original blob. Something similar occurs in the simple two-dimensional model system that we investigate: For small shear rates, we observe a self-organization of the particles, ending up in a lattice configuration. Above a critical shear rate, an abrupt change takes place, and the system is found - and remains - in an unordered, chaotic state. An indicator of this transition is the diffusivity of the system which becomes nonzero. We are able to associate the transition with a loss of stability of the sheared lattice. In the chaotic regime, the radial correlation function exhibits features typical for a liquid or a gas, provided that shear rates are sufficiently large. The spatially resolved correlations, on the other hand, reveal more details and allow us to extract phase information. Additionally, they provide a possible explanation why diffusion parallel to the shear is enhanced beyond the known advection-diffusion coupling.

In the further course of this work, we turn toward a transition known from everyday life, the melting of a solid. There, we again restrict ourselves to a two-dimensional model similar to the one in the first part, though this time we use a screened Coulomb potential. The experimental complement may be found for example in complex plasmas. We are especially interested in the microscopic processes which eventually result in the melting of the crystal. Therefore, we perform molecular-dynamics (MD) simulations which confirm a two-step process of melting. Furthermore, the computed trajectories allow us deeper insights into the dynamics of the system. In the critical temperature range, we initially observe isolated localized processes where several particles exchange their positions. With the help of a projection on the energetically lowest configuration, these transitions can be identified as hopping events on the hexagonal lattice. As temperature is increased, more processes occur simultaneously, and eventually secondary, more complex transitions are stimulated which result in the melting of the solid.

On this account, we investigate the melting transition in view of a rate activated process induced by localized reorganizations of a few particles. In a first step, we examine a vastly simplified system consisting of a hexagonal crystal in which only two or three neighboring

particles are allowed to move. At low temperatures, the transitions between the optimal configurations of the system occur via so-called transition states, energetically activated equilibrium states which are unstable and will decay to one of the two adjacent minimum configurations. It turns out that those states form the energetically most favorable connections between minima, emphasizing their importance for the dynamics, at least at low temperatures. Furthermore, we investigate the system with focus on the transition rates, and to which extent they may be described by harmonic approximations.

In order to apply the idea of a rate induced melting process to the actual system, we have to take a step back and consider all the particles once again. First of all, possible transitions - and more importantly transition states - have to be identified. To this end, we adopt the edge tracking algorithm, a simple yet versatile dynamical bisection method. In this course, we find transitions and their corresponding transition states which comprise up to 18 particles and only affect up to approximately 25 particles, implying that the states are well localized. We characterize the states, both by their arrangement in configuration space as well as by their thermodynamically relevant properties such as the energy barriers. The latter are considerably higher than the thermal energy at the melting point so that special significance for the dynamics can be attributed to the transition states close to the temperature of melting. We determine the dependence of the transition rates on the temperature, and compare them to the melting temperature of the system. Apparently, the rates are too low to explain melting on their own. Nevertheless, this is in accordance with previous observations in the simulations, where localized reorganizations lead to secondary transitions which break up the lattice structure and hence initiate the melting process.

In the course of our studies, we also investigate the elastic properties of the system. The crystal, consisting of individual particles, can be described by the elastic constants of a continuous solid body. We show that the displacement field induced by the local disturbance of the transition state can be approximated by a superposition of several displacement fields of singular forces acting on an elastic medium. The screening of the potential not only gives rise to a rescaling of the energy of the system, but alters its elastic properties as well. This is partly reflected in the transition states. Though their basic configuration remains unaffected, energy barriers and displacement fields change considerably. We once again refer to the rate model in order to determine the transition rate at the critical temperature. A concluding comparison with results from MD-simulations and other predictions reveals that the model captures the dependence of the melting temperature on the screening parameter of the potential very well.

Zusammenfassung

Diese Arbeit befasst sich mit der Untersuchung des Übergangs von der Ordnung zum Chaos in zwei unterschiedlichen Systemen. Dabei finden sowohl numerische Simulationen als auch theoretische Überlegungen ihre Anwendung. Bekannte Beispiele solcher Übergänge sind unter anderem das Schmelzen eines Kristalls oder der Turbulenzübergang einer laminaren Strömung. Gemein ist ihnen, dass die Änderung eines äußeren Parameters, wie zum Beispiel der Temperatur, eine schlagartige Veränderung der Eigenschaften des Systems zur Folge hat: Aus der geordneten, wohldefinierten Struktur eines Kristalls entwickelt sich die ungeordnete, zufällige Konfiguration einer Flüssigkeit.

Im ersten Teil untersuchen wir den Einfluss einer linearen, periodischen Scherung auf ein System sich gegenseitig abstoßender Partikel. Dies kann als ein Modell für ein gut bekanntes Phänomen betrachtet werden, dem Vermischen eines Farbkleckses in einer Flüssigkeit zwischen zwei konzentrischen Zylindern. Werden diese langsam genug hin und her bewegt, sodass die Strömung laminar bleibt, ist ein Entmischen des Kleckses möglich, der Vorgang ist reversibel. Etwas Ähnliches lässt sich in dem hier untersuchten, einfachen zweidimensionalen Modell-System beobachten: Bei kleinen Scherraten kommt es zu einer Selbstorganisation der Teilchen in eine Gitter-Konfiguration. Allerdings findet oberhalb einer kritischen Scherrate ein abrupter Wechsel statt und das System befindet sich - und bleibt - in einem ungeordneten, chaotischen Zustand. Ein Indikator für diesen Übergang ist die Diffusivität des Systems, welche einen endlichen Wert annimmt. Es ist uns möglich, den Übergang mit dem Verlust der Stabilität des Gitters unter Scherung in Verbindung zu bringen. Im chaotischen Regime zeigt die radiale Korrelationsfunktion die typischen Charakteristika einer Flüssigkeit, bzw. bei ausreichend großen Scherraten die eines Gases. Die räumlich aufgelösten Korrelationen zeigen hingegen mehr Struktur und es ist uns möglich Phaseninformationen aus ihnen zu entnehmen. Des Weiteren bieten sie einen Erklärungsansatz, wieso die Diffusion parallel zur Scherung über die bekannte Kopplung an die Advektion hinaus verstärkt wird.

Im weiteren Verlauf der Arbeit widmen wir uns einem aus dem Alltag bekannten Übergang, dem Schmelzen eines festen Körpers. Dabei beschränken wir uns auf ein zweidimensionales Modell ähnlich demjenigen aus dem ersten Teil, wobei wir allerdings ein abgeschirmtes Coulomb-Potential betrachten. Das experimentelle Gegenstück ist hierbei beispielsweise in Form komplexer Plasmen gegeben. Wir interessieren uns hier insbesondere für die mikroskopischen Prozesse, die letztendlich im Schmelzen des Kristalls münden. Daher führen wir zunächst Molekular-Dynamik (MD) Simulationen durch, welche einerseits einen zweistufigen Schmelzmechanismus bestätigen, andererseits aber auch durch die errechneten Trajektorien tiefere Einblicke in die Dynamik erlauben. Im kritischen Temperaturbereich beobachten wir zunächst vereinzelte, lokale Prozesse bei denen mehrere Teilchen ihre Positionen austauschen. Mittels einer Projektion auf den energetisch minimalen Zustand können diese Übergänge als Tauschprozesse im zugrundeliegenden hexagonalen Gitter identifiziert werden. Sobald mehrere dieser Prozesse gleichzeitig auftreten, die Tem-

peratur also erhöht wurde, kommt es zu weiterführenden Umordnungen und letztlich zum Schmelzen des Festkörpers.

Aus diesem Grund untersuchen wir im weiteren Verlauf den Schmelzvorgang im Hinblick auf einen Raten-aktivierten Prozess, welcher durch lokalisierte Umordnungen einiger weniger Teilchen induziert wird. In einem ersten Schritt betrachten wir dazu ein stark vereinfachtes System, bestehend aus einem hexagonalen Kristall in dem nur zwei oder drei benachbarten Teilchen die Möglichkeit gelassen wird sich zu bewegen. Die Übergänge des Systems zwischen den unterschiedlichen optimalen Konfigurationen erfolgen bei niedrigen thermischen Anregungen über sogenannte *Transition States*, energetisch angeregte Gleichgewichtspunkte, welche instabil sind und in Richtung zweier benachbarter Minima zerfallen. Dabei zeigt sich, dass diese Zustände die energetisch günstigsten Verbindungen darstellen und somit tatsächlich von besonderer Bedeutung für die Dynamik sind, zumindest im Bereich niedriger Temperaturen. Des Weiteren untersuchen wir die entsprechenden Übergangsraten und inwieweit diese mittels einfacher Näherungen erfasst werden.

Um die Idee eines rateninduzierten Schmelzens auf das eigentliche System anwenden zu können, kehren wir zum Ausgangspunkt zurück und betrachten wiederum alle Teilchen. Zunächst müssen jedoch mögliche Übergänge und insbesondere die *Transition States* identifiziert werden. Dazu nutzen wir den *Edge Tracking* Algorithmus, eine einfache und dennoch vielseitige dynamische Bisektionsmethode. Im Zuge dessen finden wir Umordnungen und zugehörige *Transition States*, welche bis zu 18 Teilchen umfassen sowie Auswirkung auf bis zu etwa 25 Teilchen haben und somit gut lokalisiert sind. Wir charakterisieren diese Zustände, sowohl durch ihre Anordnung im Konfigurationsraum, als auch durch thermodynamisch relevante Größen wie etwa Energiebarrieren. Letztere sind wesentlich höher als die thermische Energie am Schmelzpunkt, weshalb den *Transition States* eine besondere Bedeutung für die Dynamik in diesem Temperaturbereich beizumessen ist. Wir bestimmen die Übergangsraten in Abhängigkeit von der Temperatur und vergleichen diese mit der Schmelztemperatur des Systems. Es zeigt sich, dass die Raten alleine nicht ausreichen um ein Schmelzen zu ermöglichen. Allerdings ist dies im Einklang mit der Beobachtung, dass die lokalisierten Umordnungen zu sekundären Prozessen führen, welche letztendlich das Gitter aufbrechen und somit den Schmelzvorgang einleiten.

Im Laufe unserer Untersuchungen betrachten wir auch die elastischen Eigenschaften des Systems. Der Kristall, bestehend aus einzelnen Partikeln, kann mit elastischen Konstanten eines kontinuierlichen Körpers beschrieben werden. Dabei kann das Verschiebungsfeld, welches durch die lokale Störung eines *Transition States* hervorgerufen wird, durch die Überlagerung der Verschiebungsfelder mehrerer Punktkräfte, die auf ein elastisches Medium wirken, angenähert werden. Die Veränderung der Abschirmung des Potentials führt nicht nur zu einer Reskalierung der Energie des Systems, sondern verändert auch dessen elastische Eigenschaften. Dies spiegelt sich teilweise auch in den Übergangszuständen wider. Die grundlegende Konfiguration bleibt zwar nahezu unverändert, jedoch ändern sich die Energiebarrieren und Verschiebungsfelder. Wir bemühen ein weiteres Mal das Ratenmodell um die Übergangsrate an der kritischen Temperatur zu bestimmen. Ein abschließender Vergleich mit Ergebnissen aus MD-Simulationen und weiteren Vorhersagen zeigt, dass das Modell die Abhängigkeit der Schmelztemperatur von der Abschirmung des Potentials sehr gut erfasst.

Contents

Abstract III

Zusammenfassung V

1 Introduction 1

2 The transition to irreversibility in a sheared many-body system 7
2.1 The model and its parameters . . . 7
2.1.1 Numerical implementation . . . 9
2.1.2 Reduced representation and stroboscopic maps . . . 9
2.2 Ordered and disordered states . . . 11
2.2.1 Ordered states . . . 11
2.2.2 Diffusion constants . . . 12
2.2.3 Transitions for fixed Γ_1 . . . 14
2.2.4 Anisotropy in diffusion . . . 16
2.2.5 Exploration of the Γ_1-Γ_2-parameter plane . . . 17
2.3 Linear stability analysis . . . 19
2.3.1 Local stability: Lyapunov exponents . . . 19
2.3.2 Quasi-static approximation . . . 23
2.3.3 Floquet analysis . . . 24
2.4 Particle correlations . . . 27
2.4.1 Radial correlation . . . 27
2.4.2 Spatial correlation . . . 29
2.5 Summary . . . 34

3 Melting of a two-dimensional system 37
3.1 Definition of the potential . . . 37
3.2 Molecular dynamics simulations . . . 42
3.2.1 Theory of melting . . . 44
3.2.2 Translational ordering . . . 46
3.2.3 Sixfold orientation . . . 48
3.2.4 Lindemann criterion . . . 50
3.2.5 The principle of inherent minima . . . 55
3.2.6 Defect analysis . . . 58
3.2.7 Isolated point defects . . . 59
3.3 Summary . . . 61

4 Restricted few-particle dynamics 63
4.1 Theory of transition rates . . . 64

4.2 Two free particles . . . 66
4.2.1 Rate calculations . . . 68
4.3 Three free particles . . . 71
4.3.1 Three-dimensional reduction . . . 73
4.4 Summary . . . 80

5 The two-particle exchange 83
5.1 Identification of conformational changes in minima . . . 83
5.2 The technique of edge tracking . . . 84
5.2.1 Implementation . . . 87
5.2.2 Other algorithms for locating transition states . . . 88
5.3 Finding the transition state: An example . . . 89
5.3.1 Localization of the transition state: The participation number . . . 92
5.4 Effects of the system size and boundary conditions . . . 93
5.4.1 Dependence on boundary conditions . . . 94
5.4.2 Dependence on system size . . . 95
5.5 Connection to continuum elasticity . . . 97
5.5.1 Linear elasticity theory . . . 98
5.5.2 Determining elastic properties . . . 100
5.5.3 Singular force . . . 103
5.5.4 Approximating the transition state . . . 106
5.6 Summary . . . 111

6 Localized many-particle transition states 113
6.1 Transition states . . . 113
6.1.1 Symmetry failure of the algorithm . . . 120
6.2 Properties of the transition states . . . 121
6.2.1 Localization . . . 123
6.2.2 Neighborhood relations . . . 124
6.2.3 Energy barriers . . . 127
6.2.4 Transition rates . . . 129
6.2.5 Comparison to MD-simulations . . . 132
6.2.6 Comparison to the reduced models . . . 133
6.3 Variation with the screening parameter . . . 134
6.3.1 Displacement field . . . 135
6.3.2 Localization . . . 137
6.3.3 Energy barriers . . . 138
6.3.4 Variation of transition rates . . . 139
6.3.5 Comparison to simulations and the Lindemann criterion . . . 140
6.4 Summary . . . 143

7 Conclusion 145

A Appendix 149
A.1 Thermalization . . . 149

A.2 Reformulations of the rate equation 151
A.3 Computing invariant manifolds 152
A.4 Algorithms to locate transition states 154
A.5 Analytical solution for the singular force in an infinite 2d-solid 157
A.6 Discretization on a hexagonal lattice 159
A.7 Displacement fields of superimposed singular forces 161
A.8 Spectrum reductions 161

Bibliography **165**

List of Figures

2.1 Reduced trajectories . . . 10
2.2 Stroboscopic maps . . . 11
2.3 Asymptotic states . . . 12
2.4 Displacement on different timescales . . . 13
2.5 Mean square displacements . . . 14
2.6 Diffusion constants, slice . . . 15
2.7 Diffusion constants, collapsed . . . 17
2.8 Diffusion constants, collapsed, $\Gamma_1 = 1.0$ . . . 17
2.9 Diffusion constants, $\Gamma_1 \times \Gamma_2$ . . . 18
2.10 Local Lyapunov exponents . . . 21
2.11 Tipping point trajectory . . . 22
2.12 Lattice configurations, 2d . . . 24
2.13 Lattice stability . . . 25
2.14 System stability: Floquet multipliers . . . 26
2.15 Radial correlation function . . . 28
2.16 2d correlation function, pt. I . . . 29
2.17 2d correlation function, pt. II . . . 30
2.18 Depletion zone . . . 32
2.19 2d correlation function, $\Gamma_1 = 1.0$ . . . 34

3.1 Shape of the Yukawa potential . . . 38
3.2 Critical interaction range of the Yukawa potential . . . 40
3.3 Configurations, pt. I . . . 43
3.4 Disloactions and disclinations . . . 45
3.5 Radial correlation function . . . 47
3.6 Orientational order parameter g_6 . . . 49
3.7 Lindemann parameter . . . 52
3.8 Configurations, pt. II: Local lattice . . . 54
3.9 Configurations, pt. III: Inherent minima . . . 56
3.10 Distance to inherent minima . . . 57
3.11 Defect concentration . . . 58
3.12 Isolated defects . . . 60

4.1 Schematic of transitions in 1d . . . 65
4.2 Stationary states and potential energy landscape, two-particle system . . . 67
4.3 Survival probability, two-particle system . . . 69
4.4 Comparison of rates, two-particle system . . . 70
4.5 Stationary states in the three-particle system, four dimensions . . . 72
4.6 Stationary states in the three-particle system, three dimensions . . . 74

4.7 Visualization of the reduced system . . . 77
4.8 Visualization of the invariant manifolds of the transition states . . . 78
4.9 Visualization of the unstable manifolds . . . 79
4.10 Rates varying with number of free particles . . . 81

5.1 Schematic edge tracking . . . 85
5.2 Edge Tracking, time series . . . 90
5.3 Edge Tracking, time line . . . 91
5.4 Two-particle exchange . . . 92
5.5 Two-particle exchange, fixed boundaries . . . 95
5.6 Comparison of displacements: 2500 and 10000 particles . . . 97
5.7 Force-displacement relation . . . 98
5.8 Elastic constants as function of the screening parameter . . . 103
5.9 Elastostatic displacements, analytical solution . . . 104
5.10 Comparison simulation - elastostatic equations . . . 105
5.11 Displacements, elastostatic equations . . . 107
5.12 Displacements . . . 108
5.13 Displacements, simulation . . . 109
5.14 Comparison of displacements . . . 110

6.1 Transition States, pt. I . . . 115
6.2 Transition States, pt. II . . . 116
6.3 Transition States, pt. III . . . 117
6.4 Transition States, pt. IV . . . 118
6.5 Symmetry failure . . . 121
6.6 Participation numbers . . . 123
6.7 Triangulations, pt. I . . . 125
6.8 Triangulations, pt. II . . . 126
6.9 Energy barriers . . . 128
6.10 Rate of events . . . 131
6.11 Relative rates . . . 132
6.12 Displacement field, variation with μ . . . 136
6.13 Participation numbers, variation with μ . . . 137
6.14 Energy barriers, variation with μ . . . 138
6.15 Relative rates . . . 139
6.16 Comparison of melting temperatures . . . 141

A.1 Velocity distribution . . . 149
A.2 Energy relaxation . . . 150
A.3 Schematic fat trajectories . . . 153
A.4 Displacement fields, superimposed singular forces . . . 161
A.5 Convergence of the spectrum, pt. I . . . 162
A.6 Convergence of the spectrum, pt. II . . . 162

List of Tables

4.1 Properties of the stationary states, two-particle system 68
4.2 Properties of the stationary states, three-particle system 73
4.3 Properties of the stationary states, three-dimensional reduction 75

5.1 Parameters edge tracking 86
5.2 Heuristics edge tracking 87
5.3 Dependence on boundary conditions 96
5.4 Dependence on system size 96

6.1 Properties of transition states 122
6.2 Multiplicity of transition states 130
6.3 Comparison to the low-dimensional model 134
6.4 Existence of transition states 135

1

Introduction

> Das berühmte Problem, Geschehenes ungeschehen zu machen, hat damit zwar keine Lösung, doch eine einfache Formulierung erhalten, welche in der simplen Anweisung besteht, die momentanen Geschwindigkeiten aller Atome des Universums plötzlich umzukehren.
>
> The famous problem of undoing what has happened still does not have a solution, but a simple formulation, which consists in the plain instruction to suddenly reverse the current velocities of all the atoms in the universe.
>
> *J. Loschmidt, 1876*

Dating back to Loschmidt (1876), the issue of reversibility of a system has fascinated generations of physicists. And although equations of motion are often symmetric in time, in general the dynamics of many-body systems are expected to be irreversible due to the immense number of interactions. An experiment which defies these expectations is the recovery of a blob of dye in a periodically sheared liquid (Taylor, 1960; Homsy, 2008). A viscous liquid is filled in between two concentric cylinders, and a blob of dye is injected into the liquid. Then, the inner cylinder is rotated several turns, and the blob gets stretched and vanishes. Afterwards, the cylinder is turned back. If done slowly enough, the liquid remains in the laminar regime, and after one period the initial blob reappears, showing only some slight blurring due to diffusive effects. A similar phenomenology can also be observed in quantum mechanical systems, where it is referred to as *Loschmidt echoes*, for example for spins precessing in a magnetic field (Hahn, 1950; Carr and Purcell, 1954). After application of an appropriate magnetic pulse, the original orientation of the spins is restored. In later experiments, time reversal of trajectories in a classical system showing both regular and chaotic motion was investigated (Chaiken et al., 1986), revealing an irreversibility of the mixing process for initial positions lying in the chaotic region of phase space. Consequently, in the context of chaotic dynamical systems, the absence of echoes and the inability to return to initial conditions has frequently been used as a test for chaotic dynamics (Casati et al., 1986; Roberts and Quispel, 1992; Pastawski et al., 1995; Eckhardt, 2003).

While in the previously mentioned cases the behavior changes gradually with the external parameter, Pine et al. (2005) described an unexpected phenomenology. Their experiment is similar in spirit to the well-known experiment by Taylor mentioned earlier. However, instead of injecting a single blob of dye, they investigated a suspension of small spheres ($d \approx 200\mu m$) dispersed in a viscous liquid, with volume fractions between 0.1 and 0.4. For small strain amplitudes, almost perfect reversibility is attained, and the diffusiv-

ity of the dispensed particles drops to zero. For large strains, on the other hand, a chaotic motion is observed, characterized by a finite diffusivity. The change between the two regimes shows features of a phase transition, characterized by a critical strain amplitude separating them. Subsequent studies have demonstrated a similar transitional behavior in other hydrodynamic experiments, using different flow geometries (Guasto et al., 2010; Metzger and Butler, 2012; Jeanneret and Bartolo, 2014) or different types of particles, for example fibers (Franceschini et al., 2011, 2014). However, long-range hydrodynamical interactions do not seem to be the source of the irreversibility, as has been investigated in a numerical study (Metzger and Butler, 2010). Hence, it is unsurprising that similar transitions have been observed in many more systems, for example particle systems (Keim and Arratia, 2013, 2014) or in systems of superconducting vortices (Mangan et al., 2008; Zhang et al., 2010; Okuma et al., 2010, 2011; Motohashi and Okuma, 2011). It has also been put into the context of more general order-disorder transitions in amorphous solids and glasses (Mohan et al., 2013; Regev et al., 2013; Fiocco et al., 2013, 2014) and granular systems (Slotterback et al., 2012; Schreck et al., 2013; Royer and Chaikin, 2014). The demonstration of the transition in several quite different systems suggests that it is a more general phenomenon for sheared many-body systems. And indeed, the transition has also been recovered in simple statistical models (Corté et al., 2008, 2009; Düring et al., 2009; Menon and Ramaswamy, 2009; Keim and Nagel, 2011).

> Ja es ist klar, daß jede einzelne gleichförmige Zustandsverteilung [...] gerade so unwahrscheinlich ist wie eine einzelne noch so ungleichförmige Zustandsverteilung. [...] Nur daher, daß es viel mehr gleichförmige als ungleichförmige Zustandsverteilungen gibt, stammt die größere Wahrscheinlichkeit, daß die Zustandsverteilung mit der Zeit gleichförmig wird.
>
> Yes, it is evident that every single uniform distribution of states [...] is just as unlikely as a single, however non-uniform distribution of states. [...] Only from the fact that there are many more uniform than non-uniform distributions of states comes the greater probability that the distribution of states becomes uniform over time.
>
> *L. Boltzmann, 1877*

In case of a thermodynamical system with the accompanying local fluctuations, no one seriously expects it to show reversible behavior. Yet, on a macroscopic level one observes that, depending on for example the ambient temperature, very different states of the system are attained. At low temperatures the system is in a solid or even crystalline phase, characterized by rigid next-neighbor relations. With increasing temperature, a phase transition takes place and the system liquefies. Bonds between particles break up and neighborhood relations change frequently. Just as in the case of sheared systems, this state of the system is characterized by a finite self-diffusivity.

Several mechanisms of melting have been proposed over the years (see e.g. Dash, 1999, for a brief overview). One possibility is a collective melting of the solid. A first idea of bulk melting was proposed by Lindemann (1910). In a crystal, particles vibrate about their lattice positions. He then suggested that melting occurs when amplitudes of vibrations become so strong that particles collide halfway their separating distance. Another

theory suggests that melting is mediated by thermal activation of lattice defects, namely dislocations. Since each dislocation reduces the activation energy of further defects in its neighborhood, upon exceeding a certain threshold in the defect concentration an avalanche of dislocations is triggered. However, solids in general have a surface, and this gives rise to a second kind of mechanism, surface melting. At the interface between the solid and the vapor a thin liquid layer forms out, optimizing the surface energy. This happens at temperatures below the melting temperature of the bulk. At the melting point, the layer thickness diverges and the solid melts. This mechanism is not limited to the outer surface of a crystal, but may also occur at internal surfaces, such as grain boundaries. When cooling down a liquid below the freezing temperature, the phenomenon of *supercooling* may be observed. Due to the interfacial energy between the two phases, lower temperatures are needed to trigger crystallization. However, experiments show that the opposite behavior, the *superheating* of a crystal, is more difficult to achieve and requires sophisticated experimental setups (Siders et al., 1999; Rousse et al., 2001) or numerical simulations of the bulk (Jin et al., 2001). This suggests a prevalence of the second mechanism, surface melting.

In an attempt to better understand melting, smaller systems consisting of only a few clustered particles have been investigated (Berry and Wales, 1989; Wales and Berry, 1990; Berry, 1990, 1993). An advantage of such small systems is that their potential energy landscape can be explored in much greater detail. Hence, it is possible to generate a mapping of the dynamical system onto different minimum configurations and describe the dynamics as a rate process, where the system hops between the minima (Stillinger and Weber, 1984a,b). With increasing temperature, the system will then become more volatile, corresponding to a liquefaction.

In this thesis, we restrict ourselves to a two-dimensional system of repelling particles, similar to a Wigner crystal. However, we add a screening to the Coulomb interaction. On the conceptual end, this allows us to gradually change the potential, from a very soft long-range potential to the short-range interaction of hard spheres. On the numerical end, it gives us the possibility to introduce a cut-off radius and reduce the computational demand. Additionally, a system of particles interacting via a screened Coulomb potential can be - and has been - realized in several experimental setups using macroscopic particles. A prime example are colloid systems, with micro-spheres immersed in an aqueous suspension (Van Winkle and Murray, 1986; Murray and Van Winkle, 1987; Tang et al., 1989). Typical particle diameters are in the range of $0.1\mu m$ to $1\mu m$, and each sphere acquires approximately 10^4 elementary charges. The preparation of the experiments is technically demanding, and once set up, the geometry of the experiment cannot be changed. Moreover, the system typically exhibits a strong damping which requires long observation times.

More flexibility is achieved by using complex plasmas (Thomas et al., 1994; Chu and I, 1994; Melzer et al., 1996a). The basis is a noble-gas plasma, generated by a biased capacitively coupled radio frequency discharge where the potential of the lower electrode is kept at a constant negative offset. The discharge is operated at low gas pressures of $1 - 100$ Pa. In the plasma, dielectric plastic spheres with diameters of approximately $10\mu m$ are dispensed. Free electrons attach to their surface, so that the charge of each sphere reaches $10^3 - 10^5$ elementary charges. Due to the balance between electric and gravitational forces, the spheres levitate. With the background of ions in the plasma, the

charging results in a screened Coulomb interaction between the macroscopic spheres, which is also confirmed by experiments (Konopka et al., 2000). When preparing the experimental conditions carefully, quasi-2d structures with spheres confined to only a few layers can be attained (Thomas and Morfill, 1996), and even true two-dimensional crystals consisting of a single layer of particles can be produced (Quinn and Goree, 2001; Nosenko et al., 2006; Knapek et al., 2007; Nosenko et al., 2009).

As a peculiarity, two-dimensional systems can exhibit a somewhat different melting transition (summarized in Strandburg, 1988, and references therein). Defect-mediated bulk melting proceeds as a two-step process. In a first step, defects emerge which destroy the long-range ordering of the crystal, but preserve the orientation between next neighbors. Only in a second step at a higher temperature, defects of another kind emerge that break the orientational order, and the transition towards the liquid phase takes place. Alternatively, an edge melting mechanism is possible, equivalent to surface melting. It gives rise to a single transition, preempting the two-step process. Similar to its three-dimensional counterpart, it can occur at internal surfaces, such as grain boundaries between differently orientated crystallites.

The outline of this thesis is as follows. In chapter 2, we will discuss the phenomenon of the order-disorder transition in sheared suspensions in a simplified system where we only consider key features of the suspension experiment. To this end, we take mutually repelling particles, confined in a two-dimensional box and subject to an external periodic shear. This allows a much more detailed study of the long-term behavior as well as a broader inspection of parameter space. That this approach appears to be promising has already been proven by the reproduction of the transition using a simple statistical discrete time model (Corté et al., 2008). In the course of our studies, we will also investigate stability properties, which help to understand the transition to irreversibilty, as well as spatial particle correlations, allowing deeper insight into the system.

In chapter 3, we turn towards the melting transition in two-dimensional systems. In a first step, we perform molecular-dynamics simulations of a screened Coulomb system. To characterize the transitions, several reliable indicator functions are taken into account. Special attention is put on the microscopic effects that lead to melting, decoded in the computed trajectories. Here, we observe that the melting transition is accompanied by localized structures where neighboring particles exchange their places. At this point, we pick up on the idea of cluster melting and minimum hopping and aim in a similar direction. For obvious reasons, the approach to characterize the potential energy landscape of the full system is futile in a large system comprising several thousand particles. Hence, we concentrate on the localized processes which initiate the melting process and try to determine in which way they can be linked to a melting of the crystal. The idea to connect the solid-to-liquid phase transition to a rate process was already brought up several decades ago by Penner (1948). Although he made very elementary assumptions, he was able to reproduce Einstein frequencies on the order of magnitude of several other approaches.

Thus, the remaining part of the thesis is dedicated to the examination of the localized structures. In chapter 4, we start by investigating a reduced system. There, we consider a large crystalline lattice, and allow only two or three particles to move. This gives us access to lattice dynamics which are slightly more complicated than the well-known formation of vacancies and interstitials, for example the exchange of two or three particles. In

the limit of low enough temperatures, transitions only occur along trajectories of low potential energy. They pass through transition states, energetically activated equilibrium configurations of the system which are metastable and decay towards the one or the other minimum. Hence, these bottlenecks of the dynamics dominate the transitions and are of particular interest.

We generalize the results in chapter 5, where we return to the full system with all particles being free to evolve. We introduce an algorithm, edge tracking, which allows us to identify the transition states in the high-dimensional potential energy landscape. For demonstration, we take the exchange of two neighboring particles and, in this context, discuss the connections between the many-body system and the continuum description of an elastic medium. There we are able to model the displacement field induced by the transition state with a simple approach, mimicking the central displacements by singular forces in an elastic body.

In chapter 6 we apply the edge tracking algorithm on more complicated transitions and gather localized transition states for up to 18 participating particles. Thereafter, we analyze the properties of the different transition states in detail. We consider for instance the localization, their associated energy barriers and transition rates and see how they fit with the anticipated temperature of melting. In case of two- and three-particle exchanges, we also compare them to the reduced model. Finally, we investigate the influence of the potential on the transition states by varying its screening parameter, and examine various quantities such as the displacement fields and the localization. We again compute overall rates and compare their dependence on the potential both to experimental melting temperatures and to predictions of the Lindemann criterion (Lindemann, 1910).

We briefly conclude in the final chapter with some remarks and ideas for future work.

2

The transition to irreversibility in a sheared many-body system

The topic covered in this section has been addressed in collaboration with Georg Ehlers and Tobias Bischoff, who were involved in the simulation of the smaller system and first analyses.

Parts of the results presented in this chapter have been submitted for publication in Physical Review E *on June 17, 2015. A pre-print is made publicly available at http://arxiv.org/abs/1507.04926.*

In this chapter, we investigate the transition from reversible to irreversible motion in a sheared suspension. We start with a short introduction on our simplified model, before we turn to a thorough investigation of its properties. We demonstrate that it shows the same abrupt transition to irreversibility observed in experiments by Pine et al. (2005). We characterize both states of the system, and perform a linear stability analysis to connect the onset of chaotic behavior to stability properties of the underlying regular lattice configuration. Finally, we analyze the particle correlations of the system, how they change with the shear rate and to which extent they can explain previous observations.

2.1 The model and its parameters

For our model we do not aim to calculate the detailed hydrodynamic interaction or exact forces between charged colloids, as done in the simulations of Pine et al. (2005). Rather, we pick an interaction force that captures key features of the fluid-particle system. This is similar in spirit to the proposal in Corté et al. (2008), but differs in the fact that the model is a continuous one and not an event-driven mapping. We assume that the motion of the many body system is overdamped, so that there is no motion if the external forcing ceases. The forces on the particles are hence balanced by viscous friction, and the equations of motion become

$$\mu \frac{\mathrm{d}\boldsymbol{x}_i}{\mathrm{d}t} = \boldsymbol{F}_i, \tag{2.1}$$

where μ is the damping coefficient. We take the interaction between the particles as repulsive, thereby mimicking the repulsion due to liquid pressure when two particles come close. With this repulsive interaction, the system is reminiscent of Wigner crystals and clusters of charged particles in plasmas (Melzer et al., 1996a,b; Schweigert et al., 1998). The particles are confined to a plane, and the domain is taken to be rectangular, and not

curved as between the cylinders in the experiments of Pine et al. (2005). It is periodically continued in both directions. The main control parameter will be the amplitude of the forcing. A second parameter controls the strength of the interaction between the particles; it is also related to the density of the system, as will be discussed below.

Forces

The repulsion between the particles is modeled as a potential with power-law decay, $V(r_{ij}) \propto r_{ij}^{-\alpha}$, with r_{ij} the distance between particles i and j. We here take $\alpha = 2$ as a compromise between strong repulsion for short distances (i.e. larger α) and a numerically controllable range of the interaction (where hydrodynamics would suggest a decay as slow as $\alpha = 1$). Coordinates are x along the direction of shear and y normal to it. Particle positions are denoted $\boldsymbol{x}_i = (x_i, y_i)$. The total force acting on the i-th particle is the sum of the mutual interactions with all other particles in the system and a periodic shear force in the x-direction whose amplitude increases linearly with y_i,

$$\boldsymbol{F}_i = -\boldsymbol{\nabla} \left(\sum_{j \neq i} \frac{A}{\|\boldsymbol{x}_i - \boldsymbol{x}_j\|^2} \right) + S y_i \cos(\omega t) \boldsymbol{e}_x. \tag{2.2}$$

The parameter A determines the strength of the inter particle potential, Sy_i is the amplitude of the shear force and ω is its frequency. Substituted into eqn. (2.1), we obtain the full expression for the time evolution of the position of the i-th particle,

$$\frac{\mathrm{d}\boldsymbol{x}_i}{\mathrm{d}t} = 2\frac{A}{\mu} \sum_{j \neq i} \frac{\boldsymbol{x}_i - \boldsymbol{x}_j}{\|\boldsymbol{x}_i - \boldsymbol{x}_j\|^4} + \frac{S}{\mu} y_i \cos(\omega t) \boldsymbol{e}_x. \tag{2.3}$$

Parameters

In order to expose the independent parameters of the system, we introduce a length scale λ and a time scale T, i.e. $\boldsymbol{x}_i = \lambda \boldsymbol{x}'_i$ and $t = Tt'$. The time T can naturally be identified with the period of the shear, $T = 2\pi/\omega$. The length scale is not related to a quantity explicitly displayed in the equations, but it enters implicitly in the many-body system via the mean distance between particles, and is thus related to the density. Therefore, variations in period and density are absorbed into the two remaining parameters of the system, the dimensionless interaction strength

$$\Gamma_1 = 2AT/\mu\lambda^4 \tag{2.4}$$

and the dimensionless shear rate

$$\Gamma_2 = ST/\mu. \tag{2.5}$$

The evolution equations then become

$$\frac{\mathrm{d}\boldsymbol{x}'_i}{\mathrm{d}t} = \Gamma_1 \sum_{j \neq i} \frac{\boldsymbol{x}'_i - \boldsymbol{x}'_j}{\|\boldsymbol{x}'_i - \boldsymbol{x}'_j\|^4} + \Gamma_2 y'_i \cos(2\pi t) \boldsymbol{e}_x. \tag{2.6}$$

In favor of a concise notation we will drop the primes in the subsequent sections.

The instantaneous strain $\gamma(t)$ follows from the time evolution of the distance between two particles being advected that initially are displaced by Δy perpendicular to the shear. The separation in x-direction is then given by $\Delta x(t) = \gamma(t)\Delta y$ with

$$\gamma(t) = \frac{\Delta x(t)}{\Delta y} = \Gamma_2/(2\pi)\sin(2\pi t) = \gamma_0 \sin(2\pi t). \tag{2.7}$$

Here, $\gamma_0 = \Gamma_2/(2\pi)$ is the amplitude of the affine shear, and directly related to the shear rate. This also gives a notion of the shear process: At the start of the period, $t = 0$, the strain is zero. Over the next half period, the system gets tilted to the right, reaching its apex at $t = T/4$. Here, the flow comes to a halt and reverses its direction. After half a period, strain is again zero and the same process repeats to the left. The mean accumulated strain over one period then reads[1]

$$\gamma = 1/T \int_0^1 |\gamma(t)|dt = \Gamma_2/\pi^2. \tag{2.8}$$

2.1.1 Numerical implementation

In order to solve equation (2.6), we introduce Lees-Edwards boundary conditions (Lees and Edwards, 1972) to account for the sheared images in the y-direction. We use a modified minimum image convention, taking several closest images of each particle into account, typically one or two in each direction. Time integration is performed using a 4th order Runge-Kutta-Fehlberg integrator provided by the GNU Scientific Library (GSL) (Galassi et al., 2010). To speed up computations, the right-hand side of eqn. (2.6) is parallelized using openMP.

The width of the box (in the x-direction) is $L_x = k$, whereas its height (in the y-direction) is $L_y = \sin(\pi/3)l$, with $k, l \in \mathbb{N}$ even and $kl = N$ the total number of particles. The ratio is chosen such that a perfect hexagonal lattice[2] can be accommodated. The typical number of particles in the main domain is about 100, and in a few examples we went up to 900 particles. The simulation was carried out with random initial conditions, and the motion was typically followed over several thousand periods in order to obtain clear evidence for the asymptotic state and to extract reliable statistics in the case of chaotic states.

2.1.2 Reduced representation and stroboscopic maps

Even for small shear, particles undergo large scale motions along the shear axis the further they are displaced in the normal direction. In order to remove this affine deformation, we

[1] The variable γ due to Pine et al. (2005) is defined as $4\gamma_0$, and hence corresponds to 2π the present γ. It adds up the maximum strain per quarter period.

[2] By 'hexagonal lattice', we denote the regular 2d-lattice where each lattice site has six nearest neighbors and space is tessellated with triangles. Accordingly, in literature the lattice is sometimes referred to as 'equilateral triangular lattice'.

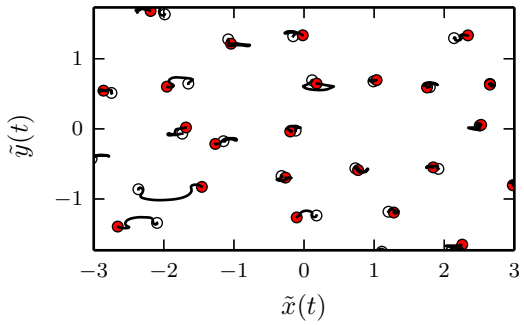

Figure 2.1: Particle trajectories over one period. Initial positions are marked by open circles, final positions by filled red circles. Shown are the reduced positions, eqn. (2.9), after subtracting the affine transformation. Non-reversible motions (in particular in the lower left corner) are connected with close encounters and large displacements. The parameters are $\Gamma_1 = 0.1$ and $\Gamma_2 = 16.0$. Movies of the full motion are found online[3].

introduce a reduced representation where the translation by the shear is removed, i.e. we study

$$\begin{aligned} \tilde{x}_i(t) &= x_i(t) - y(t_0)\gamma_0 \sin(2\pi t) \\ \tilde{y}_i(t) &= y_i(t). \end{aligned} \tag{2.9}$$

Figure 2.1 shows examples of such reduced motions: for the chosen parameters the amplitudes of the motion around the reference positions are small and most particles stay close to their initial positions, but as the group in the lower left corner shows, some of them can experience large displacements as a consequence of close encounters. In addition, movies of the full dynamics at two different shear rates are found online[3].

The long time behavior of the system shows up after a large number of periods only, and it is more appropriate to study it in the form of stroboscopic maps, with particle positions sampled at multiples of the period, $\boldsymbol{x}_i(n) = \boldsymbol{x}_i(nT)$. Figure 2.2 compares two examples, one for smaller shear rate and one for larger shear rate. Corresponding movies are found online[4]. For moderate shear rates, only small displacements are observed, and as we will study in more detail in section 2.2, the particles evolve slowly towards regular lattices. Larger positional changes are subject to local reorganizations, seen e.g. in the lower right corner of the left diagram. The pictured process takes about 500 time units. For larger shear, almost all particles travel large distances from their initial position. Accordingly, we do not observe an underlying lattice structure, and in the course of only 25 time units the whole domain gets mixed with particles being displaced over several next neighbor distances. This corresponds to the disordered state of Pine et al. (2005). The random motion of the particles can be captured by diffusion coefficients, which are anisotropic and differ in the longitudinal and transverse directions.

[3] `https://youtu.be/oFcrWo9Vs6E`, `https://youtu.be/tcowb7o05JQ`
[4] `https://youtu.be/GkEUwycn7V4`, `https://youtu.be/k-XCo8CWFU8`

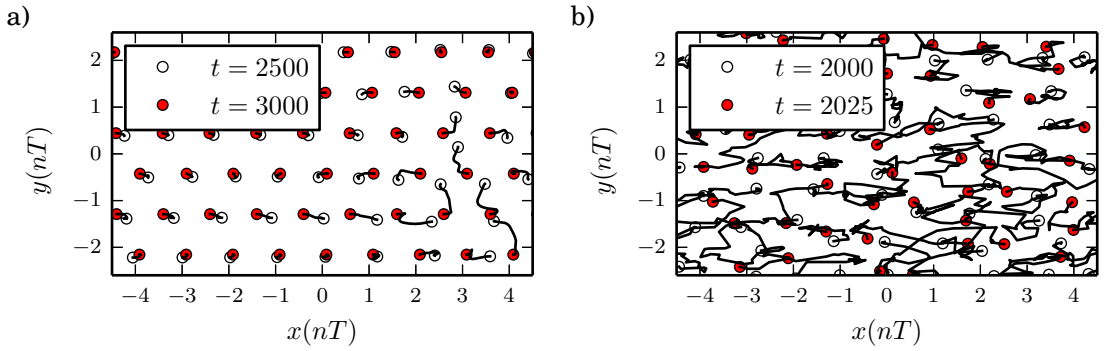

Figure 2.2: Stroboscopic maps of particle trajectories for low shear ($\Gamma_2 = 8$, (a)) and large shear ($\Gamma_2 = 16$, (b)). Initial positions are marked by open circles, final positions by filled red circles. In the left diagram with the system subject to low shear, over a period of 500 time units particles show only little movement. In the right part of the figure, a local reorganization is initiated which results in large displacements for a few particles. In the right diagram for large shear, all particles are displaced substantially and rather randomly in a much shorter interval of 25 time units. In both cases $\Gamma_1 = 0.1$. Corresponding movies are found online[4].

2.2 Ordered and disordered states

2.2.1 Ordered states

In the absence of external forcing, the interactions between the particles push a random initial condition towards a force equilibrium. A regular lattice, such as a hexagon, is an example of such an equilibrium, but it will rarely be reached from a random initial condition since particles will be trapped in a state with a few dislocations or in a state showing several oriented patches, separated by grain boundaries.

As soon as shear is added to the system, particles will start to rearrange and to self-organize. After sufficiently long times, states like the ones shown in figure 2.3 for $\Gamma_2 = 2$, 6, and 8 are obtained. They all show regular lattice configurations with a few defects. For very low shear rates the system settles into the hexagonal configuration, with an orientation relative to the shear direction that depends on the initial conditions and not so much on the shear. Since the regular hexagonal state is a possible force-equilibrium, the external forcing can be regarded as a minor perturbation that barely affects particle interactions. With increasing shear rate, the lattice orientation may change, and the lattice will align parallel or perpendicular to the external force. At a shear rate $\Gamma_2 \approx 6$, the asymptotic state is given by a rectangular lattice configuration. However, at $\Gamma_2 \approx 8$ we again observe a hexagonal lattice, though this time it is always oriented parallel to the shearing motion. Increasing the rate further, the system will at some point fail to approach an asymptotic ordered state, and instead it shows random particle displacements over a period: a chaotic, disordered state is attained. We will return to the different lattice configurations in section 2.3.3, where we further discuss their occurrences in the course of a linear stability analysis.

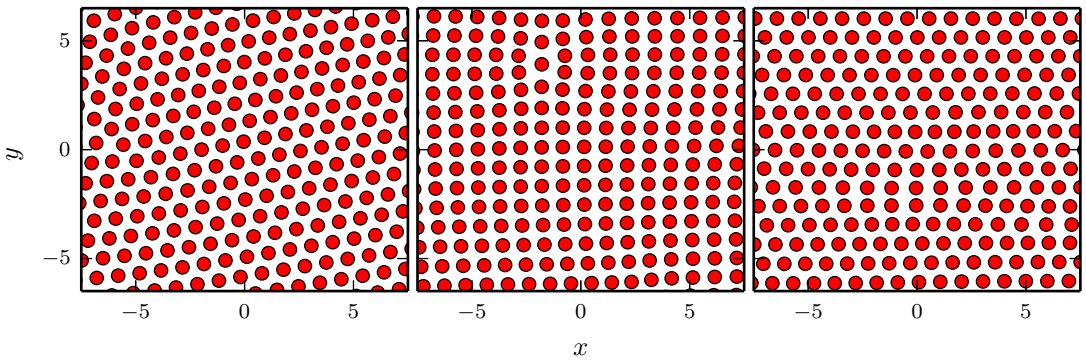

Figure 2.3: Asymptotic states at moderate shear rates, from left to right $\Gamma_2 = 2$, 6, and 8, respectively. Except for minor defects they are either a hexagonal or a rectangular lattice configuration. At $\Gamma_2 = 2$, shearing is a small perturbation and the lattice orientation is determined by the initial conditions. At higher shear rates, the lattice aligns with the external forcing. $\Gamma_1 = 0.1$ in all three cases. Examples are taken from 900-particle ensembles.

2.2.2 Diffusion constants

Suitable scalar quantities that can be used to distinguish the different long-time dynamics are related to the diffusive motion of the particles. The local and instantaneous quantity is the mean displacement of particles over one period,

$$\delta(t) = \langle \| \boldsymbol{x}_i(t) - \boldsymbol{x}_i(t-1) \| \rangle_i \tag{2.10}$$

It provides a convenient measure to quickly distinguish between regular and irregular states, as shown in figure 2.4. For large shear ($\Gamma_2 = 16$) the mean displacement is large and varies little in time, indicating a disordered, chaotic state. For low shear ($\Gamma_2 = 8$) it decreases, eventually reaching machine precision: the system evolves towards a stable state. The intermediate maxima, such as the one near $t = 2800$ in figure 2.4(b), indicate reorganizations which remove lattice defects. The denoted event is related to the rearrangement in the lower right corner in figure 2.2(a) and clearly visible in the movie[4].

In the irregular state, we can calculate diffusion constants. In view of the asymmetry in the system in the directions along the shear and perpendicular to it, we consider two separate diffusion constants. We will give the definitions for diffusion along the shear, with the ones in the perpendicular direction being defined by corresponding expressions. The diffusion constants can be obtained either by averaging in time over the mean displacements over one period,

$$\left\langle \frac{1}{N} \sum_{k=1}^{N} |x_k(n) - x_k(n-1)|^2 \right\rangle_{n > n_{\text{transient}}} = 2 D_x \gamma, \tag{2.11}$$

or by approximating the development of the mean square displacement of the particles by a linear relationship,

$$\langle \Delta x^2(n) \rangle = 2 D_x \gamma n. \tag{2.12}$$

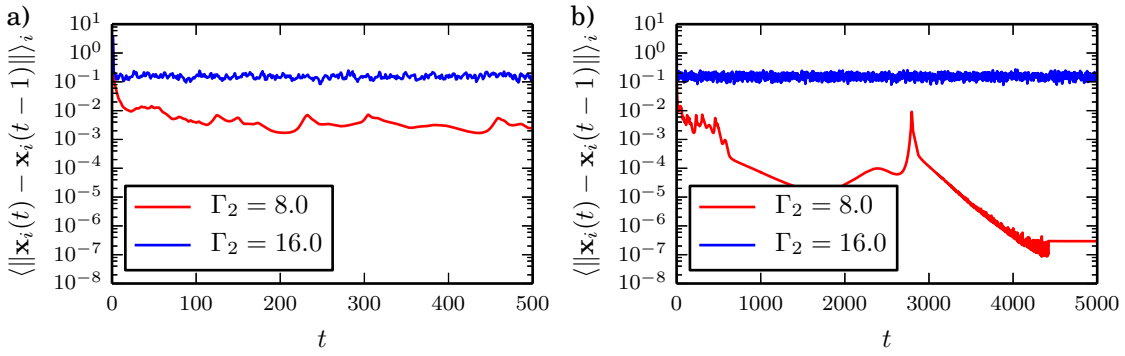

Figure 2.4: Average displacement after one period for different shear rates Γ_2 on two different timescales, starting from random initial conditions. (a) On short timescales both shear rates result in fluctuations of the mean displacements, with higher frequencies for larger shear rates. (b) On longer timescales the displacements for lower shear rate drop to numerical precision, with intermediate bumps indicating local reorganizations. For larger shear rates, the mean displacements approach a finite value reflecting the random motion. $\Gamma_1 = 0.1$.

The factor γ is adopted from the definitions in Pine et al. (2005). Due to the slightly different definitions, we call eqn. (2.11) short term diffusivity, whereas eqn. (2.12) is its long term cousin. For an uncorrelated diffusive process, both values are expected to coincide. Averages are taken after initial transients have decayed. The number of periods one has to wait depends on the system size and the asymptotic behavior: In the disordered regime, the system approaches its final state quickly. However, it may take several thousand periods when in the reversible regime and the system approaches an ordered configuration. Once the final state is attained, data is collected over $n \approx 10^3$ to 10^4 periods.

We start by investigating the two shear rates considered in the previous section, $\Gamma_2 = 8.0$ and 16.0. In order to gain better statistics, we consider a 900-particle system and eliminate transient effects by dismissing the initial 5000 periods. Thereafter, data is collected continuously over each 200 consecutive periods for several thousand periods. The resulting squared displacements as a function of accumulated strain γt are shown in figure 2.5 in a double logarithmic representation. At the lower shear rate, displacements are very small, as expected, and grow steadily over time. Apparently, they are not generated by a diffusive process as they grow quadratically, which is a sign of ballistic transport. Additionally, the displacements are slightly larger than in the corresponding 100-particle system shown in figure 2.4. Both observations can be easily explained: In contrast to the smaller system which reached the hexagonal state, the 900-particle system still exhibits some lattice defects implying small but non-zero forces. At the higher shear rate of $\Gamma_2 = 16.0$, the mean square displacements are much larger with initial displacements on the order of 0.1 particle distances. They quickly grow over time, reaching the regime of regular diffusion. We can extract the short time diffusivity from the left-most data point. At least in this example, the long term diffusion is larger than its short term counterpart. Consequently, when fitting data to eqn. (2.12) the first few periods are neglected. More generally, with increasing accumulated strain, the squared displacements will at some point saturate due

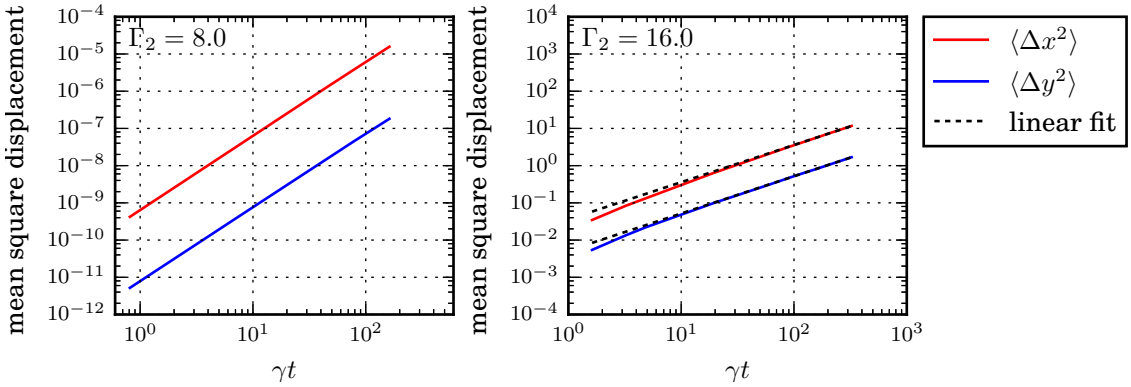

Figure 2.5: Mean square displacements at the two shear rates discussed in the previous section, $\Gamma_2 = 8.0$ and 16.0, plotted against the accumulated strain in a doubly logarithmic plot. Data was taken with the 900-particle system after 5000 initial periods, permitting the system to find its asymptotic state. At $\Gamma_2 = 8.0$, the system slowly approaches a reversible state. Hence, the mean square displacements are very small and not generated by a diffusive process, as can be determined from the slope of $b = 2$. In the irreversible regime at $\Gamma_2 = 16.0$, mean square displacements grow fast over the first few periods and then reach the regime of regular diffusion with a slope $b = 1$. Linear fits were performed over the last 100 of 200 data points.

to the limited box-size. In such a case further data points would have to be excluded. We also observe that for both shear rates the parallel displacements are enhanced in comparison to the perpendicular ones by at least one order of magnitude. We will address this in more detail in section 2.2.4.

2.2.3 Transitions for fixed Γ_1

Since the simulation of large ensembles is computationally expensive, we concentrate on a system size of $N = 100$ from here on. To verify that the results are not affected by the system size, we occasionally investigate systems of size $N = 900$ for a few parameter values. While the results for the diffusion constants seem to be independent of the system size, the time for transients to decay increases rapidly with system size and adds to the numerical challenges.

We begin the exploration of the parameter space of the system with a fixed interaction parameter $\Gamma_1 = 0.1$ and different shear rates Γ_2. We compare both short term and long term diffusivities in figure 2.6. As anticipated from the results in the previous section, we notice two qualitatively different states. They are characterized by the diffusion constant: In the one case, we find zero diffusivity and motion is reversible. In the other case, the diffusivity attains a finite value and the system is in an irreversible state. For this specific set of parameters, we computed the diffusivities both for a 100 and a 900 particle system. Up to a shear rate of Γ_2 just above 30.0, the results are in very good agreement. Beyond this value, the system with 100 particles gives slightly higher values. This is most likely caused by finite size effects: At $\Gamma_2 = 36$, which corresponds to a strain amplitude $\gamma_0 = 5.73$,

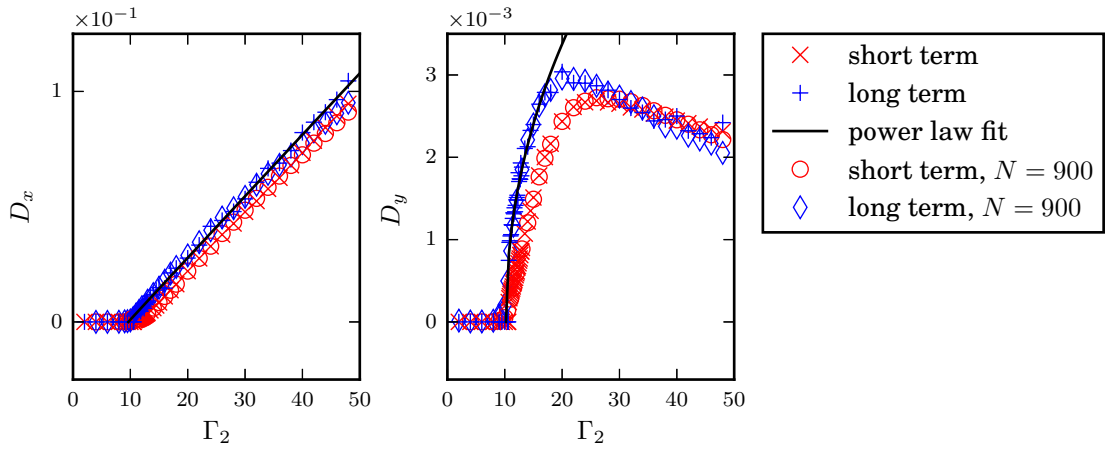

Figure 2.6: Diffusivities along the x- and y-direction, left and right panel respectively, for $\Gamma_2 = 0.1$. For low shear rates, no diffusion is observed, corresponding to a reversible state. At a critical point $9.5 < \Gamma_{2,c} < 10.5$ diffusions start to grow, both parallel and perpendicular to the shear, corresponding to an irreversible state. The short term diffusivity is slightly smaller than the long term diffusivity. Moreover, diffusion parallel to the shear is strongly enhanced and shows a different behavior: It grows linearly with increasing shear whereas diffusion in the perpendicular direction saturates and even decreases for very strong shear. Boundary effects due to the system size seem to be negligible up to $\Gamma_2 \approx 30.0$ since data points for 100- and 900-particle systems coincide well.

particles separated by the spacing of lattice rows $\Delta y = \sqrt{3}/2$ in the normal direction get advected by one box length relative to each other in the course of one period. Therefore, at the left and right turning points of the shearing motion, a particle experiences the same neighborhood.

The transition between reversible and irreversible motion as the shear rate is varied shows up rather clearly. For $\Gamma_1 = 0.1$, this transition takes place near $\Gamma_2 \approx 10.5$. Fitting a power law of the form $D = \delta\,(\Gamma_2 - \Gamma_{2,c})^{\beta}$ returns an exponent $\beta_x = 1.00$, a critical value $\Gamma^x_{2,c} = 9.6$ for the diffusivity in the shear direction, and $\beta_y = 0.47$ and $\Gamma^y_{2,c} = 10.2$ for the diffusivity in the normal direction. The values for the critical shear rate are lower than the point where a non-zero diffusivity is first observed. Closer inspection of the variations near the critical point reveals that diffusivities drop to zero abruptly, suggesting a small region where ordered and disordered motions coexist, so that the transition could be subcritical. Unexpected are the differences in the exponents: Parallel to the shear direction, the diffusivity grows linearly with the shear, but perpendicular to it, the diffusivity varies with a square root. Overall, the sharp transition is in qualitative agreement with the results both from experiments and simulations by Pine et al. (2005) and Metzger and Butler (2010) as well as Guasto et al. (2010), who investigated an oscillatory channel flow.

We find that the short term diffusivity eqn. (2.11) is slightly lower than its long term counterpart. Parallel to the shear direction, the difference approaches a constant value, whereas in the perpendicular direction, it diminishes for larger shear rates. Our interpre-

tation is that on short time scales, each particle is captured in a matrix of surrounding particles. Their presence introduces memory and correlations into the process, thereby reducing the diffusion coefficient. This effect is most pronounced in the parameter range close to the transition and becomes weaker with increasing shear.

2.2.4 Anisotropy in diffusion

We also notice that horizontal diffusivities are much stronger than vertical ones. This is due to the shear acting only along the x-direction and was also observed in other investigations considering similar systems (Pine et al., 2005; Metzger and Butler, 2010). Moreover, for very larger shear rates the vertical diffusivity decreases, probably approaching a fixed value, whereas the horizontal diffusivity grows linearly in the investigated parameter range.

The phenomenon of enhanced diffusion in the presence of a shear flow is known as advection-diffusion coupling and has been solved in the case of Brownian motion by Young et al. (1982). They showed that both diffusion constants are related to each other by

$$D_x = D_{x,0} + \frac{1}{2}\gamma_0^2 D_y, \tag{2.13}$$

where γ_0 is the strain amplitude, cf. eqn. (2.7). Thus, parallel diffusion is enhanced by a coupling between normal diffusion and shearing. The bare longitudinal diffusivity adjusted for this effect is denoted $D_{x,0}$. The mechanism can be illustrated in a three step process by decoupling diffusion and advection: In the first step, we observe diffusion perpendicular to the shear so that particles are found in the layer above. In the next step, this layer is advected by the shear over some distance. In the last step, particles in the upper layer diffuse back to the original layer. Since they have been transported by the flow, they have traveled further than by horizontal diffusion alone. For an isotropic system, both the corrected longitudinal and the transversal diffusivity coincide.

In figure 2.7, we show the corrected parallel in relation to the perpendicular diffusivity. Data was taken with the 900-particle system. Since D_y is two orders of magnitude smaller than D_x, combinations of D_x and D_y are to be expected of low accuracy. Therefore, we consider the quotient $D_x/(1 + \frac{1}{2}\gamma_0^2)$, presuming the underlying diffusive process is isotropic. In the limit $\gamma_0 \gg 1$, this expression should approach D_y and $D_{x,0}$. We observe that the corrected parallel diffusivity is noticeably larger than the perpendicular diffusivity, contrary to the expectations for an isotropic system. Moreover, we can extract a factor between the two of approximately 1.5 over the whole range, even in the limit $\Gamma_2 \approx 50$, i.e. $\frac{1}{2}\gamma_0^2 \approx 32$. In order to preserve this relation, the bare horizontal diffusivity $D_{x,0}$ has to grow with the shear rate. We verified that this effect is independent of the boundary conditions, by repeating the simulations in a quadratic box which yields the same results.

The situation changes for stronger interactions Γ_1. The diffusivities for $\Gamma_1 = 1.0$ are presented in figure 2.8. Due to the strong interaction and the resulting steeper gradients, integration times increase considerably. Below $\Gamma_2 = 28$, the system has not yet converged towards an ordered state: While most particles are arranged in a lattice configuration, unordered regions exist which slowly settle. This is also reflected in the squared displacements: Instead of approaching a linear growth for larger γt such as in figure 2.5(b), they obey a power law, $\langle \Delta y^2 \rangle = 2D_y(\gamma t)^\alpha$ with $\alpha > 1$. For larger shear rates, the simulation

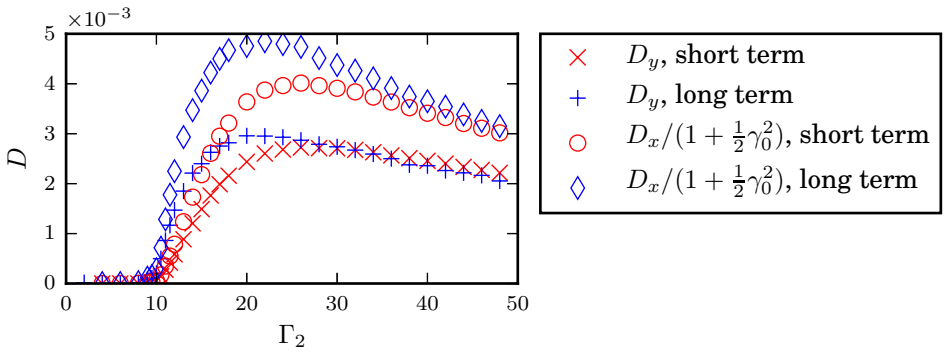

Figure 2.7: Relation of the corrected parallel diffusivity (eqn. (2.13)) to the perpendicular diffusivity. The rescaled parallel diffusivity (open symbols) is still stronger, indicating a true anisotropy. Data was taken with the 900-particle system.

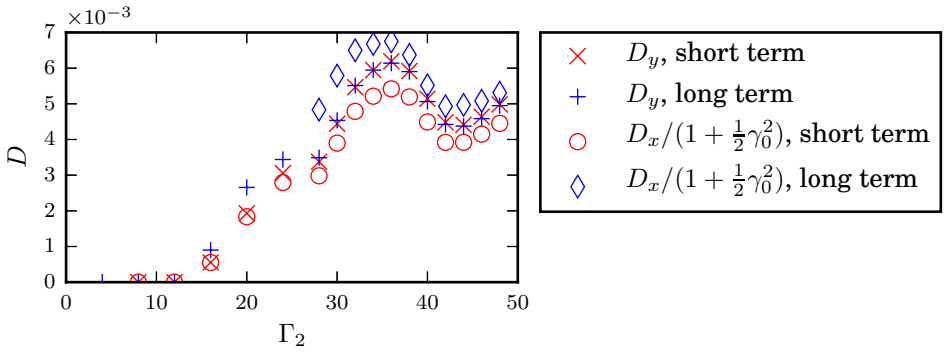

Figure 2.8: (Rescaled) diffusivities at $\Gamma_1 = 1.0$. Below $\Gamma_2 = 28$, the simulation has not converged towards the asymptotic ordered state: While most particles are arranged in a lattice structure, multiple defects exist which slowly grow out. Therefore, the long term diffusivity strongly deviates from the short term diffusivity and is neglected. At larger shear rates $\Gamma_2 \geq 28$, we observe good agreement with eqn. (2.13), i.e. the anisotropy is caused by advection-diffusion coupling.

has converged and both the short term and long term diffusivity perpendicular to the strain coincide. Virtually the same applies to the longitudinal diffusivity, though we do not observe perfect agreement. The cause for the deviation is the same as for $\Gamma_2 = 0.1$. The motion of particles parallel to the shear is correlated over a few periods before they show diffusive behavior. The more important observation is that the rescaled diffusivities $D_{x,0}$ in figure 2.8 nicely bracket the perpendicular diffusivity. Thus, the anisotropy can be explained completely by advection-diffusion coupling.

2.2.5 Exploration of the Γ_1-Γ_2-parameter plane

The question which arises is what makes the difference between the two entirely different observations, the only parameter changed being the strength of particle interactions. Before we address this further below in section 2.4, we first want to get a broader un-

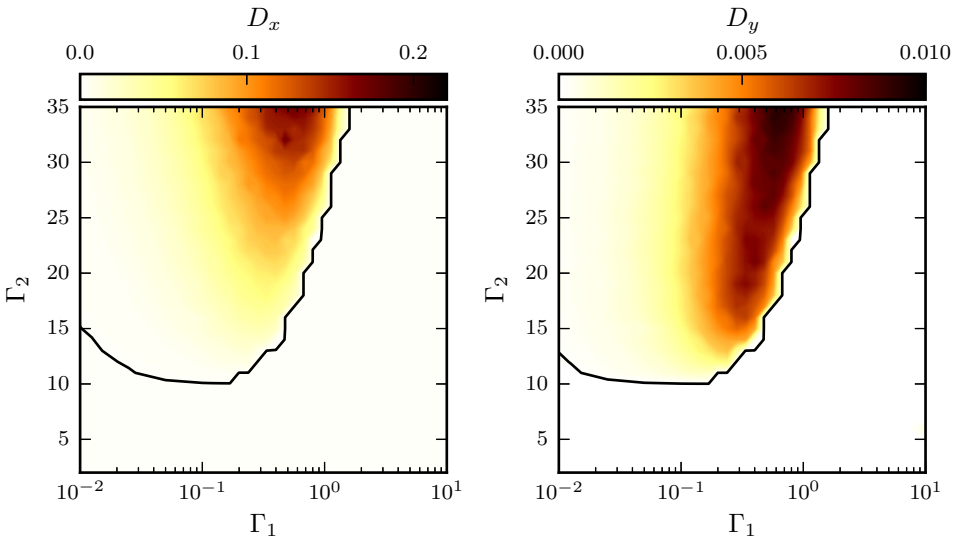

Figure 2.9: The long term diffusion constants D_x (left panel) and D_y (right panel) for different values of Γ_1 and Γ_2. The diffusivity is obtained by fitting data with eqn. (2.12). The black lines indicate $D_x = 1 \times 10^{-4}$ and $D_y = 1 \times 10^{-5}$, respectively. Data was taken with the 100-particle system. Hence, values for $\Gamma_2 > 35$ are ignored due to boundary effects.

derstanding of the dependence on both the shear rate and the interaction strength. In figure 2.9, both parallel and perpendicular diffusivities are shown in a large domain of the parameter space $\Gamma_1 \times \Gamma_2$. We observe a general increase of diffusivity with the interaction parameter Γ_1 up to a critical value where diffusivity drops to zero. A small diffusivity D for small values of the interaction parameter Γ_1 is plausible, since a relatively higher shear rate Γ_2 is needed to bring particles closer together and to allow the system to display large spatial fluctuations. For large interaction parameters we see the same behavior, but for a different reason. Since the interaction is comparatively strong, we need a high shear rate to keep the particles away from their equilibrium positions. For small Γ_1 the dominant force is the external forcing, and hence, after one period the particles are very close to where they were one period before. This leads to a small diffusion constant. In fact, the settling timescale becomes so long that we cannot measure a proper diffusion constant. However, there are qualitative differences depending on the shear rate Γ_2: For small shear rates, the particles are evenly distributed, but unordered, whereas for larger shear rates, the particles are uniformly distributed. This is also supported by two-particle correlation functions. However, the transition is not sharp. On the other hand, for large Γ_1, the settling time scale is shorter, and since the period of the external forcing is fixed to 1, we expect to find a critical region where particles settle into an ordered state before they can start moving in a random fashion. This is reflected in a relatively sharper transition in figure 2.9 for Γ_1 around 1.

2.3 Linear stability analysis

In this section, we will try to explain some of the properties of the system with the help of linear stability theory. Therefore, we linearize the evolution equation (2.6) around a solution trajectory,

$$\boldsymbol{x}_i(t) = \boldsymbol{x}_i^o(t) + \boldsymbol{\delta}_i(t). \tag{2.14}$$

This yields a system of linear ordinary differential equations for the perturbation vector $\boldsymbol{\delta}(t)$,

$$\frac{\mathrm{d}\boldsymbol{\delta}}{\mathrm{d}t} = \Gamma_1 \left(\mathcal{D}(t) - \mathcal{M}(t)\right) \boldsymbol{\delta} + \Gamma_2 \mathcal{S}(t)\boldsymbol{\delta} = \mathcal{W}(t)\boldsymbol{\delta}. \tag{2.15}$$

The right-hand side of this system consists of a time-periodic coefficient matrix $\mathcal{W}(t)$ composed of $2N \times 2N$ matrices

$$\mathcal{D}(t) = \begin{pmatrix} G_1 & & 0 \\ & \ddots & \\ 0 & & G_n \end{pmatrix}, \tag{2.16}$$

and

$$\mathcal{M}(t) = \begin{pmatrix} 0 & B_{1,2} & \cdots & B_{1,n} \\ B_{1,2} & 0 & \cdots & B_{2,n} \\ \vdots & \vdots & \ddots & \vdots \\ B_{1,n} & B_{2,n} & \cdots & 0 \end{pmatrix}, \tag{2.17}$$

where $G_i(t) = \sum_{j \neq i} B_{i,j}(t)$ with the 2×2 Jacobi matrices $B_{i,j}(t)$ of the pairwise particle interactions,

$$B_{i,j}(t) = \frac{\mathbb{I}_2}{\|\boldsymbol{x}_i^o - \boldsymbol{x}_j^o\|^4} - \frac{4\left(\boldsymbol{x}_i^o - \boldsymbol{x}_j^o\right) \otimes \left(\boldsymbol{x}_i^o - \boldsymbol{x}_j^o\right)}{\|\boldsymbol{x}_i^o - \boldsymbol{x}_j^o\|^6}. \tag{2.18}$$

Here, $\otimes$ denotes the dyadic product and $\mathbb{I}_2$ is the identity-matrix in two dimensions. Additionally, we have the Jacobi matrix of the external forcing,

$$\mathcal{S}(t) = \begin{pmatrix} S_2(t) & & 0 \\ & \ddots & \\ 0 & & S_2(t) \end{pmatrix}, \quad S_2(t) = \begin{pmatrix} 0 & \cos(2\pi t) \\ 0 & 0 \end{pmatrix}. \tag{2.19}$$

2.3.1 Local stability: Lyapunov exponents

Before investigating the limit cycles of the simulations, we take a look at typical trajectories. More specifically, we are interested in the stability of single-particle trajectories which may be the origin of tipping points from whereon the system evolves into two opposite directions.

A means to study the dynamical properties of a system is the Lyapunov exponent λ. It describes the rate at which neighboring trajectories separate from each other,

$$\|\delta\boldsymbol{x}(t)\| \approx \exp(\lambda t)\, \|\delta\boldsymbol{x}(0)\|. \tag{2.20}$$

Hence, the maximum Lyapunov exponent may be defined as

$$\lambda = \lim_{t\to\infty} \lim_{\delta Z(0)\to 0} \frac{1}{t} \log \frac{\|\delta \boldsymbol{x}(t)\|}{\|\delta x(0)\|}. \tag{2.21}$$

From a system which is stable against small perturbations we would thus expect a negative Lyapunov exponent, whereas for a chaotic system, the Lyapunov exponent will be positive. However, this definition is unfeasible in our current problem of investigating the single-particle Lyapunov exponents: With time, not only the trajectories of a single perturbed particle will diverge but also the trajectories of the whole system containing all particles. As a consequence, in order to measure the single-particle Lyapunov exponent, we would have to compute a system trajectory, keep it fixed and allow only for a single particle to freely evolve in time.

A more general approach is to compute Lyapunov vectors and thus determine the complete Lyapunov spectrum. To this end, the system

$$\dot{\mathbf{M}} = \mathcal{W}(\boldsymbol{x}, t)\mathbf{M} \tag{2.22}$$

is integrated along a trajectory $\boldsymbol{x}(t)$ fulfilling the evolution equation eqn. (2.6). Each column of $\mathbf{M}$ represents a displacement along a different direction, and hence we start with the identity matrix. After time t, one obtains $\mathbf{M}(t)$, and the Lyapunov exponents can then be determined by evaluating the eigenvalues α_i of the matrix $\mathbf{M}(t)\mathbf{M}(t)^T$ (e.g. Politi, 2013):

$$\lambda_i(t) = \frac{\log(\alpha_i)}{2t}. \tag{2.23}$$

When restricting the Jacobian by setting mixed derivatives to zero, $\mathcal{M} \equiv 0$ (eqn. (2.17)), this integration will produce the single-particle Lyapunov exponents. The problem which arises is that for long times t, most vectors will align along the most unstable direction or diminish to zero. For too short times, on the other hand, the Lyapunov exponents will become unreliable due to the division by t. To circumvent this, we follow the approach of Eckmann and Ruelle (1985): After some time δt, we orthogonalize the matrix $\mathbf{M}(t + \delta t)$. For an appropriate stepsize δt, this will lead to $\mathbf{M}$ containing vectors aligned with the 'directions' of the Lyapunov exponents in descending order. To extract the exponents, we use QR-decompositions at every re-orthogonalization,

$$\mathbf{M}(n\delta t) = \mathbf{Q}_n \mathbf{R}_n \dots \mathbf{R}_1.$$

The Lyapunov exponents then are obtained from the diagonal elements of the matrix product $\mathbf{R}_n \dots \mathbf{R}_1$,

$$\lambda_i = \lim_{n\to\infty} \frac{1}{\delta t} \langle \log R_{ii}^{(k)} \rangle_k, \tag{2.24}$$

where R_{ii}^k are the i-th diagonal element of the k-th upper triangular matrix.

For the full system, the Lyapunov exponents behave as expected: In the reversible regime, they are all negative. In the irreversible regime, however, some exponents become positive, reflecting the chaotic nature of the system. Exemplary results for a single-particle

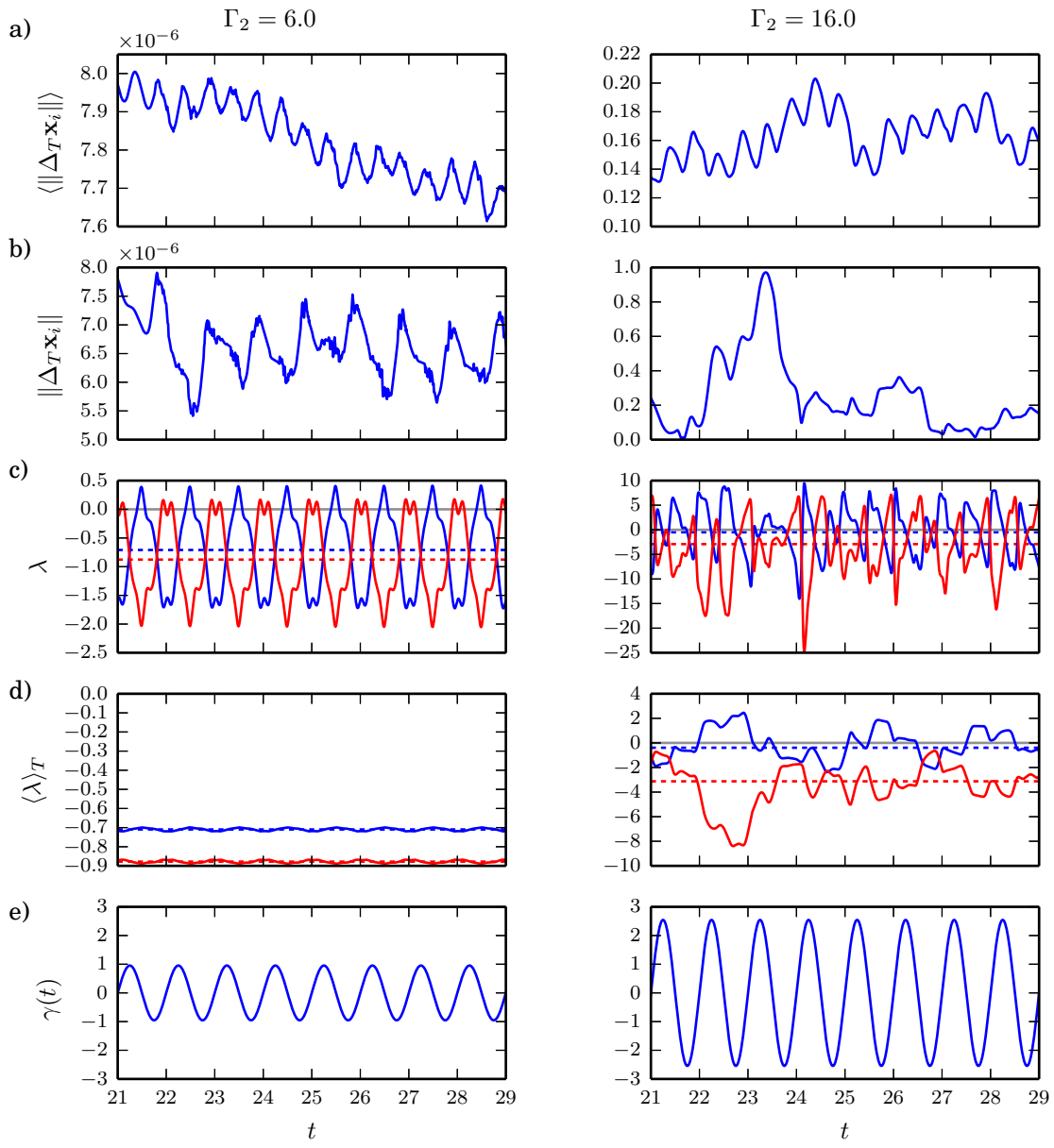

Figure 2.10: Local Lyapunov exponents for a single particle, at two different shear rates representing the reversible and irreversible state, left and right column respectively. Rows (a) and (b) show displacements over one period, both for the whole system and a single particle. The short scale fluctuations are due to the affine shear. Rows (c) and (d) display the single-particle Lyapunov exponents, in the latter row time-averaged over one period. The dashed lines indicate the mean values. In the irreversible state, the exponents become positive over longer times, enabling tipping point trajectories. For a clearer understanding of the oscillations, the lowermost row (e) shows the strain over time. Please note that the scales differ between left and right column.

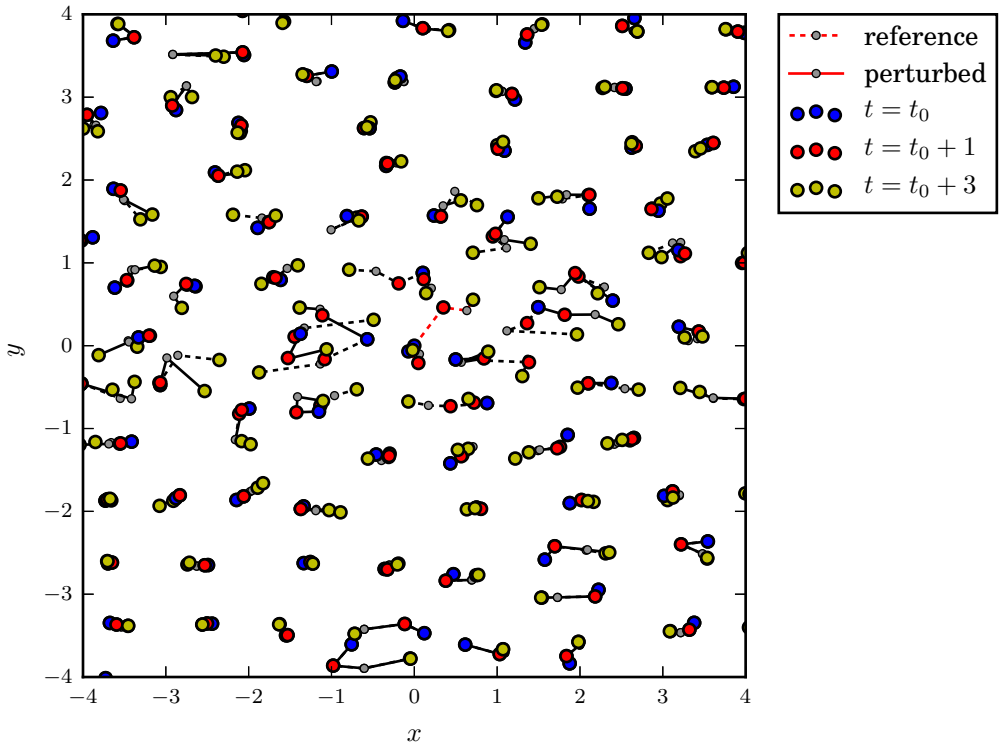

Figure 2.11: Tipping point of the system of figure 2.10 (right column). Shown is the stroboscopic map starting at $t_0 = 22.0$, with the particle in question perturbed along the unstable Lyapunov direction by 0.1. Shown are both the reference and perturbed trajectories (dots connected by dashed and solid lines, respectively; the unperturbed particle is centered at the origin, the perturbed one is distinguished by red lines). Lines do not represent actual trajectories but are a guide to the eye. In close vicinity to the perturbation, the two trajectories deviate strongly from each other: Several neighboring particles change directions and are displaced on the order of a particle distance. Further away, the trajectories separate much slower indicating that the tipping event is localized.

Lyapunov exponent at two different shear rates $\Gamma_2 = 6.0$ and 16.0 are shown in figure 2.10. The displacements per period reflect the state of the whole system: At low shear rates, the particle is quasi-static, with displacements on the order of the numerical precision. The single-particle Lyapunov exponent shows the periodic oscillations of the shear. Although the system is in the reversible state and thus stable, the Lyapunov exponents become positive for short time intervals. This happens whenever the system is close to the rectangular lattice configuration. When averaged over one period, they remain negative at all times. At a shear rate of $\Gamma_2 = 16.0$, i.e. well in the irreversible regime, the particle moves distances on the order of the lattice constant. The corresponding Lyapunov exponents exhibit larger fluctuations. When time-averaged over one period, the Lyapunov exponents are positive over times on the order of one period. During this time, the single-particle trajectory is unstable and thus sensitive to small changes in particle positions, possibly

leading to tipping points. Averaged over the whole timespan on the other hand, the individual Lyapunov exponents are negative. This is due to the fact that all other particles are fixed on the prescribed trajectory and form a time-varying, caging external potential for most of the time. It also suggests that locally, particles move in a cooperative manner.

The results of a perturbation experiment of the corresponding particle are shown in figure 2.11. There, we take the system at $t = 22.0$, displace the particle along the direction of its unstable Lyapunov exponent, and let the system evolve for several periods. The resulting trajectory is then compared with the reference trajectory of the undisturbed system. The initial perturbation is set to 10% of the lattice constant, and for convenience the figure is centered around the unperturbed particle. In close vicinity of the perturbation, several single-particle trajectories separate up to the order of an average particle distance in the first period, and two more periods later many neighborhood relations have changed. An example are the two particles to the left of the center, which swapped positions in the perturbed system. Moreover, the event is localized and trajectories of particles further away from the initial perturbation show significantly smaller separation.

These trajectories can be seen as an example of a tipping point event: A small change in the system configuration leads to a huge, i.e. macroscopic, reply one or a few periods later. Arguably, a perturbation of about 10% of the average inter-particle distance might not be considered a microscopic change in initial conditions. However, only one out of a hundred particles has been shifted, which makes it a disturbance on the order of 1% when compared to system dimensions. Moreover, in principle it should be possible to find configurations which behave similarly upon smaller displacements, be it either by prolonged investigations or by construction. To achieve this, the system has to be brought closer to the edge which separates it from a macroscopically different state.

2.3.2 Quasi-static approximation

Investigation of the long term trajectories of simulations in the reversible regime show that they approach regular lattices. That regular lattices are force equilibria, even under periodic shear, follows from the fact that to each particle pair there is a corresponding one with opposite forces. More formally, consider a lattice configuration with a point symmetry in particle spacings, i.e. a situation where for every pair i, j there is a second pair i, k, such that $\boldsymbol{x}_{ij} = -\boldsymbol{x}_{ik}$. Then it is easy to see that the inter-particle forces in eqn. (2.6) vanish. Since the shear force only introduces an affine transformation, the force balance stays unaffected during the shear process. The regular lattices under shear therefore correspond to a periodic cycle of system (2.6),

$$\boldsymbol{x}_i^o(t) = \boldsymbol{x}_i^{\text{lattice}} + \frac{\Gamma_2}{2\pi} y_i^{\text{lattice}} \sin(2\pi t)\boldsymbol{e}_x, \tag{2.25}$$

for all parameter values Γ_1 and Γ_2. The initial regular lattice points are denoted $\boldsymbol{x}_i^{\text{lattice}}$, and their time-dependent cousins are $\boldsymbol{x}_i^o(t)$. The regular lattices we consider are the ones obtained under small shear shown in figure 2.12: the hexagonal lattice with particles aligned along the shear direction, the same lattice rotated by 90°, and the rectangular lattice aligned with the shear. The question which naturally arises is whether, and for which parameter values, these states are linearly stable.

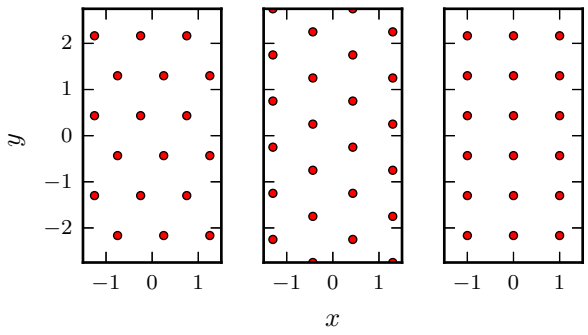

Figure 2.12: The three lattice configurations considered in the linear stability analysis, from left to right: hexagonal lattice, rotated hexagonal lattice and rectangular lattice. These are also the asymptotic states found in the simulations.

In order to understand the transition point at $\Gamma_2 \approx 10.5$, we first take a look at the Jacobian of the inter-particle potential $\mathcal{J} = \mathcal{D} - \mathcal{M}$ for different configurations $\boldsymbol{x}_i^{\text{hex}} + s\frac{\Delta x}{\Delta y} y_i^{\text{hex}}$, where $\Delta x = 1$ and $\Delta y = \sqrt{3}/2$ are the nearest neighbor distances in x- and y-direction. Hence, the hexagonal lattice is reproduced with period $S = 1$ and, by symmetry, it thus suffices to investigate $s \in [0, 0.5]$: $s = 0$ corresponds to the hexagonal lattice whereas $s = 0.5$ yields the rectangular lattice.

We compute the spectrum of the Jacobian of the 400-particle system, shown in figure 2.13 where we neglected the two neutral modes which emerge due to translational invariance.[5] We find that the configuration is only stable close to the hexagonal state and unstable around the rectangular one, the transition located at $s \approx 0.19$. This is not surprising since inter-particle distances are maximized in the hexagonal configuration, and the rectangular lattice can be deformed easily towards the hexagonal one, for example by collectively perturbing every second row of particles. When shearing the system, the system picks up unstable modes. Thus, we would expect that the shear flow is only stable up to a shear rate corresponding to s slightly larger than the transition point. Indeed, the critical shear rate $\Gamma_2 \approx 3.0$ where the hexagonal lattice first loses stability equals to $s = 0.41$. Thus, dynamical effects seem to play a crucial role for the stability of the sheared system, especially since the rectangular lattice becomes stable at larger shear rates.

2.3.3 Floquet analysis

Next, we analyze the stability of the periodic orbits in eqn. (2.25). To this end, we consider the linearized evolution equation (2.15) along the orbit. Since the coefficient matrix has a periodic time-dependence, the linear stability analysis requires an integration of the equations over a full period (Chicone, 2006). We compute the principal fundamental matrix $\Phi(t)$ of system eqn. (2.15) with initial condition $\Phi(0) = \mathbb{I}_2$. The matrix after a full period, $\Phi(1) \equiv \Phi$ is the Floquet Matrix and it is not necessarily a symmetric matrix.

[5] Since we are only interested in the eigenvalues with the largest real part, it suffices to utilize an iterative scheme, specifically the Arnoldi package (ARPACK) (Lehoucq et al., 1998). Convergence is confirmed by checking the neutral modes.

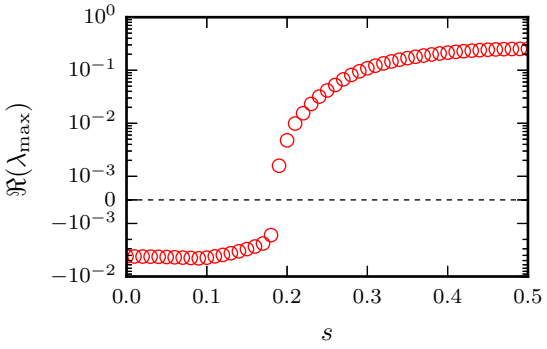

Figure 2.13: Stability of the invariant lattice, only considering inter-particle interactions. $s = 0$ corresponds to the hexagonal lattice which is shifted towards the rectangular lattice at $s = 0.5$. The system is stable close to the hexagonal configuration ($\lambda_{\max} < 0$) and unstable close to the rectangular one ($\lambda_{\max} > 0$). $N = 400$, $\Gamma_1 = 0.1$.

The stability properties of system (2.15) then depend on the eigenvalues of Φ only. The eigenvalues σ of Φ are called Floquet multipliers. For stability, we require $|\sigma|$ for all possible eigenvalues to be less than one. Two neutral modes ($\sigma = 1$) arise from the invariance of perturbations along the orbit and translational invariance in the x-direction.

As an important technical detail we mention that the boundary conditions have to be implemented such that they are compatible with the symmetries of the system so that the symmetries of the matrices are preserved. To achieve this, we introduce an interaction radius around each particle, and take all interactions with particles inside the circle into account. The radius is chosen to be at least of the order of the box dimensions. Calculation of the whole spectrum is computationally intensive, especially for larger system sizes. Since we are only interested in the mode with largest magnitude, we use the iterative Arnoldi package (ARPACK) to compute only 10 to 20 eigenmodes.

Stable and unstable configurations

We studied the stability of configurations with $N = 100, 400$ and 900 particles. Results are qualitatively the same, with the stable modes being closer to unity for more particles taken into account. We investigated three different configurations as described above, and for the rotated hexagonal configuration we swapped L_x and L_y.

It turns out that for $\Gamma_1 = 0.1$, at least one configuration is stable for values of $\Gamma_2 \lessapprox 10.5$. This value corresponds to a shear rate where each particle is shifted by 1.5 particle distances in relation to the neighboring rows. For larger values, the periodic cycles remain unstable. The largest multipliers are shown in figure 2.14 for a wide range of the shear rate. We find three regions with different stable configurations. For $\Gamma_2 \lessapprox 3.5$, both the hexagonal state and its rotated counterpart are stable. Thereafter, the rectangular state is stable up to a shear rate of $\Gamma_2 \lessapprox 7.5$ until finally the hexagonal configuration is stable again. The changes occur at shear rates corresponding to relative displacements of neighboring rows of approximately 0.5, 1 and 1.5 particle distances. Only in a small interval at $\Gamma_2 \approx 7.5$, all considered lattices appear to be unstable. The inspection of long

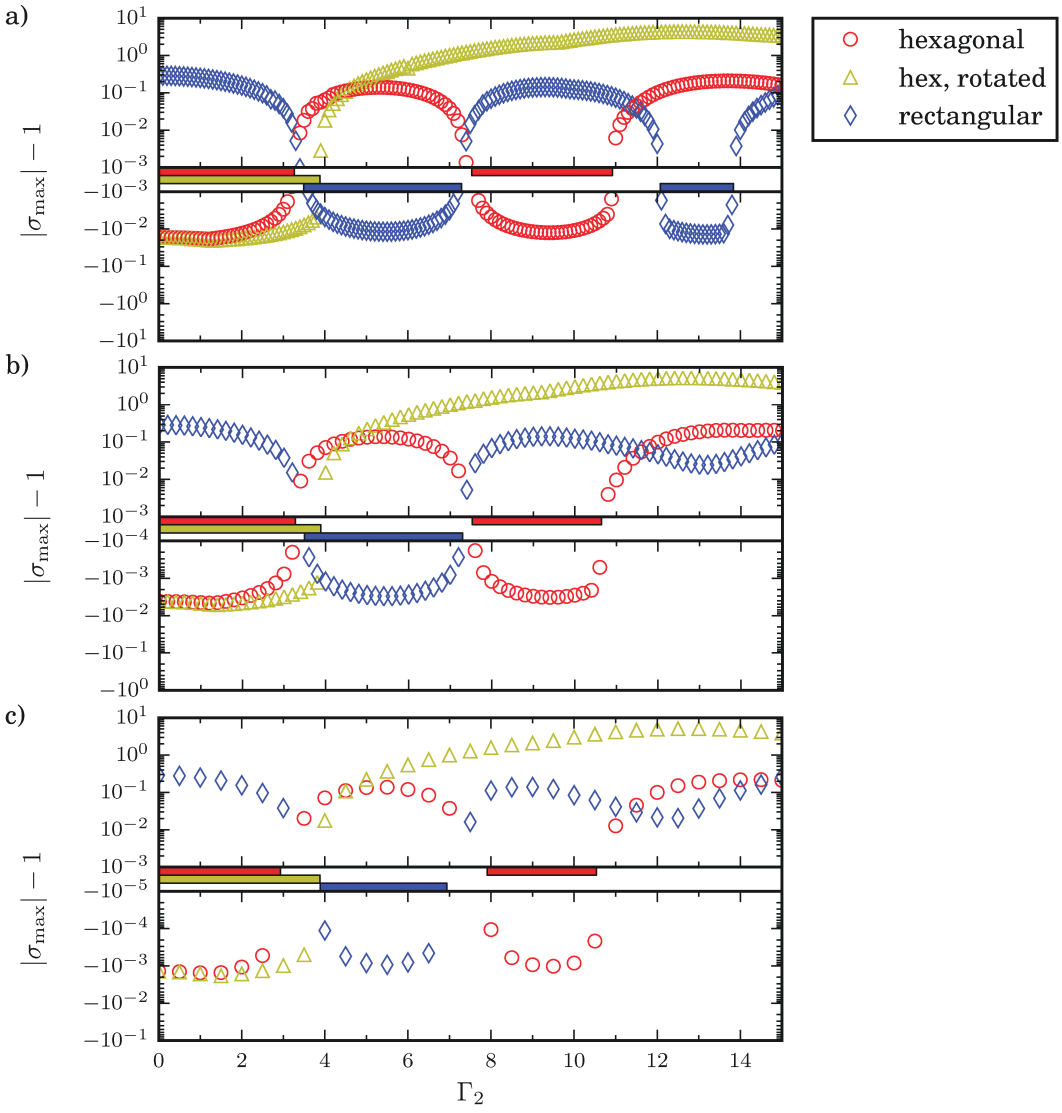

Figure 2.14: The largest eigenvalues $\sigma_{\max}$ of Φ in dependence on Γ_2 for the three investigated configurations with $N = 100$ (a), $N = 400$ (b), and $N = 900$ particles (c). Neutral modes are omitted. Markers indicate eigenvalues $|\sigma_{\max}| > 1$ and thus unstable configurations in each upper panel, and stable modes ($|\sigma_{\max}| < 1$) in the lower panels. In between, the regions of stability are represented by colored bars. We find that for values of $\Gamma_2 \lessapprox 11$, linearly stable states exist. Beyond, linear stability is lost. This is in good agreement with the diffusion constant calculated earlier. With increasing number of particles from (a) to (c), the stable modes become less stable, the qualitative difference between 400 and 900 particles being rather marginal. The stable patch at $\Gamma_2 > 12$ in the 100-particle system can clearly be identified as a finite size effect due to the limited boxwidth. The value of Γ_1 is set to 0.1 in all calculations.

term trajectories shows, that the system relaxes towards a mixture of both the hexagonal and rectangular lattice.

The rotated hexagonal lattice shows a different behavior than the other two lattice configurations: As soon as it becomes unstable, it remains unstable whereas the other two configurations show modulations where they regain their stability, or at least become less unstable in case of the rectangular lattice and $\Gamma_2 > 11$. This behavior can be understood from a geometrical point of view. For the hexagonal lattice with particles aligned along the shear direction, the initial configuration is reproduced after a relative shear displacement of neighboring rows by one particle distance. For the rotated lattice, a shift by four particle distances is needed before the lattice is reproduced, corresponding to a shear rate of $\Gamma_2 \approx 20$. Indeed, this seems to correspond with the Floquet multipliers, which show a slight decrease for $\Gamma_2 > 14$. It also gives a notion on how stability of the rectangular lattice comes into place. Although it is unstable in the stationary case, upon shearing it sufficiently strong it gets distorted towards the stable hexagonal lattice during most of a period.

Upon comparing the different system sizes, we observe no qualitative differences between the 400 and 900 particle ensemble. Quantitatively, the stable modes become less stable with increasing number of particles. Additionally, the points where the configurations change stability are slightly shifted. The magnitudes of the unstable modes, however, are almost identical. The 100 particle system, on the other hand, clearly shows signs of boundary effects. In the range $12 \lessapprox \Gamma_2 \lessapprox 14$, the rectangular lattice becomes stable again. This is neither observed in the larger systems, nor in the simulations. The origin might be the limited box width in conjunction with the long range potential. Except for this detail, the 100 particle system qualitatively agrees with the larger ensembles as well.

2.4 Particle correlations

Additional information about the structure of the system that goes beyond the value of the diffusion constants and reversibility can be obtained through correlation functions that contain information about the arrangements of particles. The first indicator to look at are radial correlations. They display the typical change attributed to the transformation from a solid to a liquid medium. More interesting though are the spatially resolved correlations. As we will see further below, they reveal a phase information and help to explain the observed anisotropy.

2.4.1 Radial correlation

The radial two-particle correlation function counts the number of particles within a ring bounded by the radii $r - \delta r$ and $r + \delta r$, normalized by the mean number of particles in such a ring,

$$g(r) = \frac{1}{N} \frac{\int_{r-\delta r/2}^{r+\delta r/2} \sum_{ij} \delta(r_{ij} - \tilde{r}) \mathrm{d}\tilde{r}}{\int_{r-\delta r/2}^{r+\delta r/2} 2\pi \tilde{r} \rho \mathrm{d}\tilde{r}}, \tag{2.26}$$

where $\rho = N/(L_x L_y)$ is the average particle density of the system. For a crystalline structure, one expects sharp peaks corresponding to the underlying lattice, the first one

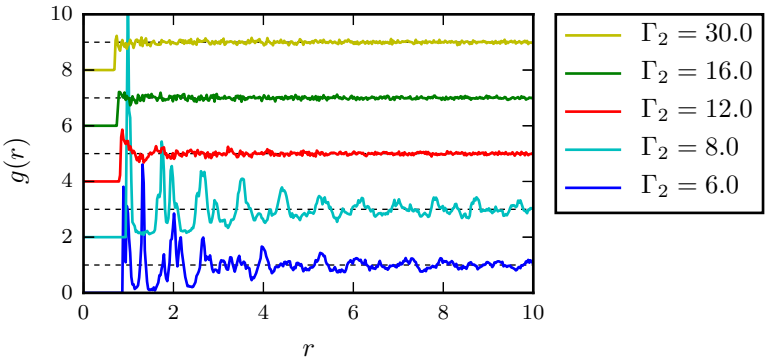

Figure 2.15: Radial correlation functions of ensembles at different shear rates. For clearer distinction, graphs are shifted by a constant. The dashed lines indicate the asymptotic value $g(r) = 1$. At low shear rates ($\Gamma_2 = 6.0$ and 8.0), the crystalline structure is reflected by isolated peaks at the next neighbor distances of the attained lattices, the rectangular for $\Gamma_2 = 6.0$ and the hexagonal for $\Gamma_2 = 8.0$. At higher shear rates, in the irreversible regime, the correlation function shows features of a liquid ($\Gamma_2 = 12.0$) and a gas ($\Gamma_2 = 30.0$). Simulations were performed with 900 particles at $\Gamma_1 = 0.1$.

at the next neighbor distance, and so on. In a liquid state no long range ordering is found so that the correlation approaches one at larger distances. As neighboring particles repel each other, one expects a gap close to the particle and a strong peak at the position of the nearest neighbors. Figure 2.15 shows the correlation functions of the system for different shear rates Γ_2 (and $\Gamma_1 = 0.1$). To obtain better statistics all simulations are done for systems of 900 particles. Inspection of the final states and the per particle displacements show that they behave exactly as the smaller systems of 100 particles. Each ensemble is taken at a full period after a total simulation time of 11000 periods, i.e. we assume the system has reached its asymptotic state, which is certainly the case for the systems at larger shear rates.

As expected, at low shear rates the ordered structure of the state is reflected in the correlation function. At $\Gamma_2 = 6.0$, we find two superimposed peaks at $r = \sqrt{3}/2$ and 1.0, corresponding to the rectangular lattice. At a slightly increased shear rate of $\Gamma_2 = 8.0$ the asymptotic state changes, as can be seen in the correlation function which exhibits isolated peaks at $r = 1.0$ and $\sqrt{3}$, corresponding to the next neighbor distances in a hexagonal lattice. At higher shear rates after the motion became irreversible, $\Gamma_2 = 12.0$, the correlation function shows features of a liquid. Beyond a minimum distance owing to the repelling interaction between particles, we observe further peaks. However, only few of them are clearly distinguishable and the correlation function quickly decays to one. At $\Gamma_2 = 16.0$, the first two peaks are barely noticeable and the correlation function resembles the one of a gas-like system. Consequently, no spatial information except for the next neighbor distances r_{nn} can be extracted. They are identified as $r_{\mathrm{nn}} = 0.8$ at $\Gamma_2 = 16.0$, and it decreases to $r_{\mathrm{nn}} = 0.7$ at $\Gamma_2 = 30.0$. This points to an improvement of the mixing process with increasing shear rate, leaving the particles less time to relax and to return to larger separations.

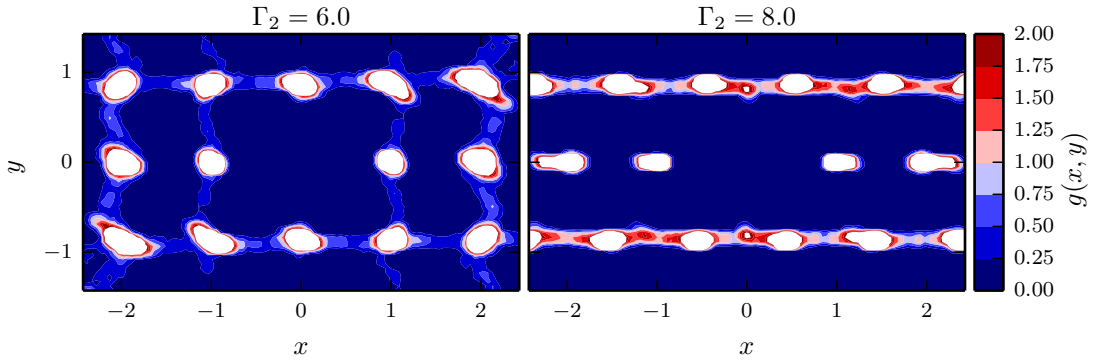

Figure 2.16: The 2-dimensional correlation function $g(x, y)$ at low shear rates. Colors indicate the neighbor density: $g(x, y) < 1$ (blue) and $g(x, y) > 1$ (red); at the white patches, $g(x, y)$ exceeds 2.0. Just as the radial correlation function $g(r)$, $g(x, y)$ reflects the crystalline structure. We observe the rectangular lattice structure at $\Gamma_2 = 6.0$, and the hexagonal lattice at $\Gamma_2 = 8.0$ In both cases, deviations are caused by minor lattice defects, at which in the latter case almost perfect vertical alignment is observed.

2.4.2 Spatial correlation

In order to obtain more spatial information, we now turn towards the spatially resolved two-particle correlation function

$$g(x, y) = \frac{1}{N\rho\delta x\delta y} \int_{x-\delta x/2}^{x+\delta x/2} \int_{y-\delta y/2}^{y+\delta y/2} \sum_{ij} \delta(x_{ij} - \tilde{x})\delta(y_{ij} - \tilde{y}) \mathrm{d}\tilde{x}\mathrm{d}\tilde{y}. \tag{2.27}$$

Just as its radial counterpart, the 2d correlation function relates the number of particles in a rectangular box of size $\delta x \times \delta y$ around the distance x and y to the mean number of particles expected in such a region.

Figure 2.16 shows the 2d correlations for the ordered configurations at low shear rates. Data was acquired in the same manner as for the radial correlation function. In the plot, the correlation function is color coded, blue for densities less than unity, red for larger densities, and white for densities exceeding 2.0. As expected from the radial correlation, for $\Gamma_2 = 6.0$ we find a rectangular lattice with most particles gathered closely to the lattice points and a few particles found on the grid lines. This is due to some minor lattice defects. Accordingly, at $\Gamma = 8.0$ we find the hexagonal lattice. Again, particles gather closely to the lattice sites, at which vertical alignment is almost perfect. The horizontal scatter is due to over- or underpopulations in rows which locally lead to rectangular arrangements of particles. Note that both ensembles show mirror symmetries along the x- and y-axis, i.e. there is no memory in the system if it has been sheared to the left or to the right over the previous half period.

The picture changes upon advancing to higher shear rates. Figure 2.17 shows the 2d correlations $g(x, y)$ across half a period at $\Gamma_2 = 16.0$ and 30.0, respectively. As in figure 2.16, the correlation function is color coded blue (low denstiy) and red (high density). In the upper part, (a), we show snapshots for $\Gamma_2 = 16.0$ at the beginning of a period, at

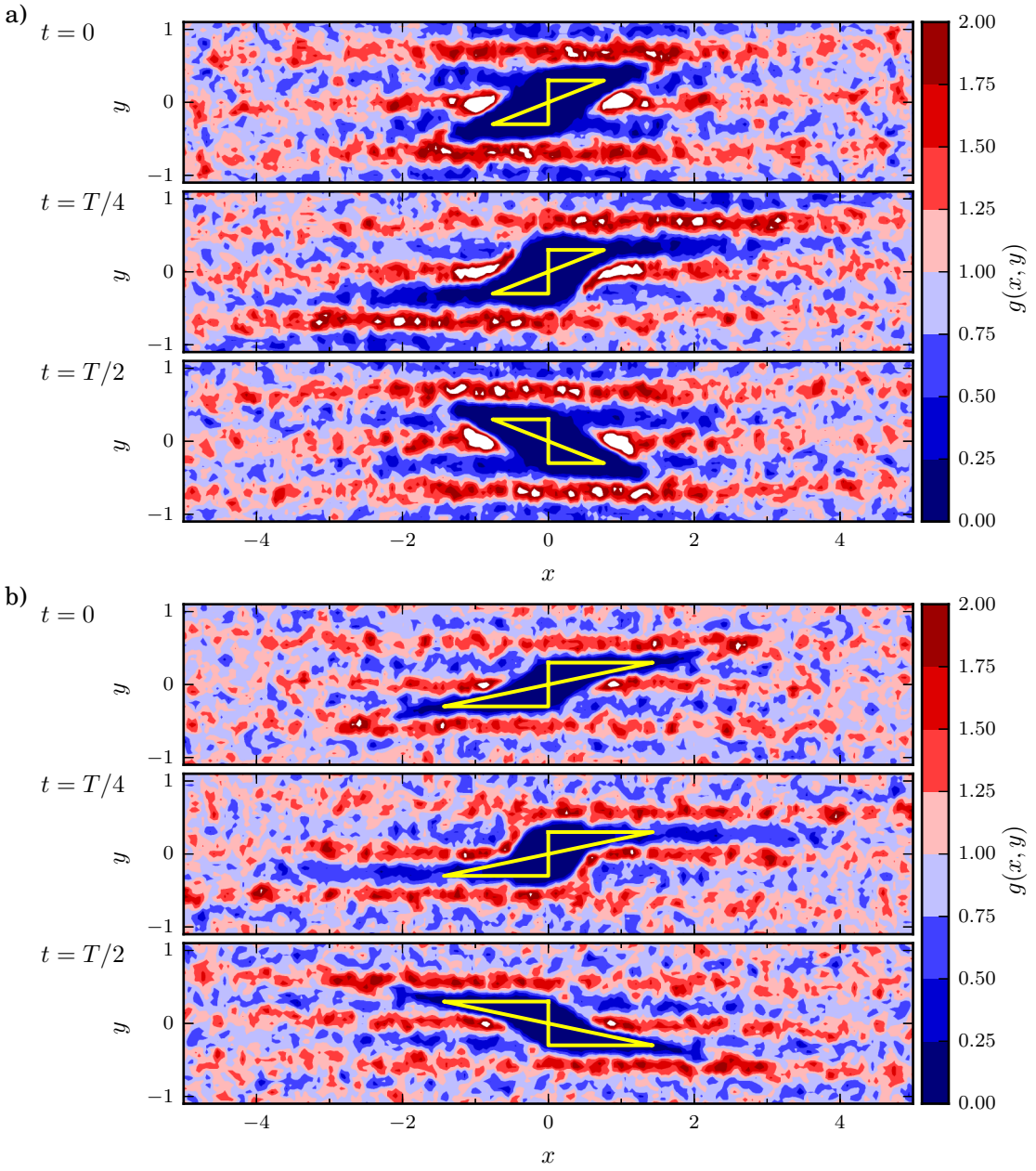

Figure 2.17: The 2-dimensional correlation function $g(x, y)$ at high shear rates over half a period at a) $\Gamma_2 = 16.0$ and b) $\Gamma_2 = 30.0$. Colors indicate the particle density: $g(x, y) < 1$ (blue) and $g(x, y) > 1$ (red); at the white patches, $g(x, y)$ exceeds 2.0. We observe a break-down of the mirror symmetry found at lower shear rates. While the free space is tilted to the right at the beginning of a period, half a period later it is tilted to the opposite direction. Moreover, we find remnants of the hexagonal lattice in the form of stripes of increased density spaced by roughly the layer distance of the crystal. The yellow triangles indicate how far the populated rows have been sheared against each other over the past quarter period. They are set at arbitrary height so that features of the correlation function are not occluded.

the turning point of $t = T/4$ when the flow has stopped and strain is maximal, and after half a period $t = T/2$, when the flow has reversed its direction and strain is zero again. The most prominent feature is the break-down of symmetry. At the start of the period, $t = 0$, we observe a dark blue rhombic region around the origin where no other particles are found. It is oriented to the right. As would be expected from the symmetry of the flow, half a period later we observe a similar rhombus, but this time oriented to the left. In between, at the turning point of the flow, its outer boundary at $y \approx \pm 0.5$ is stretched even more, while at the centerline $y = 0$ the depletion zone keeps its boundaries. In effect, this leads to less populated protrusions above and below the centerline, concurrent with the relative strain. A 'propeller-shaped' region was also described by Keim et al. (2013) in their study of the model of Corté et al. (2008). Due to a different definition of the shear protocol, our snapshot at $t = T/4$ corresponds to $t = T/2$ in their system, which by symmetry relates to $t = T$. In contrast to our observations, they found it in the reversible regime. Hence, at least for the interactions considered here, even in the irreversible state a memory of the shear process is perpetuated.

We can understand this phenomenon when starting at $t = -T/4$ (which is the mirrored image of $t = T/4$). At this time, the flow is at its left turning point. We now look at the vertical line at $x = 0$. At short distances, particles on the left of this line get repelled to the left, and over the next quarter period, the flow is not fast (i.e. strong) enough to pull them beyond $x = 0$. Thus, at $t = 0$ we observe the mentioned rhombus: It corresponds to the line $x = 0$, advected over the last quarter period. This suppression of transport continues up to $t = T/4$. Since particles on the centerline $y = 0$ are not affected by the shear, the rhombic shape gets distorted and we observe the aforementioned protrusions. As soon as the low density area leaves the core area, particles from above and below are pushed into the void. This is reflected by a slight increase in $g(x, y)$ towards the tips of the protrusions. However, at $t = T/2$, the remnants are still visible (the light blue areas in the upper right and lower left of the figure).

The maxima of the correlation function are found at $x \approx \pm 1.0$ and $y = 0$ at every time step. Their strong expression corresponds to a strong localization of next neighbors parallel to the shear. Additionally, in the perpendicular direction we find a modulation in particle density, with maxima at $y \approx 0$ and $\pm 0.6 \ldots 0.8$, and multiples thereof. The modulations extent over several particle distances parallel to the shear direction before they become weaker and decay. This has two implications. First, although the system is far from its equilibrium of a hexagonal lattice configuration, it still shows the vertical density modulation corresponding to the layers in the lattice. With increasing shear rate, this becomes less pronounced, but is still detectable. Second, those maxima in the correlation function hint at a general anisotropy: The next neighbor distance parallel to the shear is conspicuously larger than the next neighbor distance in the perpendicular direction.

At the higher shear rate $\Gamma_2 = 30.0$ in figure 2.17(b), the picture qualitatively stays the same. We still observe the density modulations and the flow dependent variation of the next neighbor distances. What changes though is the shape of the particle-free space. At the beginning of the period, it gets stretched even more, and no longer resembles a rhombus. This is due to the fixed neighbor relations along the centerline at $x \approx \pm 0.8 \ldots 1.2$ At the turning point, $t = T/4$, the free space is a slightly tilted oval instead of a rounded rhombus. Additionally, the density modulations in the perpendicular direction show a

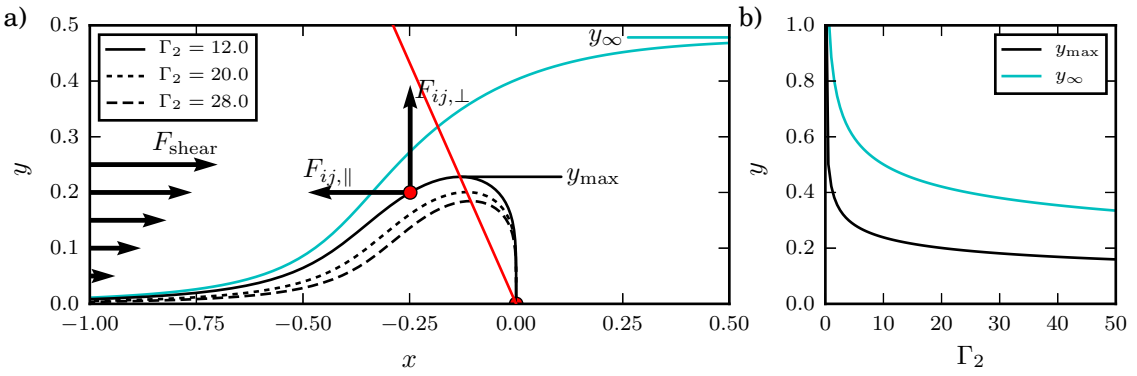

Figure 2.18: (a) Formation of a shear rate dependent depletion zone. We consider two particles (●), one being fixed at the origin, and the other one being subject to the forces (arrows) due to particle interaction $\boldsymbol{F}_{ij}$ at $\Gamma_1 = 0.1$ and the shear $\boldsymbol{F}_{\text{shear}}$, which linearly increases with the separation in the y-direction. Black lines represent the points where horizontal forces are balanced, for three different shear rates. In the area below the line, the free particle moves to the left, i.e. particles outside the area cannot enter it. With increasing shear rate, the maximum value $y_{\max}$ decreases. The red line marks the position of largest thickness of the depletion zone, changing with Γ_2. Taking into account the vertical component of $\boldsymbol{F}_{ij}$, we compute the streamline of a particle starting at $x = -10$ and close to the x-axis (−). It results in an asymptotic separation y_∞. (b) Thickness $y_{\max}$ of the depletion zone (−), and the asymptotic separation y_∞ of the streamline (−), in dependence on the shear rate Γ_2. Both decrease slowly for $\Gamma_2 > 20$, similar to the vertical diffusivity D_y.

smaller wavelength than at $\Gamma_2 = 16.0$, and the first maxima are found at $y \approx \pm 0.5 \ldots 0.6$. At $t = T/4$, we also observe a deflection of the sheared particles, the red patches to the upper left and lower right of the center.

These observations might help us to shed some light on the features of the diffusivity plot in figure 2.7. First, the decrease in the next neighbor distances perpendicular to the shear sets a shorter length scale in the y-direction, whereas parallel to the shear next neighbor distances remain unaffected. This gives an idea of how the slight decrease of D_y at larger shear rates comes into place. However, it does not explain why the diffusivity $D_{x,0}$ considerably increases with Γ_2. Possibly, the other observation might help in the interpretation: The protrusions of low particle density ($g(x, y) < 0.25$, dark blue in figure 2.17), grow parallel to the shear with increasing shear rate, setting a longer length scale and thus presumably affect the diffusivity D_x. Unfortunately, while those observations give a qualitative explanation, a quantitative agreement is not achieved.

We can try to understand the reduction of the vertical spacing with shear rate from some simple considerations. We take two particles, a fixed one placed at the origin and a free one, see also figure 2.18(a). For now, we replace the periodic shear by a constant one which linearly increases with the separation y. Thus, the free particle is subject to two different forces, the inter-particle force $\boldsymbol{F}_{ij}$ and the shear force $\boldsymbol{F}_{\text{shear}}$ acting along the x-direction. Taking only forces parallel to the shear into account, we can compute the

particle position where horizontal forces balance,

$$F_{\text{shear}} = -F_{ij,\parallel}, \tag{2.28}$$

$$\Gamma_2 y = -\Gamma_1 \frac{x}{r^4}. \tag{2.29}$$

For the mobile particle close to the x-axis, forces are balanced at large distances, whereas for a large separation in y the particle is barely affected by the stationary one. The curves of horizontal force equilibrium are shown in figure 2.18(a) for various shear rates. Particles in the area below the curves move to left and are deflected upwards, until they are finally far enough away to pass. Translating it to the periodically sheared system, this leads to the formation of a depletion zone where $g(x, y)$ is very low. This mechanism can also be seen in the correlation functions at $t = T/4$ in figure 2.17, where the maximum at $x = \pm 1.0$ is bent away from the centerline. When increasing the shear rate, forces are balanced closer to the origin and the area of the depletion zone decreases, as well as the maximum separation $y_{\max}$. It approaches the origin in the limit of very large shear rates. Taking into account the vertical component of $\boldsymbol{F}_{ij}$ as well, we can compute the streamline of a particle. In the sheared system, the final state is only attained after many periods, and hence we are interested in the long time behavior. Since the free particle is repelled from the origin, streamlines starting nearby will quickly run off, and we investigate streamlines starting far away from the origin, $x_0 \ll 0$. The most interesting streamline is the one starting ϵ-close to the x-axis at $x_0 \to -\infty$. It is the one to get closest to the origin. Fortunately, the particle interaction drops off considerably fast, and we can approximate it by a shorter streamline starting at $x = -10$, close to the horizontal force equilibrium. It is shown in figure 2.18(a) in light blue, and it approaches an asymptotic separation y_∞ for large x.

The dependence of both the thickness of the depletion zone $y_{\max}$ and the asymptotic separation of the streamline y_∞ on the shear rate is shown in figure 2.18(b). In the irreversible regime ($\Gamma_2 > 10$) they slowly decrease with shear rate, the dependence quite similar to the decay of D_y at larger shear rates as shown in figure 2.6. Admittedly, the horizontal layers form at a slightly larger height. This is not too surprising, since we neglected the presence of other particles as well as the periodic repetition of the shear process. However, the above considerations give a qualitative explanation. Moreover, since this mechanism takes place for every particle, it adds up to the formation of the horizontal modulations. By contrast, the hard-core interactions used by Keim et al. (2013) should not lead to a shear rate dependent separation. And indeed, they report a constant separation in the perpendicular direction with boundaries at $y = \pm 1$.

In order to conclude this topic, we finally take a look at the correlation function $g(x, y)$ at a stronger particle interaction $\Gamma_1 = 1.0$ and $\Gamma_2 = 48.0$, shown in figure 2.19. For these parameter values, the system is in the irreversible regime. The correlation function shares some similarities with the ones discussed in figure 2.17. We observe the transversal modulation as well as the breakdown of symmetry. The modulation however is more pronounced: The separate rows of high particle densities can be distinguished over the whole domain, whereas for weaker particle interactions they quickly wash out. Apparently, the strong interaction leads to the formation of horizontal bands of particles even at high shear rates and, at the same time, non-reversible motion. It also explains the correlated

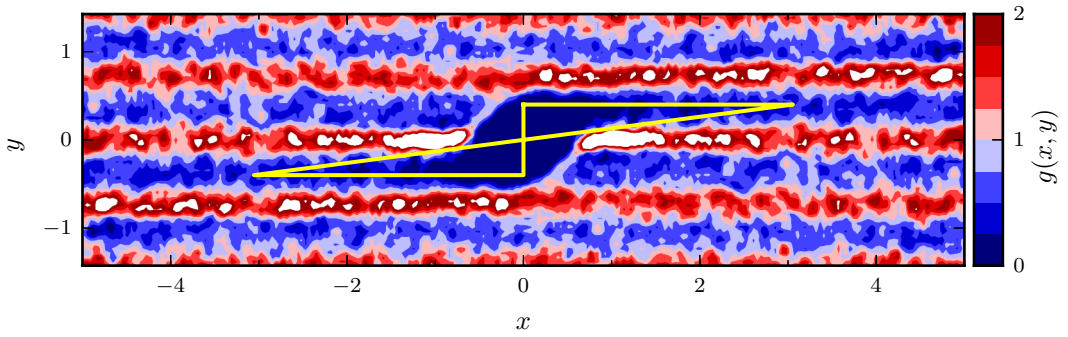

Figure 2.19: Correlation function $g(x, y)$ for $\Gamma_1 = 1.0$, $\Gamma_2 = 48.0$. Colors indicate the particle density: $g(x, y) < 1$ (blue) and $g(x, y) > 1$ (red); at the white patches, $g(x, y)$ exceeds 2.0. The yellow triangles indicate how far the populated rows have been sheared against each other over the past quarter period. The correlation function shares some features with its counterparts in figure 2.17, e.g. the breakdown of mirror symmetry and transversal modulations. The main difference is the formation of horizontal rows of particles, reflected in the persistence of the modulations.

motion parallel to the shear. When trapped inside a horizontal band, diffusion along this direction is strongly inhibited by the strong repulsion of the neighboring particles in the band. However, this does not affect the perpendicular diffusion as is suggested by D_y in figure 2.8.

While these distinctive rows form out, the low-density protrusions ($g(x, y) < 0.25$, dark blue) become less pronounced. At low interaction strength, they can be approximated by the strain over the previous quarter period (yellow triangles). At $\Gamma_1 = 1.0$ though, those regions are significantly reduced and roughly extend over only one or two next neighbor distances. Again, this can be attributed to the strength of the particle interaction: Due to the increased repulsion and hence shorter settling time, particles fill in the voids more rapidly. This agrees with the transversal diffusivity D_y, which is roughly twice as large as in the case of weaker interaction $\Gamma_1 = 0.1$.

Even more, the bare horizontal diffusivities in figure 2.8 would virtually look the same if $D_{x,0}$ were prescribed to zero (i.e. when considering $D_x/\frac{1}{2}\gamma_0^2$ instead). This suggests the following behavior: Direct diffusion parallel to the flow is largely inhibited by the formation of particle rows and only generated by the indirect mechanism of advection-diffusion coupling.

2.5 Summary

We have seen that even a model as simple as (2.6) displays features usually associated with much more complex systems. We found chaotic and ordered behavior which can occur in different regions of the parameter space (Γ_1, Γ_2). The transition is similar for each value of the interaction strength: For small shear strains, after some transient time the system becomes reversible and shear can be considered as a small perturbation. Beyond

an interaction-dependent critical shear rate, this feature is lost and we observe chaotic motion. For stronger particle interactions, the critical point is delayed to higher shear rates.

We identified the diffusivity as an indicator of chaotic motion. As would be expected for a diffusive system subject to shear, we observe advection-diffusion coupling: The diffusivity parallel to the external forcing is strongly enhanced compared to the perpendicular diffusivity. For large interaction strengths between particles, this is covered well by eqn. (2.13) derived by Young et al. (1982). For weak interactions though we observe additional anisotropic effects. We can attribute them to spatial structures, revealed in the 2d-correlation functions: The length scales parallel and normal to the shear motion are different. Moreover, whereas the former is independent of the shear rate, the latter decreases with increasing Γ_2. Additionally, we were able to identify a phase dependence of the particle distributions, which is concealed when looking upon e.g. stroboscopic maps.

We can directly relate the loss of reversibility to the stability properties of sheared regular lattices. Depending on the shear rate, different lattice configurations are preferred. This is somewhat surprising since in two dimensions, in the static case only the hexagonal lattice is found to be stable. For the investigated system sizes, besides finite size effects for the smallest system, the stability properties are independent of the number of particles.

We were also able to identify tipping events where small displacements of a single particle lead to strong divergence of neighboring system trajectories within short timespans. An indicator for possible critical configurations are the local Lyapunov exponents.

3

Melting of a two-dimensional system

We might look at the results of the last chapter from a slightly different perspective. By actively shearing the system, we put energy into it and, so to say, increased its temperature. Eventually, this led to a phase transition where the system changed from an ordered – or crystalline – to an unordered – or liquid – state. Therefore, a more straightforward approach would be to directly put the system in contact with a heat bath. Naturally, two different questions come to mind. Obviously, in the limit of very low temperatures, the system should be found in the ordered state of a solid. At high temperatures on the other hand, we would expect to find a liquid-like behavior. Thus, the first question we might ask is at which temperature a phase transition of the system occurs. The second question is closely related to the first, as we might want to investigate the microscopic mechanism that accompanies the phase transition. Hence, besides a characterization of the state of the system, we will also focus on particle dynamics.

3.1 Definition of the potential

In contrast to the previous chapter, we use a slightly modified inter-particle potential. We are guided by two considerations. On the one hand, it may be complicated to obtain exact absolute values, as for example rates, when investigating microscopic changes. What should be easily accessible and universal though is the variation of such quantities with an external parameter. On the other hand, since we mainly focus on the mechanism, we would like to use a potential where the melting temperature has been investigated. A potential which fulfills both criteria is the well-known Yukawa potential. Additionally, due to the screening, it can be tuned to be relatively short ranged, simplifying computations by the introduction of a cut-off radius. The Yukawa potential is widely used as a model for e.g. dustly plasma (Thomas et al., 1994; Melzer et al., 1996a; Konopka et al., 2000; Merlino and Goree, 2004; Hartmann et al., 2011; Ott et al., 2011) or charged colloids (Van Winkle and Murray, 1986; Murray and Van Winkle, 1987; Tang et al., 1989; Löwen, 1992; Naidoo and Schnitker, 1994; Löwen et al., 2003). It combines the long-range Coulomb interaction with an exponential shielding, which can be explained by the presence of background charges due to e.g. a solvent.

The pairwise potential energy is given by

$$\Phi_{ij}\left(r_{ij}\right) = \sigma_{ij} \exp(-\mu r_{ij})/r_{ij}, \tag{3.1}$$

with screening parameter μ, interaction strength σ_{ij}, and $r_{ij} = \|\boldsymbol{x}_i - \boldsymbol{x}_j\|$ the distance

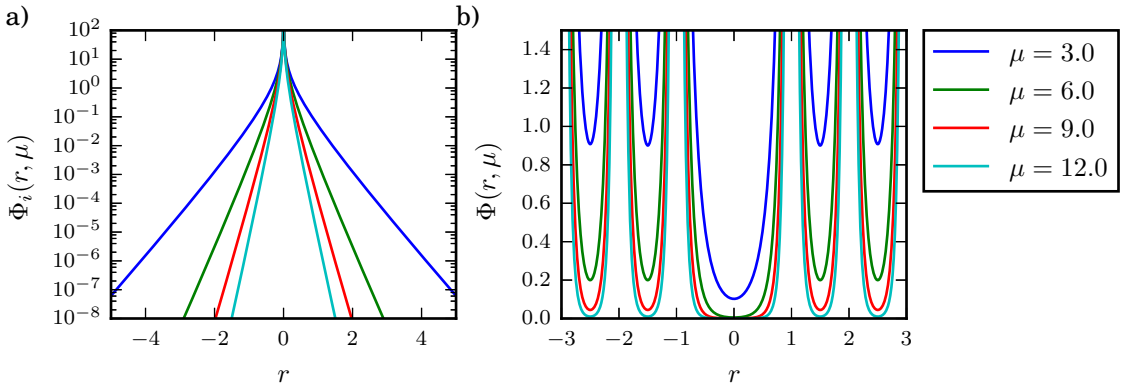

Figure 3.1: Shape of the Yukawa potential for different values of the screening parameter μ. (a) Single-particle potential. (b) Potential for a particle in a 1-dimensional chain with particles fixed at $r = k$ and $k \in \mathbb{Z}^0$. With increasing μ the potential becomes steeper close to particle positions and flat in the intermediate regions, thus resembling a solid-core interaction.

between the particles in units of the lattice spacing. Since for now all particles are chosen to be identical, σ_{ij} just gives an multiplicative offset and we set $\sigma_{ij} = 1$. A large μ corresponds to a short interaction range, mimicking hard cores, whereas the potential shifts towards a Coulomb potential for $\mu \to 0$. This dependence is also shown in figure 3.1, both for the pairwise potential and a 1-dimensional array of interacting particles. By convention, the potential energy is split between the two interacting particles so that the per-particle energy is defined as

$$\Phi_i = \sum_{j \neq i} \tfrac{1}{2} \Phi_{ij}. \tag{3.2}$$

Hence, the full potential energy is given by

$$E = \Phi = \sum_i \Phi_i = \sum_{i,j<i} \Phi_{ij}. \tag{3.3}$$

Physical units and scaling

The Yukawa potential describes a shielded electrostatic interaction, hence the parameters in eqn. (3.1) correspond to physical units as follows. The interaction strength σ_{ij} represents the Coulombic interaction between particles,

$$\sigma_{ij} = \frac{Q_i Q_j}{4\pi\epsilon_0 r_0}, \tag{3.4}$$

where Q_i are particle charges, ϵ_0 is the vacuum permittivity and r_0 represents the lattice spacing. The screening parameter, on the other hand, is given by

$$\mu = \frac{r_0}{\lambda}, \tag{3.5}$$

where λ is the Debye-length.

We measure energies, including thermal energy, in units of the mean interaction strength $\langle\sigma_{ij}\rangle$. The unit of masses is m, and the relevant length-scale is the lattice constant r_0. Accordingly, the unit of time is $\tau_0 = \left(mr_0^2/\langle\sigma_{ij}\rangle\right)^{1/2}$.

Forces

The two-particle forces are given by the negative of the gradient,

$$\boldsymbol{F}_{ij} = -\boldsymbol{F}_{ji} = -\boldsymbol{\nabla}_i \Phi_{ij} = (\mu r_{ij} + 1)\, \frac{e^{-\mu r_{ij}}}{r_{ij}^3}\, (\boldsymbol{x}_i - \boldsymbol{x}_j) \tag{3.6}$$

The Jacobian, on the other hand, is constructed by matrices

$$\mathbf{J}_{ij} = -\,(\mu r_{ij} + 1)\, \frac{e^{-\mu r_{ij}}}{r_{ij}^3} \mathbb{I}_2 + \left(\mu^2 r_{ij}^2 + 3\mu r_{ij} + 3\right) \frac{e^{-\mu r_{ij}}}{r_{ij}^5}\, (\boldsymbol{x}_i - \boldsymbol{x}_j) \otimes (\boldsymbol{x}_i - \boldsymbol{x}_j) \tag{3.7a}$$

for $i \neq j$, where $\otimes$ denotes the dyadic product. The diagonal part $\mathbf{J}_{ii}$ is given by the negative sum over all matrices $\mathbf{J}_{ij}$ in a row or column,

$$\mathbf{J}_{ii} = -\sum_{j \neq i} \mathbf{J}_{ij} = -\sum_{j \neq i} \mathbf{J}_{ji}. \tag{3.7b}$$

As a consequence, the inter-particle Jacobian is symmetric, which is favorable when investigating the spectra. Within this definition, unstable modes of the spectrum have positive eigenvalues, whereas stable modes have negative ones.

When evaluating the potential numerically, we naturally have to cut off the potential at an appropriate radius r_{cut}. As a condition we chose

$$\Phi_{ij}(\mu, r_{\text{cut}}) \leq 1 \times 10^{-8}.$$

The critical radius where this is fulfilled is shown in figure 3.2. It allows us to optimize stationary states up to a precision of $\|\boldsymbol{F}\| < 10^{-8}$. Consequently, we considered a cut-off radius of $r_{\text{cut}} = 8.0$ to be sufficient for a screening of $\mu > 2$. Below $\mu = 1$ the critical radius quickly diverges as the potential approaches its Coulomb interaction limit. Therefore, we restrict ourselves to the range $1 \leq \mu \leq 12$

System definitions

We consider a two-dimensional system. Unless stated otherwise, it is subject to periodic boundary conditions. Since the potential is purely repulsive, the system forms a Wigner crystal and its minimum energy configuration is given by a hexagonal lattice (Wigner, 1934; Meissner et al., 1976). Box-sizes are chosen such as to accommodate the hexagonal lattice with lattice constant r_0, $L_x = N_x r_0$ the width and $L_y = \sqrt{3}/2 N_y r_0$ the height. Correspondingly, $N = N_x N_y$ is the total number of particles and $n = 2N$ the system dimension. This results in a number density of $\rho = 2/\sqrt{3} \approx 1.15$. In general, we consider systems with $N = 2500$ particles and choose a screening of $\mu = 3.0$, if not stated otherwise.

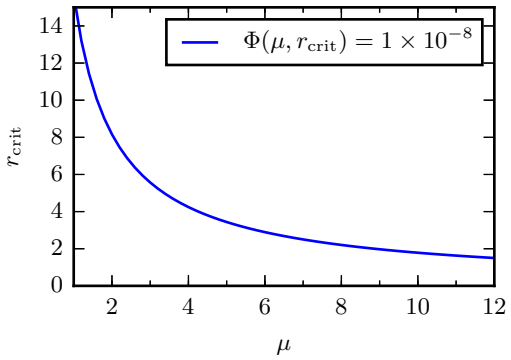

Figure 3.2: Critical interaction range of the Yukawa potential as a function of the screening parameter μ. A cut-off of $r_{\mathrm{cut}} = 8.0$ is considered sufficient for $\mu > 2$.

In some special cases we will use different boundary conditions, e.g. in the low-dimensional model system in the next chapter and when investigating the connection to elasticity theory in chapter 5. In either case, a fraction of the particles is kept fixed at positions of the underlying hexagonal lattice.

Natural oscillations

In thermal equilibrium and at low temperatures, particles in a crystalline configuration will oscillate about their lattice positions. The corresponding frequency can be estimated by the Einstein frequency ω_E. It is defined as the frequency at which a single particle in the crystal vibrates, with all other particles being held fixed at their respective lattice sites. Thus, the other particles effectively constitute a potential well. The frequency can then be extracted by the harmonic approximation of the single-particle potential,

$$\Phi_1(\boldsymbol{x}) = \sum_{j \neq 1} \tfrac{1}{2}\Phi_{1j} \approx E_{0,1} + \tfrac{1}{2}\omega_E^2 \left(u_x^2 + u_y^2\right). \tag{3.8}$$

Here, $E_{0,1}$ is the particle's potential energy at the lattice position, and u_x and u_y are the displacements in the x- and y-direction, respectively. Comparing eqn. (3.8) to the Taylor expansion of the potential, ω_E^2 is found to be the negative eigenvalue of the single-particle Jacobian, eqn. (3.7b), which is degenerate due to rotational invariance of the single-particle potential in the crystalline configuration[1]. Moreover, since the submatrices $\mathbf{J}_{ii}$ are given by the single-particle Jacobians, and the trace of a matrix equals the sum of its eigenvalues, the Einstein frequency is readily obtained by

$$\omega_E^2 = \frac{1}{2N}\mathrm{tr}\left(\mathbf{J}\right). \tag{3.9}$$

In the case of $\mu = 3$, this yields an Einstein frequency of $\omega_E^2(\mu = 3) = 2.098$.

[1] We will return to this issue later on in chapter 5.5.

Scalings in other publications

Throughout publications addressing the Yukawa system, different scalings are used. First, instead of measuring thermal energy in units of the interaction energy, often the opposite is done. Thus, an interaction strength is defined as

$$\Gamma = \frac{\sigma_{ij}}{k_B T}. \tag{3.10}$$

As a consequence, the temperature of the system is kept fixed and the interaction strength is varied in order to find e.g. phase transitions. The physical motivation is found in the experiments, where it is easier to adjust the interaction between particles instead of increasing the temperature of the heat bath. Moreover, changing the temperature in general also affects the Debye length, which is closely related to the screening parameter μ. However, this is only of importance when actually simulating a specific physical system. With our choice of $\sigma_{ij} = 1$, the relation between Γ and the temperature in our system is readily given by

$$\Gamma = 1/k_B T, \tag{3.11}$$

i.e. Γ is the inverse temperature.

Another issue is the choice of the relevant length-scale. In place of the lattice spacing r_0, frequently the Wigner-Seitz radius b is considered. In a two-dimensional system it is defined as the radius of the circle whose area equals the average area per particle in the system,

$$\frac{L_x L_y}{N} = \frac{1}{\rho} = \pi b^2. \tag{3.12}$$

It is thus an indicator of the density of the system. The relation (3.12) is essential when comparing to results in other publications, since it changes both the screening parameter μ as well as the interaction strength. For a box commensurate with the lattice, i.e. $L_x = N_x r_0$ and $L_y = \sqrt{3}/2 N_y r_0$, we find a direct relation between r_0 and b:

$$r_0 = \sqrt{\frac{2}{\rho\sqrt{3}}} = \sqrt{\frac{2\pi}{\sqrt{3}}} b \approx 1.9 b. \tag{3.13}$$

Accordingly, our system is characterized by a Wigner-Seitz radius of $b \approx 0.53 r_0$, and the parameters μ and Γ have to be rescaled by

$$\mu = 1.9 \mu_b \qquad \text{and} \qquad \Gamma = \frac{\Gamma_b}{1.9}, \tag{3.14}$$

where the index b denotes the parameters rescaled to the Wigner-Seitz radius.

A second length scale may be introduced when treating the system as a liquid instead of a crystal. The average distance between particles is then directly related to the particle density,

$$r_p = \sqrt{\rho^{-1}} = \sqrt{\frac{\sqrt{3}/2 r_0^2 N}{N}} = \sqrt{\frac{\sqrt{3}}{2}} r_0. \tag{3.15}$$

Similarly to the Wigner-Seitz radius, quantities have to be rescaled according to

$$\mu = 1.075\mu_p \qquad \text{and} \qquad \Gamma = \frac{\Gamma_p}{1.075}. \tag{3.16}$$

Here, the index p refers to the parameters rescaled to the average particle distance.

3.2 Molecular dynamics simulations

In order to understand the underlying structural changes which can occur in the system, we start by simulating the system in contact with a heat bath. To this end we use a Langevin thermostat (Schneider and Stoll, 1978) yielding the evolution equations

$$\ddot{\boldsymbol{x}}_i = \sum \boldsymbol{F}_{ij} - \gamma \dot{\boldsymbol{x}}_i + \boldsymbol{\eta}_i(t), \tag{3.17}$$

with $\boldsymbol{F}_{ij}$ the inter-particle forces, γ the damping parameter and $\boldsymbol{\eta}_i(t)$ a stochastic force which component wise obeys

$$\langle \eta_i(t) \rangle = 0 \tag{3.18a}$$

$$\langle \eta_i(t)\eta_j(t') \rangle = 2\gamma k_B T \delta_{ij} \delta(t - t'), \tag{3.18b}$$

such that the whole equation satisfies the fluctuation-dissipation theorem. The value of the damping sets both the amplitude of the fluctuation, as well as the time scale on which they decay. We choose $\gamma = 10.0$, and results are qualitatively the same for smaller values of γ. Larger values though considerably increase the times after which a transition is observed. Since the integration of large systems is computationally demanding, we rely on the program package LAMMPS[2] (Plimpton, 1995) which uses a Velocity-Verlet integrator. The optimal step-size Δt was determined by integrating the undamped system using Newton's equations of motion and verifying energy conservation over the range of 100 time units. In the case of $\mu = 3.0$ and $r_{\text{cut}} = 8.0$, this is accomplished for $\Delta t = 1{\times}10^{-3}$. We start with the crystalline configuration and achieve thermal equilibrium at a temperature of $k_B T_0 = 0.003$ by integrating several thousand time units. Simulations show that at this temperature and for a screening parameter $\mu = 3.0$, the system is well in the crystalline phase. Thereafter, we slowly heat the system at a rate of $k_b \dot{T} = 1/11000000 \approx 1 \times 10^{-7}$. However, an inspection of fluctuations of the potential energy suggests that this rate might still be too large to adiabatically drive the system towards the melting point. Therefore, in the critical temperature range close to phase transitions we take configurations along this trajectory as initial conditions and evolve them at constant temperature for 20000 or 60000 additional time units. After this time, in most cases thermal equilibrium is established, which is verified by several criteria summarized in appendix A.1. Since many simulations at different temperatures are required, all simulations were performed on the MaRC2 cluster at Philipps-Universität Marburg.

Figure 3.3 shows some typical configurations encountered in the simulations. We use the coordination number c_i to visualize disorder in the system. It is defined as the number

[2] `http://lammps.sandia.gov`

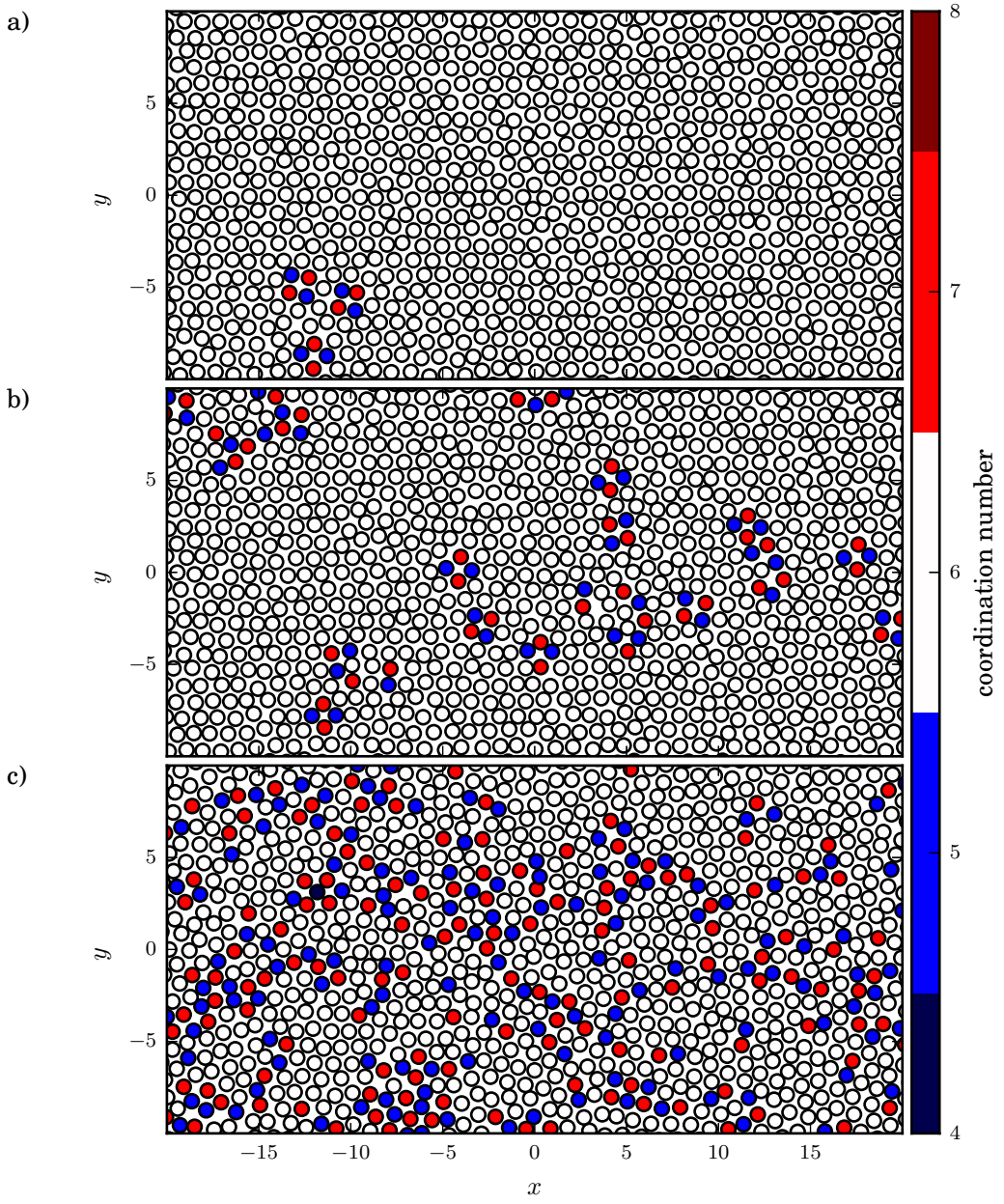

Figure 3.3: Typical configurations encountered in a MD-simulation, with temperature increasing from top to bottom, $k_BT = 0.006$, 0.007, and 0.008 respectively. Color-coded is the coordination number, i.e. the number of nearest neighbors, white for 6 neighbors, blue for less, and red for more. (a) At the lowest temperature the system is in the crystalline phase, where in general each particle has six neighbors. Every now and then, isolated pairs of dislocations emerge, i.e. groups of particles with 5 and 7 neighbors. (b) At higher temperatures, more pairs of defects emerge which partially start to dissociate. Locally, the crystalline structure persists. (c) At even higher temperatures, the number of defects considerably increases and the crystal lattice breaks down. Each configuration has been evolved for 9000 additional time units at constant temperature. Simulation details are described in the text.

of next neighbors of each particle, determined by a Delaunay triangulation. In a two-dimensional hexagonal lattice, each particle has exactly six nearest neighbors, i.e. $c_i = 6$. At low temperatures, figure 3.3(a), the ensemble is close to the perfect lattice with particles wiggling around their equilibrium positions. The system exhibits some minor large-scale fluctuations, hardly noticeable as long wavelength modulations of the lattice. Most particles have six next neighbors, as would be expected. Every now and then, thermally activated pairs of dislocations emerge, i.e. groups of four particles where two of them have seven next neighbors and the other two only have five. With increasing temperature, figure 3.3(b), more of those pairs of dislocations are found. It can be observed that some of them start to dissociate, resulting in isolated dislocations. Still, most particles are part of a crystalline neighborhood. Upon further increasing temperature in (c), those crystalline clusters diminish and the number of isolated dislocations increases. Furthermore, disclinations emerge, i.e. isolated particles with a coordination number differing from six. Apparently, the system has undergone a phase transition.

3.2.1 Theory of melting

In two-dimensional systems, it is still a matter of debate on how the transition from solid to liquid takes place. Depending on the interaction and other factors as for example system size or heating procedures, both experiments and simulations give partially contradictory results. For instance, single-step first order transitions were reported both for dipole (Bedanov et al., 1985a) and Lennard-Jones interactions (Bedanov et al., 1985a; Kleinert, 1989). Other authors found single-step continuous transitions, for example for the Coulomb potential (Kleinert, 1989) or in experiments with dusty plasmas (Melzer et al., 1996a; Nosenko et al., 2009; Knapek, 2010), which are commonly described using a Yukawa potential. A third group of authors observed two-step continuous transitions involving an intermediate phase, covering colloidal suspensions (Zahn et al., 1999; Zahn and Maret, 2000; Keim et al., 2007; Deutschländer et al., 2013), hard disks (Binder et al., 2002), and again the Coulomb potential (Bedanov et al., 1985a).

Even when considering the Yukawa potential alone, contradictory results are obtained. Besides in the experiments with dusty plasmas, a single step continuous transition was also observed in simulations at constant energy (Hartmann et al., 2007). Other simulations using Brownian (Qi et al., 2008, 2010) and Langevin dynamics (Vaulina and Koss, 2014; Vaulina and Vasilieva, 2014) gave evidence of an intermediate phase. Qi et al. found signs of a phase coexistence close to the liquid transition, hinting at a first order transition. More recently, this was bolstered by large-scale Monte-Carlo simulations (Kapfer and Krauth, 2015). They found that the second transition from the intermediate to the liquid phase changes from continuous to first order for a strong screening parameter. Other authors observed two-step transitions as well (Murray and Van Winkle, 1987; Naidoo and Schnitker, 1994), but remarked a more complex mechanism than would be predicted by the theory. Furthermore, some groups noticed hysteresis effects (Zheng and Earnshaw, 1998; Radzvilavičius, 2012), which might be attributed to an intermediate phase, but equally likely might be caused by rapid heating and/or cooling.

The most widely accepted theory for two-dimensional melting is the KTHNY-theory describing a continuous two-step process of melting, put forward by Kosterlitz, Thouless,

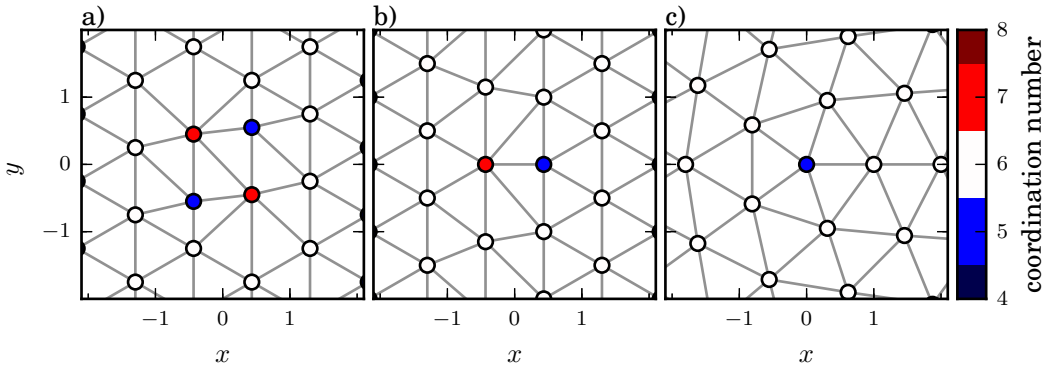

Figure 3.4: Example for typical lattice defects, a pair of dislocations (a), an isolated dislocation (b) and a disclination (c). A similar structure emerges for an isolated sevenfold coordinated particle. Whereas the first defect does not affect the surrounding lattice, isolated dislocations break translational symmetry, and disclinations break the long-range orientational order.

Halperin, Nelson, and Young (Kosterlitz and Thouless, 1973; Halperin and Nelson, 1978; Nelson and Halperin, 1979; Young, 1979). In three dimensions, a crystal is characterized by its long range translational order. At finite temperatures, the individual particles vibrate about their lattice sites, until at a critical temperature the crystal as a whole melts into a liquid phase. In contrast, in two dimensions crystals are thermally unstable due to long-wavelength phonons (Mermin, 1968). Consequently, lattice sites are shifted along the phonon modulations and thus translational order slowly decays with distance, resulting in a quasi long-range translational order. However, the orientation among neighboring particles remains intact, and the crystal thus shows long-range orientational order.

KTHNY-theory describes a defect-mediated melting process. For illustration, the defects in question are shown in figure 3.4. Due to thermal fluctuations, pairs of dislocations as in figure 3.4(a) will emerge every now and then. They constitute of four neighboring particles, two of them having five next neighbors and the other two having seven. Obviously, the defect does not interfere with the surrounding lattice and thus has no effect on the crystalline structure. At a critical temperature, those pairs dissociate into isolated dislocations. As can be seen in figure 3.4(b), those defects show the splitting of an additional lattice row, here to the right of the dislocation. In consequence, the quasi long-range order of the system is lost, but a quasi-long range orientational order is still preserved, as can be seen from the orientation of the hexagons left and right of the defect. The system is thus in a different phase, which is termed hexatic. Upon further increasing temperature, a second transition is encountered. It is characterized by the formation of isolated disclinations, figure 3.4(c). While locally most particles are still sixfold coordinated, their orientation considerably varies in space. Therefore, quasi long-range orientational order is lost as well and the system has entered the liquid phase.

While KTHNY theory predicts a two-step process, there are also theories which promote a single first order transition, for example by the spontaneous formation of grain boundaries (Chui, 1982, 1983), i.e. chains of alternating disclinations of five and seven

neighbors. This results in an abrupt increase in the number of defects at the melting point. The process preempts the KTHNY-scenario of a transition towards the hexatic phase in favor of a polycrystalline phase.

The question which scenario takes precedence can be answered by examining the two competing energies, namely the energy needed for the unbinding of a dislocation, and the core energy of a dislocation, E_c. Whereas the former specifies how easily a pair of dislocations breaks up and thus is important for the KTHNY mechanism, the latter describes the excess energy needed to generate a dislocation, and hence determines the number of dislocations in a system through the corresponding Boltzmann distribution. Therefore, for large core energies, at the temperature of melting only few dislocations are found in the system which then will dissociate and lead to a KTHNY-like transition. For small core energies, on the other hand, the number of dislocations will quickly grow with temperature until a critical density is reached and the system melts. As this happens before the temperature is large enough to enable the dissociation of dislocations, a single-step transition is observed. As pointed out by Chui (1983) and Strandburg (1988), the critical core energy is given by $E_c = 2.84 k_B T_0$, where $k_B T_0$ is the temperature of dislocation unbinding.

To the casual eye, the configurations in figure 3.3 seem to be in general agreement with KTHNY-theory as we see an increase of isolated dislocations and, at higher temperatures, disclinations. Nevertheless, we also observe an increase of the total number of defects, which might be attributed either to the increasing temperature, or to the formation of grain boundaries.

Still, it is complicated to identify isolated defects, and there is no clearly defined threshold in defect densities as to determine the critical temperatures, especially since most defects are thermally activated pairs of dislocations which quickly decay. Hence, in the next sections we will focus on more robust quantities to characterize the system. Several of them have been developed over the last decades (see e.g. Dillmann et al. (2012) for an overview). We will make use of some of them, revealing translational and orientational order as well as the system's diffusivity.

3.2.2 Translational ordering

As a first indicator of the state of the system, we take the radial correlation function $g(r)$, introduced in the previous chapter (eqn. (2.26)). With increasing temperature, we expect it to show the typical transition from solid- to liquid-like correlations. In order to further characterize $g(r)$, we also investigate its Fourier transform, $g(k)$. Both are shown in figure 3.5(a) and (b) for various temperatures. Data has been taken after the system reached thermal equilibrium. At low temperature, $k_B T = 0.0030$, the radial distribution shows oscillations which continue to exist even on large distances r. Although in a two-dimensional system long-range order cannot exist, we observe several isolated peaks characteristic of a crystalline configuration. For instance, we find peaks at $r = 1$, $\sqrt{3}$, 2, and $\sqrt{7}$ which correspond to the distances of neighbor shells in the crystal. The rich structures found at large radii quickly vanish with increasing temperature, and at $k_B T = 0.0060$ only the first few peaks can be vaguely discerned. Upon further increasing the temperature, oscillations become more regular and featureless. At higher temperatures (e.g. $k_B T = 0.0070$), the

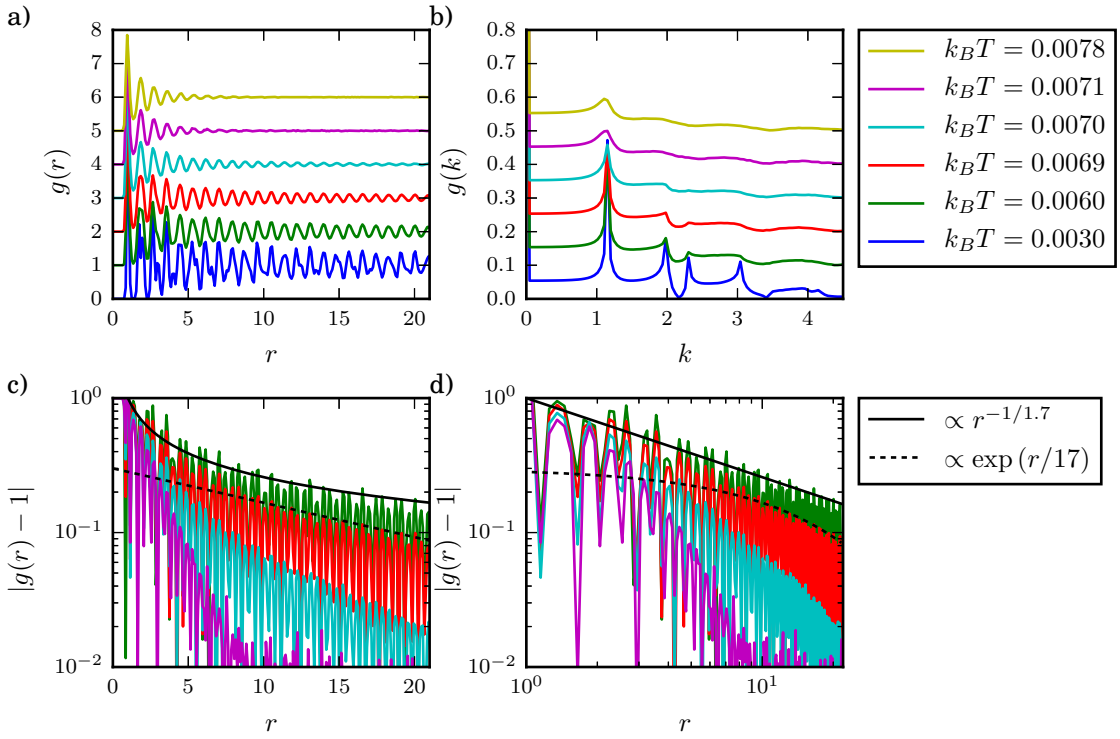

Figure 3.5: Radial correlation function $g(r)$ (eqn. (2.26)). Data has been taken after the system has reached thermal equilibrium, and has been averaged over eight independent ensembles for each temperature. (a),(b) The correlation function $g(r)$ and its Fourier transform $g(k)$ at different temperatures, averaged over eight independent realizations. For clearer distinction, graphs are shifted by an arbitrary constant. We observe a change from the rich correlations of a crystalline solid to featureless oscillations, which quickly decay at higher temperatures. This reflects in the decaying peaks of $g(k)$ as well. (c),(d) In order to characterize the decay we consider $|g(r)-1|$, both in semilogarithmic and doubly logarithmic representation. For larger distances, $r > 10$, we observe a change from algebraic to exponential decay with increasing temperature: The system loses its quasi-long range translational order. The black solid and dashed lines are guides to the eye to illustrate the different types of decay.

long distance correlations start to decay noticeably. For even higher temperatures, radial correlations beyond $r \approx 10$ are lost, and the correlation function shows typical features of a liquid, with a few strong peaks on short distances reflecting the repelling nature of the interaction, and oscillations quickly diminishing with distance indicating a short-range order of the system. The first maximum of $g(r)$ is located at $r_{\max} \approx \sqrt{\rho^{-1}} \approx 0.93$, which equals the next-neighbor distance determined from the mean particle density.

The Fourier transforms of the radial correlations $g(k)$ shown in figure 3.5(b) support these observations. At the lowest temperature, $k_BT = 0.0030$, $g(k)$ exhibits four distinctive peaks. With increasing temperature, all four of them shrink and become less sharp. At $k_BT = 0.0060$, the fourth peak has vanished. While the first peak at $k \approx 1.1$ persists

with increasing temperature, the remaining two become less pronounced and disappear beyond $k_BT = 0.0070$. This is accompanied by the stronger decay of the radial correlation function.

In order to further characterize the decay of the correlation function, we also consider $|g(r) - 1|$ in figure 3.5(c) and (d), both in a semilogarithmic and a doubly logarithmic representation. Of particular interest is the behavior on longer distances, $r > 10$. As long as quasi long-range translational order persists, we would expect a slow algebraic decay, which is replaced by a faster exponential decay as soon as short-range translational order is attained (Nelson and Halperin, 1979). Indeed, at low temperatures ($k_BT = 0.0060$), we observe an algebraic decay. Upon increasing temperature, we see a change and correlations decay faster and exponentially. This is clearly evident for $k_BT \geq 0.0070$, and seems plausible for $k_BT = 0.0069$. It marks the crossover to short range translational order somewhere in between $0.006 < k_BT < 0.007$. However, in this critical region of temperature, correlations decay only slowly and it is hard to tell whether they drop exponentially or algebraically. Therefore, in order to determine the exact point of the transition one would need to investigate a much larger system or rely on different criteria. Beforehand, we investigate the transition to the liquid, which is easier to verify.

3.2.3 Sixfold orientation

As mentioned above, at the solid to liquid transition the system loses its quasi long range orientational order. To quantify this, we consider the local six-fold orientation $\psi_6(\boldsymbol{x}_i)$, which is an imaginary number describing the orientation of the nearest neighbors of a particle,

$$\psi_6(\boldsymbol{x}_i) = \frac{1}{c_i} \sum_j \exp(i6\Theta_j). \tag{3.19}$$

Here, c_i the coordination of particle i and Θ_j the angle of the vector between particles i and j towards the x-axis. In a lattice, each particle has the same value of ψ_6. Moreover, in the hexagonal lattice each particle has six nearest neighbors which are separated by an angle of $\pi/3$. Consequently, they all contribute the same amount to ψ_6, and $|\psi_6| = 1$. For an ensemble in the hexatic state where locally the crystalline structure is preserved, ψ_6 lies close to the unit circle. In a disordered state, corresponding to an isotropic fluid, lattice structures are absent and the distribution of ψ_6 is spread around zero.

A measure which can be used to distinguish hexatic and liquid phase are the radial correlations,

$$g_6(r) = \langle \delta(r - r_{ij}) \psi_6(\boldsymbol{x}_i) \psi_6^*(\boldsymbol{x}_j) \rangle, \tag{3.20}$$

the so-called bond-order correlation function. According to Halperin and Nelson (1978), it shows different behavior in each phase. In the crystalline phase the system exhibits a long range orientational order, and thus $g_6(r)$ approaches a finite value for large r. In the hexatic phase, we observe a quasi long range order, i.e. the correlation function decays algebraically, $g_6(r) \propto r^{-\eta_6}$. Halperin and Nelson showed that η_6 varies between zero and $1/4$, at which point the transition to the isotropic phase occurs. Beyond, only short range ordering is observed and $g_6(r)$ decays exponentially, $g_6(r) \propto \exp(-r/\xi_6)$. In a survey of

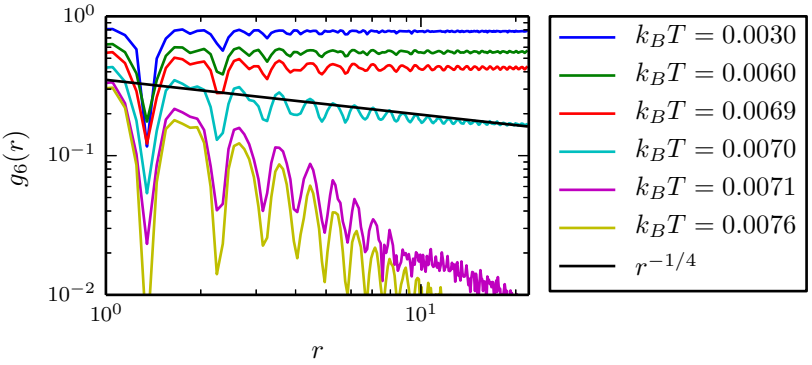

Figure 3.6: The six-fold orientation correlation function $g_6(r)$ for different temperatures in a doubly logarithmic plot. With increasing temperature, we see a change from the solid ($k_BT = 0.003$) to the hexatic to the isotropic phase ($k_BT = 0.0071$). The black line is a guide to the eye. It indicates the critical exponent of the algebraic decay before changing to the exponential decay characteristic for an isotropic liquid.

different melting criteria, Dillmann et al. (2012) showed that the bond-order correlation function $g_6(r)$ is a sensitive tool to determine the transition towards an isotropic phase.

The bond-order correlation function for different temperatures of the ensemble is shown in figure 3.6. The final configurations are generated by heating the system as described above, and a subsequent equilibration of the system at constant temperature for 60000 time units in the critical region, and 20000 time units else. Data is taken from an average of eight independent runs, each consisting of 2500 particles. One can clearly observe the breakdown of the orientational order. For low temperatures ($k_BT = 0.003$), the correlation remains constant over the entire domain. It is slightly less than unity due to the long-wavelength phonons which marginally disturb the perfect lattice configuration. When increasing temperature, $g_6(r)$ changes towards an algebraic decay. At around $k_BT = 0.007$, the exponent η_6 approaches $1/4$ (black line). For larger temperatures, we find a faster exponential decay, corresponding to a loss of orientational correlations which is characteristic for the isotropic phase. The observed transition occurs in between $0.007 < k_BT_c^{\psi} < 0.0071$. However, it should be noted that the kinetic temperature of the system fluctuates around its mean by about 2% (cf. section A.1). Therefore, we might locally see a liquefaction which temporarily destroys orientational correlations, and, in effect, leads to an underestimation of the temperature of melting. On the other hand, close to the critical temperature transients become very long, and despite our efforts to establish thermal equilibrium we might have overestimated the temperature of melting. Nevertheless, the result is in good agreement with Hartmann et al. (2005)[3], who found $k_BT_c \approx 0.0071$ and who used a different thermostatting and melting criterion. It also is in fair agreement with the findings of Vaulina and Koss (2014), $k_BT_c \approx 0.00775$, who use a semi-empirical scaling law to predict the melting point. We will return to this later when discussing the impact of a varying screening parameter in chapter 6. A slightly higher melting temperature

[3]Quantities have to be rescaled using eqn. (3.14).

was reported by Zheng and Earnshaw (1998)[4], $k_B T_c \approx 0.0091$. We obtained a similar critical temperature when heating the system more rapidly, and without the subsequent equilibration at fixed temperatures. However, they also performed a cooling experiment where they obtained a crystallization temperature of $k_B T_c \approx 0.0077$.

Lately, there have been concerns that the hexatic phase might be metastable and only present due to a lack in equilibration times (Derzsi et al., 2014). Indeed, when heating the system too rapidly, we observed a delayed transition which shows the exact same change from algebraic to exponential decay of the orientational correlations, but at higher temperatures. This issue could be resolved by thermally equilibrating the system at each considered temperature, as described earlier.

3.2.4 Lindemann criterion

The transition from crystalline to hexatic is a more subtle one, since both phases are structurally similar and hardly to tell apart by bare eye. Accordingly, Halperin and Nelson termed the latter as *liquid crystals*. Nevertheless, the breakdown of the long-range translational order provides a starting point.

In 1910, Lindemann put forward the idea that a crystalline solid melts as soon as its atoms vibrate so strongly around their equilibrium positions that two of them may collide halfway their separating distance. He then adopted it to determine natural frequencies of several substances, successfully to some extent. Later on, the idea was refined by Gilvarry (1956), who more generally considered the average displacements of particles due to thermal vibrations, $u_{\mathrm{RMS}} = \sqrt{\langle \|\boldsymbol{u}_i\|^2 \rangle}$, in relation to the lattice spacing r_0. Here, $\boldsymbol{u}_i$ is the displacement of a particle. He found that melting occurs at vibrational amplitudes of approximately 10% of r_0. This lead to the introduction of the Lindemann parameter,

$$\gamma_L = \frac{\langle \|\boldsymbol{u}_i\|^2 \rangle}{r_0^2}. \tag{3.21}$$

This quantity is easily accessible from both experiments and simulations. In the solid, particles are bound at their lattice sites and γ_L attains a constant value. In the liquid phase, though, it is closely related to the self-diffusion of the system, and hence γ_L diverges. In several studies on three-dimensional systems, it has been confirmed that at the point of the phase transition the average displacements reach approximately 10% of the lattice spacing, or $\gamma_{\mathrm{L}} \approx 0.01$ (Gupta and Sharma, 1968; Grimvall and Sjödin, 1974; Jin et al., 2001). However, it is only a rough estimate and varies for different crystals and atom types. Additionally, its harmonic approximation neglects bond breaking and, accordingly, the break-down of the lattice upon melting.

In two dimensions, the general Lindemann criterion fails. This is due to the presence of long-wavelength phonons, which lead to a divergence of the displacements u_{RMS} (Peierls, 1934, 1935; Mermin, 1968). However, it is possible to restore the Lindemann criterion, by not considering the absolute displacements but relative displacements with respect to the

[4] Due to a different definition of the potential, their reported temperatures are exactly half as large as ours

nearest neighbors $\{j\}$ (Lozovik and Farztdinov, 1985; Bedanov et al., 1985b),

$$\gamma_{\mathrm{L}} = \frac{\langle \|\boldsymbol{u}_i - \boldsymbol{u}_j\|^2 \rangle}{r_0^2}. \tag{3.22}$$

The neighborhood relations are determined from the undisturbed lattice. This way, since neighboring particles are affected equally by the long wavelength modulations, their effect is eliminated and Bedanov et al.[5] yield a finite critical Lindemann parameter of approximately $\gamma_{\mathrm{L}}^c \approx 0.028 \ldots 0.033$, corresponding to an average displacement of $u_{\mathrm{RMS}} \approx 0.17 r_0 \ldots 0.18 r_0$. This approximate value has been confirmed by several groups (Zahn et al., 1999; Qi et al., 2010; Dillmann et al., 2012). Zheng and Earnshaw (1998) introduced yet another, slightly different definition, by relating the displacements to the local lattice consisting of the six nearest neighbors,

$$\gamma_6 = \frac{\langle \|\boldsymbol{u}_i - \langle \boldsymbol{u} \rangle_6\|^2 \rangle}{r_0^2}. \tag{3.23}$$

Again, the neighbors are determined from the undisturbed lattice. In effect, displacements are measured with respect to the center of mass of the six nearest neighbors, $d_i = \boldsymbol{x}_i - \langle \boldsymbol{x} \rangle_6$. In contrast to eqn. (3.22), the consideration of the center of mass also reduces the effect of the fluctuating displacements of the neighboring particles. As a result, this method yields a somewhat lower critical Lindemann parameter of $\gamma_6^c \approx 0.0076 \ldots 0.010$, or $u_{\mathrm{RMS}} \approx 0.087 r_0 \ldots 0.10 r_0$, which is close to the values reported in three-dimensional systems.

The comparative survey of Dillmann et al. (2012) shows that the Lindemann criterion is a sensitive indicator of the crystalline to hexatic transition. In figure 3.7, we show the Lindemann parameter of our system as a function of temperature and time. The results were obtained by averaging over eight independent realizations. When considering the temperature dependence during heating in figure 3.7(a), we observe a finite Lindemann parameter γ_{L} for $k_B T < 0.0066$. Up to this temperature it increases steadily, and then jumps abruptly to a larger value. The corresponding critical Lindemann parameter is $\gamma_{\mathrm{L}}^c \approx 0.028 \ldots 0.03$, which is slightly lower than the critical values reported in literature. Slightly above the critical temperature, the increase of the Lindemann parameter is mainly due to the recurring occurrences of local reorganizations in the system, as we will see further below. Upon further increasing temperature, the Lindemann parameter starts to grow more rapidly, eventually diverging very fast as soon as the system enters the liquid phase, $k_B T > 0.007$. In the same figure, we also show the Lindemann parameter of the local lattice, γ_6. It shows the same behavior as γ_{L}, although it is slightly smaller throughout the whole temperature range. Its critical value is reached at $\gamma_6 \approx 0.014$, corresponding to an average displacement of $u_{\mathrm{RMS}} \approx 0.12 r_0$ which is close to the values obtained in three-dimensional systems.

Slightly above the critical temperature, the Lindemann parameter diverges only slowly. Therefore, in order to determine the transition point, we evolve the system at fixed temperature for several thousand time units. The corresponding Lindemann parameter γ_{L} is shown in figure 3.7(b). The initial conditions at $t = 0$ are taken from the simulations at

[5] They defined the length scale by the Wigner-Seitz radius b (eqn. (3.12)) and found $\gamma_{\mathrm{L}}^c \approx 0.10 \ldots 0.12$ ($u_{\mathrm{RMS}} \approx 0.32 b \ldots 0.35 b$)

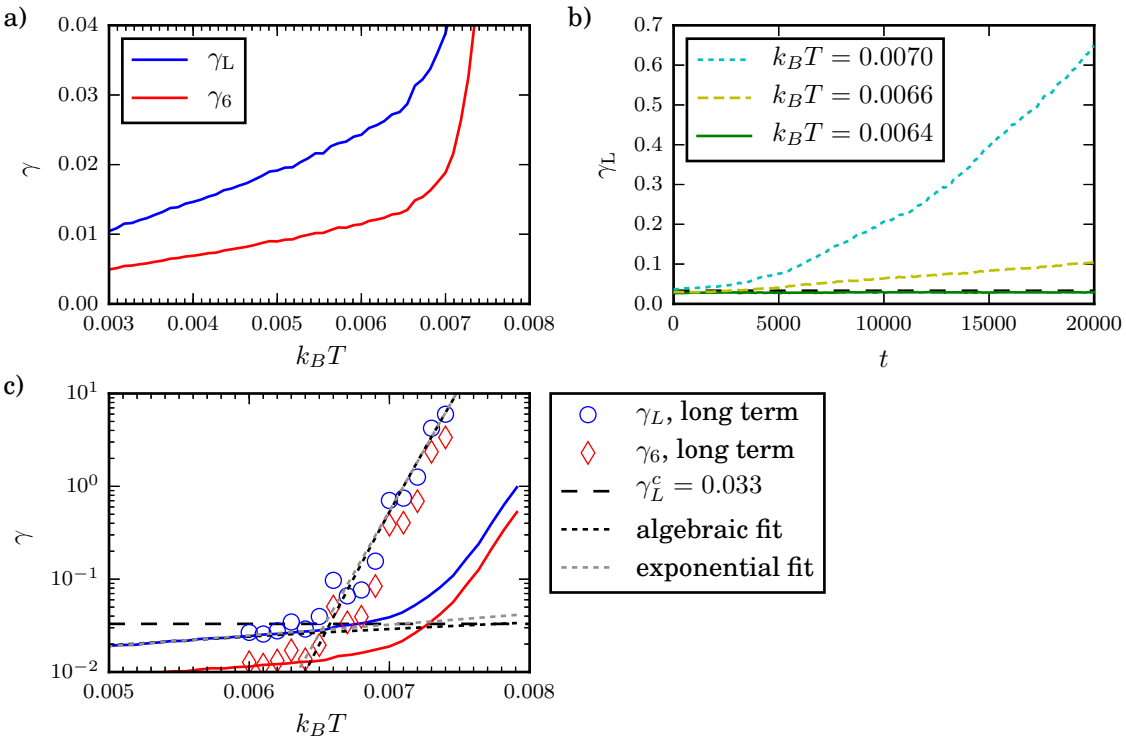

Figure 3.7: Lindemann parameters γ_L (eqn. (3.22)) and γ_6 (eqn. (3.23)) in dependence on temperature and time. (a) The two instantaneous Lindemann parameters γ_L (blue) and γ_6 (red) during heating of the system. Both show the same general behavior. With increasing temperature and below the critical point, the Lindemann parameter steadily increases with temperature. At the critical point ($k_BT \approx 0.0066$), we observe an abrupt jump and the Lindemann parameter diverges afterwards. (b) Development of the Lindemann parameter γ_L over time at fixed temperatures. Initial conditions ($t = 0$) are taken from the heated system. Below the critical temperature, the Lindemann parameter remains constant. At larger temperatures it diverges, the rate depending on the temperature. As a point of reference, the horizontal dashed black line indicates the critical Lindemann parameter of $\gamma_\mathrm{L}^c = 0.033$, as reported in literature. (c) The Lindemann parameter after 20000 time units of equilibration (open symbols) in a semilogarithmic representation of (a). The dotted lines are fits, either to an algebraic (black) or exponential (gray) dependence. Accordingly, the critical temperature is in between $0.0065 < k_BT_c^\gamma < 0.0066$. The transition to the liquid phase occurs at an approximately 7% higher temperature, $k_BT_c^\psi \approx 0.0071$. As in (b), the horizontal dashed black line indicates the critical Lindemann parameter. All data was obtained by averaging over eight independent runs.

the corresponding temperatures. Below the critical temperature, the Lindemann parameter remains constant over time. This implies that the crystalline order of the system is preserved, and in general particles wiggle around their equilibrium positions. Rarely, a few particles rearrange in the lattice and the Lindemann parameter makes a small jump. However, several thousand time units pass in between such events so that γ_L can be considered constant. At temperatures slightly above the critical temperature, e.g. $k_BT = 0.0066$, the Lindemann parameter starts to grow over time. This process is initiated by local rearrangements of only a few particles, and subsequently leads to larger rearrangements and the formation of defects such as vacancies and interstitials. At even larger temperatures, this effect is accelerated.

The divergence of the Lindemann parameter at higher temperatures can be better conceived in the semilogarithmic plot in figure 3.7(c). Here, we additionally show the Lindemann parameter obtained after 20000 time units of equilibration. In order to determine the critical temperature, we try to fit the data at high temperatures. Correlation coefficients indicate that the relation between γ_L and the temperature can be fitted either by an exponential ($c = 0.967$) or algebraic ($c = 0.964$) dependence. Both approaches yield a critical temperature in the range $0.0065 < k_BT_c^\gamma < 0.0066$, supporting our previous observations. As noted earlier, the kinetic temperature of the system fluctuates by about 2%. Even with these variations, it is safe to say that the divergence of the Lindemann parameter occurs at a noticeably lower critical temperature than the breakdown of orientational correlations ($0.0070 < k_BT_c^\psi < 0.0071$). The system therefore liquefies in a two-step process, where we first observe a finite diffusivity in a more or less intact crystal before in a second step at a higher temperature the orientational order of the crystal is lost and the system becomes liquid.

A somewhat lower critical temperature for the solid-to-hexatic transition was reported by Vaulina and Koss (2014), $k_BT_c^\gamma \approx 0.0050$. Among other indicators, they determined it as the point of vanishing diffusivity. It is crucial how this point is defined. Below $k_BT \leq 0.0065$, we still observe rearrangements of particles every now and then. Each of them increases the Lindemann parameter γ_L, so technically one might speak of a non-zero diffusivity. However, γ_L increases stepwise, and not continuously as above the critical temperature. We observe long periods of zero diffusivity, alternating with short periods of particle exchanges. Therefore, we take $k_BT_c^\gamma \approx 0.0065$ as the critical temperature. Additionally, their findings yield a rather large temperature range where the hexatic phase exists ($k_BT_c^\psi \approx 1.5 k_BT_c^\gamma$). Qi et al. (2010), who investigated a different screening parameter, found a smaller temperature range, similar to ours.

We can use the local lattice to visualize the breakdown of the neighborhood relations. In figure 3.8, we show the positions of the local lattices corresponding to the system snapshots in figure 3.3, namely at $k_BT = 0.006$, 0.007, and 0.008. In addition, the relative displacement of each particle from its local lattice site is color coded and represented by a displacement vector. At the lowest temperature in (a), the lattice is intact. As anticipated, it follows the long-wavelength modulations, and in comparison with figure 3.3(a) an almost perfect lattice configuration is restored. Each particle remains close to its local lattice site, indicated by the light and homogeneous coloring of displacements. At intermediate temperatures in between the two transitions, (b), in most of the domain the original lattice structure persists. In some regions though local reorganizations occur, mostly consisting

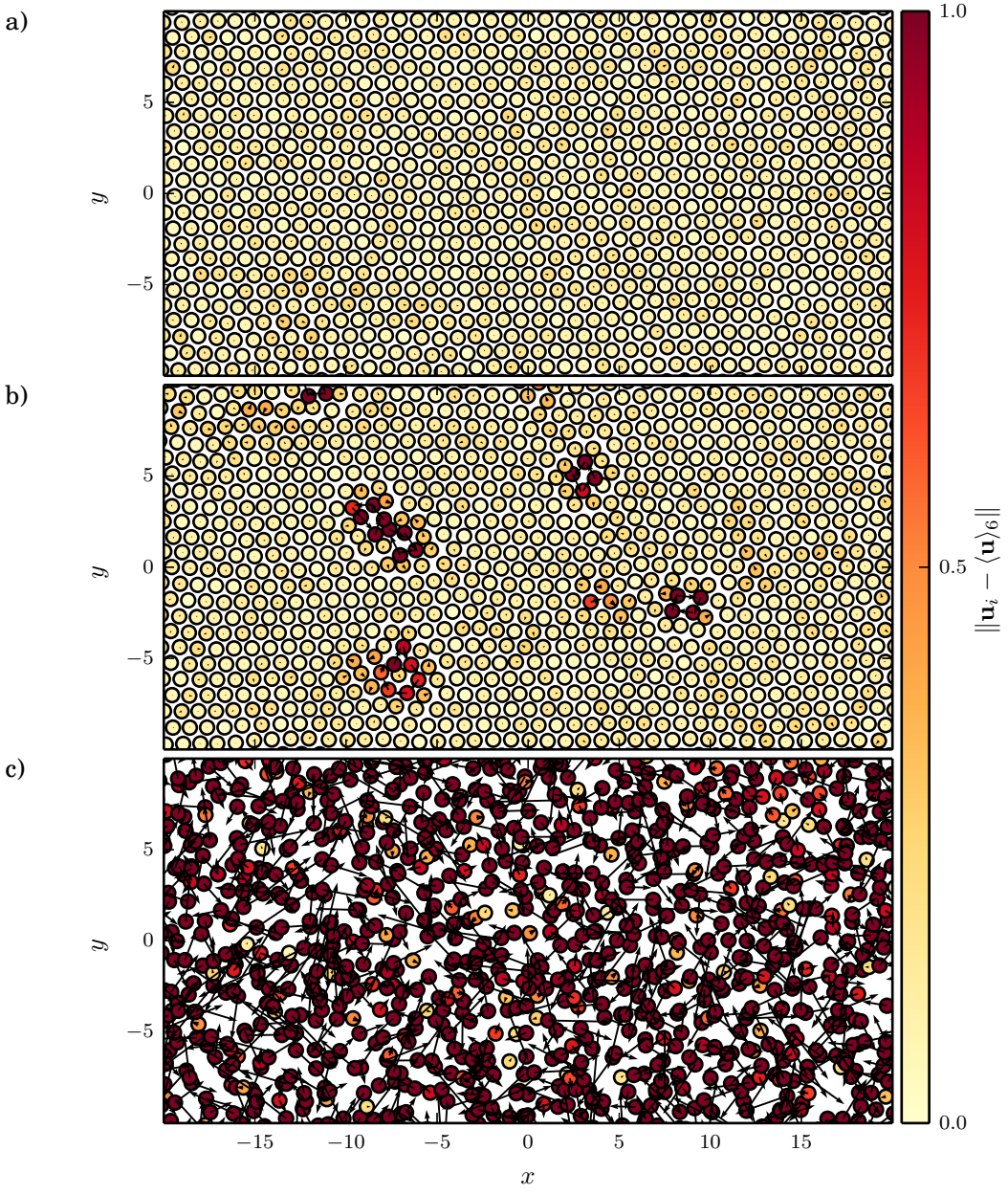

Figure 3.8: The positions of the local lattice $\langle \boldsymbol{x}_i \rangle_6$, corresponding to the configurations in figure 3.3 at temperatures $k_B T = 0.006$, 0.007, and 0.008. Arrows and colors indicate the displacements of particles in reference to their local lattice, $d_i = \|\boldsymbol{u}_i - \langle \boldsymbol{u} \rangle_6\|$. (a) At low temperatures, both the global and local lattice coincide qualitatively with only small deviations between them. (b) At higher temperatures, local reorganizations occur which distort the local lattice. Over time, more rearrangements take place such that eventually the Lindemann parameter slowly diverges. (c) At temperatures beyond the melting point of the hexatic phase, the system is mixed and most particles are far away from their local lattice sites. As a consequence, the Lindemann parameter diverges much quicker.

of few particles. Over time and at constant temperature, more and larger rearrangements will take place, and consequently those patches will grow. It is this mechanism which leads to the slow divergence of the Lindemann parameter. At temperatures beyond the hexatic-to-liquid transition shown in (c), we observe a mixing process, and most neighborhood relations are broken as can be seen from the unordered distribution of local lattice sites. Accordingly, most particles have detached from their local lattice, indicated by the large displacements. As a consequence, the Lindemann parameter quickly diverges.

3.2.5 The principle of inherent minima

We would like to describe the local rearrangements as for example in figure 3.8(b) in a more rigorous way. Therefore, in a first step we have to identify which transitions between particle configurations take place. In order to step away from noisy coordinates of the MD-simulations, we make use of the principle of inherent minima or inherent structures, introduced by Stillinger and Weber (1982, 1984a). The idea is to assign to each configuration an associated minimum. Each minimum then has its own area of attraction, and thus configuration space is partitioned into several basins of attraction. In this way, the dynamics can be described as a hopping between adjacent basins.

The mapping is achieved by considering an overdamped evolution of the system,

$$\dot{\boldsymbol{x}} = \boldsymbol{F}(\boldsymbol{x}). \tag{3.24}$$

Since this equation of motion is purely deterministic and no heat-induced barrier hopping is possible during the minimization, we consider this a rapid quench at zero temperature. This procedure yields a unique identification of the accompanying minimum for each configuration, provided the step size is small enough such that numerical errors become negligible. The latter is of particular importance when investigating systems at higher temperatures, since then particles tend to get closer to each other and are thus subject to increased forces, which in turn require smaller time steps. We use the steepest descent algorithm provided in LAMMPS. It incorporates a linesearch algorithm with the search direction given by the force vector. We take a maximum stepsize of $\Delta\boldsymbol{x}_i = 1 \times 10^{-2}$, corresponding to $\boldsymbol{F}\Delta t = 1 \times 10^{-2}$. This way, we effectively limit the time steps whenever forces become too large.

In order to further investigate configurational changes in the system, we closely inspect the inherent minima. In figure 3.9, we show the inherent minima corresponding to the configurations in figure 3.3 and 3.8. Color-coded is the magnitude of displacements with respect to the original hexagonal lattice configuration. Additionally, arrows indicate the individual displacements, visualizing the reorganizations. As would be expected, at low temperatures, figure 3.9(a), the original hexagonal lattice is restored, without any reconfigurations. The slight modulations of the displacements indicated by the color coding are due to the fact that we minimized the system only to a residual force of $\|\boldsymbol{F}\| = 10^{-3}$. In the hexatic phase, figure 3.9(b), the inherent minimum reveals the local reorganizations already observed in the local lattice representation, figure 3.8(b), more precisely. Only a few neighboring particles forming a closed loop, in this example four to nine, exchange their positions by moving by one lattice site each. When analyzing various inherent minima of snapshots in the relevant temperature range, we encounter localized transitions comprising

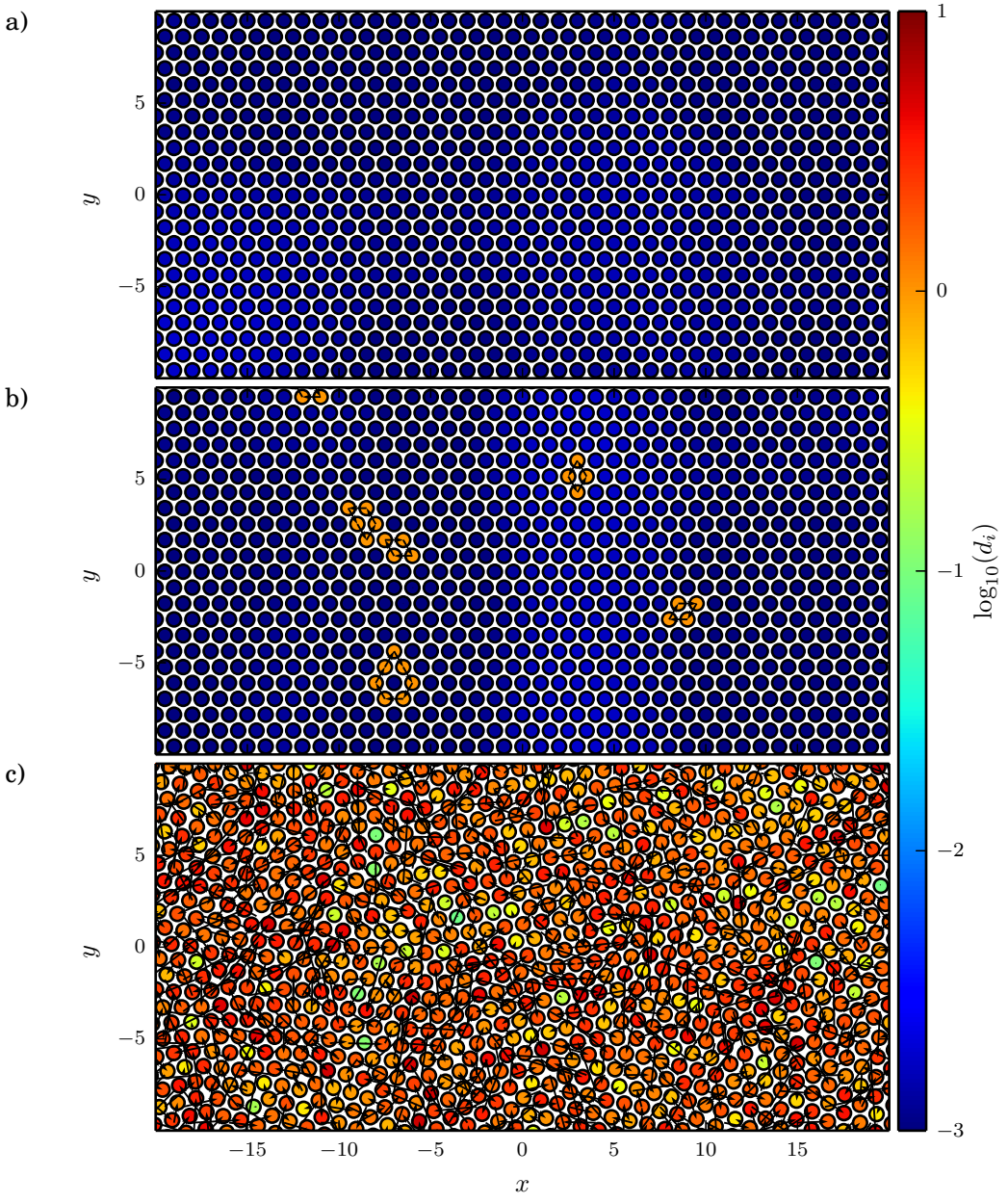

Figure 3.9: The inherent minima corresponding to the configurations shown in figure 3.3. Color coded and indicated by arrows is the displacement d_i with respect to the hexagonal lattice configuration. These configurations are representative for the three phases: Merely any reconfigurations in the crystalline phase (a), isolated reorganizations in the hexatic phase (b), mostly consisting of few particles and seldom leading to a breaking of the underlying hexagonal crystal, and many reconfigurations in the isotropic phase (c), mostly constituting of longer chains, although few-particle reconfigurations are observed. The inherent minima exhibit grain boundaries, i.e. differently oriented crystalline patches, and isolated defects.

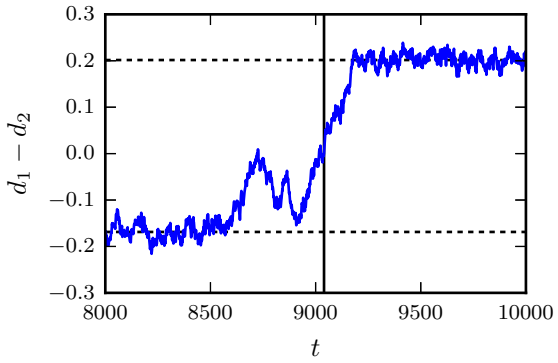

Figure 3.10: Difference of the distances of a system trajectory to two inherent minima, the first being shown in figure 3.9(b), and the second one differing by an additional four-particle exchange. In the beginning, the system is close to the first minimum (lower dashed line). At $t = 9040$ (vertical black line), the system crosses from the basin of attraction of the first minimum to the second minimum (upper dashed line) and stays in its vicinity. The apparently small difference is caused by the fact that the dynamic trajectory has a distance of $d \approx 10$ to either minimum. An exchange of four particles alters this value by ≈ 0.2.

two to around ten particles. The same transitions were also observed by van der Meer et al. (2014), who induced internal stresses by externally forcing a single particle. As soon as several exchanges take place in the same region, large scale reorganization are observed, which partly are accompanied by the formation of defects such as vacancy-interstitial pairs and eventually break the underlying lattice structure. At higher temperatures, upon entering the isotropic phase, figure 3.9(c), the inherent minimum exhibits many reconfigurations, often forming longer chains, and many particles are displaced further than the lattice constant. When quenching the system to zero temperature, many defects are frozen in, such as interstitials and vacancies, but also isolated dislocations which often form together to grain boundaries, separating several oriented crystalline patches. We ensured that the final configuration truly is a minimum by inspecting its spectrum.

In order to show that the inherent minima reflect rearrangements in the dynamic system, we take the distance of the system trajectory to the two inherent minima before and after a rearrangement,

$$d_{\min} = \|\boldsymbol{x} - \boldsymbol{x}_{\min}\|.$$

Since we only want to capture effects due to reconfigurations, we refine the minima up to $\|\boldsymbol{F}\| < 10^{-8}$ using Newton's method. We expect the system to be closer to one minimum before the transition, and closer to the other one afterwards. Typically, $d_{\min}$ is on the order of 10, which corresponds to an average displacement per particle of $d_i \approx 0.2$. Therefore, we consider the difference of both distances. Figure 3.10 shows an example of such a transition, the first minimum being shown in figure 3.9(b). The second minimum differs by four particles having exchanged their positions, similar to the marked reconfigurations in figure 3.9(b). In the beginning, the system is closer to the first minimum, $d_1 - d_2 < 0$. At $t \approx 8700$, we observe a temporary excursion of the system towards the transition state,

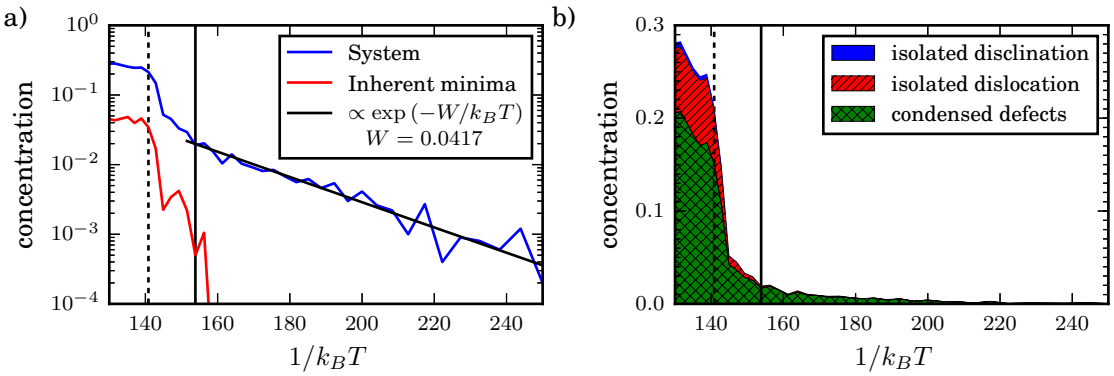

Figure 3.11: (a) The defect concentration η as function of inverse temperature $1/k_BT$. Shown are both the defects of the system (blue) and of the corresponding inherent minimia (red). The black line is a fit to the exponential distribution in eqn. (3.25). The two vertical lines indicate the temperatures of the solid-to-hexatic (solid) and hexatic-to-liquid (dashed) transitions. (b) The defect concentration in (a), broken down into different types of defects. Isolated disclinations are very rare and only appear in substantial numbers in the liquid phase.

though the system returns to the initial minimum. In between $8900 < t < 9200$, in a second attempt the system finally crosses over to the second minimum, and stays closer to it. Additionally, this time line gives us an idea of the time scale on which a transition takes place, $\tau \approx 300$.

3.2.6 Defect analysis

We can further rule out the possibility of a transition mediated by grain boundaries by investigating the core energy of a dislocation, E_c. As pointed out earlier, the grain boundary mechanism is favored for small core energies, $E_c < 2.84 k_B T_0$, where $k_B T_0$ is the temperature of dislocation unbinding and in our case given by the critical temperature at which the Lindemann parameter begins to diverge.

An approximation of the core energy can be obtained from counting the defects in the system (Tobochnik and Chester, 1982). Here, we reckon any particle which is not sixfold coordinated as a defect. In the low temperature regime, the density of defects η is expected to be exponentially distributed,

$$\eta \propto \exp(-W/k_BT)\,. \tag{3.25}$$

Here, W is the activation energy of an excitation. However, each excitation we observe consists of a quadruple of 5-7 disclinations and thus a pair of dislocations. Therefore, W is twice the activation energy of a single dislocation and we find $E_c = W/2$.

In figure 3.11(a), we show the density of defects in the system as a function of the inverse temperature. In the temperature range below the hexatic-to-liquid transition, the fraction of defects grows exponentially, and then quickly jumps to a plateau value of $\eta \approx 0.35$. We fit the data with an exponential and obtain an activation energy of $W = 0.0417$, which

corresponds to a core energy of a dislocation of $E_c^{\text{fit}} = 0.0209$. With a critical temperature of $k_B T_0 \approx 0.0066$ as an upper bound, we find $E_c^{\text{fit}} \approx 3.17 k_B T_0$, which is above the critical value of $E_c = 2.84 k_B T_0$.

As already pointed out by Tobochnik and Chester and Qi et al. (2010), defects are not spaced uniformly and many of them cancel out or are subject to small lattice distortions. Therefore, by simply counting neighbors we most likely overestimate the number of real defects. Therefore, we follow Qi et al. and in a second step consider the corresponding inherent minima. Here, unstable pairs of defects are eliminated and it should thus provide a better estimate for the number of defects. Unfortunately, in the temperature range below the melting point hardly any defects are found in the inherent minima. Therefore, we restrain from computing an activation energy, but remark that we see a steep increase in a very small temperature range close to melting, hinting at a larger excitation energy so that E_c^{fit} can be considered as a lower boundary of the actual core energy.

Furthermore, we can investigate the concentration of defects by classifying them by the number of neighboring defects, similar to Quinn and Goree (2001). We divide them into *isolated disclinations*, *isolated dislocations*, and *condensed defects*, depending on whether they are next to zero, one, or at least two particles with an coordination number $c_i \neq 6$. Examples for the latter class are bound pairs of dislocations or defects which are part of a longer string of defects, often forming grain boundaries. The corresponding concentrations are shown in figure 3.11(b). Obviously, most defects are condensed ones. However, we observe that the number of isolated dislocations starts to increase considerably at temperatures above the solid-to-hexatic transition. Likewise, the number of isolated disclinations, which are virtually absent in the hexatic phase, grows in the liquid phase. This is in agreement with KTHNY theory, which states that those two kinds of defects promote the phase transitions. Nevertheless, the defect concentrations are rather low, with the concentration of isolated disclinations $\eta_{\text{disclination}} \approx 1\%$ in the liquid phase. Similarly, the concentration of isolated dislocations increases from $\eta_{\text{dislocation}} \approx 1\%$ in the hexatic to approximately 7% in the liquid phase. Yet, the same low concentrations can also be observed in several other investigations (Murray and Van Winkle, 1987; Tang et al., 1989; Zahn et al., 1999), where a two-step melting scenario is confirmed and which show a good agreement of the correlation functions $g_6(r)$ and $g(r)$ with the predictions of KTHNY theory.

3.2.7 Isolated point defects

Over the last decades, much work has been attributed to point defects in Wigner crystals (Fisher et al., 1979; Price and Platzman, 1991) and colloidal systems (Jain and Nelson, 2000; Libál et al., 2007; DaSilva et al., 2007). They are of particular interest, since on the one hand the associated energy barriers to generate them are relatively low and, on the other hand, mass transport is largely enhanced by such defects, since once generated they are very mobile. For theses reasons, Fisher et al. (1979), who already described more involved particle exchanges such as a two- or three-particle swap, focused on isolated point defects. Therefore, before investigating the local reorganizations more deeply, we will revisit the point defects encountered in our system.

We determine the stable point defects by adding or removing a single particle in the system. At the same time, we rescale the boxsize such that the particle density $\rho =$

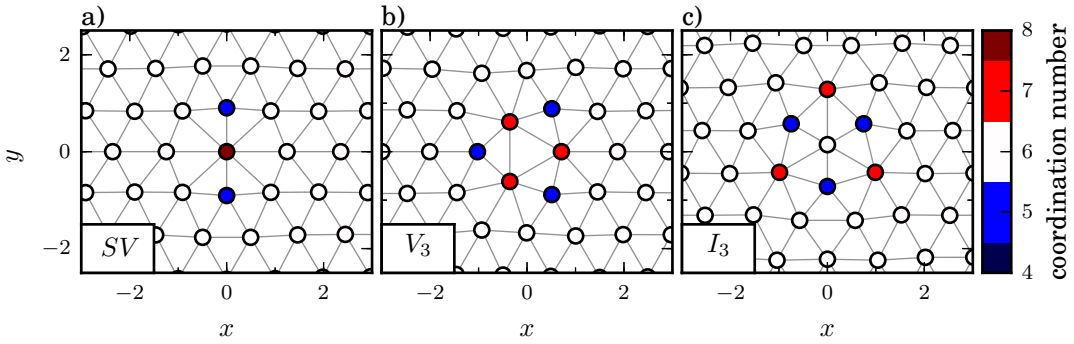

Figure 3.12: The three stable isolated defects, (a) a split vacancy (SV), (b) a threefold symmetric vacancy (V_3), and (c) a threefold symmetric interstitial (I_3). The energy increase compared to the perfect lattice are $\Delta E_{SV} = 9.49977 \times 10^{-2}$, $\Delta E_{V_3} = 9.52724 \times 10^{-2}$, and $\Delta E_{I_3} = 7.29957 \times 10^{-2}$, respectively.

N/L_xL_y remains constant. We test the defects described by Libál et al. (2007) by adjusting particle positions to meet the corresponding symmetries and subsequently minimizing the energy, using a steepest descent algorithm. Eventually, only three out of eight defect configurations turn out to be stable. This is unsurprising as already Jain and Nelson (2000) found that the stability of a configuration depends on details of the inter-particle potential. However, in the MD-simulations, as soon as the lattice is distorted and other lattice defects emerge, point defects which would be unstable if considered alone are stabilized and show up. The stable defects are shown in figure 3.12. Borrowing the notation from Libál et al., those are a split vacancy (SV), a threefold symmetric vacancy (V_3), and a threefold symmetric interstitial (I_3). The surplus energy stored in the defects when compared to a perfect crystal of identical density,

$$\Delta E = E_{\text{defect}} - \frac{N \pm 1}{N} E_{\text{crystal}}(N), \tag{3.26}$$

is $\Delta E_{SV} = 9.49977 \times 10^{-2}$, $\Delta E_{V_3} = 9.52724 \times 10^{-2}$, and $\Delta E_{I_3} = 7.29957 \times 10^{-2}$. Obviously, the interstitial has a considerably lower energy than both vacancies and we should encounter them more frequently during the simulations.

Another question is in which way these defects emerge from the perfect lattice. In case of a finite crystal with a surface, particles can leave the crystal, e.g. by vaporization, and leave behind a vacancy. In this case, the density of defects is given by the Boltzmann factor corresponding to the defect energy (Frenkel, 1946), $N_V = N \exp(-\Delta E_V / k_B T)$. For interstitials, the same applies with condensation of free particles into the crystal. This behavior would also be observed in a grand-canonical ensemble where exchanges with a reservoir of particles are allowed. However, experiments with macroscopic particles generally show a constant number of particles, as is also the case inside a crystal. As a consequence, point defects are forced to emerge in pairs consisting of a vacancy and an interstitial each. Frenkel (1946, pp. 7) termed this as *lattice dissociation*. For this reason, in the region of low temperatures where the lattice is still intact we have to argue along the lines of Tobochnik and Chester, similar to the case of the core energy of dislocations.

Then, the relevant energy is the combined energy of a defect pair, $\Delta E_{\text{pair}} \approx 0.168$.

This is supported by the MD-simulations. In inherent minima corresponding to the system in the hexatic phase, we observe the generation of pairs of opposite point defects which are separated by at least ten lattice constants, and point defects in conjunction with isolated dislocations. Therefore, at low temperatures defects should emerge in pairs, raising their activation energy drastically.

Nevertheless, as soon as defects have been generated, they are very mobile. We take the interstitial I_3 in figure 3.12(c) as an example. Here, the defect can move across the three edges of the triangle by shifting the center particle and an edge particle by a tiny bit. The intermediate configuration is a twofold symmetric interstitial termed $I_4^{'}$, resulting in a barrier height of $\Delta E_b \approx 2 \times 10^{-4}$ which is well below the melting temperature $k_B T_0 \approx 7 \times 10^{-3}$. The overall rate of particle transport is then both proportional to the barrier height and the probability to encounter a defect (Oswald, 2009),

$$k \propto \exp\left(-\frac{\Delta E_b}{k_B T}\right) \exp\left(-\frac{\Delta E_{\text{pair}}}{k_B T}\right). \tag{3.27}$$

As long as temperatures are low enough to practically prevent the formation of point defects in the first place, those defects are of secondary importance. Even more, as will be seen later on, opposing defects will most likely annihilate each other as soon as they approach each other below a distance of several lattice constants.

3.3 Summary

We found clear evidence of the transition towards a liquid phase in the range $0.007 < k_B T_c^{\psi} < 0.0071$, seen in several indicators such as radial correlations and the orientational correlation function. The Lindemann parameter on the other hand starts diverging at considerably lower temperatures $0.0065 < k_B T_c^{\gamma} < 0.0066$. This gives rise to an intermediate phase, characterized by a finite diffusivity and commonly termed hexatic. The transition is also accompanied by a loss of quasi-long range translational order, though our system is too small for this indicator to be conclusive. These results are qualitatively in good agreement with Qi et al. (2008), who considered a slightly different value of the screening parameter μ and found the same two phase transitions. However, the obtained critical temperatures are afflicted with uncertainties. First of all, the kinetic energy and thus the temperature of the system fluctuates by approximately 2%. As expected, the fluctuations are proportional to the temperature. In order to improve statistics, we would have to increase the number of particles considerably, though the needed equilibration times would increase simultaneously (Derzsi et al., 2014). A larger system would also allow us to fully resolve the long-range decay of translational and rotational ordering (Kapfer and Krauth, 2015). Another issue is the limited computation time, and while in most cases thermal equilibrium is achieved, close to the melting transition equilibration times might still be insufficient. Partly, this could be caused by temperature fluctuations, which can keep the system in between the two phases for very long times.

The change of orientational correlations $g_6(r)$, and to some extent radial correlations $g(r)$, are in good agreement with KTHNY theory. As predicted, we observe free dislocations in the intermediate phase and free disclinations in the liquid phase, although

only few of them are found. Moreover, when looking at the inherent minima, the majority of dislocations are unstable and in general the hexagonal lattice remains intact. Thus, the intermediate phase seems to be better characterized by the appearance of a finite diffusivity than by the dissociation of bound dislocations. Contrary to predictions of KTHNY-theory, we observe a strong increase of the defect concentration in the hexatic phase. Additionally, an inspection of trajectories shows that the transition to the liquid phase occurs via a liquefaction of local patches of the crystal, initiated by local exchanges of particles. Over time, those patches grow and form large defect clusters, until eventually the whole crystal is molten. During this process, we observe an apparent coexistence of the liquid and hexatic phase, similar to the one described by Tang et al. (1989), Qi et al. (2008) and Radzvilavičius (2012). The increase of the defect concentration in the solid phase, on the other hand, yields a comparatively large core energy of dislocations. This suggests that the grain-boundary mechanism of a first-order phase transition as proposed by Chui (1982, 1983) is less likely than a two-step KTHNY transition.

Fisher et al. (1979) suggested that mass diffusion in a crystal is mainly accomplished by isolated point defects as shown in figure 3.12, due to their relatively low formation energies. In this context we investigated the inherent minima at low temperatures and in the hexatic phase. We found that stable isolated point defects only emerge in pairs or in conjunction with isolated stable dislocations, thus raising their activation barrier and attenuating their relevance at low temperatures.

The representation of inherent minima in figure 3.9(b) gives us an idea on how to understand the process of melting towards the hexatic and liquid phase. In the solid, particles vibrate in their local lattices until at one point amplitudes become too large, and in a cooperative process of several neighboring particles a reconfiguration occurs. On a more abstract level, the local reorganizations can thus be interpreted as a hopping of a chain of particles on the hexagonal lattice. In general, each event increases the Lindemann parameter of the system, leading to its slow divergence and characterizing it as something different than a solid. Moreover, a single transition has a finite lifetime of several hundred time units. Consequently, some transitions will overlap, both spatially and in time. Eventually, when enough transitions are activated, this will break up the lattice structure and lead to more complex structures such as dislocations, point defects and misaligned crystallites. In consequence, the long range correlations, which are characteristic of a solid, disappear. Naturally, as soon as the underlying lattice structure is broken, the aforementioned picture of a hopping process on a lattice does not hold anymore. At temperatures slightly above the hexatic-to-liquid melting point, trajectories reveal that melting is a stepwise process. We observe a coexistence of both crystalline and liquid patches, similar to the one described by Tang et al. (1989) and Qi et al. (2008). During the time evolution the liquid patches grow until finally the whole system is molten.

On this basis, we will explore the nature of the local transitions in the upcoming chapters. To this end, we will investigate the properties of particle exchanges starting from a crystalline configuration. In a first step, we will consider a reduced system where only a few particles are free to move.

4

Restricted few-particle dynamics

In order to establish and understand some basic concepts, in a first step we analyze a low dimensional model system with only two or three free particles, confined in a crystalline structure. Here, we can study the most simple transitions besides point defects, namely exchanges of two or three particles. To break down the problem to a feasible number of dimensions, additional restrictions are introduced when required.

Reduced coordinates

The potential energy of the few-particle system is given by the potential energy of the free particles,

$$E = \sum_p \Phi_p = \sum_{p,q\neq p} \tfrac{1}{2}\Phi_{pq} + \sum_{p,j} \Phi_{pj}, \tag{4.1}$$

which constitutes of the interaction between the free particles and with the background. Accordingly, p and q extend over the free particles, whereas j references background particles. The energy of the reduced system differs from the energy of the full system, eqn. (3.3), only in the fact that it neglects interactions between background particles. Hence, total energies are not directly comparable. Energy differences on the other hand are, since the potential energy between fixed particles is constant and thus cancels out when taking the difference. Additionally, the individual per particle energies $E_i = \sum_q 1/2\Phi_{iq} + \sum_j 1/2\Phi_{ij}$ can be compared. We introduce a new coordinate system via an affine transformation,

$$\boldsymbol{x} = \boldsymbol{x}_0 + \delta_i \tilde{\boldsymbol{e}}_i = \boldsymbol{x}_0 + \mathbf{P}\boldsymbol{\delta}, \tag{4.2}$$

with $\boldsymbol{x}_0$ the configuration of the hexagonal lattice and $\delta_i\tilde{\boldsymbol{e}}_i$ the displacements in the new coordinates, which can also be written as a matrix product using the transformation matrix $\mathbf{P}$. Accordingly, force components, which are given by the negative gradient of the energy, read

$$F_{\delta_i} = -\frac{\partial E}{\partial \delta_i} = -\sum_{x_j} \frac{\partial E}{\partial x_j}\frac{\partial x_j}{\partial \delta_i} = \sum_{x_j} F_{x_j} P_{x_j\delta_i} = (\mathbf{P}^T \boldsymbol{F}(\boldsymbol{x}))_{\delta_i}, \tag{4.3}$$

i.e. we can express the forces in the reduced system by a linear transformation of those in the full system: The components f_{x_j} are identical both in the reduced and the full system, since eqn. (4.1) only lacks terms between background particles. Consequently, due to the imposed restrictions, stationary points of the reduced system will in general differ from those in the full system. An exception is the global minimum, given by the hexagonal

lattice configuration. In analogy to eqn. (4.3), the Jacobian of the reduced system is given by

$$\mathbf{J}(\boldsymbol{\delta}) = \mathbf{P}^T \mathbf{J}(\boldsymbol{x}) \mathbf{P}. \tag{4.4}$$

In the following paragraphs, we will identify and classify the stationary points, with special attention on co-dimension one points. Further, we investigate the physically relevant transitions and their rates. By this, we denote transitions between minima which would be stable in the full system as well. We also try to grasp the meaning of higher-order stationary points where this is conceptually feasible, i.e. in two- or three-dimensional reductions. Later on, we will take the obtained results and compare them against the full system where all particles can evolve. Before turning to the analysis of the system, in the next section we will give a brief overview of the concept of transition states and how the rates of transitions between configurations can be computed.

4.1 Theory of transition rates

To get an intuition about transition states, let us picture the relief of a landscape, with various hills, valleys and sinks. In this picture, the altitude represents the potential energy, and the stable states of a system are located at the local minima, i.e. the sinks. Correspondingly, the valleys form their areas of attraction. In order to get to another minimum, the system has to cross over a hill. Most likely, it will take the path of lowest potential energy, the so-called minimum energy path. It connects neighboring valleys via low-lying saddles in the potential energy landscape. Those saddles, called transition states, are characterized by their stability properties: They are stationary points, and Murrell and Laidler (1968) showed that they can have only one unstable direction. Otherwise, a second path around with lower potential energies would have to exist. While this concept is easy to conceive in a 2-dimensional landscape, it gets complicated as soon as additional degrees of freedom are introduced. Then, many more semi-stable equilibria with more than one unstable direction exist, and it becomes more challenging to identify the saddles.

The minimum energy path defines a reaction coordinate along which the system can evolve from the one to the other configuration, see figure 4.1 for a sketch. Eyring (1935a,b) put forward a theory on how to compute the rates at which such transitions take place. The basic idea is to count all trajectories which leave the region around the minimum and pass the transition state, and relate them to the average population density in the same region. In its most fundamental formulation (cf. e.g. Hänggi et al., 1990), the rate according to transition state theory (TST) it is given by

$$k^+_{\mathrm{TST}} = \frac{\left\langle \chi^S_*(\boldsymbol{x}) \hat{\boldsymbol{n}} \cdot \boldsymbol{v} \Theta\left[\hat{\boldsymbol{n}} \cdot \boldsymbol{v}\right] \right\rangle}{\left\langle \chi^V_0(\boldsymbol{x}) \right\rangle}. \tag{4.5}$$

Here, $\langle \cdot \rangle$ denotes the equilibrium average over the canonical probability density and $\Theta(z)$ is the Heavyside step function, with $\Theta(z) = 1$ if $z > 0$ and $\Theta(z) = 0$ else. χ^V_0 and χ^S_* are the characteristic functions of the area of attraction of the minimum and the separating surface at the transition state, respectively. The superscripts denote whether they describe a n-dimensional volume (V) or a $(n-1)$-dimensional hypersurface (S). Accordingly, $\hat{\boldsymbol{n}}$ is

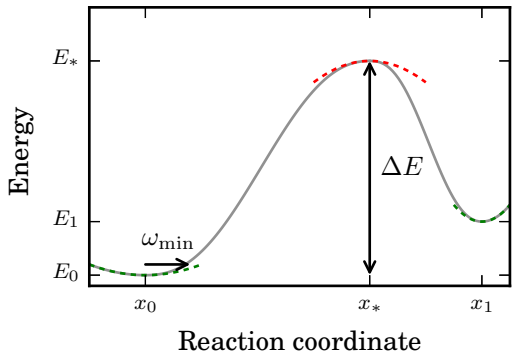

Figure 4.1: Sketch of a metastable potential. The system vibrates around the minimum at x_0 with angular frequency $\omega_{\min}$. In order to cross over the barrier at x_*, it has to overcome the energy barrier $\Delta E = E_* - E_0$. The dashed lines indicate the harmonic approximations.

the normal vector of said surface. Hence, each trajectory on the dividing surface ($\chi_*^S(\boldsymbol{x})$) with positive normal velocity ($\Theta[\hat{\boldsymbol{n}} \cdot \boldsymbol{v}]$) is taken into account. In one dimension, this reduces to the equilibrium average of all positive velocities at the transition state. The characteristic function becomes a delta-function, and we end up with the well-known rate equation,

$$k_{\mathrm{TST}}^{+} = \frac{\omega_{\min}}{2\pi} \exp\left(\frac{-\Delta E}{k_B T}\right). \tag{4.6}$$

Here, $\omega_{\min}$ is the angular frequency at the well bottom and ΔE is the barrier height. Therefore, in order to cross over a barrier, two factors are of importance:

1. How large is the barrier, and which is the probability to reach this energy level. This is given by a Boltzmann factor.

2. How frequently does the system try to overcome the barrier. This is given by the angular frequency of the system in the lower well.

When considering higher dimensional systems, eqn. (4.5) can be evaluated analogously, and it can be expressed using restricted partition functions (see appendix A.2, or e.g. Vineyard, 1957; Vanden-Eijnden and Tal, 2005),

$$k_{\mathrm{TST}}^{+} = k_B T \frac{Z_*}{Z_0}. \tag{4.7}$$

Here, Z_0 is the partition function evaluated in the area of attraction of the minimum, and Z_* denotes the (restricted) partition function computed on the separating surface of the transition state. Upon plugging in the harmonic approximations both for the minimum and the transition state, we end up with the harmonic transition rates,

$$k_{\mathrm{TST}}^{+} = \frac{1}{2\pi} \frac{\prod_{i=1}^{n} \sqrt{-\lambda_i^{(0)}}}{\prod_{i=2}^{n} \sqrt{-\lambda_i^{(*)}}} \exp\left(\frac{-\Delta E}{k_B T}\right). \tag{4.8}$$

The computation is performed in appendix A.2. Here, λ_i^0 are the eigenvalues of the minimum configuration whereas λ_i^* are the stable eigenvalues of the transition state, ignoring neutral modes due to translational symmetry. Overall, their ratio gives us an effective frequency ω_{eff}. With the harmonic approximation in mind, we can identify the individual frequencies with the opening of the corresponding parabolas and hence the opening of the potential. The ratio in eqn. (4.8) thus measures the change in the curvature of the potential when approaching the transition state. For example, when the (harmonic) potential widens up in one direction, transitions are more likely to occur. Here, we might again employ the picture of a potential energy landscape. When the curvature is low and thus the saddle wide, it does not matter for the system if it slightly misses the transition state: In its vicinity, the energy increases only moderately. Interestingly, the rates are independent of the path the system takes to reach the transition state. They only rely on static quantities, determined by the potential and thus in our case on the particle interactions at two well-defined configurations.

With the well known identity $Z = \exp(-F/k_BT) = \exp(-(E-TS)/k_BT)$, relating the partition function to the free energy F and the entropy S, we can recast the rate equation (4.7) as

$$k^+_{\text{TST}} = k_BT \exp\left(\frac{\Delta S}{k_B}\right) \exp\left(-\frac{\Delta E}{k_BT}\right) \tag{4.9}$$

Thus, the pre-exponential factor can be interpreted as an entropic weight. It is to note that this is a somewhat crude definition of ΔS, comparing entropies in to differently defined subspaces. A more systematic approach is given by Vineyard (1957), who introduced an additional constricted partition function at the minimum.

In the limit of low temperatures ($k_BT \ll \Delta E$) and strong friction $\gamma \gg \sqrt{\lambda_+^{(*)}}$, transitions may be described more accurately by the Kramers rate (Kramers, 1940),

$$k^+_{\text{Kramers}} = \frac{\sqrt{\lambda_+^{(*)}}}{2\pi\gamma} \frac{\prod_{i=1}^n \sqrt{-\lambda_i^{(0)}}}{\prod_{i=2}^n \sqrt{-\lambda_i^{(*)}}} \exp\left(\frac{-\Delta E}{k_BT}\right) \tag{4.10}$$

where $\lambda_+^{(*)}$ is the unstable eigenvalue of the transition state. Naturally, Kramers rates are lower than the harmonic transition rates, eqn. (4.8).

The idea of connecting the melting of a solid to a rate process is not a new one though. Already in 1948, Penner combined the two fields by comparing the rates subject to partition functions of the solid and the liquid phase. Although he made very elementary assumptions, for example that at the point of melting all frequencies both of the solid and the activated state are given by identical Einstein frequencies, he was able to obtain estimates for said frequencies which match the order of magnitude of several other approaches.

4.2 Two free particles

We consider two neighboring particles confined in the matrix of an infinite crystal. The system is shown in figure 4.2(a), with the two particles in question colored and the back-

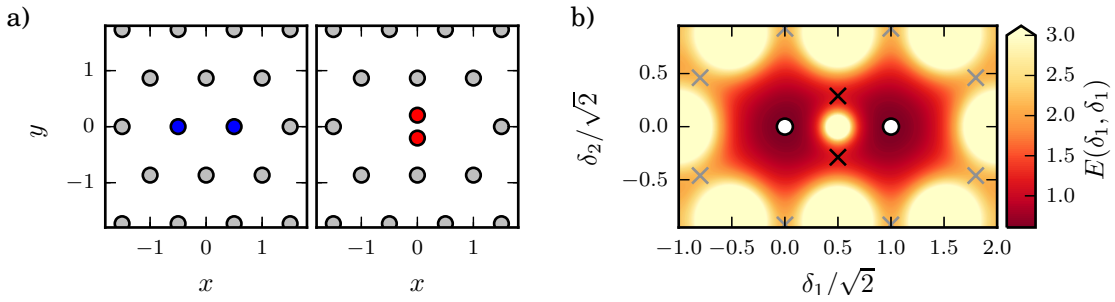

Figure 4.2: The two-dimensional two-particle model. (a) In physical space, the global minimum corresponds to the crystalline configuration (blue dots, left), whereas at the transition state, both particles align vertically along the symmetry axis (red dots, right). Fixed background particles are shown in gray. (b) The potential energy landscape in reduced coordinates (δ_1, δ_2). The positions of the global minima (white dots), the connecting transitions states (black crosses) and the exiting channels (gray crosses) are marked. Singularities are found at the center of the bright spots of the potential.

ground particles constituting the crystal represented by gray dots. Naturally, each particle has two spatial degrees of freedom. In order to further reduce dimensions, we only take antisymmetric motion of the particles into account,

$$\begin{pmatrix} \boldsymbol{x}_1 \\ \\ \boldsymbol{x}_2 \end{pmatrix} = \begin{pmatrix} -1/2 \\ 0 \\ 1/2 \\ 0 \end{pmatrix} + \frac{\delta_1}{\sqrt{2}} \begin{pmatrix} 1 \\ 0 \\ -1 \\ 0 \end{pmatrix} + \frac{\delta_2}{\sqrt{2}} \begin{pmatrix} 0 \\ 1 \\ 0 \\ -1 \end{pmatrix}, \tag{4.11}$$

yielding new coordinates δ_1 and δ_2. The reasoning behind is that, first, the two particles are repelling each other and, second, we search for a particle exchange, i.e. they have to move anti-parallel along the x-axis. The global minima correspond to $(\delta_1, \delta_2) = (0, 0)$ and $(\sqrt{2}, 0)$, where in the latter case particles have exchanged their positions. It is to note that for two free particles, the center of mass is not a conserved quantity in the first place, since the particles are confined in an external potential. With the choice of coordinates (4.11) though we impose this restriction, which then coincides with the full system where no external potential is present and all particles are allowed to move.

The potential energy landscape in the (δ_1, δ_2)-space is shown in figure 4.2(b). It closely resembles the location of background particles in physical space, as for example shown in figure 4.2(a) as gray dots. They form the hexagonal cage of a double vacancy. Naturally, the potential energy diverges whenever the free particles collide with the fixed ones as can also be seen from the light patches in (b). In between the surrounding singularities, we find exiting channels where both particles leave the inner cage, indicated by gray crosses in the figure. Due to the antisymmetric motion, both particles leave the cage simultaneously and on opposite sides, rendering the new configuration unstable in the full system: There, two of the boundary particles would fill in the voids, restoring the crystalline configuration. Inside the cage, we find two basins of attraction, separated along the symmetry axis

$\delta_1 = \sqrt{2}/2$ and each one belonging to one of the two possible hexagonal configurations. Along the line connecting the minima, we find another singularity at $(\sqrt{2}/2, 0)$ where the two free particles collide. Nevertheless, in order to exchange positions both particles have to cross the vertical symmetry axis simultaneously. In between the singularities in the center and on the boundaries, we find two additional stationary points of the potential, indicated by black crosses. At this point, the potential energy on the symmetry axis is minimal, and both of them correspond to the same process with the first particle hopping from the left to the right basin of attraction, and vice versa. Obviously, by symmetry two possible paths exist in which one particle passes above the other. The stationary points are transition states with their unstable directions pointing towards either minimum configuration. The configuration in physical space is shown in the rightmost panel of figure 4.2(a). The features of the transition state are listed in table 4.1.

4.2.1 Rate calculations

In the limit of low temperatures, i.e. $k_B T$ lower than the activation energy of the transition state, trajectories connecting the two basins of attraction are expected to cross close to this state. In this low-dimensional model system, we are now able to compare three different approaches and the rates they yield. It will give us an idea of how viable the different approximations of transition state theory are.

The first possibility, which we will utilize in the further course of this work, is the multidimensional harmonic transition state theory, as described in section 4.1. It solely depends on the energy barrier at the transition state and the eigenspectra of both the transition state and its associated minimum, which makes its computation relatively easy, especially in the case of only two free coordinates.

The second method drops the harmonic approximation, and instead resorts to computing the partition function of the basin of attraction and the restricted partition function along the separating manifold, eqn. (4.7). In this simple model, this reduces to the computation of a two-dimensional and a one-dimensional integral, respectively, but leads to high-dimensional integrals in the full system considered later on. This brings us to the question of defining the integrational domain. Here, since the potential raises fast close to

Table 4.1: Properties of both the minimum and the transitions state of the two-particle exchange in the two-dimensional (δ_1, δ_2)-model. Summarized are per-particle energies E_i, the total energy E, the barrier height, the unstable eigenvalue and the effective frequency ω_{eff} as defined by eqn. (4.8).

	minimum	transition state
E_i	0.163674	0.371542
E	0.604909	1.17973
ΔE		0.574824
λ^+		6.75787
$\omega_{\text{eff}}/2\pi$		0.0766271

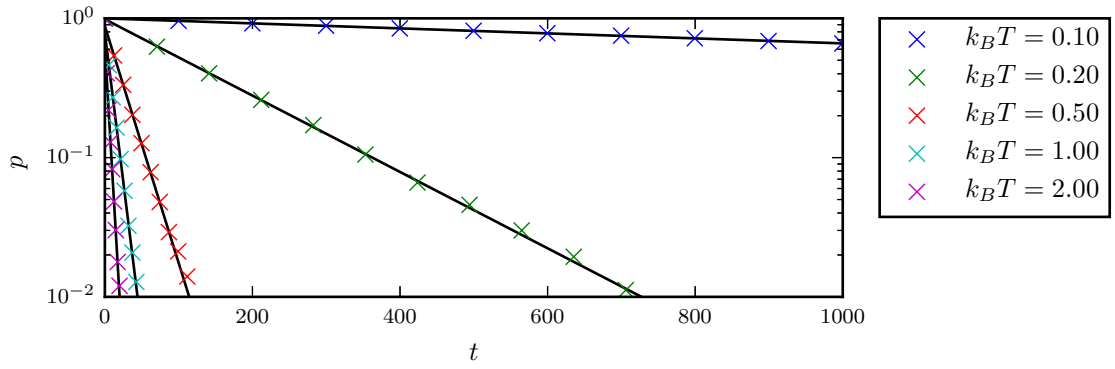

Figure 4.3: Probability of a trajectory to stay in the basin of attraction of the global minimum (crosses), and fits to the exponential distribution (black lines). For a clearer representation, some intermediate data points were omitted in the figure. At temperatures below $k_BT <\leq 0.5$, transitions occur almost exclusively between the two global minimum configurations. Beyond, this transition channel still dominates the escape, though transitions through the other exiting channels are observed as well. Their relative occurrences coincide with the corresponding Boltzmann factors.

the singularities and the integrands thus become negligible, we take lines intersecting the transition states as an approximation to the dividing manifolds. In higher dimensional systems, the identification of the limits of integration becomes correspondingly more complex.

The third approach to obtain rates is to actually calculate them by simulating the system in contact with a heat bath, and monitor the escape from the basin of attraction of the global minimum at varying temperatures. To this end, we implement a Langevin thermostat, eqn. (3.17), using an Euler-Maruyama scheme and a friction of $\gamma = 0.1$. We extract lifetime statistics, considering 5000 trajectories for each temperature. In order to sample from a thermally well defined ensemble, initial positions are chosen such that the potential energy is Boltzmann distributed. At the same time, velocities are taken from a Maxwell-Boltzmann distribution. In order to capture the transitions at low temperatures, a total integration time of 2000 time units is chosen. Nevertheless, for very low temperatures this is still insufficient as only few (or no) escape events occur during the computation time. As a consequence, no data is generated below $k_BT = 0.1$. As an upper limit we take $k_BT = 2.0$, which is roughly four times the barrier height. With increasing temperatures, additional exiting channels where both particles leave the central area become available. Hence, the lifetime of a trajectory is determined as soon as it leaves the area of attraction of the global minimum at $\boldsymbol{\delta} = (0, 0)$. In order to minimize the counting of recrossings, we only consider particles which moved a distance of 0.1 lattice constants beyond a separating manifold.

From the lifetimes, we can extract the so-called survival probability of a trajectory, i.e. the probability p that a trajectory which started in the basin of attraction of the global minimum is still found in the same domain after time t. The survival probability

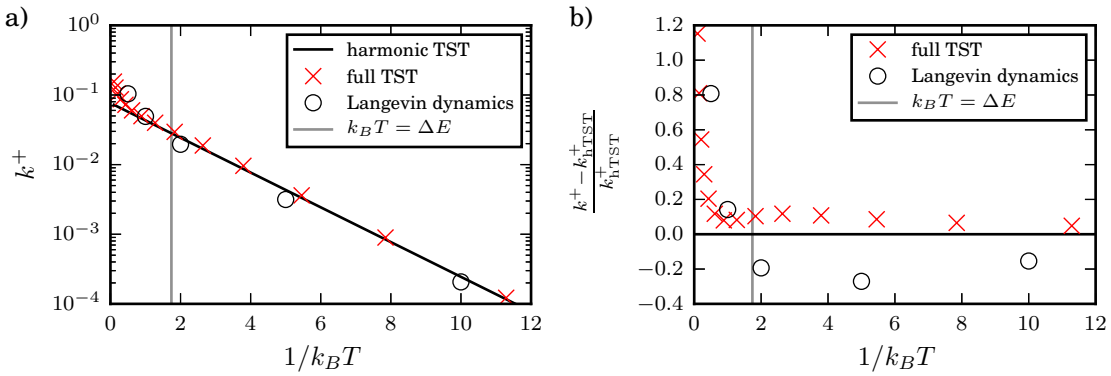

Figure 4.4: Comparison of rates obtained from three different approaches. (a) Rates for the transition between the two global minima as function of inverse temperature, either by extracting it from simulations (∘), or by using transition state theory (× , eqn. (4.7)) and its harmonic approximation (−, eqn. (4.8)). (b) Relative deviations with respect to the harmonic rates. In both figures, the vertical gray line indicates the characteristic temperature at which the thermal energy equals the barrier height. For temperatures below, we find the Arrhenius law and good agreement between all three approaches with almost constant deviations $< 30\%$.

is then given by an exponential decay,

$$p(t) \propto \exp\left(-k_{\mathrm{escape}} t\right). \tag{4.12}$$

The results from the simulations are presented in figure 4.3. The expected exponential relationship is recovered for all considered temperatures. For temperatures below $k_BT \leq 0.5$, transitions occur almost exclusively between the two global minimum configurations. Hence, the obtained rate of escape directly corresponds to the transition rate of interest. Only at higher temperatures, trajectories are found which leave the central cage. However, the corresponding barriers are roughly three times as high as the one of the two-particle exchange. This is also reflected in the relative occurrences which coincide with the Boltzmann factors. Hence, the two-particle exchange still dominates the escape dynamics, and the rate of escape can be considered as a decent approximation to the transition rate.

The rates obtained with these three approaches are compared in figure 4.4(a), along with relative deviations in (b). The characteristic or critical temperature of the transition is given by the barrier height, indicated by a vertical gray line. For temperatures well below it ($1/k_BT \geq 2$), we recover the well-known Arrhenius law of an exponentially activated process for any of the three methods. Unsurprisingly, the harmonic approximation fails when exceeding the characteristic temperature. Whereas the rates extracted from simulations as well as the rates computed using the partition functions increase much faster, the harmonic approximation is fixed to the Arrhenius law. This becomes more evident when examining the relative deviations in figure 4.4(b). Conventionally, one would take the rates extracted from the simulation as a reference. However, since only few data points exist we decide to put it the other way around and plot deviations with respect

to the harmonic approximation. Below the critical temperature ($1/k_BT \geq 2$), all three methods are in fair agreement with relative deviations well below 30%. Moreover, they are roughly constant over the whole temperature range. The approximations of transition state theory overestimate the true rates, as would be expected (Hänggi et al., 1990). Beyond the critical temperature, the harmonic approximation still follows the Arrhenius law, whereas both the simulation and the approach using partition functions yield considerably higher rates, off by up to 100%. Even more, the rates found in the simulations exceed the approximations using partition functions. This might be attributed to the fact that we only considered the rate of escape, combining all possible transitions that leave the basin of attraction of the global minimum in one rate. Although most trajectories in the simulations escaped over the transition state in question, the other escape channels might have affected the computation of transition times. At low temperatures however, this effect is negligible since no other transitions were observed in the simulations.

In principle, we could also have considered the Kramers rate, eqn. (4.10). However, we are out of the regime of strong friction with our choice of the damping $\gamma = 0.1$ and an unstable mode at the transition state of $\lambda^+ = 6.76$. In the further course of our studies, we will investigate the onset of disordering transitions. Therefore, we find ourselves at the lower end of the temperature scale which allows us to base our further analysis on harmonic transition state theory.

4.3 Three free particles

To make things a bit more complicated, we now consider three free particles situated on the corners of a triangular base cell. Accordingly, they are trapped in a triangular cage of background particles, visualized in figure 4.5(a) by gray dots. Imposing preservation of the center of mass, we end up with four spatial degrees of freedom which we can write as

$$\begin{pmatrix} \boldsymbol{x}_1 \\ \boldsymbol{x}_2 \\ \boldsymbol{x}_3 \end{pmatrix} = \begin{pmatrix} -1/2 \\ 0 \\ 1/2 \\ 0 \\ 0 \\ \sqrt{3}/2 \end{pmatrix} + \overbrace{\frac{\delta_1}{\sqrt{3/2}} \begin{pmatrix} 1 \\ 0 \\ -1/2 \\ 0 \\ -1/2 \\ 0 \end{pmatrix}}^{\delta_1 \tilde{\boldsymbol{e}}_1} + \overbrace{\frac{\delta_2}{\sqrt{1/2}} \begin{pmatrix} 0 \\ 0 \\ -1/2 \\ 0 \\ 1/2 \\ 0 \end{pmatrix}}^{\delta_2 \tilde{\boldsymbol{e}}_2} + \overbrace{\frac{\delta_3}{\sqrt{15/16}} \begin{pmatrix} 0 \\ \sqrt{3}/2 \\ 0 \\ -\sqrt{3}/4 \\ 0 \\ -\sqrt{3}/4 \end{pmatrix}}^{\delta_3 \tilde{\boldsymbol{e}}_3} + \overbrace{\frac{\delta_4}{\sqrt{3/2}} \begin{pmatrix} 0 \\ 0 \\ 0 \\ \sqrt{3}/2 \\ 0 \\ -\sqrt{3}/2 \end{pmatrix}}^{\delta_4 \tilde{\boldsymbol{e}}_4}. \tag{4.13}$$

The orthonormal basis vectors are chosen such that particle exchanges can be easily represented. $\tilde{\boldsymbol{e}}_1$ and $\tilde{\boldsymbol{e}}_2$ describe x-components of the particles whereas the other two basis

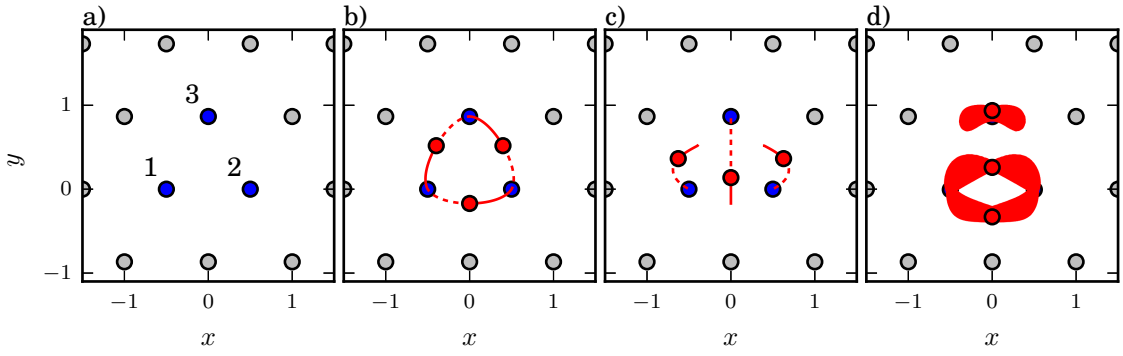

Figure 4.5: Stationary states in the four-dimensional three-particle system. Gray points represent the background particles. (a) The global minimum (blue dots), with particles labeled according to their positions at $\boldsymbol{\delta} = 0$; the configuration defines the center of mass of the system. (b) Transition state of the three-particle exchange (red dots). The red lines (solid and dashed) mark the two directions of the unstable manifold. The three particles rotate around the origin. (c) Starting from the transition state in (b), the central lower particle can move to the top, with the lateral particles giving way. Across the depicted transition state, the system then evolves towards the global minimum. In succession, the transitions in (b) and (c) lead to a two-particle exchange along the diagonals. (d) A third stationary state can be achieved by vertically aligning all three particles. However, it is of co-dimension two, and depicted is a projection of the two-dimensional unstable manifold (red area).

vectors describe their y-components, hence the $\sqrt{3}/2$ in the definition which is the separation in y-direction. The lower left particle is solely controlled by $\tilde{\boldsymbol{e}}_1$ and $\tilde{\boldsymbol{e}}_3$, with the other two particles compensating motion to keep the center of mass fixed. Correspondingly, $\tilde{\boldsymbol{e}}_2$ and $\tilde{\boldsymbol{e}}_4$ describe an opposing motion of the two remaining particles. In total, $3! = 6$ global minima exist. Since they are all equal in their properties, we restrict ourselves to discuss transitions of the first one situated at $\boldsymbol{\delta} = \mathbf{0}$.

In principle, two kind of exchanges may be observed: either a two-particle swap with one particle resting at its original position, or a ring exchange involving all three free particles. Of course, due to the increase in dimensionality, we find many more stationary (and stable) states, complicating structures in configuration space. Indeed, the relevant transitions are not as obvious as one might expect, as is shown in figure 4.5. In (a) we see the hexagonal minimum configuration, the free particles indicated by blue dots. Since all considered transitions connect permutations thereof, we also plot them in the remaining panels for reference. In figure 4.5(b), we see the transition state with the lowest energy barrier, the three-particle ring exchange indicated by red dots. Additionally, the unstable manifold is depicted as dashed and dotted lines, corresponding to the two different directions of the transition. It involves all particles rotating around their common center of mass, either clockwise or counterclockwise. As might be expected, it is threefold symmetric. Starting from the transition state, we can move the lower particle to the top while the two at the top move aside. This way, we can realize the transition shown in figure 4.5(c).

It essentially inverts particle positions along the y-axis, turning the triangle of particles upside down. Both transitions in (b) and (c) combined lead to a two-particle exchange along the diagonals. Naturally, the same transition exists along any of the three symmetry axes so that all possible two-particle exchanges can be realized by this mechanism. Since it involves the transition state of the three-particle exchange, its energy barrier is larger, actually by almost 50%. Finally, the two-particle exchange found in the two-particle system where all three particles align along a line now takes place via a co-dimension two point, figure 4.5(d). Therefore, the unstable manifold is not just given by a line but by a surface, its projection onto physical space indicated in red. In the transition, the two lower particles exchange their positions, either clockwise or counterclockwise, while the upper particle wiggles around its position so as to keep the center of mass fixed. The associated energy barrier is again 10% higher than in the combined two-particle exchange. For reference, the main properties of the stationary points are also summarized in table 4.2.

4.3.1 Three-dimensional reduction

In order to gain more insight into phase space, we reduce the dimension by one so that we are able to visualize the different configurations and their connections. Hence, we drop one coordinate of eqn. (4.13), restricting movement of the lower left particle to the x-direction. This yields the coordinates

$$\begin{pmatrix} \boldsymbol{x}_1 \\ \boldsymbol{x}_2 \\ \boldsymbol{x}_3 \end{pmatrix} = \begin{pmatrix} -1/2 \\ 0 \\ 1/2 \\ 0 \\ 0 \\ \sqrt{3}/2 \end{pmatrix} + \frac{\delta_1}{\sqrt{3/2}} \begin{pmatrix} 1 \\ 0 \\ -1/2 \\ 0 \\ -1/2 \\ 0 \end{pmatrix} + \frac{\delta_2}{\sqrt{3/2}} \begin{pmatrix} 0 \\ 0 \\ 0 \\ \sqrt{3}/2 \\ 0 \\ -\sqrt{3}/2 \end{pmatrix} + \frac{\delta_3}{\sqrt{1/2}} \begin{pmatrix} 0 \\ 0 \\ -1/2 \\ 0 \\ 1/2 \\ 0 \end{pmatrix}. \quad (4.14)$$

Again, the center of mass is preserved and the vectors $\tilde{\boldsymbol{e}}_i$ form an orthonormal basis. Essentially, the first coordinate describes a displacement of the lower left particle along the

Table 4.2: Properties of both the minimum and the relevant stationary states of the three-particle system in four-dimensional center-of-mass coordinates. Summarized are the same quantities as in table 4.1, namely energies, unstable eigenvalues and effective frequencies ω_{eff} as defined by eqn. (4.8). Since the energy is not distributed equally among the free particles, the maximum per-particle energy $\max(E_i)$ is considered.

	minimum	transition state three-particle swap	transition state two-particle swap	co-dim 2 state two-particle swap
$\max(E_i)$	0.163674	0.251557	0.298999	0.394199
E	0.832682	1.16198	1.31793	1.36737
ΔE		0.329299	0.485249	0.534686
λ^+		2.27280	2.85458	6.15, 0.912
$\omega_{\text{eff}}/2\pi$		0.0573463	0.0875018	

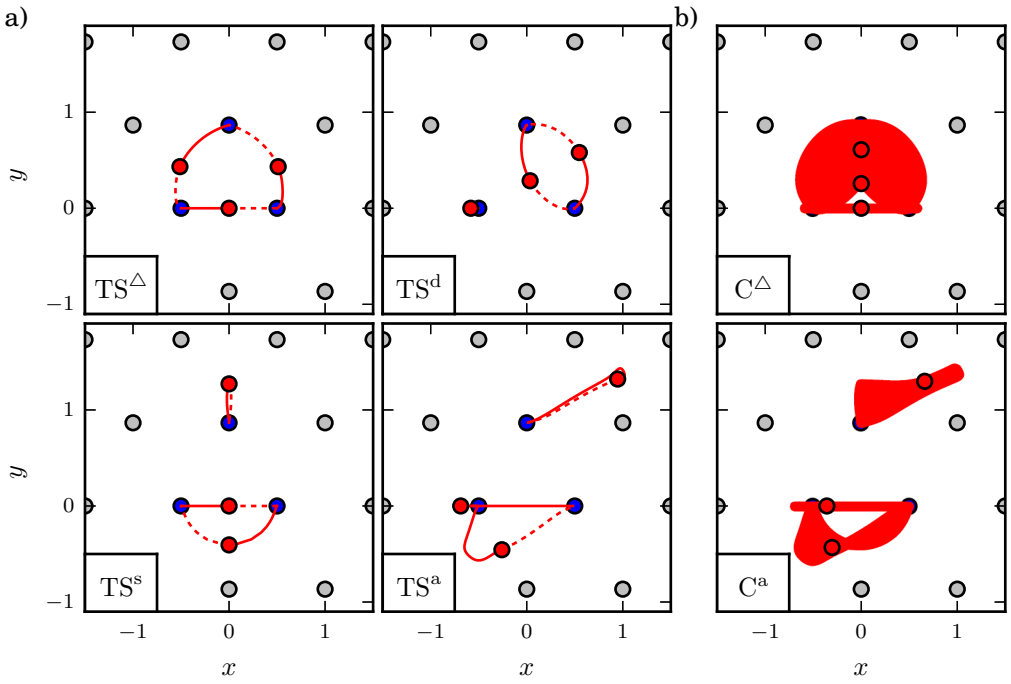

Figure 4.6: Stationary states of the three-dimensional reduction of the three-particle model. (a) Transition states (red), namely the three-particle ring exchange $\mathrm{TS}^{\triangle}$, the two-particle exchange along the diagonal TS^{d} and, in the bottom row, the two-particle exchange along the x-axis, directly via a symmetric configuration (TS^{s}), or with a large, asymmetric excursion of the upper particle (TS^{a}). Marked as red lines are the two directions of the unstable manifolds (solid and dashed). The blue dots represent the minimum configuration. (b) Co-dimension two states $\mathrm{C}^{\triangle}$ and C^{a} (red dots), along with a projection of the unstable manifolds. Since the particles only move in union, it is less instructive. However, it gives an idea which minima might be connected through a co-dimension two point. For instance, the transition states in (a) to the left of each state in (b) are part of the respective unstable manifold. A better understanding may be conceived when looking at three-dimensional plots, figures 4.7 - 4.9.

x-axis (along with a compensatory motion of the other particles), whereas the remaining two coordinates describe relative displacements of the other two particles along the y- and x-axis, respectively. As a consequence of the reduction, only four global minima exist, namely $(0,0,0)$, $(\sqrt{3/2},0,\sqrt{1/2})$, $(\sqrt{3/2},\sqrt{3/2},0)$, and $(0,\sqrt{3/2},\sqrt{1/2})$. Additionally, starting from the initial configuration $\boldsymbol{\delta} = \mathbf{0}$, the clockwise three-particle exchange, as well as two-particle exchange along the diagonal involving the lower left particle, are prohibited.

In figure 4.6 we show the possible transitions involving the motion-restricted particle being situated in the lower left corner. By symmetry, the exact same transitions are found with the restricted particle being located at the lower right position. The figure is structured as follows: In the left part (a) transition states are depicted whereas on the right (b) co-dimension two points are shown. The states plotted in each row are linked:

The two transition states on the left are part of the unstable manifold of the corresponding stationary point on the right. The properties of the transition- and co-dimension two states are also summarized in table 4.3. In the upper row of the figure, leftmost panel, we see the three-particle exchange, named $\mathrm{TS}^{\triangle}$. Due to the restriction of the lower left particle, the symmetry observed in figure 4.5(b) is broken. Nevertheless, the key feature of particles cooperatively rotating around the center still persists. In the central panel, we have a diagonal two-particle exchange, TS^{d}. Here, all three particles are almost aligned, and it closely resembles the co-dimension two point in figure 4.5(d) and the transition state in the two-particle system. The restricted particle hardly moves, and the two particles on the diagonal rotate about their common center. In the rightmost panel, the connecting co-dimension two point $\mathrm{C}^{\triangle}$ is depicted. Here, all three particles align along the vertical line of symmetry, and except for particles being closer to each other, it corresponds to the co-dimension two state of the four-dimensional system in figure 4.5(d). Again, the energy barrier of the three-particle exchange is the lowest, with the barrier of the two-particle exchange being 25% higher. In contrast, the connecting co-dimension two point on the right has an energy barrier which is again five times larger. Hence, at low temperatures transitions should generally take place in the vicinity of the transition states. See also table 4.3 for a comparison of the energy barriers.

In the second row of figure 4.6, we see two possible realizations of a horizontal two-particle exchange. The first, symmetric one, TS^{s} in the leftmost panel, is qualitatively quite similar to the diagonal transition TS^{d} in the upper row: All three particles align

Table 4.3: Properties of the relevant transition states (a) and co-dimension two points (b) of the three-particle system in three-dimensional center-of-mass coordinates. Summarized are energies (maximum per-particle, absolute, and the energy barrier), unstable eigenvalues and effective frequencies ω_{eff} as defined by eqn. (4.8), if applicable.

a)

transition	three-particle $\mathrm{TS}^{\triangle}$	two-particle TS^{d}	two-particle TS^{s}	two-particle TS^{a}
$\max(E_i)$	0.282708	0.393975	0.698958	0.543523
E	1.25920	1.36625	2.08761	2.28919
ΔE	0.426516	0.533567	1.25493	1.45651
λ^+	2.10460	6.08076	22.2616	2.13147
$\omega_{\mathrm{eff}}/2\pi$	0.0693373	0.0470078	0.0828344	0.0761424

b)

co-dim 2	three-particle $\mathrm{C}^{\triangle}$	two-particle C^{a}
$\max(E_i)$	1.45949	0.593733
E	3.51863	2.41081
ΔE	2.68594	1.57813
λ^+	107.654, 24.3448	13.5999, 2.60151

along the symmetry axis. In contrast to $C^{\triangle}$, one particle passes below the restricted one. Since the latter is fixed to the x-axis, it cannot make way. Additionally, the center of mass is conserved, and the upper particle has to move further to the top. However, the distance between the particles is larger, and the energy barrier is thus lower than that of $C^{\triangle}$. Nevertheless, it is more than two times larger than the one of TS^{d}. The second, asymmetric transition TS^{a} is a bit more intricate and involves a large excursion of the upper particle which temporarily leaves the cage of surrounding particles, making it a rather unphysical transition: In an unrestricted system, this would lead to a relaxation where one of the caging particles fills in the void. In the first step of the transition, the restricted lower left particle moves a bit to the left, whereas the remaining two particles move diagonally into opposing directions, approaching the transition state. In the second step, the restricted particle passes by its original minimum position and moves to the right corner. The lower particle takes over the lower left position, whereas the upper particle returns to its starting point. By symmetry, the mirrored transition where the upper particle makes an excursion to the left exists as well. Unsurprisingly, the energy barrier of TS^{a} is again over 10% higher than the one of TS^{s}. At the connecting co-dimension two state, C^{a} in the rightmost panel, the two lower particles get closer to each other, and correspondingly the energy barrier rises slightly by approximately 10%. Just as in TS^{a}, particles are found in an asymmetric configuration.

With the reduction of the system to three dimensions, we can now easily visualize it, see figures 4.7 - 4.9[1]. In each of the figures, we chose a simplified representation of the potential by plotting the equipotential surface of $E_p = 5$, yielding a network of columns. Thereby, the location of the singularities in $\boldsymbol{\delta}$-space is readily clarified. To put them into perspective, the surfaces of the pictured cubes show cross-sections of the potential energy, analogous to figure 4.2(b). Physical motion of particles in the x-direction corresponds to paths in the δ_1-δ_3 plane, and relative displacements in the y-direction of the two free particles are found along the δ_2-axis to the right. In this landscape, the stationary points are depicted in blue (minima), green (transition states) and black (co-dimension two points).

To get an idea of the configuration space, an overview plot is shown in figure 4.7. There, some of the points have been labeled according to the previously introduced classification. The minimum M_1 at $\boldsymbol{\delta} = (\sqrt{3/2}, 0, \sqrt{1/2})$ corresponds to the restricted particle being in the lower right corner, the second particle in the lower left, and the third particle at its original position at the top. At the point M_2, the two free particles have swapped their positions. The configuration with each particle at its initial position is found behind M_1, occluded by the equipotential surface. The singularities, visualized by the enclosing isosurfaces, can be identified with specific particle configurations, where the two free particles are confined at distinct heights y. For instance, the central column corresponds to both particles colliding halfway at $y_2 = y_3 = \sqrt{3}/4$. Accordingly, the other columns correspond to singularities due to both particles colliding on lattice planes at $y_2 = -\sqrt{3}/2$, 0, $\sqrt{3}/2$, and $\sqrt{3}$, from left to right in the figure. They either collide with background particles (outermost columns), or with the restricted, first particle (inner columns). The unlabeled points in the right and back of the figure are equivalent to the labeled ones,

[1] Animations of configuration space are found online at: `https://youtu.be/xbSYaveTjwk`, `https://youtu.be/tFLehv4cCSo`, `https://youtu.be/k4WtmVt1IK4`, and `https://youtu.be/DLM8_oiVgQs`.

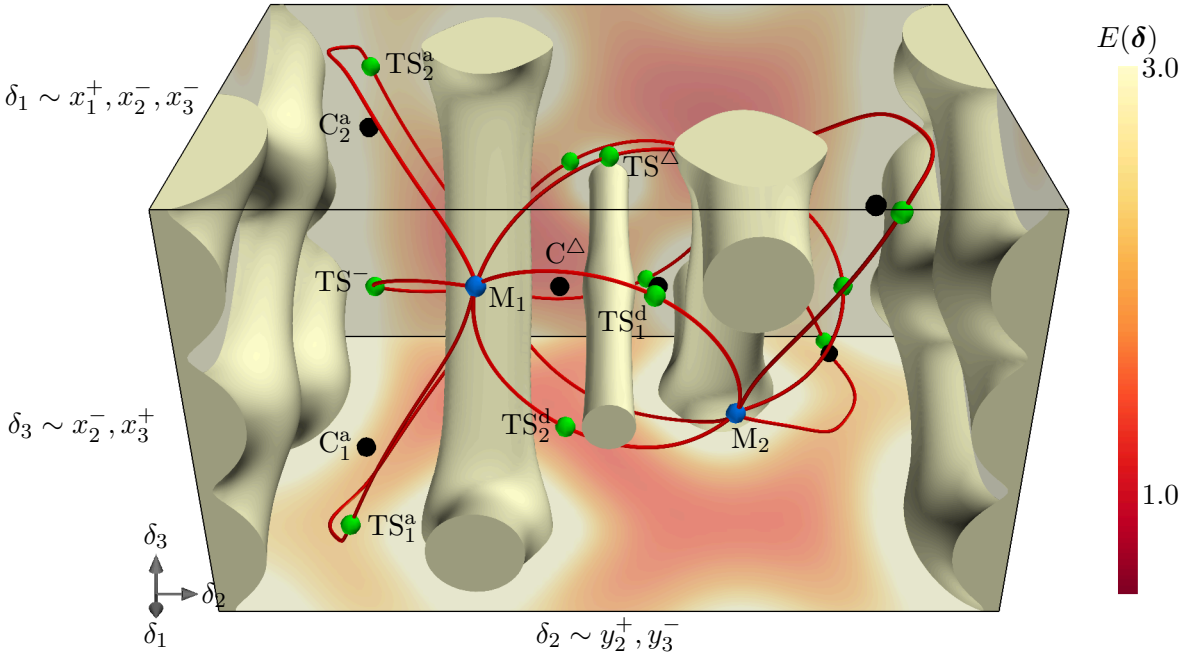

Figure 4.7: Visualization of the reduced 3-particle system, confined to three dimensions, eqn. (4.14). The labels on the three axes indicate the relative motion of the particles along each axis. For instance, the position of the first, restricted particle is determined by δ_1 alone. It moves from the left to the right with increasing δ_1. Shown as colored dots are the stationary states, minima (blue), transition states (green), and co-dimension 2 points (black). For reference, some of the points have been labeled in accordance with figure 4.6. The minima are connected via the unstable manifolds of the transition states (red lines). They wrap around regions of large potential energy due to singularities (white isosurface $E_p = 5$). In the background, the surface of the cube displays a cross-section of the potential energy, analogous to figure 4.2(a).

and can be transformed into each other by a rotation about the δ_3-axis. The minima are connected by a network of the unstable manifolds of the transition states, indicated as red lines wrapping around the singularities. Each minimum is connected to each of the other three (in the figure, two of them are occluded by the isosurface). In this representation, we neglected all connections leading to minima outside of the cube. They belong to unphysical configurations where at least one particle forms an interstitial in the surrounding particle-matrix, leaving behind a corresponding vacancy.

In order to get a more detailed view on the dynamics in the system, we take a look at the stable and unstable manifolds of the transition states and co-dimension two points. To this end, we use the method of *fat trajectories*, which is described in more detail in appendix A.3. As the name suggests, this technique approximates the manifolds by

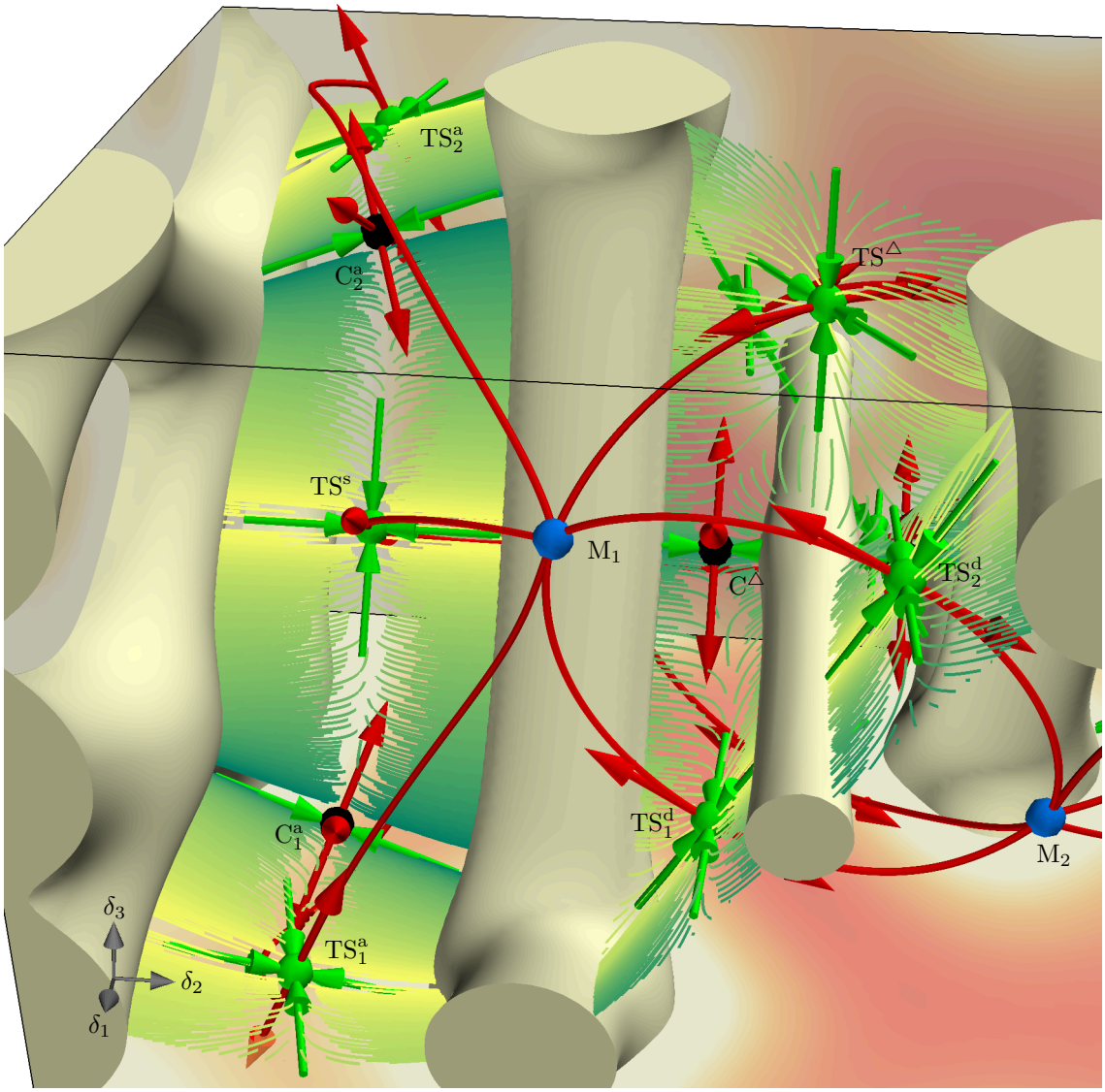

Figure 4.8: Visualization of the invariant manifolds of the transition states. The potential energy landscape and stationary states are depicted as in figure 4.7. Arrows indicate the stable (green) and unstable (red) eigendirections. The unstable manifolds of the transition states are shown as red lines, the thin greenish lines are trajectories approximating their stable manifolds. Color-coded is the integration time from short (yellow) to long (dark green). The volume of attraction of the minimum M_1 is determined by the stable manifolds, which are stitched together along the stable manifolds of the co-dimension two points and the singularities, represented by the white columns. An animation of the depicted scene is found online at `https://youtu.be/xbSYaveTjwk`, `https://youtu.be/tFLehv4cCSo`, and `https://youtu.be/k4WtmVt1IK4`.

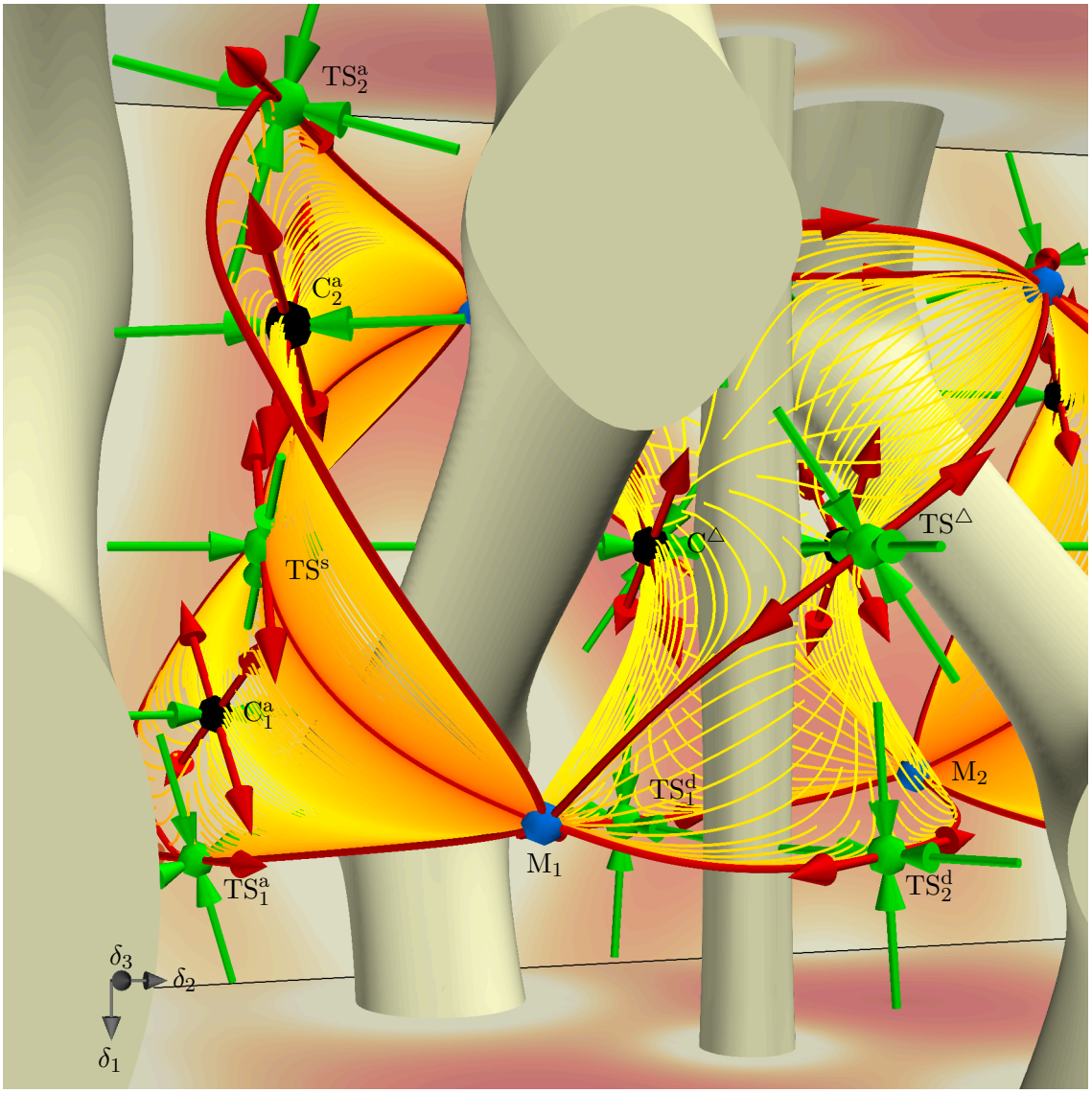

Figure 4.9: Visualization of the unstable manifolds. The potential energy landscape and stationary states are depicted as in figure 4.7. The cube has been rotated about the δ_2-axis so that M_1 is shifted towards the bottom and M_2 to the back. Arrows indicate the stable (green) and unstable (red) eigendirections of unstable equilibria. The red lines are the unstable manifolds of the transition states, whereas the thin orange lines approximate the unstable manifolds of the co-dimension two points. Color-coded is the integration time from short (yellow) to long (red). They are found midway between singularities (white columns). Since they are attractive to other trajectories approaching the minima, they give us an idea of the dynamics. An animation of the depicted scene is found online at `https://youtu.be/DLM8_oiVgQs`.

trajectories lying therein, and combines them to form a hypersurface. The stable and unstable manifolds are shown in figure 4.8 and 4.9, respectively. Additionally, the stable and unstable eigendirections of the unstable equilibria are indicated by arrows.

In figure 4.8, we see the stable manifolds of the six transition states which connect the minimum M_1 with all other global minima. In the left part of the figure, we see the horizontal particle exchanges (cf. the 2nd row in figure 4.6), the symmetric exchange TS^{s} in the center and the transitions where one particle temporarily leaves the cage, TS^{a}, at the top and bottom. Their stable manifolds are stitched together along the stable manifold of the corresponding co-dimension two state C^{a}, and they are confined by the singularities, either due to collision with background particles, left, or a collision of the second particle with first, restricted one, right. In the upper right of figure 4.8, we see the three-particle exchange $\mathrm{TS}^{\triangle}$. In the foreground on the lower right, the two possibilities of the diagonal two-particle exchange TS^{d} with particles passing clockwise or counterclockwise are situated. Their respective stable manifolds intersect on the singularity where the two swapping particles would collide. Again, the corresponding co-dimension two state, $\mathrm{C}^{\triangle}$ is located on the intersection of stable manifolds.

This confirms our picture of the configuration space. The stable manifolds of the transition states form the outer boundary of the volume of attraction of the minimum. The manifolds are stitched together, either along the stable manifolds of more unstable equilibria, or along singularities of the inter-particle potential. Thus, transition states form the bottlenecks of the dynamics, and transitions through co-dimension two points are unlikely to occur as long as the temperature and hence the energy in the system is low enough.

In figure 4.9 on the other hand, we focus on the unstable manifolds. Since the unstable manifolds themselves are attractive to other trajectories approaching the minima, they give us an idea of the possible dynamics in the system. While the unstable manifolds of the transition states, red lines in the figure, directly connect adjacent minima, the unstable manifolds of the co-dimension two points form surfaces, situated midway between singularities. Hence, we find that the co-dimension-two points $\mathrm{C}^{\triangle}$ in the center connect all four minima each. Similar to the stable manifolds, each manifold is confined by the unstable manifolds of the transition states. More importantly, the energy barrier at the co-dimension two points are roughly five times higher than at the transition states, compare table 4.3. The case is slightly different for the outer co-dimension two points C^{a} seen in the left part of the figure: They only connect two minima each. Consequently, their unstable manifolds are enclosed by the unstable manifolds of two transition states each. The distance to the singularities is similar for all stationary points, and so the energy barrier at the co-dimension two point is only slightly larger than at the neighboring transitions states. Nevertheless, the barriers are much larger than those of TS^{d} and $\mathrm{TS}^{\triangle}$, and hence in the regime of low temperatures, transitions are expected to occur in the vicinity of the transition states with lowest potential energy.

4.4 Summary

What we have seen so far is that transition states truly are bottlenecks of the dynamics. At very low temperatures, only every now and then a trajectory of the system will get close to

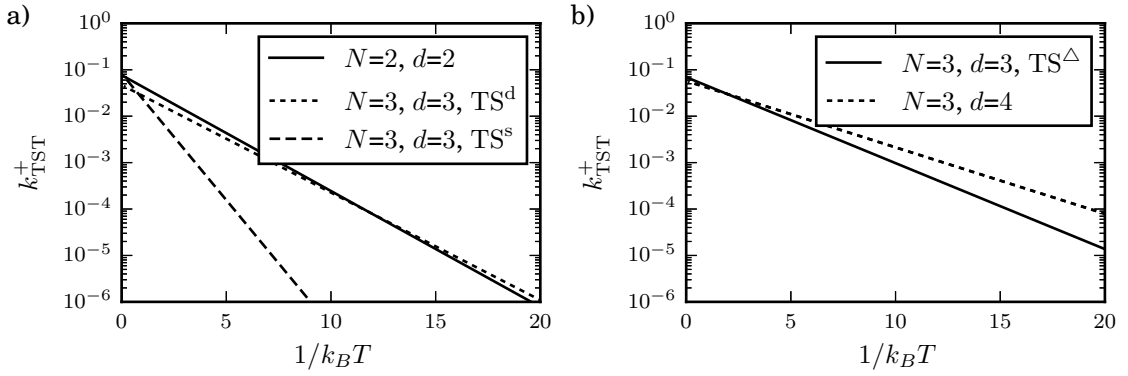

Figure 4.10: Comparison of transition rates (eqn. (4.8)) for the two-particle exchange in the two- and three-particle system (a) and the three-particle exchange TS$^{\triangle}$ for the two reductions in the three-particle system (b). N denotes the number of free particles, and d the system dimension. (a) When increasing the number of free particles, the energy barrier drops despite the total energy increasing, whereas the angular frequency roughly remains constant. (b) A similar observation can be made for the three-particle exchange. As more dimensions are taken into account, transitions occur at lower temperatures but with lower maximum rates. This is due to the particles fitting better at the intermediate transition state, which results in lower potential energy barriers and thus the earlier onset at lower temperatures. At the same time, the maximum rates remain similar in magnitude, showing a slight decrease.

a transition state and cross over to another basin of attraction. In this specific example, this holds up to a temperature which roughly corresponds to the height of the energy barrier, cf. figure 4.4. In the temperature range below, the approximation of harmonic transition state theory gives reasonable results.

To conclude, we compare transition rates of different reductions in figure 4.10, both for two-particle exchanges (a) and the three-particle exchange (b). As we allow for more degrees of freedom, the obtained transition states should get closer to the transition states found in a system where all particles interact freely. A visual inspection in physical space, figure 4.2(a), figure 4.5 and figure 4.6, reveals that in general inter-particle distances increase with the number of degrees of freedom. Naturally, this lowers the energy barrier and consequently increases the transition rates. An exception is the symmetric two-particle exchange TS$^{\mathrm{s}}$ where the particles form a void in the center, resulting in a large potential energy. This can also be seen in the steepness of the slopes in figure 4.10(a), which directly correspond to the height of the energy barriers. The same observation applies to the three-particle exchanges in (b), with the transition state in the four-dimensional system fitting better into the surrounding lattice and thus reducing the energy barrier. The maximum rates, on the other hand, decrease only slightly with additional degrees of freedom. This is confirmed both by TS$^{\mathrm{d}}$ in figure 4.10(a) and the 4-dimensional three-particle exchange in figure 4.10(b).

5

The two-particle exchange

So far, we only considered a few free particles confined in a static crystalline matrix. Obviously, this description is incomplete: At the transition states, the free particles are squeezed in their configuration, exerting forces on the particles bound in the matrix. As a result, they should move to the side minimizing the forces. Therefore, from hereon we let all particles freely evolve. Naturally, the task to find the transition states becomes more challenging as we increase the number of degrees of freedom from four to $2N$.

In this chapter, we will study the first particle exchange that comes to mind, two neighboring particles swapping their positions, and discuss how it can be embedded in the picture of a continuum theory. However, the first questions which arise are how to distinguish the two minima, since their structure is identical except for a permutation of two identical (yet distinguishable) particles, and how to locate the transition and its corresponding transition state.

5.1 Identification of conformational changes in minima

When investigating transitions, we have to identify and distinguish different minima. In the case of a crystalline structure, two minima only differ by a permutation of some particles. Thus, their potential energy is the same and cannot be used as a distinctive feature.

Another straight-forward approach would be to compare particle positions. This leaves us with two problems. First, we would have to determine minima very accurately - or accept some deviations of the positions. In a crystalline system, this is acceptable due to well defined isolated particle positions and distances prescribed by the lattice constant. With regard to a future investigation of amorphous systems with their varying inter-particle distances, the question arises of how to define acceptable deviations. Second, translational invariance of the system can lead to a constant offset between two otherwise identical configurations. This problem is aggravated by resetting particles at the periodic boundaries, which each time changes the location of the center of mass. As a result, it is not possible to identify the offset between two configurations with a motion of the center of mass.

A solution to this problem is to drop the exact positions and instead focus on the nearest neighbor relations. To identify them, we use a Delaunay triangulation of the coordinates.

This gives a unique tessellation[1] of space with vertices at each particle position, in two dimensions composed of triangles. Each edge of a triangle defines a nearest-neighbor connection which we represent in an adjacency matrix,

$$(\mathbf{M})_{i,j} = \begin{cases} 1 & \text{if } \exists \text{ edge}(i,j) \\ 0 & \text{else} \end{cases} . \tag{5.1}$$

The neighborhood relations are robust both in the sense of minimization and translation. For a structurally different ensemble, some of those relations are different. To quantify this change, we compute the signature

$$\sigma_{k,l} = \sum_{i,j} \text{XOR}\left(\mathbf{M}^k_{i,j}, \mathbf{M}^l_{i,j}\right) = \sum_{i,j} |\mathbf{M}^k_{i,j} - \mathbf{M}^l_{i,j}| \tag{5.2}$$

of two states k and l. It gives two times the number of changes (lost or gained connections) in the neighborhood relations and helps to distinguish adjacent minima. Moreover, it can be used to identify equivalent transition states since two structurally identical transitions yield the same signature.

In order to account for the boundary conditions, we implement a periodic Delaunay triangulation by reproducing the computational domain in each direction. Since the tesselation is needed only once after each minimization, the computational overhead is negligible. The triangulation itself is performed using the qhull package (Barber et al., 1996).

5.2 The technique of edge tracking

Transition states in high-dimensional spaces can be obtained by various methods. Typically, they are composed of a two-step procedure: First, a force equilibrium of the system is determined. In the second step, its stability properties are examined. Here, we will make use of the fact that transition states have exactly one unstable direction. Starting integration on the one or the other side, the time-evolution of the system will bring us to different minima. Therefore, by refining the initial conditions, we should be able to determine a system-trajectory which directly evolves towards the transition state. Specifically, we adopt the edge tracking algorithms developed in connection with the turbulence transition (Toh and Itano, 2003; Skufca et al., 2006; Schneider et al., 2007, 2008) and applied to magnetic reconnection (Cassak et al., 2007) to the case of solids.

To begin with, we take two (or more) particles, and move them in a specific direction, and let them relax, for example by using overdamped dynamics. If they return to their original positions, then the initial perturbation was not sufficiently big to induce the transition. The initial displacement is then increased until the time evolution carries it to the new minimum with the positions exchanged. In theory, the initial conditions can then be refined until one is identified that does not fall into either one of the minima. Since there are no other unstable directions, this trajectory will then follow the stable directions of the

[1] At the transition state, the Delaunay tessellation may show non-simplicial facets, e.g. squares. The triangulation thereof is then ambiguous. Since the square configuration is structurally unstable, this is of minor significance in case of minima and can be neglected.

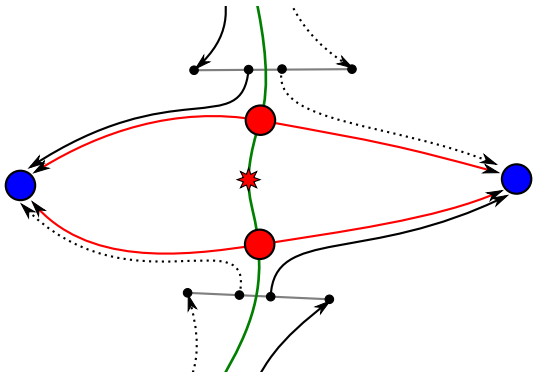

Figure 5.1: Schematic of the edge tracking algorithm with two particles, one starting at the top and the other at the bottom. The filled circles represent the minimum (blue) and transition state (red) configurations, whereas the green and red lines indicate the stable and unstable manifolds of the latter. At the red star, stable manifolds intersect in a stationary point of higher co-dimension. The solid and dashed black lines are matching trajectories, approaching opposite minimum configurations. Either, the upper particle approaches the left minimum and the lower particle the right minimum, or vice versa. As soon as the separation of the trajectories exceeds a threshold, a bisection along the gray line generates new initial conditions and a new set of trajectories . Overall, this approximates a trajectory on the unstable manifold which approaches the transition state.

transition state and approach it. In practice, it is merely impossible to generate starting points which evolve exactly onto the transition state. The reason are tiny numerical deviations from the exact solution, which will grow along the trajectory and cause it to miss the transition state. Therefore, we recursively repeat the procedure. A sketch of the algorithm is shown in figure 5.1. We evolve two neighboring trajectories leading to the different minima and monitor their separation. As soon as a critical threshold d_{evolve} is exceeded, we stop the time evolution and restart bisecting along the connecting line, until we finally generate two new initial conditions, separated by $\varepsilon_{\text{bisect}}$ and each one leading to a different minimum. We then again monitor the separation of the trajectories, and the algorithm repeats itself. Virtually, this procedure brackets a trajectory which runs into the transition state and eventually will get us arbitrarily close to it. As a stopping criterion, we take two indicators, namely the norm of the force $\|\boldsymbol{F}\|$ and the number of unstable eigenvalues. The latter is necessary whenever we start the algorithm at points of large potential energy. On the way towards the transition state, we might get so close to stationary points of higher co-dimension that $\|\boldsymbol{F}\|$ falls below the threshold f_ε. Since we know the Jacobian analytically and are only interested in the most unstable modes, the few eigenvalues required can be obtained inexpensively using an iterative Arnoldi algorithm. Here, another benefit of the edge tracking algorithm shows up: During a bisection close to such a critical point, we might end up with initial conditions leading to a third intermediate minimum, i.e. the transition between the two initial minima involves a chain of several transition states. With the edge tracking algorithm at hand, we can

easily split our search to find all of them. Finally, when all requirements are met, we refine the transition state by applying Newton's algorithm. The parameters of the edge tracking algorithm are summarized in table 5.1.

It is to note that the edge tracking algorithm is similar to the method of fat trajectories used for the computation of invariant manifolds, appendix A.3. Both implement a bisection algorithm, and while the additional information of the trajectories is discarded in the edge tracking algorithm, they are used in the latter one to visualize the unstable manifolds.

Generating starting conditions

Since edge tracking is a top-down approach, we have to construct initial conditions which evolve to different minima. Several approaches are possible. The most elementary one is a linear interpolation between the two minima. However, this has some drawbacks. First, it might introduce singularities where particles are put atop each other. The issue can be solved by a rotation of the displacement vectors. For a sufficiently small angle, the resulting initial conditions will still evolve to both minima. The second, closely related problem is that by interpolating along a straight line, particles might be put close to each other. This results in large energy deposits and hence strong forces pulling apart a few particles. While this is manageable for crystalline structures, with regard to the application to disordered systems this may lead to a disarrangement of the whole system, generating a different set of minima than the ones intended. Due to the large energy input, we call this approach non-adiabatic in the meaning of non-reversible.

An approach which softens the impact of the potential is to gently pull the particles in question towards the new minimum, for example by attaching moving springs to them. That way they have time to rearrange themselves. Initial conditions are taken along the generated trajectory, and we verify to which minimum they evolve. Using edge tracking, we can then investigate all transitions along the path. Of course, special care has to be taken as soon as the system overcomes a barrier, since then both the force due to the potential and the external force are aligned and the system quickly leaves the vicinity of the transition state. We have two parameters controlling this procedure, namely the spring constant k and the velocity $\boldsymbol{v}$ with which we pull on the particles. The spring constant determines how close particles remain to the prescribed displacement, whereas the velocity sets the timescale of the procedure: Pulling fast leaves the system no time to adjust to the displacements, in contrast to a slow velocity. In the latter case, we speak of

Table 5.1: Parameters of the edge tracking algorithm. Additionally, in order to guarantee numerical precision an appropriate maximum stepsize has to be determined.

parameter	meaning
s_{evolve}	consecutive steps during evolution of two separating trajectories before the separation is checked
d_{evolve}	maximum per particle distance of separating trajectories
$\varepsilon_{\text{bisect}}$	bisection threshold; minimum separation of initial conditions
f_ε	maximum force at transition state

an adiabatic deformation.

Another possibility is to use one of the bottom-up algorithms described in appendix A.4. By construction, they will most likely stop in the vicinity of a transition state, and edge tracking can be used to refine the results. Their shortcoming is that only a single transition state can be investigated at a time.

Heuristics

Sometimes, the edge tracking algorithm gets stuck due to inappropriate parameter values, e.g. for the maximum trajectory separation. This happens for example when the unstable manifold has a strong curvature close to the transition state, picture for example a tuning fork: Both initial conditions lead away from the transition state, locally in opposite directions. However, in the global picture they stay close together on long timescales and drift far away from the transition state before the required separation is reached. To address this issue, we implement a heuristic which checks for specific patterns and then refines the parameters. The implemented measures are given in table 5.2. The procedure will either adjust the maximum separation of the diverging trajectories, or increase the accuracy of the bisection in order to get closer to the transition state.

5.2.1 Implementation

The time evolution and minimization of a high-dimensional system is computationally expensive. Since it seems unreasonable to develop an efficiently parallelized code ourselves when fast and tested programs are at hand, we decided to use the LAMMPS package for driving and minimizing the system. It is written in C++ and although it is mainly used as a script controlled binary, it also provides a library interface to directly interact with the program. It is parallelized using the message passing interface (MPI). In order to use the package, we had to implement some additionally routines, for example for the spring displacements in the initial bisection step. Since LAMMPS is written in a modular way, this can be easily achieved.

In contrast to the LAMMPS library, the rest of our program is mostly serial, with some parts parallelized using openMP, e.g. the computation of the Jacobian and matrix products in the Newton algorithm. Therefore, we decided to write the program with a *multiple program, multiple data* (MPMD) paradigm: The main program runs on a single

Table 5.2: Heuristics of the edge tracking algorithm used to improve convergence towards the transition state (TS).

event	measure
Repeating transition	Reduce maximum trajectory separation d_{evolve}
	Reduce maximum number of steps s_{evolve} (i.e. check separation more frequently)
Approaching TS	Reduce bisection threshold $\varepsilon_{\text{bisect}}$, i.e. increase number of bisections

thread, whereas the LAMMPS program runs in parallel on additional threads. To achieve this separation, a small wrapper library is used which runs on a single thread (the parent) and spawns new threads (children) on which LAMMPS runs. Communication between the two parts takes place using MPI: The parent process takes a command, e.g. to integrate for 500 timesteps, communicates it via MPI and waits for the result, in this case a final status. The cildren on the other hand receive the command via MPI, perform the requested task and return the result or a status flag[2].

The main program is written in C++ as well, with classes representing the different functionalities. The most fundamental class holds the system features such as system size, particle positions, and potentials and gives access to time integration and minimization. It is part of several other classes which provide specialized algorithms, such as a Newton algorithm, eigenvalue decomposition and triangulation. They are all combined in the edge tracking program.

5.2.2 Other algorithms for locating transition states

The importance of transition states, for example for the understanding of chemical reactions, has led to the invention of several algorithms which try to locate possible transition states and make extensive use of the special properties of a potential energy landscape. A few common representatives are described in appendix A.4. They can be loosely divided in two classes, based on whether they start somewhere in the potential energy landscape and locate the minima afterwards, or whether they start at the minimum and evolve towards the transition state. Accordingly, they are termed *top-down* or *bottom-up* algorithms.

The first class of algorithms starts at higher points (i.e. energies) in the potential energy landscape, and approaches both the transition state and the corresponding minima from above. The most simple realization are sampling algorithms, which more or less systematically examine the potential energy landscape. More complex algorithms comprise the ridge-algorithm, which is closely related to edge tracking but skips part of it due to the special structure of the potential energy landscape, and the nudged-elastic-band (NEB) method. It involves the combined optimization of several copies of the system, and is described in more detail in the appendix.

The second kind of algorithm works the other way round, starts at a minimum and from there on tries to locate a transition state. Examples are the step-and-slide algorithm, which prescribes the potential energy level and successively increases it, and the activation-relaxation technique, eigenvector following and the dimer method. The latter try to determine the direction in which a transition state will be located, for example by examining the curvature or the whole spectrum of the potential landscape.

An overview on how the mentioned algorithms actually work is given in the appendix. In comparison, besides the NEB method, edge tracking is the only algorithm which can systematically trace out a chain of subsequent transitions connecting two distant minima.

[2]While one part of the complete program is performing calculations, the other one is waiting for new commands or results. Communication using the standard MPI_Send and MPI_Recv commands leads to full CPU load due to permanent status requests. Therefore, we had to use modified send and receive commands which incorporate a waiting time between status requests (written by Jeff Squyres and Douglas Guptill)

The bottom-up algorithms have to be restarted after a transition is determined, the step-and-slide algorithm will end up on the transition state with the highest energy barrier, and the ridge algorithm will stop at a random transition state. However, in the latter cases it should be possible to adapt the methods to achieve a similar functionality. Both the ridge method and edge tracking follow the separating manifold, i.e. the separating surface between the different basins of attraction, generating some additional information about configuration space. The other algorithms only yield the transition states and thus the minimum energy path. Another advantage is that the edge tracking algorithm is intrinsically repelled by stationary states with more than one unstable direction. Nevertheless, ill posed initial conditions or symmetries of the system may bring the algorithm to a halt at such points. This will be illustrated in the next chapter, altogether with a possible approach to solve the problem. In contrast to all the presented algorithms, edge tracking does not depend on special properties of the dynamical system at hand, as long as the two sides of the separating manifold can be readily discerned. Hence, it is applicable to externally driven or time-varying systems, as for example particles subject to an external shear force discussed in chapter 2. Additionally, edge tracking is conceptually straightforward and thus easy to implement.

The versatility has its price, though. Compared with for example the NEB method or the ridge algorithm, edge tracking is rather inefficient due to the many minimizations needed. Yet, this can be attenuated to some degree by using suitable stopping criteria and an early identification of different minima, for example by changes of the neighborhood relations.

5.3 Finding the transition state: An example

We now want to demonstrate the edge tracking algorithm on the example of the two particle exchange. We take the same system as in the MD-simulations in chapter 3, with 2500 particles in a periodic domain. The screening of the Yukawa potential is set to $\mu = 3$. In order to evolve the system in the potential energy landscape, we use the same minimization algorithm as in chapter 3, where we determined inherent minima. It is equivalent to an overdamped evolution of the system, eqn. (3.24). We illustrate the algorithm with snapshots of the ensemble at different stages of the algorithm in figure 5.2, along with the corresponding time line in figure 5.3. It has proven to be reasonable to measure the distance d between two system copies A and B on a per-particle basis,

$$d\,(\mathrm{A},\mathrm{B}) = \max\left(\|\boldsymbol{x}_i(\mathrm{A}) - \boldsymbol{x}_i(\mathrm{B})\|\right). \tag{5.3}$$

This way, it is independent of the number of particles and sensitive to the particles exchanging their positions. We start by generating initial conditions using the spring algorithm. Eventually, this leads us to the two configurations shown in the outermost columns in the top row of figure 5.2. Although both are indistinguishable by eye they evolve to different minima, with the two central particles rotating around their common center of mass. With those two configurations as a starting point, we begin the edge tracking algorithm. Yet, the system shows two competing timescales: On the one hand, the approach towards the transition state is a slow process. The four central particles have to align and, accordingly,

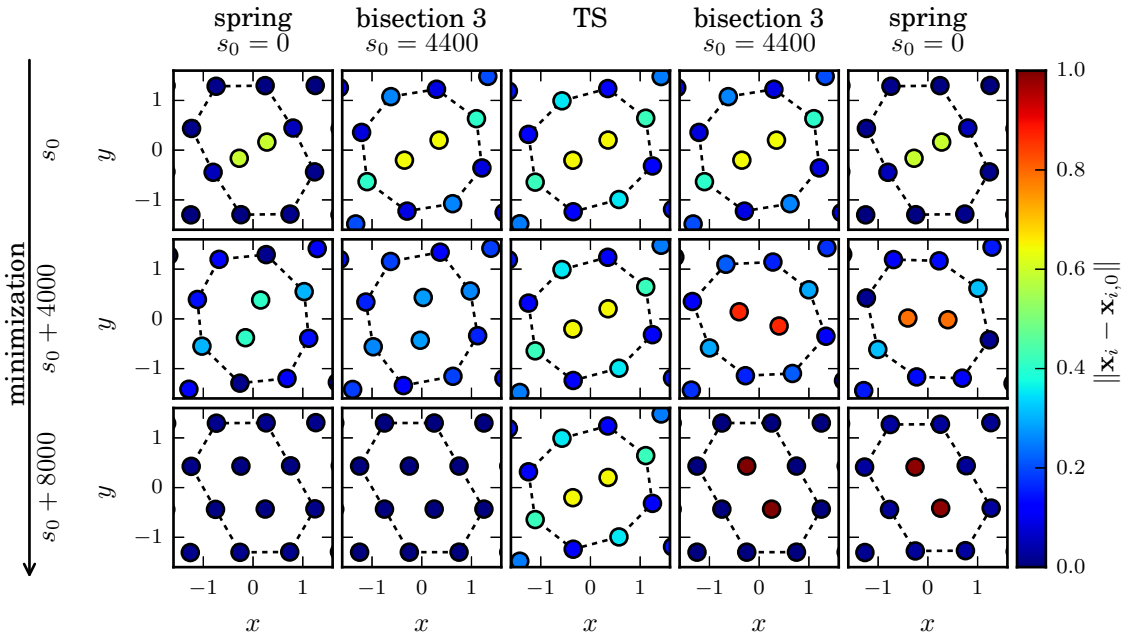

Figure 5.2: Time series of the edge tracking process. In the top row, from left to right are different initial conditions, and each column shows snapshots of the corresponding minimization. The outermost columns show the two closest trajectories generated with the initial spring displacements. On the left, the two central particles rotate counterclockwise, back to their original position. On the right, they rotate clockwise and eventually swap their positions. Correspondingly, the inner columns show the initial conditions and their minimization after three consecutive applications of the edge tracking routine. The central column finally shows the transition state itself, determined by Newton's algorithm. Colors indicate displacements with respect to the reference minimum in the lower left panel. The dashed lines visualize the distortion of the lattice. The corresponding time lines of the procedure are shown in figure 5.3.

many particles in the surroundings have to be pushed away to free the space. Since the system approaches a force equilibrium, this process slows down. The escape towards the minima on the other hand happens on a faster timescale, at least as soon as the system is slightly off the separating manifold. More importantly, as soon as the two central particles leave the intermediate position, the two particles which should be pushed outwards will quickly relax towards their original minimum positions, reversing the approach towards the transition state. Therefore, we use heuristics to improve convergence of the algorithm by reducing both the maximum separation of neighboring trajectories d_{evolve} and the bisection threshold $\varepsilon_{\text{bisect}}$. This can also be seen in the time line in figure 5.3: The initial bisection takes a rather large separation and bisection threshold so that a rough estimate of the transition state is quickly obtained. After the bisection has finished, the two minima of the final initial conditions are compared with the two minima of the starting initial conditions. In principle, at this point a third, intermediate minimum might have been

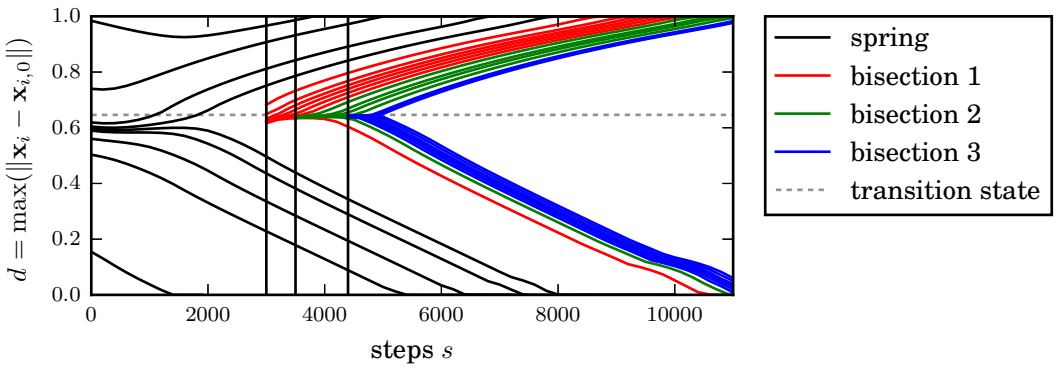

Figure 5.3: Time line of the edge tracking process. Each line represents a different trajectory and its distance to the reference minimum. At $s = 0$, we start with initial conditions generated using the spring algorithm. Minimization yields either the original minimum ($d = 0$) or the swapped configuration ($d = 1$). Snapshots of the two innermost trajectories are shown in figure 5.2 in the outermost columns. At $s = 3000$, 3500, and 4400 the bisection is restarted due to neighboring trajectories separating beyond the threshold value. Over time, this approximates the transition state, in this particular case it was found after the third bisection by a final Newton-search.

encountered, which would correspond to a chain of several transitions leading to the investigated exchange of particles. However, the minima remained the same, and thus the next bisection will investigate the same transition. Therefore, the maximum separation is reduced so that the separating manifold is kept closely bracketed, giving particles far away from the center of displacement time for relative equilibration. After the second bisection, only one positive eigenvalue remains, indicating that the algorithm almost reached the transition state. Thus, the bisection threshold is decreased to pin the transition state. The final initial conditions are then refined using Newton's algorithm: the transition state is found.

It is shown in figure 5.4, along with the displacement field. In the left part of the figure, we see the resulting transition with the two central particles exchanging their positions. In the middle panel, the transition state itself is depicted. Color-coded are the individual displacements with respect to the starting minimum on a logarithmic scale. Similarly, arrows indicate the displacement from the starting configuration in blue and towards the final minimum in red. We observe that the two particles exchanging their positions align with two more particles, significantly displacing them. On the other hand, particles along the perpendicular axis are pulled towards the center of deformation, filling the emerged void. Consequently, the transition state is twofold mirror symmetric. The corresponding displacement field hence exhibits a quadrupolar structure, which is shown in the rightmost panel of the figure. We see that displacements quickly drop below 10% of the lattice spacing r_0. Moreover, the mirror symmetry observed close to the center is broken by the boundary conditions, so that only a twofold rotational symmetry persists. Additionally shown as solid lines are points of vanishing radial displacement. They spiral out of the center such that they connect across the cell boundaries. Correspondingly, at

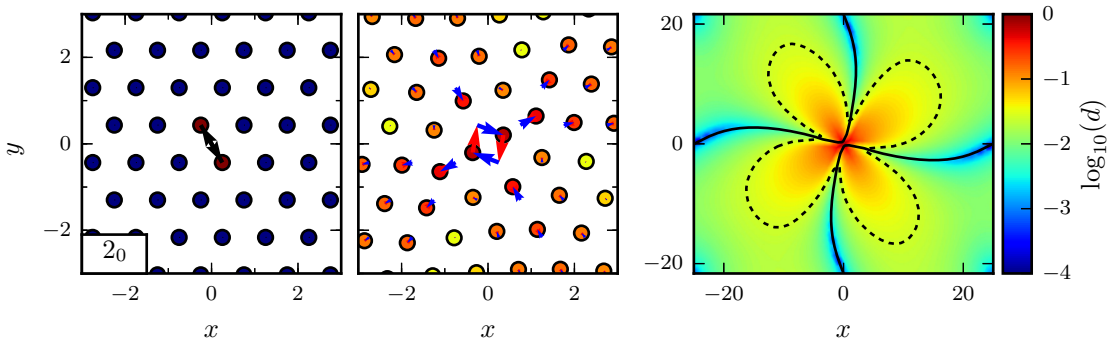

Figure 5.4: The two-particle exchange (left, indicated by arrows), the corresponding transition state (middle) and displacement field (right). Color coded is the logarithm of displacements with respect to the starting configuration. The arrows in the middle panel represent the displacement vectors from the starting configuration (blue) and towards the final minimum (red). The solid black lines in the right panel indicate vanishing radial displacements, whereas the dashed lines mark $d = 0.025$. The displacement field shows a quadrupolar structure (orange-red) with particles pushed outwards towards the upper right and lower left, and pulled inwards in the perpendicular direction.

the boundary the total displacements diminish as well. Although the localization of the transition state is recognizable from the displacement field qualitatively, we still have to quantify it, e.g. by computing a participation number as is done in the next section.

5.3.1 Localization of the transition state: The participation number

When investigating a transition, it is of interest to know which particles, or on a more basic level, how many particles participate in it. For a global transition, we would expect almost all particles to take part. On the other hand, for a local rearrangement we would expect that only few particles participate. Following the example of Bell and Dean (1970), we define the participation number as

$$\mathrm{PN}_{k=2} = \frac{\left(\sum_i |d_i|^2\right)^2}{\sum_i |d_i|^4}, \tag{5.4}$$

where d_i are particle displacements with respect to a reference configuration. It gives a measure of the number of particles involved in an event. For only one particle participating, $d_i = \delta_{ij}$, it yields $\mathrm{PN}_2 = 1$, whereas for all particles being displaced equally, $d_i = 1/N$, the result is $\mathrm{PN}_2 = N$, the number of particles.

A similar definition is given by Swayamjyoti et al. (2014) for $k = 4$. We generalize this by using normalized weights of order k,

$$\omega_i^{(k)} = \frac{|d_i|^k}{\sum_j |d_j|^k}. \tag{5.5}$$

Then, the participation number is given by

$$\mathrm{PN}_k = \frac{1}{\sum_i \left(\omega_i^{(k)}\right)^2} \tag{5.6}$$

with $k \in \mathbb{N}$ even. For any k, it still varies between 1 and N. With increasing order in k, only particles with larger displacements get a substantial weight whereas small displacements lead to almost zero weight. Thus, for localized structures the participation number will decrease with increasing k whereas for structures with homogeneous displacements, the participation number will not be affected.

When investigating transition states, we are also interested in global quantities describing it, for example the average energy increase. The problem which arises when looking at such measures is that only few particles contribute. Thus, when increasing the number of particles, these quantities tend to shrink with system size. The issue can be solved by the computation of weighted averages,

$$\langle a \rangle_k = \sum_i \omega_i^{(k)} a_i. \tag{5.7}$$

The participation numbers of the current transition state reflect its localized nature: $k = 2$ gives us $\mathrm{PN}_2 \approx 35$. This corresponds to a patch of roughly 6 by 6 particles, which quite well captures the extent of the transition state, as can be seen from the displacement field in figure 5.4. At order $k = 4$, we find a participation number $\mathrm{PN}_4 = 3.6$. It matches the observations made earlier: At the transition, four particles have to align, with the central two displaced on the order of a lattice constant. For completeness, we should note that $\mathrm{PN}_6 = 2.5$. Bearing in mind that our system consists of 2500 particles, it is save to say that the transition state is well localized.

We will discuss more properties of the transition state in more detail in the next chapter, in union with further transition states. Beforehand, we will discuss the impact of both the system size and the boundary conditions on the transition state, as well as the correspondence of the displacement field to the continuum theory of an elastic solid.

5.4 Effects of the system size and boundary conditions

At the transition state, stresses emerge in the system due to the central particles being squeezed in. Naturally, they have to be compensated for by the remaining particles, or alternatively be diverted towards the boundary of the domain. When looking closely at the displacement field in figure 5.4, the curved shapes far from the origin attract our attention. Clearly, they are owed to the periodic boundary conditions: Particles being pushed out of the domain at the top reenter at the bottom, and consequently the displacement field has to be connected across the boundary self-consistently. The question which immediately arises is whether this specific boundary condition with the accompanying distortion of the displacement field affects the transition state itself, and consequently alters its thermodynamically relevant properties. Additionally, rotations about $2\pi/6$ should leave the transition unaltered due to the symmetry of the underlying hexagonal lattice. However,

the orientation of the transition in reference to the computational box changes and thus the transition state might be different. Likewise, a larger domain might change the behavior as well: With more particles to compensate the stresses, displacements and ultimately the edge state could be altered.

In order to estimate the quality of our results, we compare systems of sizes $N_1 = 2500$ and $N_2 = 10000$. We use either periodic or fixed boundaries, where particles outside a circle of radius $r_{\text{fix}} = L_y/2 - 4.75$ around the origin are fixed at the global minimums' positions. This definition allows us to use the same cut-off radius as with periodic boundaries. The difference of the new boundaries is that forces are balanced at the walls, whereas with periodic conditions forces constitute additional pressures across the cell boundaries. In addition, we consider the transition parallel to the x-axis in the periodic 2500-particle system. It will provide us insight into the dependence on the orientation of the lattice in relation to the computational domain. For each of the five systems we compute the transition state of the two-particle exchange. In figure 5.5 we show the transitions of the 2500-particle systems, both the horizontal transition with periodic boundaries (a) and with fixed boundaries (b). Naturally, in the latter case the orientation of the transition is irrelevant. Visually, close to the center of deformation no qualitative differences between the states can be spotted. They both show the same quadrupolar structure as the original transition state in figure 5.4. However, the displacement fields differ in the region close to the boundaries: With a periodic domain, displacements extend to the next cell and have to be continued across the boundary. When considering the horizontal transition in figure 5.5(a), distortions of the field are minimized since the transition state fits symmetrically into the box, showing mirror-symmetries about both axes. With fixed boundaries, on the other hand, displacements have to vanish at a set radius. As a result, the shape of the computational domain becomes irrelevant, the accompanying artifacts completely disappear, and the displacement field decays much faster and only exhibits the symmetry of the transition state.

To quantify the similarities, we compute several indicator functions, namely the energies, barrier heights, participation numbers PN_k and the spectra, which we characterize by the unstable mode and the effective frequency. The results are summarized in table 5.3 for different boundary conditions in the 2500-particle system and in table 5.4 for the 10000-particle system, and will be discussed in the next two paragraphs.

5.4.1 Dependence on boundary conditions

As would be expected, changing the boundary conditions leads to slightly different results. When aligning the transition with the x-axis, the energy barrier slightly increases. The source can be found in the symmetry of the displacement field: Since it shows mirror symmetries both along the x- and y-axis, displacements have to drop off to zero on the boundaries. As a consequence, relative displacements have to be larger and thus the energy is increased. Likewise, for the same reason the participation numbers are smaller. The same arguments apply to the system with fixed boundaries. Here, the effect is even emphasized because particles are fixed on their positions beyond a radius of $r_{\text{fix}} = L_y/2 - 4.75$. In both cases, the higher order participation numbers, PN_4 and PN_6, are only slightly affected indicating that the transition state itself is quite unaffected by the change

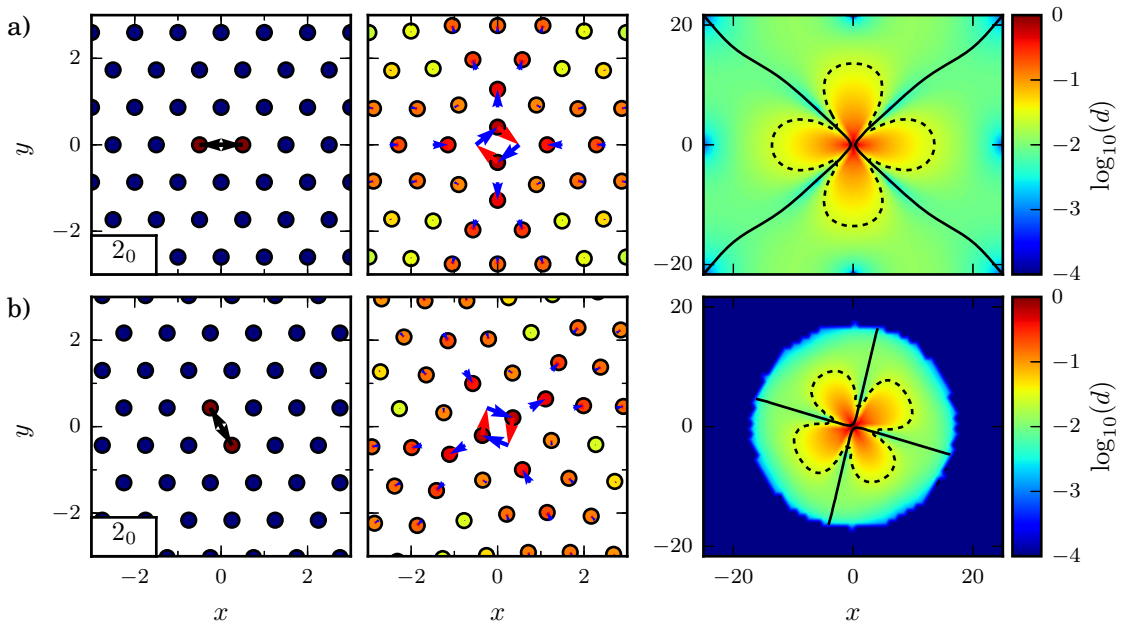

Figure 5.5: The two-particle exchange (left, indicated by arrows), the corresponding transition state (middle) and displacement field (right), both for a horizontal transition with periodic boundary conditions (a), and for particles fixed on their lattice sites beyond $r_{\mathrm{fix}} = L_y/2 - 4.75$ (b). Comparison with figure 5.4 shows that in either case structures are qualitatively identical, and that the displacement field is mostly affected close to the boundary. Color coded in the figure is the logarithm of displacements with respect to the starting configuration. The arrows in the middle panel represent the displacement vectors from the starting configuration (blue) and towards the final minimum (red). The solid black lines in the right panel indicate vanishing radial displacements, whereas the dashed lines mark $d = 0.025$.

of boundaries. This is confirmed by the corresponding spectra: Both the unstable mode and the effective frequency are in good agreement in all three cases. Therefore, the small difference between the results indicates that the effect of the central deformation diminishes quickly with distance and is negligible for systems of $N \geq 2500$ particles. Hence, when investigating further transition states we will not inspect different orientations on the lattice.

5.4.2 Dependence on system size

For both system sizes, the absolute energy barrier is the same within 1%. Consequently, the per-particle barrier is approximately four times smaller for the larger system. When taking weighted averages (eqn. (5.7)), we observe that both systems converge with increasing order in k. This indicates that the transition state is well localized in both systems and thus independent of the number of particles for $N \geq 2500$. The larger deviation of $\langle \Delta E \rangle_{\mathrm{PN}_2}$ can be understood by looking at the displacements as a function of distance to the center, figure 5.6: They exhibit a long tail which drops to zero only close to the

Table 5.3: Comparison of several quantities such as energies, energy barriers, averaged energy barriers, participation numbers PN_k, the unstable mode and effective frequency for a system size of 2500 particles and different boundary conditions. With fixed boundary conditions, 1034 free particles remain. Orientation of the transition state has merely an effect on thermodynamically relevant quantities, the same is true for fixed boundary conditions.

	periodic diagonal	periodic horizontal	deviation	fixed	deviation
$E_{\min}$	409.185	409.185		409.185	
E_{TS}	409.337	409.337	$< 10^{-3}\%$	409.338	$< 10^{-3}\%$
ΔE	0.152002	0.152444	0.29%	0.153366	0.90%
$\langle \Delta E \rangle_N$	6.08009×10^{-5}	6.09776×10^{-5}	0.29%	6.13465×10^{-5}	0.90%
$\langle \Delta E \rangle_{\mathrm{PN}_2}$	4.44217×10^{-3}	5.25764×10^{-3}	18.36%	6.33172×10^{-3}	42.54%
$\langle \Delta E \rangle_{\mathrm{PN}_4}$	1.10507×10^{-2}	1.11782×10^{-2}	1.15%	1.13772×10^{-2}	2.95%
$\langle \Delta E \rangle_{\mathrm{PN}_6}$	1.15770×10^{-2}	1.16340×10^{-2}	0.49%	1.17164×10^{-2}	1.20%
PN_2	35.28	25.61	27.32%	18.06	48.72%
PN_4	3.62	3.58	1.10%	3.49	3.59%
PN_6	2.45	2.45	$< 10^{-3}\%$	2.43	0.82%
λ^+	0.282862	0.286159	1.17%	0.292931	3.56%
$\omega_{\mathrm{eff}}/2\pi$	2.849	2.870	0.74%	2.948	3.47%

Table 5.4: The same quantities as in table 5.3 for a system size of 10000 particles, compared to the corresponding 2500-particle systems. With fixed boundary conditions, ≈ 5390 free particles remain. Additionally, deviations of the corresponding 2500-particle system subject to identical boundary conditions and between the 10000-particle systems are given. The thermodynamically relevant quantities coincide nicely for both system sizes.

	periodic diagonal	deviation 2500	fixed	deviation 2500	10000
$E_{\min}$	1636.74		1636.74		
E_{TS}	1636.89		1636.89		$< 10^{-3}\%$
ΔE	0.151941	0.04%	0.152210	0.76%	0.18%
$\langle \Delta E \rangle_N$	1.51941×10^{-5}	300.16%	1.52210×10^{-5}	303.04%	0.18%
$\langle \Delta E \rangle_{\mathrm{PN}_2}$	3.78302×10^{-3}	17.42%	4.86983×10^{-3}	30.02%	28.73%
$\langle \Delta E \rangle_{\mathrm{PN}_4}$	1.10210×10^{-2}	0.27%	1.11019×10^{-2}	2.48%	0.73%
$\langle \Delta E \rangle_{\mathrm{PN}_6}$	1.15622×10^{-2}	0.13 %	1.15920×10^{-2}	1.07%	0.26%
PN_2	48.40	27.12%	29.48	38.74%	39.09%
PN_4	3.64	0.43%	3.60	3.06%	1.10%
PN_6	2.46	0.14%	2.45	0.82%	0.41%
λ^+	0.282396	0.17%	0.284426	2.99%	0.72%
$\omega_{\mathrm{eff}}/2\pi$	2.840	0.32%	2.869	2.8%	1.02%

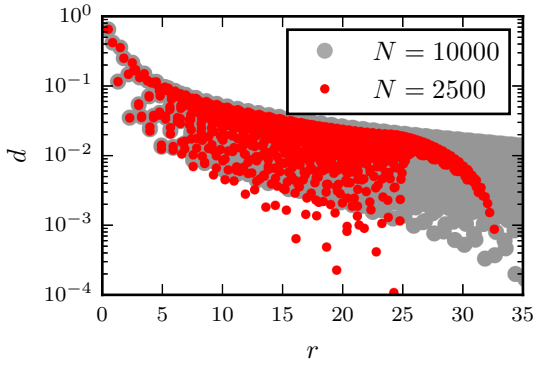

Figure 5.6: Displacements as a function of distance to the center of deformation, for both the 10000 particle system (gray) and the 2500 particle system (red), subject to periodic boundary conditions. Up to a distance of $r \approx 10$, both distributions coincide well. Beyond, the displacement field is governed by linear elasiticity and the boundaries. See also chapter 5.5 for a discussion.

system boundaries. This is consistent with elasticity theory, as will be discussed in the next section. However, on short distances both distributions coincide. The localization is also confirmed by comparison of the participation numbers PN_k. When taking only the strongest displacements into account ($k = 6$), they are virtually identical. In view of computation of transition rates, we also compare the unstable mode of the transition state and the effective frequency ω_{eff}. In the case of frozen boundaries, we find small deviations whereas with periodic boundary conditions, both values are less than 1% apart. When comparing the two 10000-particle systems with each other, deviations are found to be considerably smaller than between the respective 2500-particle systems. A reason might be that the fixed 2500-particle system consists of only 1034 free particles, which might be too small eventually. However, a comparison of the 10000-particle system with fixed boundaries with the two 2500-particle systems with periodic boundaries shows that they are in very good agreement, as the participation numbers of the large system are bracketed by the participation numbers of the smaller systems.

This survey clearly shows that with our system size of 2500 particles the transition states we compute are universal, i.e. independent of system size and boundary conditions. Additionally, the orientation of the transition state only marginally affects its thermodynamically relevant properties, such as the energy barrier and the effective frequency.

5.5 Connection to continuum elasticity

The first question which arises is whether it is possible to describe a system consisting of individual particles using means of a continuum theory. As a first test, we take our system, fix its outer boundary, displace the central particle and fix it at its new position. Then, we let the rest of the system equilibrate and measure the resulting virtual force on the displaced particle. The results are shown in figure 5.7, where we collected data for several values of the screening parameter μ. The forces vary over several orders of magnitude,

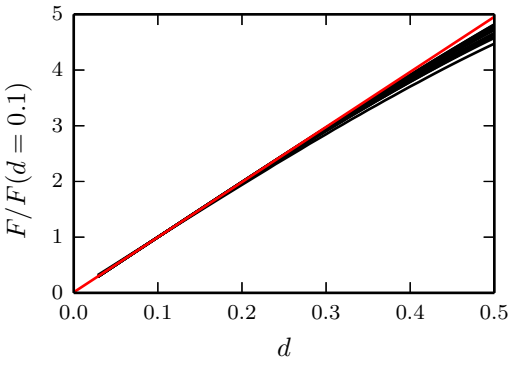

Figure 5.7: Dependence of the forces on the central particle as function of the prescribed displacement (black lines). Each line corresponds to a different value of the screening parameter in the range from 2 to 12. For comparability, they have been normalized by $F(d = 0.1)$. The linear relation (red line) observed at small displacements is lost for larger displacements, irrespective of the screening parameter.

which is why we rescaled them by their value for a displacement of $d = 0.1$. For small displacements, we find a linear dependence of the forces, indicating that we are in a linear regime which obeys Hooke's law. For larger displacements, we see a small deviation from the linear behavior with forces being smaller than expected. Most likely, this is due to the breakdown of the exact crystalline symmetry and a mismatch inherent to the setup: we relate the force at the displaced position to a displacement at the origin, in contrast to a continuum theory where both points coincide.

However, the results for small displacements confirm that application of a linear continuum theory might be possible. Therefore, we will now discuss the connection to continuum elasticity in more detail.

5.5.1 Linear elasticity theory

Before moving on with our analysis, we have to establish some definitions of linear elasticity theory, the notation follows Weinberger et al. (2005)[3]. For instance, the Cartesian coordinates x, y, z are identified by 1, 2, and 3. In favor of a more compact notation, partial derivatives are shortened, $\frac{\partial A_y}{\partial x} \equiv A_{y,x} \equiv A_{2,1}$. Throughout this section, Einstein's convention is used for summations.

Stresses

Stresses are described by the stress tensor σ_{ij}. In a Cartesian frame of reference, it holds the forces per unit area on the i-face, pointing in the j-direction. On a surface with normal vector $\boldsymbol{n}$, we can thus determine forces per unit area with respect to the normal vector, called tractions $T_j = \sigma_{ij} n_i$. For an elastic body in equilibrium, the tractions have to be

[3]For a complete introduction on elasticity theory, we also refer to Landau and Lifschitz (1966); Oswald (2009)

balanced by body forces b_j,

$$\int_S \sigma_{ij} n_i dS + \int_V b_j dV = 0. \tag{5.8}$$

With the help of Gauss's theorem, we end up with

$$\sigma_{ij,i} + b_j = 0, \tag{5.9}$$

which has to be fulfilled pointwise throughout the solid. Since the stress tensor is symmetric, this gives us 3 equations for the 6 unknowns (or 2 equations for 3 unknowns in two dimensions, respectively), i.e. the equation cannot be solved at this point. Fortunately, it can be rewritten in terms of displacements, as will be shown further below.

Strains

The strain tensor ε_{ij} is a measure for the stretching of a solid. It is given by

$$\varepsilon_{ij} = \frac{1}{2}\left(u_{i,j} + u_{j,i}\right) \tag{5.10}$$

in the linear approximation. Here, u_i is the displacement in the i-direction. Following previous notations, the absolute displacement is denoted $d = \|\boldsymbol{u}\|$.

Generalized Hooke's law

In the linear regime, stresses and strains are related by a constant tensor,

$$\sigma_{ij} = C_{ijkl}\varepsilon_{kl} \tag{5.11}$$

where C is called the stiffness tensor. This linear relation between forces and displacements is often termed Hooke's law. At first glance, the stiffness tensor has $3^4 = 81$ entries (or $2^4 = 16$ in two dimensions, respectively). However, it obeys several symmetries, and in the case of an isotropic medium, only two independent constants remain:

$$C_{ijkl} = \lambda_L \delta_{ij}\delta_{kl} + \mu_L\left(\delta_{ik}\delta_{jl} + \delta_{il}\delta_{jk}\right). \tag{5.12}$$

Here, λ_L and μ_L are called Lamé coefficients[4], where μ_L is also known as the shear modulus, termed G in literature. Plugging this back into eqn. (5.11), we end up with a greatly simplified relation,

$$\sigma_{ij} = \lambda_L \delta_{ij}\varepsilon_{kk} + 2\mu_L \varepsilon_{ij}. \tag{5.13}$$

In order to sort out the coefficients in a more obvious way, we can rewrite the strain using the identity

$$\varepsilon_{ij} = \left(\varepsilon_{ij} - \frac{1}{2}\delta_{ij}\varepsilon_{kk}\right) + \frac{1}{2}\delta_{ij}\varepsilon_{kk}. \tag{5.14}$$

[4]We use the index L to distinguish them from the screening parameter μ defined earlier.

For the left part of the right-hand side, the trace vanishes, indicating that it only describes a pure shear. The right part, on the other hand, describes a homogeneous dilatation, as e.g. caused by an external isotropic pressure. Substituting it into Hooke's law, we find

$$\sigma_{ij} = (\lambda_L + \mu_L)\,\delta_{ij}\varepsilon_{kk} + 2\mu_L\left(\varepsilon_{ij} - \frac{1}{2}\delta_{ij}\varepsilon_{kk}\right) \tag{5.15a}$$

$$= K\delta_{ij}\varepsilon_{kk} + 2\mu_L\left(\varepsilon_{ij} - \frac{1}{2}\delta_{ij}\varepsilon_{kk}\right), \tag{5.15b}$$

with $K = \lambda_L + \mu_L$ the bulk modulus[5], and μ_L the already defined shear modulus, living up to its name in this representation. At this point, we are able to rewrite the equilibrium equation (5.9) in terms of displacements, which are easily accessible both from measurements and simulations,

$$\mu_L u_{i,jj} + (\mu_L + \lambda_L)\,u_{j,ij} + b_i = 0, \tag{5.16a}$$

or in vector notation

$$\mu_L \Delta \boldsymbol{u} + (\mu_L + \lambda_L)\,\text{grad div}\ \boldsymbol{u} + \boldsymbol{b} = 0. \tag{5.16b}$$

It is called the Navier-Cauchy equation. In two dimensions, this is a set of two equations and two unknowns. For further application, we can write down the equations explicitly. Let u_x and u_y denote the displacements in x- and y-direction, respectively. Then, we find

$$\begin{pmatrix} (2\mu_L + \lambda_L)\partial_x^2 + \mu_L\partial_y^2 & (\mu_L + \lambda_L)\,\partial_{xy} \\ (\mu_L + \lambda_L)\,\partial_{yx} & \mu_L\partial_x^2 + (2\mu_L + \lambda_L)\partial_y^2 \end{pmatrix} \begin{pmatrix} u_x \\ u_y \end{pmatrix} + \begin{pmatrix} b_x \\ b_y \end{pmatrix} = \begin{pmatrix} 0 \\ 0 \end{pmatrix}, \tag{5.16c}$$

which has to be fulfilled at any point of the solid. It is a linear partial differential equation so that linear combinations of solutions solve the equation as well. It is to note that the operator on the left-hand side is linear in the pair (λ_L, μ_L), i.e. the qualitative features of the solution only depend on the ratio of the Lamé coefficients μ_L/λ_L. For example, doubling (λ_L, μ_L) leads to halving (u, v) for fixed external forces.

An issue which has yet to be resolved is the question whether our system is isotropic. In the crystalline state, the system exhibits a trigonal symmetry, i.e. rotations in the plane about $2\pi/3$ leave the system invariant. As is shown e.g. in Slawinski (2010), this condition already suffices for the system to be isotropic. Another possibility would be to inspect the single-particle Jacobian $\mathbf{J}_{ii}$, eqn. (3.7b). Only considering next neighbors ($r_{ij} = 1$), J_{xx} and J_{yy} coincide, and hence the system is isotropic:

$$\begin{aligned} J_{xx} &= J_{yy} = 6\left[(\mu + 1)\,e^{-\mu}\right] - 3\left[\left(\mu^2 + 3\mu + 3\right)e^{-\mu}\right] \\ J_{xy} &= J_{yx} = 0. \end{aligned} \tag{5.17}$$

5.5.2 Determining elastic properties

In order to characterize the system, we determine its elastic coefficients. Since the potential is known analytically, it is possible to extract them from its second derivatives. In the next two paragraphs we will show how the bulk and shear modulus can be obtained.

[5] Throughout literature, only the three-dimensional case is considered where $K = \lambda_L + \frac{2}{3}\mu_L$

Bulk modulus

For an isotropic stress, e.g. the hydrostatic pressure, we can write $\sigma_{ij} = -p\delta_{ij}$. Plugging this into eqn. (5.15b) and summing over the diagonal yields

$$\sigma_{ii} = -3p = 3K\varepsilon_{ii}, \tag{5.18}$$

since the right part of eqn. (5.15b) vanishes. Equivalently, we can write

$$K = -\frac{p}{\varepsilon_{ii}}. \tag{5.19}$$

However, ε_{ii} is nothing more than the relative volume change $\Delta V/V$. For infinitesimal changes, this yields

$$K = -V\left(\frac{\partial p}{\partial V}\right), \tag{5.20}$$

i.e. the bulk modulus describes how much pressure is needed for a relative deformation of a body, which is why eqn. (5.20) also serves as a definition of K. At zero temperature, we have $dU = -pdV$ and thus

$$K = V\frac{\partial^2 U}{\partial^2 V}, \tag{5.21}$$

where the inner energy is given by the potential energy of the system. As a consequence, we have to rewrite $U = \Phi$ in terms of the volume V. To this end, we note that compressing the system is equivalent to a rescaling of the lattice spacing r_0, cf. eqn. (3.13). Hence, we can rewrite eqn. (3.3) in terms of the volume,

$$\Phi = \frac{N}{2}\sum_{n\neq 1}\hat{\sigma}_{1n}\frac{\exp\left(-\hat{\mu}\sqrt{\frac{V}{N\sqrt{3}/2}}r_{1n}\right)}{\sqrt{\frac{V}{N\sqrt{3}/2}}r_{1n}}. \tag{5.22}$$

Here, $\hat{\sigma}_{1n} = \sigma_{1n}r_0$ and $\hat{\mu} = \mu/r_0$ are the parameters of the potential, independent of the lattice spacing, and r_{1n} is the distance between the first and the n-th particle. A twofold differentiation with respect to the volume yields

$$\frac{\partial^2\Phi}{\partial^2 V} = \frac{N}{2}\sum_{n\neq 1}\hat{\sigma}_{1n}\frac{\exp\left(-\hat{\mu}\sqrt{\frac{V}{N\sqrt{3}/2}}r_{1n}\right)}{4\sqrt{\frac{V}{N\sqrt{3}/2}}V^2 r_{1n}}\left(\hat{\mu}^2\frac{V}{N\sqrt{3}/2}r_{1n}^2 + 3\hat{\mu}\sqrt{\frac{V}{N\sqrt{3}/2}}r_{1n} + 3\right). \tag{5.23}$$

Since we have to evaluate this term at $r_0 = 1$, it simplifies and we end up with an expression for the bulk modulus,

$$K = \frac{1}{\sqrt{3}/2}\frac{1}{2}\sum_{n\neq 1}\frac{\exp\left(-\mu r_{1n}\right)}{4r_{1n}}\left(\mu^2 r_{1n}^2 + 3\mu r_{1n} + 3\right). \tag{5.24}$$

Shear modulus

In order to determine the shear modulus, we consider the strain energy density function[6] W, which is the free energy density of the strained solid,

$$W = \frac{F}{V} = \frac{1}{2}\sigma_{ij}\varepsilon_{ij} = \frac{1}{2}C_{ijkl}\varepsilon_{kl}\varepsilon_{ij}. \tag{5.25}$$

From this, we can derive an expression for the components of the stiffness tensor,

$$C_{ijkl} = \frac{\partial^2 W}{\partial\varepsilon_{ij}\partial\varepsilon_{kl}}. \tag{5.26}$$

At zero temperature, the free energy equals the inner energy, $F = U - TS = U$, and we again end up with the task to compute second derivatives of the potential Φ. For instance, from eqn. (5.12) we can identify $C_{1212} = C_{2121} = C_{1221} = C_{2112} = \mu_L$. By definition, the strain tensor is symmetric, $\varepsilon_{12} = \varepsilon_{21}$. Plugging this into eqn. (5.25), we end up with

$$W = 4\left(\frac{1}{2}C_{1212}\varepsilon_{12}\varepsilon_{12}\right) = \frac{1}{2}\mu_L u_{1,2}^2, \tag{5.27}$$

where we used that $\varepsilon_{12} = \frac{1}{2}u_{1,2}$ for a strain solely along the x-axis. The corresponding distances between particles m and n are given by

$$r_{mn}(u_{1,2}) = \sqrt{(x_{mn} + u_{1,2}y_{mn})^2 + y_{mn}^2}, \tag{5.28}$$

with $x_{mn} = x_m - x_n$. Finally, we can compute the shear modulus as

$$\mu_L = \frac{1}{V}\frac{\partial^2\Phi}{\partial^2 u_{1,2}} = \frac{N}{V}\frac{1}{2}\sum_{n\neq 1}\frac{\exp\left(-\mu r_{1n}\right)}{r_{1n}^3}\times \\ \times\left[\frac{1}{r_{1n}^2}\left(\mu^2 r_{1n}^2 + 3\mu r_{1n} + 3\right)\left(x_{1n}y_{1n} + y_{1n}^2 u_{1,2}\right)^2 - (\mu r_{1n} + 1)y_{1n}^2\right], \tag{5.29}$$

which we have to evaluate at $u_{1,2} = 0$. Similarly, we might consider compressions along an axis, which corresponds to $C_{1111} = \lambda_L + 2\mu_L$ and $\varepsilon_{11} = u_{1,1}$.

With eqns. (5.24) & (5.29) at hand, we are now able to determine the elastic properties of the Yukawa crystal in dependence on the screening parameter μ. The results are shown in figure 5.8. In (a), we observe a decrease in all three elastic constants, λ_L, μ_L and K, over several orders of magnitude with increasing μ , thus describing a drastic decrease in material rigidity. However, this alone could simply be compensated by a rescaling of the inter-particle potential. As a result, the only effect of the variation of the screening length would be a change in time- and energy scales. The more important ratio μ_L/λ_L is shown in (b). It continuously increases with the screening parameter. This implies that for each value of the screening parameter, we have an intrinsically different system with a different elastic behavior. Accordingly, the ratio μ_L/K shown in the same figure varies as well: The system becomes relatively more rigid against shear.

[6] Landau and Lifschitz (1966, ch.1, §4); Oswald (2009, ch.4.1); please note that F denotes the free energy, and not the force.

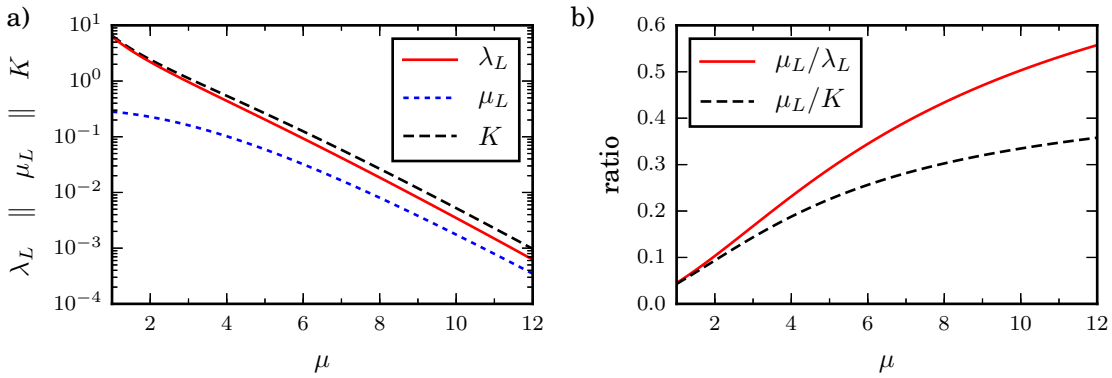

Figure 5.8: The elastic constants of the Yukawa-system, K, μ_L, and λ_L, in dependence on the screening parameter μ. (a) All three decrease with increasing screening parameter, describing a less rigid material. Please note that they vary over three orders of magnitude. (b) The ratios μ_L/λ_L and μ_L/K. They significantly increase with μ, indicating that the system not only changes its energy scale, but also its elastic properties with the screening parameter.

5.5.3 Singular force

So far, we have established the elastic constants corresponding to the Yukawa potential. However, since elasticity theory is a continuum theory, we still have to analyze whether it is suitable to describe displacements in the Yukawa-system which consists of individual particles. At the beginning of this section in figure 5.7, we observed a linear response of the Yukawa-system to small displacements. Here, we want to complement this by a comparison of the displacements obtained from both simulation and numerical solution of the elastostatic equations for the corresponding elastic constants. The easiest way to compare the two is to investigate the simplest disturbance one can think of: the displacement of a single particle, located at the center of the domain. To prevent body-movement of the whole system, the boundary conditions have to be adapted by keeping the outermost particles fixed at their positions.

Analytical solution

Before turning to the simulated system, we address a slightly more general problem, the singular force in an infinite isotropic solid. It is an instructive example that will give us an idea on how localization in two dimensions should look like. In three dimensions, the analytical solution is well known, cf. e.g. Landau and Lifschitz (1966, ch. 8). It is governed by an $1/r$ decay of displacements. The two-dimensional equivalent problem is that of a singular point force in the plane, which corresponds to a line force in an infinite solid. Finding the analytical solution is possible, e.g. by using Airy stress functions and Michell-solutions (Michell, 1899) or by following the solution to the three-dimensional problem as shown in appendix A.5. The displacement field for a force F_x acting solely in

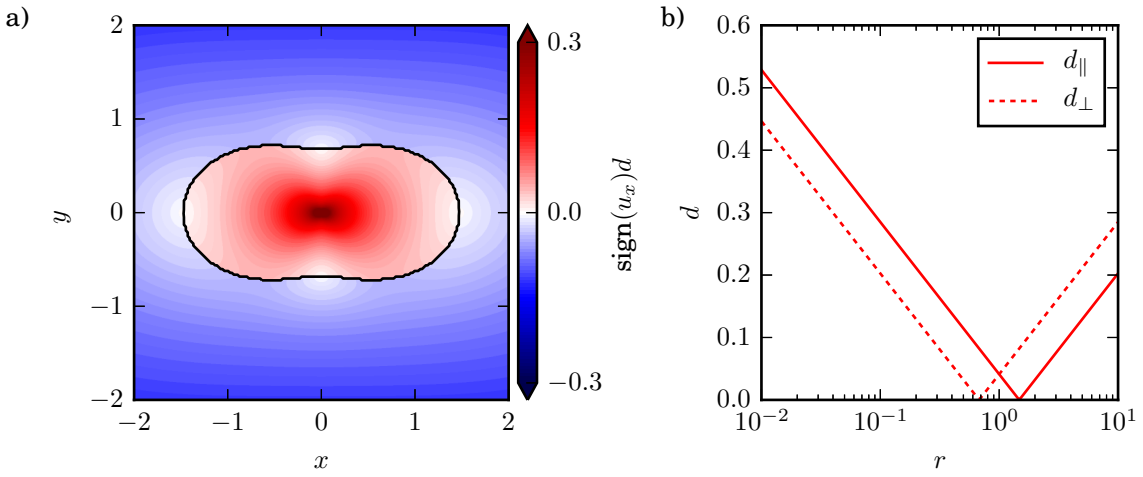

Figure 5.9: Displacements of the infinite medium subject to a singular force in the origin acting in x-direction, analytical solution. (a) The displacement field. Color coded is the absolute displacement $d = \|\boldsymbol{u}\|$, red for displacements with a component along the external force, and blue for an anti-parallel component. The black line indicates the distance where the behavior is reversed. We notice that displacements diminish faster in the perpendicular direction. This is confirmed in (b), showing total displacements along the axes parallel and perpendicular to the external force. All other displacements are found in the area enclosed by the two lines. Elastic constants correspond to $\mu = 3$, the external force is $F_x = 0.19$.

the x-direction is given by

$$\boldsymbol{u}(x,y) = \frac{\lambda_L + \mu_L}{2\mu_L + \lambda_L} \frac{F_x}{4\pi\mu_L} \begin{pmatrix} \frac{x^2}{r^2} - \frac{1}{2} - \frac{3\mu_L+\lambda_L}{\mu_L+\lambda_L} \log(r) \\ \frac{xy}{r^2} \end{pmatrix}, \tag{5.30}$$

where $r = \sqrt{(x^2+y^2)}$ is the distance from the origin where the singular force acts on. Expressing $x = r\cos\Theta$ and $y = r\sin\Theta$ in polar coordinates, we find that displacements u_y perpendicular to the external forcing are independent of the distance from the center, and determined by the angle relative to the forcing alone, $u_y \propto \cos\Theta\sin\Theta$. Similarly, displacements parallel to the external force comprise a constant, an angle-dependent part, and a radius-dependent part. A peculiarity is the logarithmic dependence, leading to a slow divergence of the displacements as r increases. Nevertheless, the displacement field fulfills eqn. (5.8) such that the tractions on any circle of radius R balance the external force at the center. The resulting absolute displacements are shown in figure 5.9(a). Close to the origin, the medium is displaced along with the external force, and the displacements diverge at the center. We also find regions where displacements disappear (black line in figure 5.9(a)), both along the axis of acting force and perpendicular to it. Beyond, we observe displacements against the external force. Along both coordinate axes displacements are parallel to the external force, and they diminish faster along the perpendicular axis. Naturally, the logarithmic decay and, ultimately, divergence is also reflected in the radial dependence of the absolute displacements in figure 5.9(b). We would expect a sim-

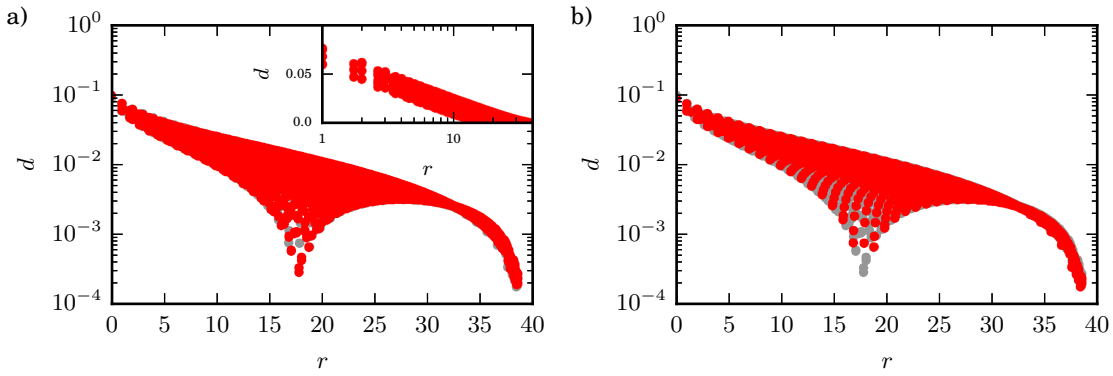

Figure 5.10: Displacements (red) for both the Yukawa system (a) and a solution of the elastostatic equations (b). Plotted in gray are the displacements of the opposite figure, verifying the excellent agreement between the two. The inset in (a) reveals the logarithmic decay of displacements, also found in the analytic solution, eqn. (5.30). External parameters: $r_{\text{fix}} = 38.55$, $d_0 = 0.1$, the corresponding force being $F_x = 0.19$. Elastic constants are $\lambda_L = 0.960$, $\mu_L = 0.161$.

ilar dependence when considering a finite system, though due to the imposed boundary conditions the displacements should drop to zero at the boundary.

Numerical solution and comparison to the Yukawa system

Analytical solutions of eqn. (5.16c) can be found for several special boundary conditions with respect to displacements, tractions, and body forces acting on the solid. In general, such solutions are hard to find and we take a different approach, we solve the equations numerically by discretizing the problem on a lattice. In order to fix the body in a solid frame, Dirichlet boundary conditions are invoked.

We discretize the derivatives using central differences on a square lattice. Since the global minimum of the two-dimensional system shows a hexagonal lattice structure, it seems appropriate to discretize the Navier-Cauchy equation (5.16c) on the hexagonal lattice as well, which is shown in appendix A.6. There, we also demonstrate some similarities between the resulting discretization matrix and the Jacobian of the Yukawa-system. In order to solve the matrix equation, we use an iterative Seidel-scheme with over-relaxation. Convergence is achieved as soon as average changes per iteration are below 1×10^{-7}.

For the comparison, we consider a large system with particles fixed on their positions for $r_{\text{fix}} > 38.55$. In total, this results in approximately 5391 free particles. The domain size for the discretized Navier-Cauchy equation is set correspondingly, with Dirichlet boundary conditions at $r = 38.55$. As previously, in the first step we take the Yukawa-system, displace the central particle and measure the restoring force after all other particles have equilibrated. In the second step, we take this force and the elastic constants and solve the Navier-Cauchy equation. Figure 5.10 shows the resulting displacements as a function of the distance to the center r, both for the Yukawa system (a) and the elastostatic equations (b). Except for very small r, they are in perfect agreement. The discrepancy close to the center of deformation is most likely owed to the mismatch in positions of the displacement and

the restoring force, which are the original and displaced particle positions, respectively. More importantly, the first minimum in the distribution which is due to displacements along the axis perpendicular of the external force, is located at the exact same position in either case. Naturally, the second minimum, found along the axis parallel to the force, is determined by the boundary conditions where we prescribe zero displacements.

5.5.4 Approximating the transition state

After establishing the elastic properties of our system, we can now turn towards the transition state described earlier, the two-particle exchange. There, we observed a quadrupolar structure of the displacement field. Thus, we will compare the localization of displacements obtained in the Yukawa system to those of an isotropic solid with two singular forces acting in the center. In this course we interpolate the positions of the two central particles between the minimum and the transition state. For small deviations from the minimum, we expect the displacements to be in accordance with predictions from linear elasticity theory. However, close to the transition state, this might not be the case as non-linear effects become important.

Elastostatic equations

Again, we solve the elastostatic equations on a lattice, with the same boundary conditions as in the previous paragraph. We choose a lattice such that we can apply external forces or displacements at $(\pm 0.5, 0)$, as in the simulations. Since we only consider opposing forces and eqn. (5.16c) is a linear partial differential equation, we can superimpose any pair of forces using two basis sets of displacement fields, namely for forces acting solely along the x-direction in one case, and along the y-direction in the other. The results for a unit force are shown in figure 5.11. Forces parallel to the connecting line (a) form a purely quadrupolar field: In the case of a compression of the medium along the x-axis, we observe a stretching along the perpendicular axis, and vice versa. Along the diagonals, displacements drop off considerably faster. On the other hand, forces acting perpendicular to the connecting line lead to a rotational displacement field (b). Displacements drop off more homogeneously, and they are strongest along the diagonals. Moreover, on short distances they drop off faster than for a singular force. The drop to 10% of the central displacement occurs within $r \approx 5$ instead of $r \approx 25$ (cf. figure 5.10). For both sets of external forces, this can be understood when considering the displacement fields themselves as a superposition of the displacement fields of two singular forces, separated by a small distance. In the first case, figure 5.11(a), along the y-axis all displacements parallel to the x-axis cancel out. This gives us the quadrupolar structure. For larger radii, the singular fields almost compensate each other which is why we see an overall decrease of displacements over four orders of magnitude. Similarly, in the second case, figure 5.11(b), radial displacements along the y-axis get canceled out. Along the x-axis, on the other hands, radial displacements are missing since both singular forces point in the perpendicular direction, cf. eqn. (5.30). Consequently, on the whole only the rotational part remains.

In both cases we observe that at the points where the external force acts on, displacements are parallel to the force. Hence, just as the forces, at the points of interest both

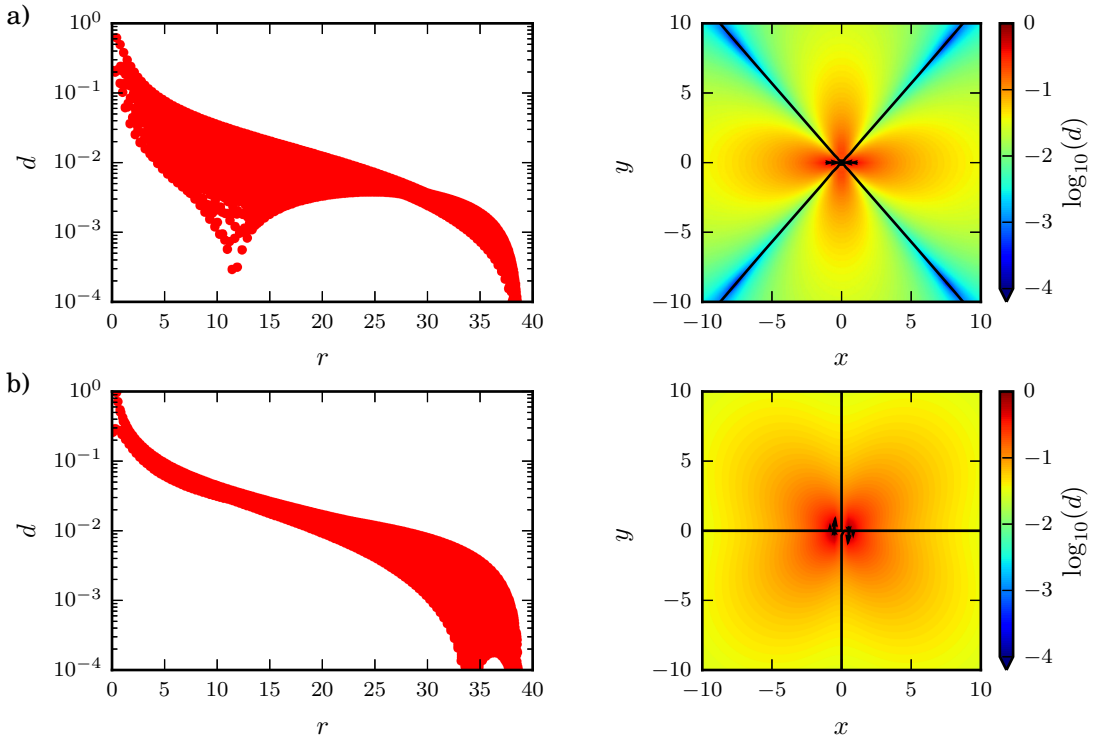

Figure 5.11: Displacements (left) and displacement field (right) due to the elastostatic equations with opposing forces acting at $(x, y) = (\pm 0.5, 0)$. (a) Forces act parallel to the connecting line (which is the x-axis), resulting in a quadrupolar field. (b) Forces act along the y-direction, leading to a rotational field. All deformations of the two central positions can be generated by superposition of the two solutions, either by prescribing the force or the displacements. Elastic constants are those of $\mu = 3$ in the particle system, $\|F\| = 1$.

displacement fields are decoupled. In the linear regime, this leaves us with two modes of operation for the simulations: We can either prescribe external forces and determine the displacement field, or put it the other way round and prescribe the displacements, compute the corresponding equilibrated configuration and extract the resulting forces on the displaced particles.

Simulation

We start the simulations by prescribing the same forces on the two central particles as in the previous paragraph, parallel ($\boldsymbol{F}_\parallel$) and perpendicular ($\boldsymbol{F}_\perp$) to the connecting line. For simplicity, we assume that both particles are oriented along the x-axis. However, in order to remain in the linear regime and obtain reasonable results, we have to reduce the magnitude of the forces. For small forces, the results of an elastic medium, figure 5.11, are reproduced exactly. Figure 5.12 shows the displacements of one of the two central particles, in dependence on the acting force. When considering only small forces in figure 5.12(a), the

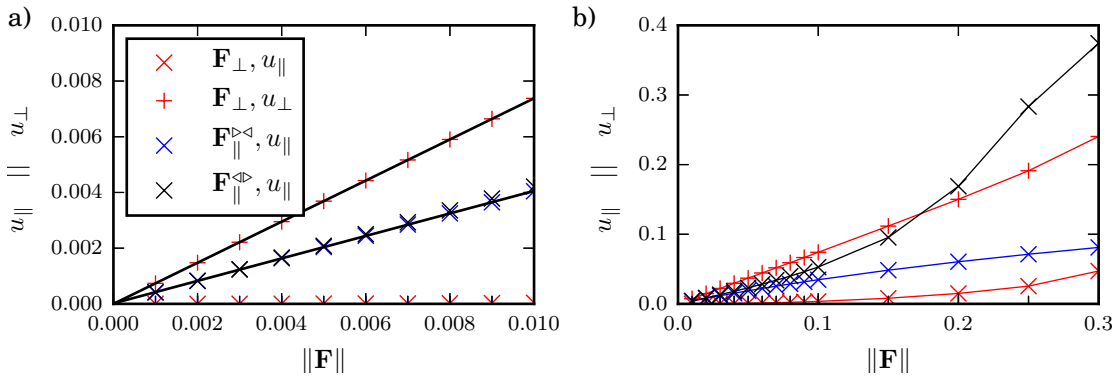

Figure 5.12: Components of the displacement vector $\boldsymbol{u}$ of a central particle due to two singular forces acting on particles at $(x, y) = (\pm 0.5, 0)$, aligned parallel ($\boldsymbol{F}_\parallel$, $u_\parallel$) or perpendicular ($\boldsymbol{F}_\perp$, $u_\perp$) to the connecting line. (a) For small external forces the linear relationship is recovered (black lines) and displacements are parallel to the force. (b) For larger forces, this is no longer the case: Depending on whether particles are pushed towards each other ($\boldsymbol{F}_\parallel^{\triangleright\triangleleft}$) or apart ($\boldsymbol{F}_\parallel^{\triangleleft\triangleright}$), the displacements differ. Moreover, the displacements due to $\boldsymbol{F}_\perp$ are not parallel to the force ($\times$, $u_\parallel \neq 0$).

linear relationship (black line) is recovered with the resulting displacements being parallel to the force. We distinguish between forces parallel to the connection line and towards each other $\boldsymbol{F}_\parallel^{\triangleright\triangleleft}$, and away from each other $\boldsymbol{F}_\parallel^{\triangleleft\triangleright}$. As would be expected in the linear regime, for $\|\boldsymbol{F}\| < 0.005$ both lead to the same displacements. Only for larger forces the displacements towards each other are slightly reduced. For forces $\|\boldsymbol{F}\| > 0.01$, figure 5.12(b), the linear relationship is gradually lost. For instance, for $\boldsymbol{F}_\perp$ we observe displacements perpendicular to the force, i.e. parallel to the line connecting the two particles. This is caused by the simultaneous motion of both particles, leaving a void at the origin and thus disturbing the force balance along the x-direction. The displacements due to the parallel forces $\boldsymbol{F}_\parallel^{\triangleright\triangleleft}$ and $\boldsymbol{F}_\parallel^{\triangleleft\triangleright}$ largely deviate from one another. The reason is found in the crystalline structure: Upon compression, the two particles get close to each other, with the inter-particle forces rising rapidly. In the opposite direction, on the other hand, the configuration is less rigid since other particles are able to make way and form voids, even enhancing the displacements as is seen in the strong increase for $\boldsymbol{F}_\parallel^{\triangleleft\triangleright} > 0.1$.

From these results, it seems unpromising to describe the transition state itself by an elastic field, moreover since close to the transition state forces vanish and their prescription in relation to the minimum positions is of no use. Nevertheless, in the next step we gradually shift from the global minimum towards the transition state of the two-particle exchange. To do so, we prescribe positions of the two central particles which eventually exchange their places by

$$\boldsymbol{x}_{\{1,2\}} = \boldsymbol{x}^0_{\{1,2\}} + \delta \left(\boldsymbol{x}^{\mathrm{TS}}_{\{1,2\}} - \boldsymbol{x}^0_{\{1,2\}} \right), \tag{5.31}$$

with δ varying between zero and one, and $\boldsymbol{x}^0_{\{1,2\}}$ and $\boldsymbol{x}^{\mathrm{TS}}_{\{1,2\}}$ the positions of the two exchanging particles at the minimum and transition state. We then determine the relative equilibria of the free particles and the corresponding forces acting on the locked ones. In

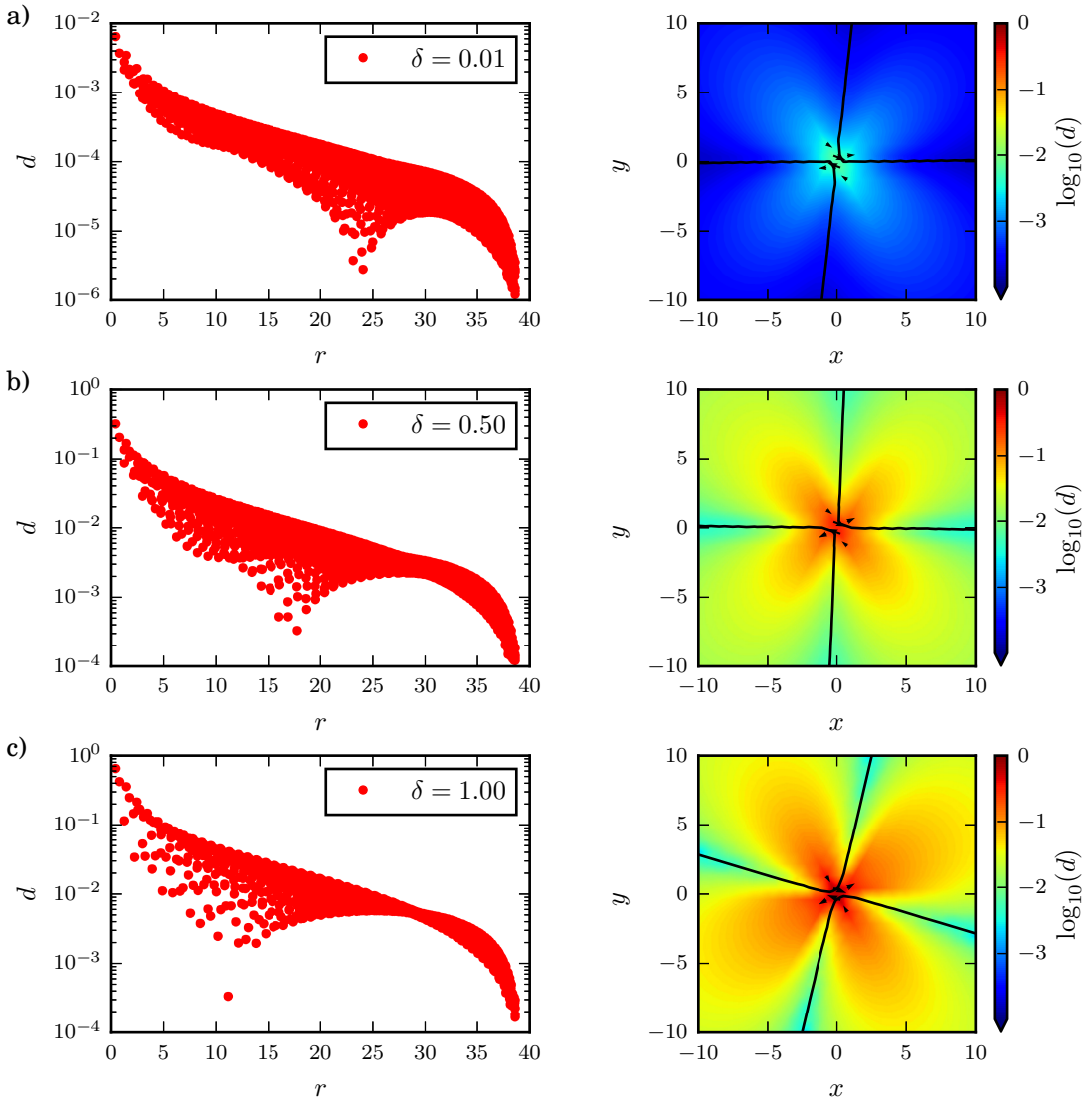

Figure 5.13: Displacement of the simulated Yukawa system at $\mu = 3$, with the two central particles shifted according to eqn. (5.31). The left column shows the displacement distribution whereas the right column shows the displacement fields with colors representing the magnitude and arrows visualizing the largest displacements. (a) For small $\delta = 0.01$, the system is slightly out of the linear regime. The field exhibits a weak quadrupolar structure and a rotational part. (b) With increasing δ, the first minimum of the distribution shifts towards lower distances. The rotational part of the field shrinks whereas the quadrupolar part grows. (c) At the transition state ($\delta = 1.0$), the rotational part of the field vanishes. In each case, we observe a faster decay of displacements than for a singular force, as would be expected in linear elasticity theory.

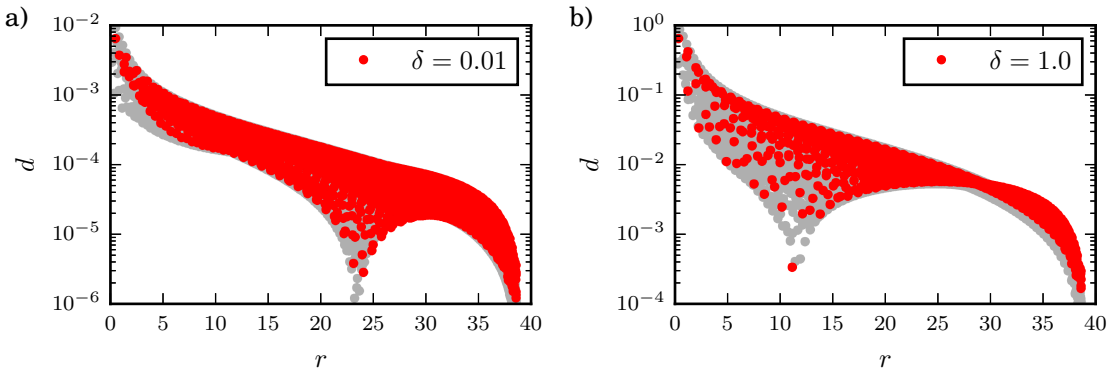

Figure 5.14: Comparison of displacements between simulation (red) and an elastic solid (gray). (a) For configurations close to the minimum, $\delta = 0.01$, both distributions agree well except for short distances. (b) At the transition state, the displacements can be modeled by two singular forces acting along the line connecting the two central particles. Free parameters are the magnitude of the external force and the distance between the points the forces act on. For this specific example we took $\|\boldsymbol{F}\| = 1.4$, with forces acting parallel at $(x, y) = (\pm 0.5, 0)$.

figure 5.13, we see the displacement distributions and fields, starting close to the minimum and approaching the transition state. With increasing δ, we see a shift of the first minimum to shorter radii. Additionally, the primarily sharp distribution washes out. This can be understood when considering the displacement fields. Getting closer to the transition state, a quadrupolar structure emerges, where particles are pushed outwards along one direction and pulled inwards along the perpendicular one. Both directions show large displacements, but with opposing directions. Therefore, on the bisectors the displacements have to reverse their radial components. Furthermore, the field displays a rotational part for small δ, as can be seen in the right panel of figure 5.13(a): In addition to their radial component, the outer arrows also have an angular one. The angular part diminishes when getting closer to the transition state at $\delta = 1.0$, where the field shows no considerable rotational part anymore.

It is to note that even at $\delta = 0.01$ the system is out of the linear regime. A first indicator are the lines of vanishing radial displacement in figure 5.13(a), which are not perpendicular to each other. A superposition of the fields of figure 5.11, weighted by the extracted forces on the two prescribed particles, only leads to an agreement in the far field but is amiss at short distances. Both distributions are also compared in figure 5.14(a). The reason for the discrepancy on short distances is due to the formation of voids. While this is not covered by elasticity theory, particles in the simulation will fill in the gaps. Consequently, displacements are enhanced compared to the elastic solid. However, since the strongest displacements also determine the displacements farther away, we nevertheless observe a very good agreement for $r \gtrapprox 5$.

At the transition state, shown in figure 5.13(c), the situation is a bit different. Naturally, since this configuration is an equilibrium, no forces act on the two central particles and the superposition of the base fields as described before is impossible. Nevertheless, we

observe the quadrupolar structure similar to the base field in figure 5.11(a). Additionally, the bisectors where radial displacements vanish are perpendicular to each other, indicating that a linear superposition might be possible after all. A similar structure of the far field was also observed by Dasgupta et al. (2012, 2013), who investigated plastic events in granular media. They modeled it with the help of elastostatics, using ellipsoidal deformations for the close proximity of the events. They lead to the quadrupolar displacement fields observed earlier. Here, we can adopt a similar approximation, which in turn is more versatile and should be applicable to more complex structures as well. A close comparison of figure 5.11(a) with figure 5.13(c) reveals that qualitatively, both the transition state and the parallel forcing share the same distribution. However, close to the center the crystalline structure is broken and an elastostatic description is pointless, in particular due to the transition state being unstable. Nevertheless, in the far field the elastostatic description still holds, and there we can model its displacement field by the displacement field induced by two singular forces as in figure 5.11(a). Altogether, this leaves us with two free parameters, namely the magnitude of the external force and the distance between the two points of attack. Figure 5.14(b) shows a quick comparison between the distributions of the transition state and an elastic solid, loosely fitted. We observe a good agreement between the two of them. In contrast to Dasgupta et al., this description could be expanded for more complicated structures by adding additional singular forces. In the case of transition states, the obvious candidates for a positioning of the singular forces are the positions of the particles which exchange their positions, at the transition state. The direction of the forces has then to be determined such that the symmetry of the transition state and its displacement field is recovered, for example in opposing directions in the case of the two-particle exchange. Naturally, the more particles are involved, the more complicated this procedure becomes. Indeed, the displacement fields of larger reorganizations involving three and six particles were recovered qualitatively, using a superposition of three and six singular forces in an infinite solid, respectively. Although the boundary conditions do not match, it supports the general applicability of the method. Some exemplary results are shown in appendix A.7, figure A.4.

5.6 Summary

In this chapter, we have taken the step from the reduced back to the full system with 2500 particles. In order to determine transition states in the high-dimensional potential energy landscape, we introduced the edge tracking algorithm as a versatile tool. We demonstrated its application on the first transition to be investigated, the two-particle exchange. We analyzed the corresponding transition state with respect to its dependence both on boundary conditions and system size. As thermodynamical quantities do not change considerably, it has been verified that the system size of 2500 particles is sufficient, and boundary effects are of minor importance.

The hexagonal particle crystal can be described using the elastostatic description inherent to a continuous solid. The corresponding elastic constants have been extracted. They show that the screening parameter in the Yukawa-system is an adequate instrument to change not only energetic scalings but the elastic properties of the system as such.

However, the elastostatic description breaks down as soon as the crystalline structure is lost. This is the case at transition states, where particles exchange their positions and thus necessarily break up the hexagonal lattice. Yet, in some distance to the event, the crystal is still intact and there, the system still behaves like an elastic solid. Finally, we were able to model the displacements induced by the rearrangement at the transition state by the displacement field generated by two singular forces acting on an elastic solid, so that both displacement fields show good agreement.

6

Localized many-particle transition states

The technique discussed in the previous chapter can be readily applied to identify more complex transition states. Therefore, in the first part of the chapter the various obtained transition states are presented, along with the corresponding transitions and the displacement fields. Additionally, we discuss some of the most prominent features regarding their arrangement in configuration space. Further properties are discussed in more detail in the second part of this chapter. There, we focus on configurational aspects, for example the extent of their localization and neighborhood relations, as well as on features relevant for the dynamics of the system, such as energy barriers and transition rates. In the course of the section, we will also draw connections to both the low-dimensional model systems in chapter 4 and the MD-simulation discussed earlier in chapter 3. To complete our studies, in the last section we will investigate the dependence of various quantities on the screening length of the Yukawa potential. Special attention will be directed at a comparison with the parameter dependence of the melting temperature, determined both by simulations and theoretical predictions as for example with the Lindemann criterion.

6.1 Transition states

In this section we will briefly present the obtained localized transition states, showing the configurations in the vicinity of the particle exchange and the resulting displacement fields. A further analysis of properties of the transition states is found in the subsequent section. In our investigations, we considered possible transitions comprising up to 18 particles. For a number of nine or less exchanging particles, we investigated all possible single-loop transitions. For this purpose, we computed all unique exchanges by means of a self-avoiding walk on a hexagonal lattice. In the mentioned case of nine particles, this reduces the number of possible closed-loop transitions from 5000 to 37. For a larger number of participating particles, we only considered such transitions which seemed promising, e.g. highly symmetric ones or those where an analogue with an exchange of fewer particles exists.

In order to start the edge tracking algorithm, an appropriate set of initial conditions is required, and we adopted two different algorithms to obtain them. First, just as for the two-particle exchange, we used the spring algorithm described in the previous chapter, to gradually drive the system from one minimum to the other thereby prescribing the transition. Second, we considered the uphill algorithm of the activation-relaxation technique, eqn. (A.12). We implemented the proposed uphill step size of $\alpha = 0.15/\|\Delta \boldsymbol{x}\|$

(Barkema and Mousseau, 2001) and a time increment of $\Delta t = 0.05$. In contrast to the spring algorithm, it gives the particles more flexibility to leave the prescribed path. However, with more particles involved and thus contributing to $\Delta \boldsymbol{x}$, the algorithm becomes unreliable. In many cases it converges towards the same energetically low-lying transition state of only a few particles exchanging, irrespective of the initial displacements.

We will now briefly discuss the identified transition states which are sorted in ascending order of participating particles in figures 6.1 to 6.4. In favor of a concise representation, in this section only some special features of their displacement fields will be addressed. As in the previous chapter, each panel shows – from left to right – the transition, the transition state with the corresponding displacement vectors, and the displacement field. Color coded are the absolute displacements with respect to the starting minimum. Additionally, in some plots black lines indicate a displacement of $d = 0.025$ (dashed) and the vanishing of radial displacements (solid). Both are helpful to estimate the localization of a transition state. The naming convention is due to the number of participating particles, where the index refers to the order in which the (possible) transitions were investigated.

We start with the three-particle exchange 3_0 in figure 6.1(a). Here, three next neighbors which are arranged on an equilateral triangle rotate around their common center. Similar to the observations in the reduced model in chapter 4, the three particles are rotated by $2\pi/6$ at the transition state and the configuration shows a three-fold rotational symmetry. In contrast to the reduced system in figure 4.5(b), the surrounding particles are able to give way. Consequently, particles in extension of the tips of the triangle are pushed outwards whereas particles on the bisectors are pulled towards the center. The displacement field, right panel in figure 6.1(a), reflects the three-fold symmetry of the transition state. Indicated by a black line are vanishing radial displacements, and we observe a separation into six patches. The regions where particles are pushed outwards, namely to the upper left and right and to the bottom, are slightly larger than regions showing opposite behavior. Apparently, the transition state fits well into the periodic box and the compression below the center is met across the periodic boundary by a complementary expansion above the center. The same holds along the diagonals. As a consequence, distortions of the far field, as seen for the two-particle exchange in figure 5.4, are almost absent. Additionally, the transition state is better localized than the two-particle exchange: The region with displacements $d > 0.025$ is limited to a small area around the center of deformation. A similar transition occurs when considering an exchange of the nine particles located on the enclosing ring of next neighbors, shown in figure 6.3(b). This transition, 9_3, shows the same features, except for the structures being slightly larger.

In figure 6.1(b), we show the four-particle exchange, denoted 4_0. Although on short distances displacements are quite different from the two-particle exchange, their far fields show great correspondence and the quadrupolar structure is recovered. The same applies when we add two more particles to the transition, 6_1 shown in figure 6.1(a). Here, six particles arranged in two layers exchange their places. Alternatively, we can repeat the procedure already employed with three particles and consider the surrounding shell of next neighbors. In this case, ten particles are expected to exchange their positions and, indeed, a transition state is obtained, 10_4 shown in figure 6.3(e). Surprisingly, its displacement field seems to be as well localized as the one of the presumably smaller transition of only four particles. We can extent the ten-particle exchange by adding two more particles,

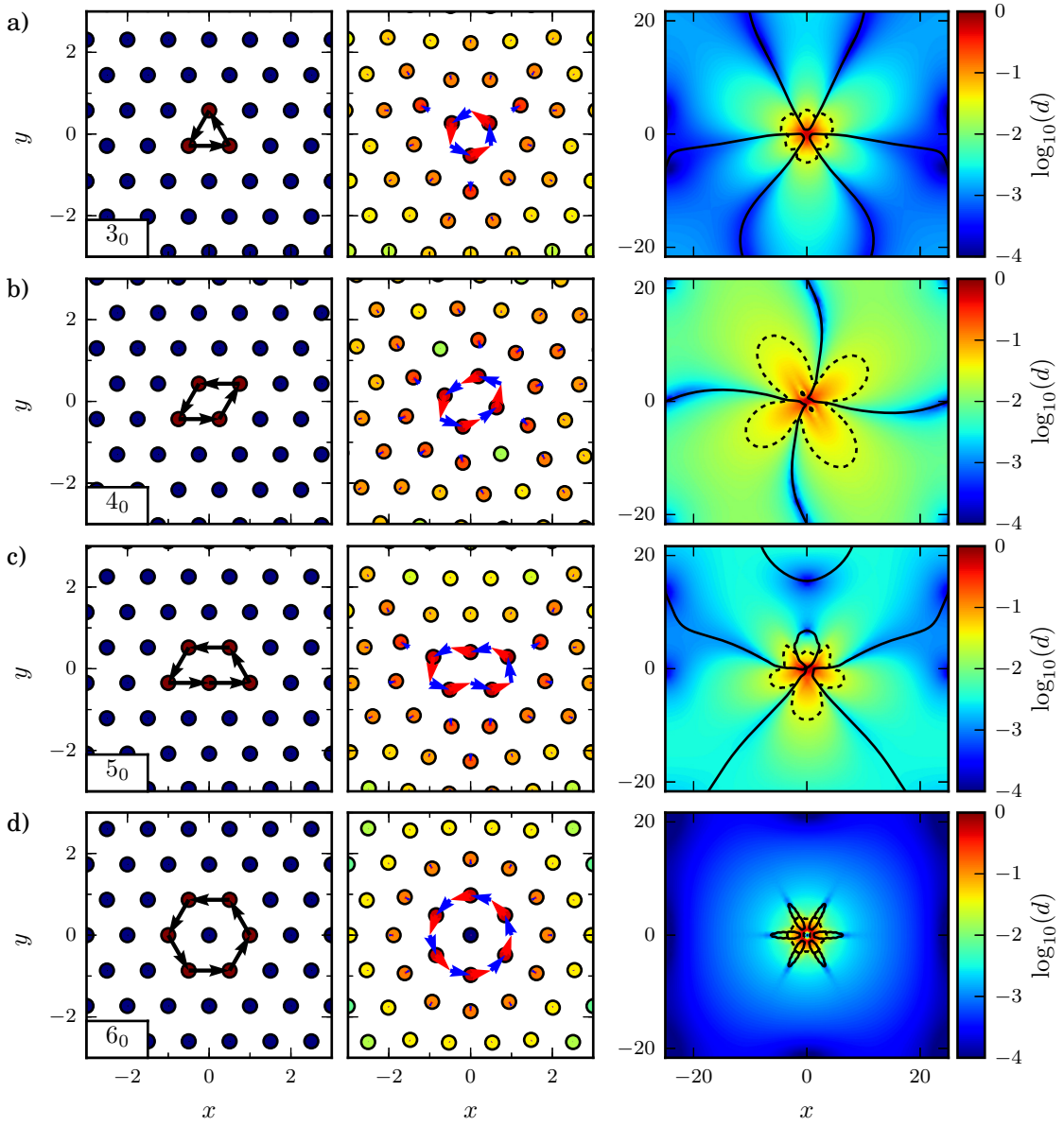

Figure 6.1: Transition States, pt. I. Plotted are particle positions, in particular the transition (left, indicated by arrows), the corresponding transition state (middle) along with the displacement vectors from the starting (blue) and to the second minimum (blue and red) , and its displacement field (right). Color coded is the logarithm of displacements with respect to the starting configuration. Solid black lines (if present) indicate vanishing radial displacements, dashed black lines a displacement of $d = 0.025$. Presented are (a) the three-particle exchange 3_0, (b) the four-particle exchange 4_0, (c) the five-particle exchange 5_0, and (d) the six-particle ring exchange 6_0.

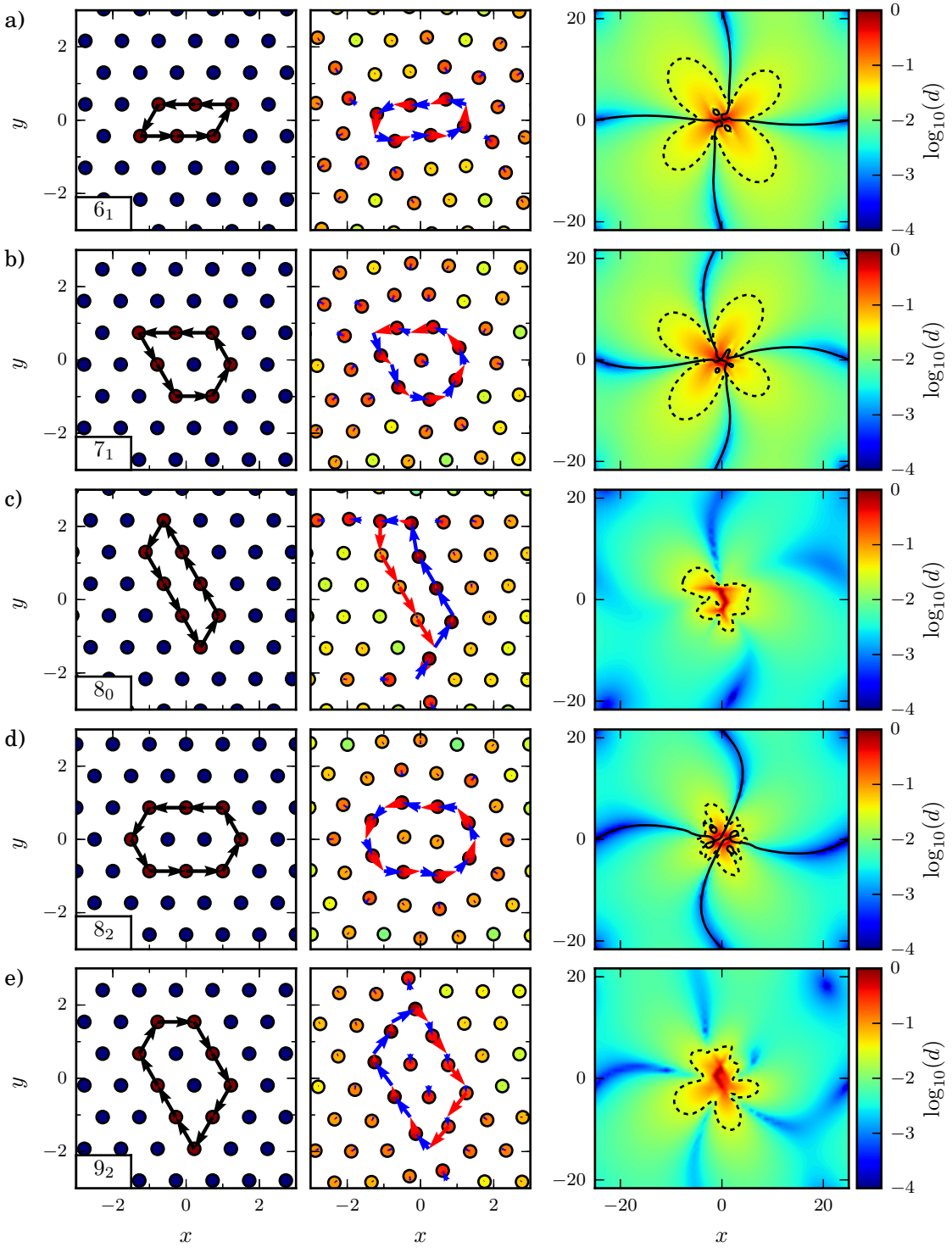

Figure 6.2: Transition States, pt. II. Details of the plots are the same as in figure 6.1. Presented are (a) the six-particle exchange 6_1, (b) the seven-particle exchange 7_1, (c) the eight-particle exchange 8_0, (d) the eight-particle exchange 8_2, and (e) the nine-particle exchange 9_2.

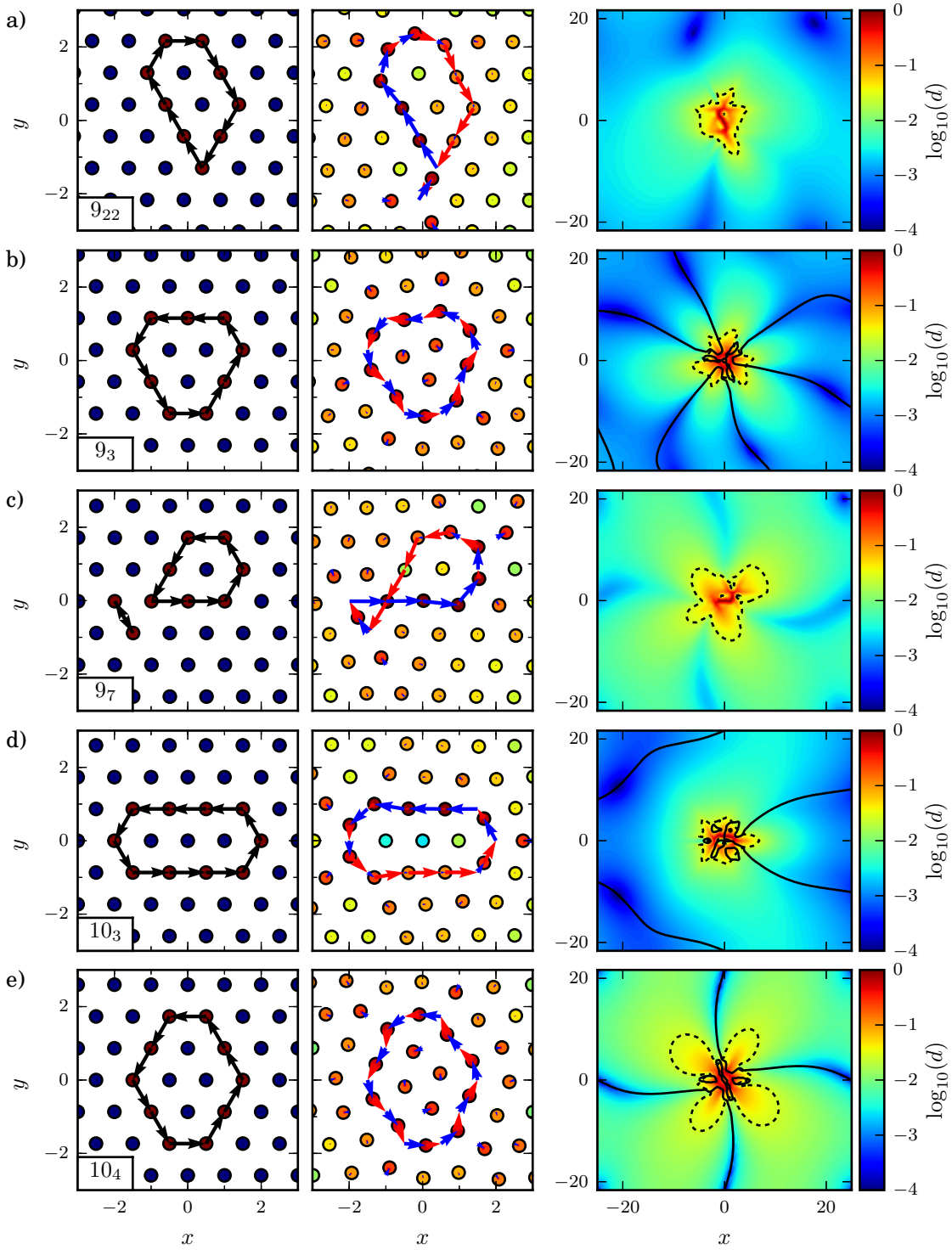

Figure 6.3: Transition States, pt. III. Details of the plots are the same as infigure 6.1. Presented are (a) the nine-particle exchange 9_{22}, which promotes the same transition as 9_2 in figure 6.2(e), (b) the circle exchange 9_3, (c) the combined seven- and two-particle exchange 9_7, (d) the ten-particle exchange 10_3, an elongation of 8_2, and (e) the ten-particle exchange 10_4, an extension of the four-particle exchange 4_0.

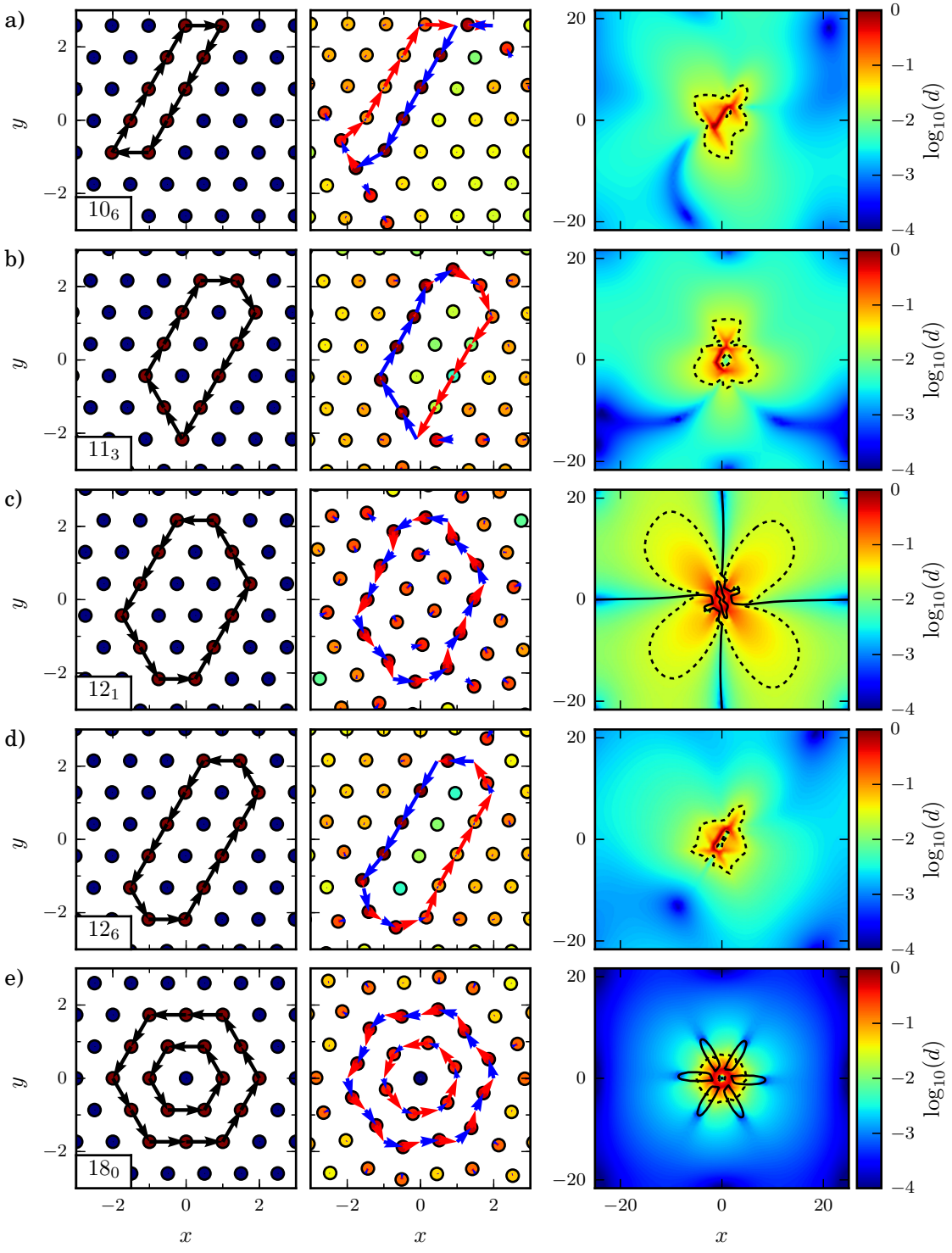

Figure 6.4: Transition States, pt. IV. Details of the plots are the same as in figure 6.1. Presented are (a) the ten-particle exchange 10_6, an elongation of the eight-particle exchange 8_0, (b) the eleven-particle exchange 11_3, (c) 12_1, an elongation of the ten-particle exchange 10_4, (d) 12_6, an elongation of the ten-particle exchange 10_3, and (e) 18_0, a rotation of 18 particles around their common center.

yielding the 12-particle exchange 12_1 in figure 6.4(d). The displacement field still shows the quadrupolar structure, though it is much less localized than its related predecessors.

In figure 6.1(c), the five-particle transition 5_0 is shown. Unlike the previous transitions, it has no rotational symmetry, yet the mirror symmetry of the transition is preserved in the transition state itself. Consequently, the displacement field is in the shape of a butterfly. Nevertheless, similar to the three-particle exchange, it exhibits three regions where particles are pushed outwards, and three regions where they are pulled towards the center, though one of them is very small, indicated by the solid black line above the center.

When considering fewer than six particles, each closed loop corresponds to a transition state. For six particles, four unique loops exist, and only for two of them the respective transition states exist, one of them, 6_1, discussed earlier. In figure 6.1(d) we present the six-particle ring exchange 6_0. Here, six particles located on the tips of a hexagon rotate around the unaffected central particle. Hence, the rotation at the transition state is about $2\pi/12$, and consequently the twelve particles on the outer ring of next neighbors are alternately pulled in towards and pushed out of the center. However, the displacement towards the center quickly vanishes (indicated by black lines) so that in total we observe a circular expansion. Combined with the boundary conditions this leads to a remarkably fast drop of the displacement field as seen by the dark blue coloring and the tiny region with displacements $d > 0.025$, indicated by dashed lines. Again, a similar transition exists when including the outer ring of next neighbors. However, in this case the next neighbors as well as the original six particles exchange their position, resulting in a rotation of two concentric rings of a total of 18 particles, 18_0 in figure 6.4(e). As expected, the displacement field is essentially the same.

In figure 6.2(b) we show a seven-particle exchange 7_1 where particles arranged like a droplet rotate around a central particle. Although it is not as symmetric as the previous transition states, it still shows a quadrupolar displacement field. However, as would be expected, displacements to the lower right and upper left show different extents, indicated by the dashed lines.

The eight-particle exchange 8_0 in figure 6.2(c) could be seen as another extension of the four- and flat six-particle exchanges 4_0 and 6_1. However, the associated transition state is distinctively different. It is the first one which consists of two separate steps, where in each step a row of neighboring particles is shifted. Consequently, at the transition state only half of the exchanging particles have been displaced substantially and the transition state itself is completely unsymmetrical. In contrast to previous transitions which exhibited a quadrupolar structure in the displacement fields, it is very well localized. As in previous cases a similar transition state is found for 10 particles, 10_6 in figure 6.4(a).

Figure 6.2(d) shows the eight-particle exchange 8_2 where eight particles forming a stretched hexagon rotate about two central particles. Again, the displacement field shows a quadrupolar structure, though displacements drop below $d = 0.025$ very fast. In close vicinity of this transition state a symmetric co-dimension two point exists. Its implications will be discussed further below. We can expand the transition along the longer axis by two or four particles, and we find again the corresponding transition states, 10_3 in figure 6.3(d) and 12_6 in figure 6.4(d). However, unlike in the previous cases where we added particles, the nature of the transition state changes: Instead of a rotation as for 8_2, we observe a two-step process in both transitions. In contrast to other two-step transitions, they show

a mirror symmetry.

In figure 6.2(e) and figure 6.3(a) we have the rare case that a single transition can be realized via two different transition states, 9_2 and 9_{22}. Both are two-step processes involving slightly different strings of particles. In the first case, the particle to the lower left of the lower tip moves into the emerging void, whereas in the second case, the particle to the lower right fills in the gap. Correspondingly, the displacement fields are rather different. For 9_2 in figure 6.2(e) we observe remnants of the quadrupolar structure, namely spirals of small displacements which connect across the cell boundaries. 9_{22} in figure 6.3(a) on the other hand is well localized, similar to the three- and five-particle exchanges. The similar transition comprising 11 particles, 11_3 in figure 6.3(b), results in yet another realization of the transition with the particle right of the lower tip moving into the void. Most surprisingly, while both the transition and the transition state are asymmetric, the displacement field shows a mirror symmetry along the y-axis.

Finally, in figure 6.3(c) we show transition state 9_7, a combination of a two- and seven-particle exchange, however in a coordinated process. It again is a two step event of two strings of particles being displaced subsequently. Unlike most other two-step transitions, the transition state shows the same mirror symmetry as the transition itself.

Besides the transition states discussed above, we investigated many more potential transitions. However, in the process of edge tracking they decomposed into a sequence of more fundamental exchanges where only a few particles change places at a time. Summarized, transition states can be classified into two categories: In the first case they describe a rotation of a patch of particles around a common center. This mostly applies to transitions of few particles or transitions which are highly symmetrical. In the second case a two-step process takes place where two strings of particles are shifted subsequently. We may take figure 6.4(a) as an example. In the first step, indicated by blue arrows in the figure, half of the exchanging particles form a string and move close to their new positions in a coordinated motion, whereas the other half remains close to their minimum positions. Beyond the transition state, when relaxing towards the other minimum (indicated by red arrows), the opposite process takes place and the particles which were barely affected by the first step shift towards their new minimum positions. Only a few particles close to the endpoints of the strings are largely displaced both on the way towards and away from the transition state, shown at the top and bottom in the figure in question. Consequently, the two-step transitions appear to show more complex rearrangements than their rotational counterparts.

6.1.1 Symmetry failure of the algorithm

In rare cases the edge tracking algorithm fails to converge towards a transition state and instead approaches a stationary point of higher co-dimension. In particular, this occurs when the latter configuration lies symmetrically in between two equivalent transition states.

An example of such a symmetry-induced failure occurs upon investigation of the eight-particle exchange, figure 6.2(c). We will discuss it with the help of figure 6.5. In the process of edge tracking, the algorithm closely follows the direct path between the minima, indicated in (a) by black arrows. It finally stops at the stationary state in (b) which is of co-dimension two and has a mirror-symmetry with respect to the x-axis. The actual

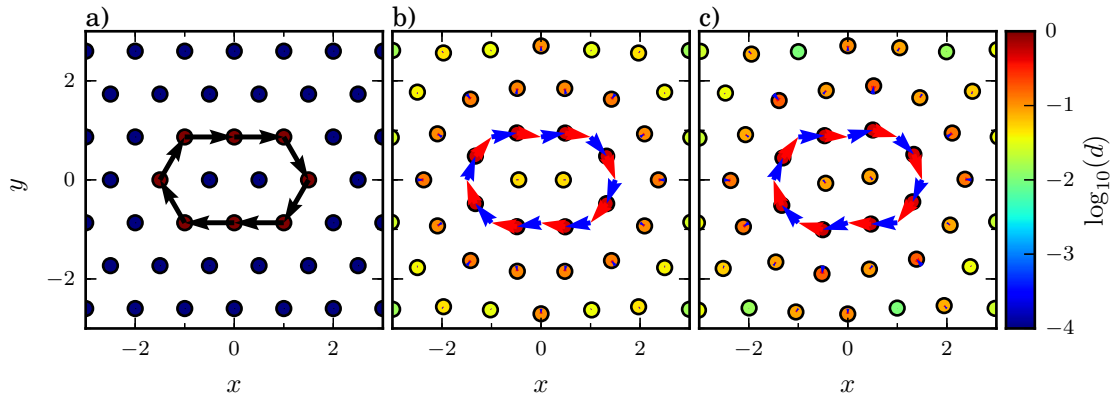

Figure 6.5: Example for a symmetry-induced failure. The edge tracking algorithm searching for the transition in (a) ends up in the symmetric state (b), which is of co-dimension two. The actual transition state is shown in (c): the particles aligned vertically left and right of the origin are sheared against each other, breaking the symmetry. Obviously, the mirrored counterpart exists as well.

transition state in (c) lacks this symmetry, the particles aligned vertically left and right of the origin are shifted down and up a bit. Obviously, the counterpart where rows are shifted up and down exists as well.

In order to break the symmetry of the stationary state in figure 6.2(b), we can add a random perturbation to the initial displacements. However, this might still leave us with a dead end: Suppose we generated two sets of initial conditions, one leading to either minimum. While the first set is displaced slightly towards the first transition state, the second set is displaced the opposite direction towards the second transition state. The edge tracking algorithm though will only capture the motion towards the minima and thus converge back towards the symmetric co-dimension two point. Nevertheless, even with those restrictions set aside, the algorithm will take many iterations to converge upon the transition state. This is caused by the unstable eigenvalues: Whereas the transition state has a single unstable mode of $\lambda^+ = 0.2224$, the symmetric state has two of them, $\lambda^+ = 0.2436$ and 0.0042. With the second mode being almost two orders of magnitude smaller, the separation of trajectories and thus the algorithm is dominated by the most unstable mode alone. To finally resolve the issue, we take the symmetric state and cautiously push it along the less unstable direction. In this specific case, this works well because the two corresponding eigenvectors are almost orthogonal at each individual particle position so that the procedure approaches the transition state and not the minimum configuration. After a few iterations, we get close to the transition state and can compute it, for example with the help of Newton's method.

6.2 Properties of the transition states

In the previous section, we only discussed the general shape of the transitions and their transition states and briefly touched the subject of localization when visually inspecting the

Table 6.1: Properties of the transition states. Summarized are the number of particles exchanging their positions N_{active}, type of the transition, rotational (R) or two-step (T) respectively, the participation numbers PN_k, energy barriers, effective frequencies $\omega_{\text{eff}}/2\pi$, and the unstable mode λ^+. Screening parameter is $\mu = 3$.

TS	FIG.		N_{active}	type	PN_2		PN_4		ΔE	$\max(\Delta E_i)$	$\omega_{\text{eff}}/2\pi$	λ^+
2_0	5.4		2	R	35.28	35.44	3.62	3.64	0.152002	3.16774×10^{-2}	2.849	0.282862
3_0	6.1	(a)	3	R	6.78	6.78	3.32	3.32	0.131697	2.57303×10^{-2}	1.588	0.381573
4_0		(b)	4	R	17.03	16.91	3.84	3.81	0.134654	2.14303×10^{-2}	2.698	0.338240
5_0		(c)	5	R	10.14	10.14	4.40	4.40	0.145820	2.51611×10^{-2}	5.064	0.258679
6_0		(d)	6	R	7.78	7.78	6.08	6.08	0.126960	1.64159×10^{-2}	1.534	0.206787
6_1	6.2	(a)	6	R	20.13	20.54	6.33	5.23	0.152303	2.49830×10^{-2}	12.718	0.226992
7_1		(b)	7	R	18.22	18.20	4.93	4.89	0.158477	1.69749×10^{-2}	12.188	0.267112
8_0		(c)	8	T	7.82	7.38	4.88	4.63	0.170925	2.73069×10^{-2}	95.205	0.063389
8_2		(d)	8	R	12.25	12.11	7.93	7.88	0.155073	1.63616×10^{-2}	12.655	0.222417
9_2		(e)	9	T	11.06	10.71	4.87	4.33	0.162975	2.62437×10^{-2}	44.119	0.027331
9_{22}	6.3	(a)	9	T	7.13	7.84	4.39	5.21	0.169105	2.47651×10^{-2}	35.422	0.034323
9_3		(b)	9	R	13.30	14.25	8.95	9.02	0.167324	1.98159×10^{-2}	11.029	0.132426
9_7		(c)	9	T	7.37	7.34	4.13	3.99	0.170136	2.70898×10^{-2}	69.391	0.002509
10_3		(d)	10	T	7.12	7.12	4.40	4.40	0.167501	2.44452×10^{-2}	21.100	0.043787
10_4		(e)	10	R	20.64	23.22	10.05	10.30	0.177886	2.05109×10^{-2}	17.314	0.107890
10_6	6.4	(a)	10	T	8.17	8.52	5.63	5.81	0.171027	2.78131×10^{-2}	118.398	0.052977
11_3		(b)	11	T	8.24	7.67	5.34	4.97	0.170103	2.66390×10^{-2}	53.207	0.030096
12_1		(c)	12	R	37.51	41.98	12.25	12.46	0.203076	2.18539×10^{-2}	98.955	0.095998
12_6		(d)	12	T	7.98	7.98	5.24	5.24	0.168501	2.52871×10^{-2}	24.541	0.023368
18_0		(e)	18	R	19.20	18.21	13.44	11.72	0.189911	1.77242×10^{-2}	61.916	0.118064

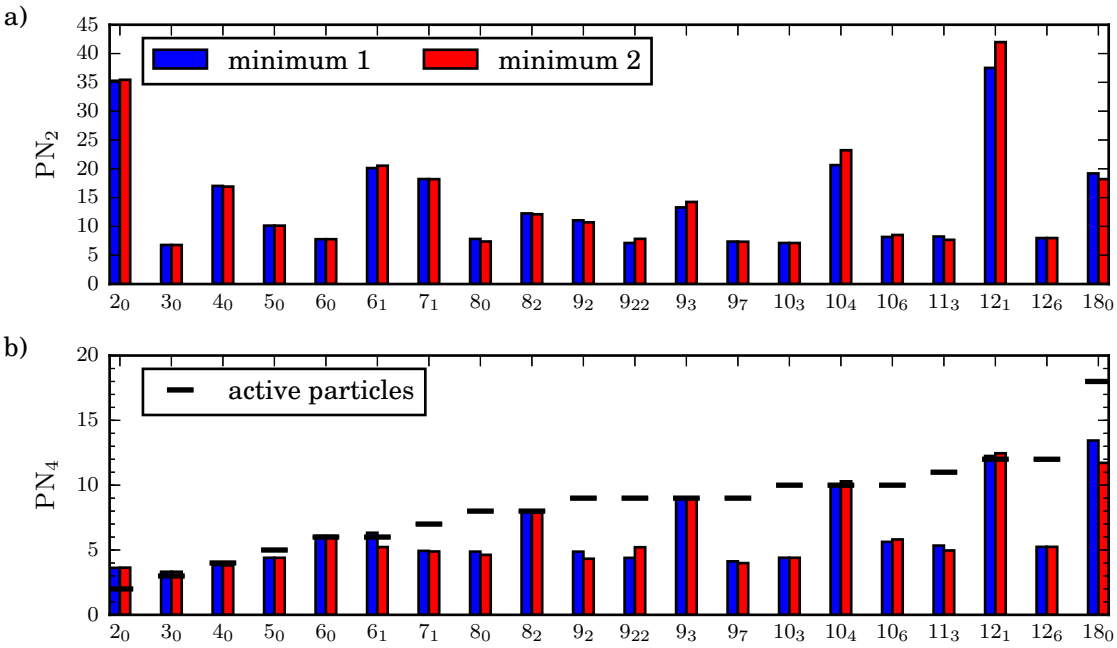

Figure 6.6: Participation numbers of the obtained transition states. Plotted are both PN_2 (a) and PN_4 (b). Colors indicate the participation number with respect to the two minima in question (blue and red). Since both minima are crystalline configurations, differences indicate non-symmetric transition states. PN_2 varies between 5 and 40, with no obvious pattern. PN_4 shows a more systematic behavior: It roughly corresponds to the number of active particles, i.e. particles exchanging their positions (black horizontal markers). For two-step transitions, PN_4 is considerably lower than the number of active particles.

displacement fields. In this section, we will discuss numerous properties of the transition states in more detail. We look into their localization and determine dynamically relevant quantities, for example the energy barriers and the associated transition rates. All relevant data such as effective frequencies, energy barriers and participation numbers are also summarized in table 6.1.

6.2.1 Localization

A good estimate for the localization of a transition state is its participation number, eqn. (5.6). They are shown in figure 6.6. Since a transition state connects two minima, we can compute one with respect to each minimum, color coded red and blue in the figure. In figure 6.6(a), we see PN_2. It varies between 5 and 40, showing no systematic behavior. A comparison with the displacement fields of the transition states reveals that it corresponds to the spatial extent of the displacements. It is largest for those states where displacements drop off slowly with $d_i > 10^{-2}$ over most of the domain, and smallest for the most localized states as e.g. the rotation of six particles. For some states the participation

number differs considerably depending on which minimum it is based on. This occurs whenever the transition state is not located symmetrically in between the two minima, an example being the two-particle exchange. The deviations are caused by the rectangular computational domain which prevents that states fit in perfectly symmetrically. While PN_2 estimates the impact of a transition state on the surrounding lattice, PN_4 shown in figure 6.6(b) only takes into account the most strongly displaced particles. Hence, it is closely related to the number of particles exchanging their positions, and for many transition states it actually characterizes this very well. However, for transitions showing a two-step process PN_4 is much lower. This is expected since only half of the exchanging particles are displaced substantially at the transition state, and hence the participation number is almost halved. The only exception where PN_4 is too large is the two-particle exchange, figure 5.4. There, PN_4 is twice as large as anticipated. As mentioned earlier, this is due to the fact that the exchanging particles have to be squeezed in between another pair of particles, which in turn are displaced substantially although they do not change places.

6.2.2 Neighborhood relations

The considered transition states connect different permutations of the global minimum. There, each particle has exactly six nearest neighbors. However, each of the configurations has different neighborhood relations. Therefore, during a particle exchange those relations have to break up. Accordingly, at the transition state some of the particles should have more or fewer neighbors, reflected in the coordination numbers. Those mismatches in the neighborhood relations are of particular interest, since we already saw in chapter 3 that they may be closely related to lattice defects which in turn promote the decay of lattice structures. In order to identify the defects at the transition state, we perform Delaunay triangulations. The results are shown in figures 6.7 and 6.8. Each neighborhood relation is indicated by a gray line. Additionally, color coding reveals the coordination number: red for particles with more than the expected six neighbors and blue for fewer neighbors.

The first observation is that defects only occur in a very localized region, close to the center of deformation. Beyond, the lattice structure remains unaffected. This would also be anticipated from the previous section and the displacement fields where we have seen that the transition states are well localized. Next, we notice that for most transition states, defects emerge on adjacent sites, often forming pairs of four to six defects. As a result, the effect of the dislocations on the whole lattice cancel out, leading to the strong localization. One exception is the two-particle exchange in figure 6.7(a) which consists of four isolated disclinations. Nevertheless, all four are close together and thus the defects have only minor impact on the surrounding lattice.

We can distinguish two different types of transition states. The first group are rotational transitions where dislocations are arranged on a closed ring. They are shown in figure 6.7. Each ring forms a grain boundary, with the inner particles constituting a small crystallite with different orientational order than the embedding lattice. In general, the crystallites show hexagonal order. An exception is the four-particle exchange in figure 6.7(c) which exhibits a rectangular lattice. The strength of the rotation varies, with the six-particle exchange in figure 6.7(d) showing the largest possible rotation of $\pi/6$.

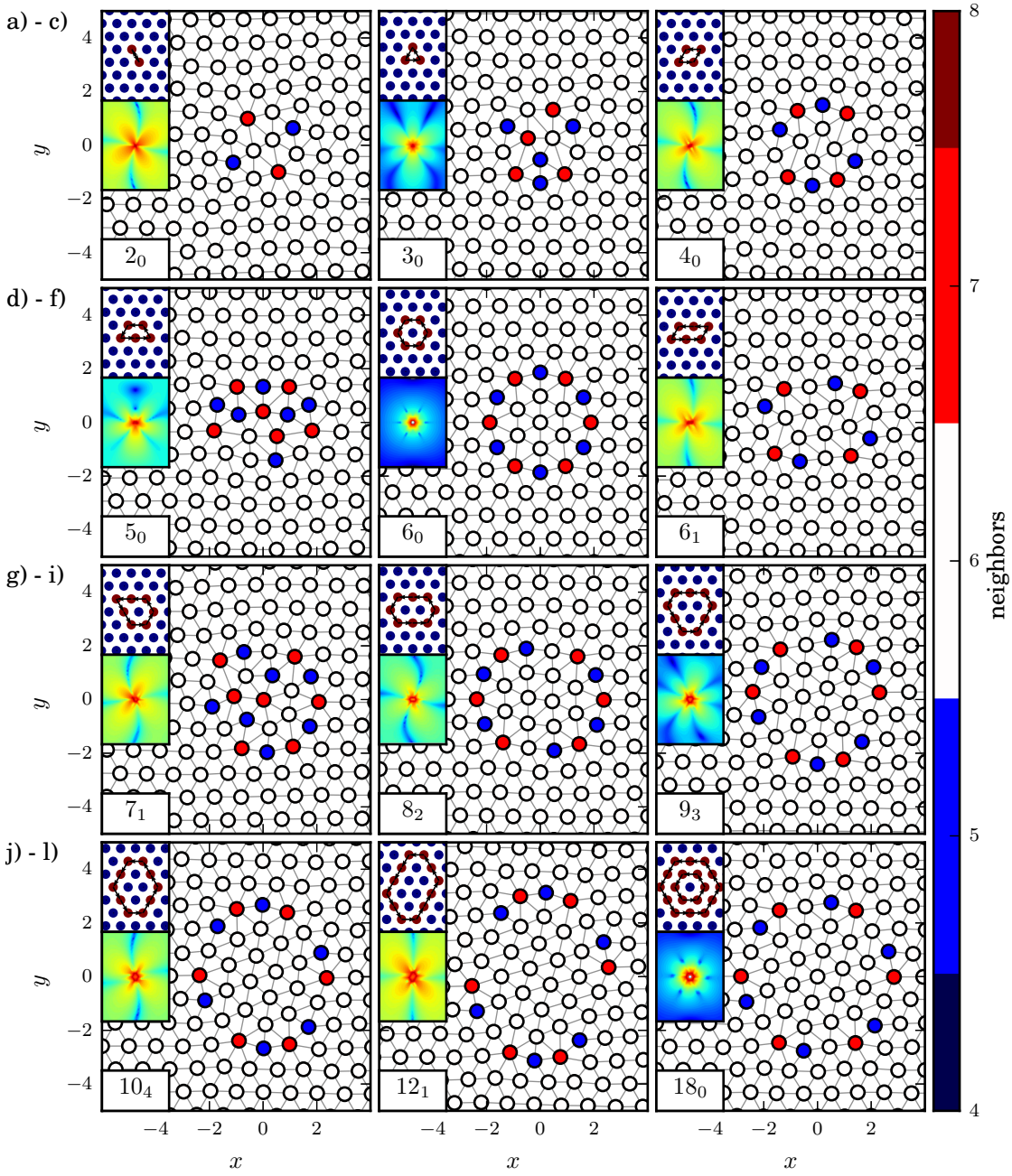

Figure 6.7: Delaunay triangulation (gray lines) of transition states for rotational transitions. Color coded is the number of next neighbors in relation to the coordination number of the hexagonal lattice $c_i = 6$. For reference, the insets show the corresponding transition (upper) and displacement field (lower) with displacements color coded as usual (cf. figure 6.1). The notations of the transition states are given in each lower left corner. Depicted are all transition states which form a temporary grain boundary, with the central patch rotated against the surrounding lattice.

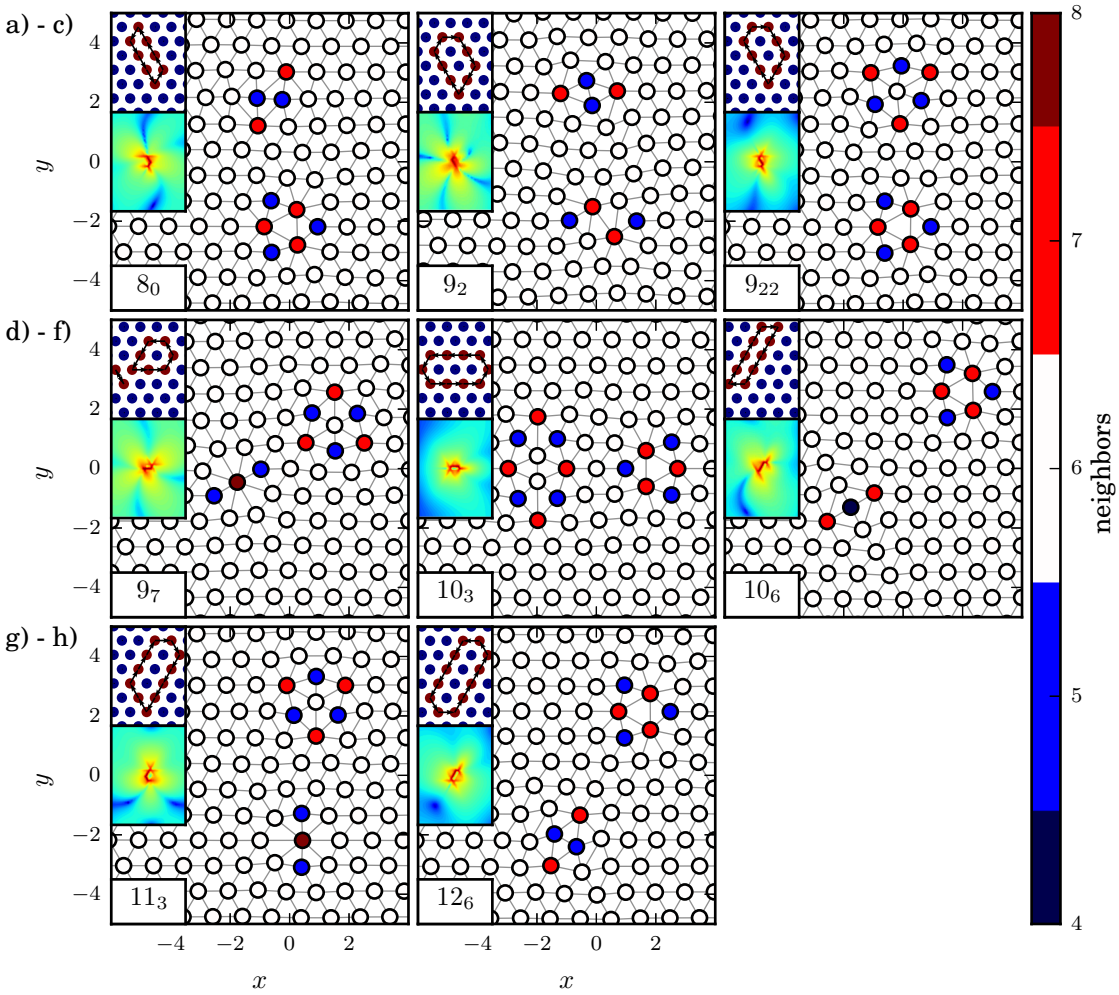

Figure 6.8: Delaunay triangulation (gray lines) of transition states for two-step transitions. The details of the plots are the same as in figure 6.7. Depicted are all transition states showing a two-step process. At the transition state, a temporary vacancy-interstitial pair is formed.

The second group of transition states is composed of two-step transitions, collected in figure 6.8. Here, we see the formation of a pair of an interstitial and a vacancy. We observe the stable defects discussed earlier in chapter 3 and shown in figure 3.12, namely split vacancies (SV), threefold symmetric vacancies (V_3), and threefold symmetric interstitial (I_3). Additionally, defects which would be unstable if considered alone emerge as well, for example a twofold crushed vacancy V_{2a} (figure 6.8(b)), deformed versions of the twofold symmetric interstitial I_2 (figure 6.8(a), (b), and (h)), a twofold symmetric interstitial I_4' (figure 6.8(e)), and an edge interstitial (figure 6.8(f)). The notation is due to Libál et al. (2007). This provides us with a mechanism to generate or destroy pairs of interstitials and vacancies. Instead of taking up one particle, and displace it over several lattice constants, and put it back down, the defect pair emerges by shifting a string of neighboring

particles. That way, the required excess energy to overcome intermediate barriers is greatly reduced. Yet, the pair is only metastable. An inspection of the spectrum of the transition states reveals that two-step processes are very slow in general, both compared with the rotational exchanges and the typical frequency of the crystal, the Einstein frequency $\omega_E^2 = 2.098$. Moreover, the defects themselves are very mobile, cf. chapter 3.2.7. Consequently, instead of returning to a minimum configuration and thus complete a transition, the two activated defects may separate, forming two isolated defects which are far enough separated to become stable on their own. Another mechanism would be the simultaneous occurrence of two transitions, resulting in a total of four defects where two of them might annihilate, one from each activated state. This would again result in a possibly stable distant vacancy-interstitial pair. Additionally, the transition states show that a minimum separation between opposite point defects is required. If they get closer than approximately five lattice constants, they become unstable and annihilate each other.

6.2.3 Energy barriers

The energy barrier of a transition state is a first indicator for its thermodynamical relevance. For temperatures much lower than the barrier, they pose unsurmountable obstacles. For temperatures well above, on the other hand, they merely constitute small modulations of an otherwise flat potential energy surface. The barriers are shown in figure 6.9, together with the maximum per-particle barriers $\max(\Delta E_i)$ and their relation to the mean per-particle barriers $\langle \Delta E_i \rangle_{k \in \{2,4,6\}}$. In general, the absolute barrier shown in figure 6.9(a) in blue grows moderately with the number of particles exchanging their position and is in the range $0.1 < \Delta E < 0.2$. It is roughly on the order of the single-particle equilibrium energy $E_i = 0.163674$. However, the likelihood to find the system at the higher energy is given by a Boltzmann factor where even small differences in the energy barrier can lead to drastic changes in the probabilities. Two noteworthy exceptions are the two-particle exchange, which has a considerably higher energy barrier than expected, and the six-particle hexagon rotation 6_0. It has the lowest energy barrier among all considered transition states, though MD-simulations suggest that it is not the most frequent transition. The transition states which lead to temporary formation of a vacancy-interstitial pair all have an energy barrier of approximately the same magnitude, $\Delta E \gtrapprox 0.17$, which is also close to the combined surplus energy of the two defects, as has been shown in section 3.2.7, and larger than the barriers of few-particle exchanges with a typical energy barrier $\Delta E \lessapprox 0.15$. This agrees well with the observations from MD-simulations where at low temperatures mostly few-particle exchanges are observed and only at higher temperatures the generation of vacancies and interstitials occurs.

The maximum per-particle barriers shown in red in figure 6.9(a) bring this down to a per-particle level. It varies between $0.015 < \Delta E < 0.03$. Not too surprisingly, the two-particle exchange has the highest per-particle barrier of all investigated transitions. In general, when comparing transitions with an equal number of active particles, it turns out that rotational exchanges have lower maximum per-particle barriers compared to transitions showing a temporary vacancy-interstitial formation. Two examples are the nine- and ten-particle exchanges 9_3 and 10_4, respectively. Seemingly, those transition states fit better into the surrounding lattice, showing smaller relative displacements and hence lower energy

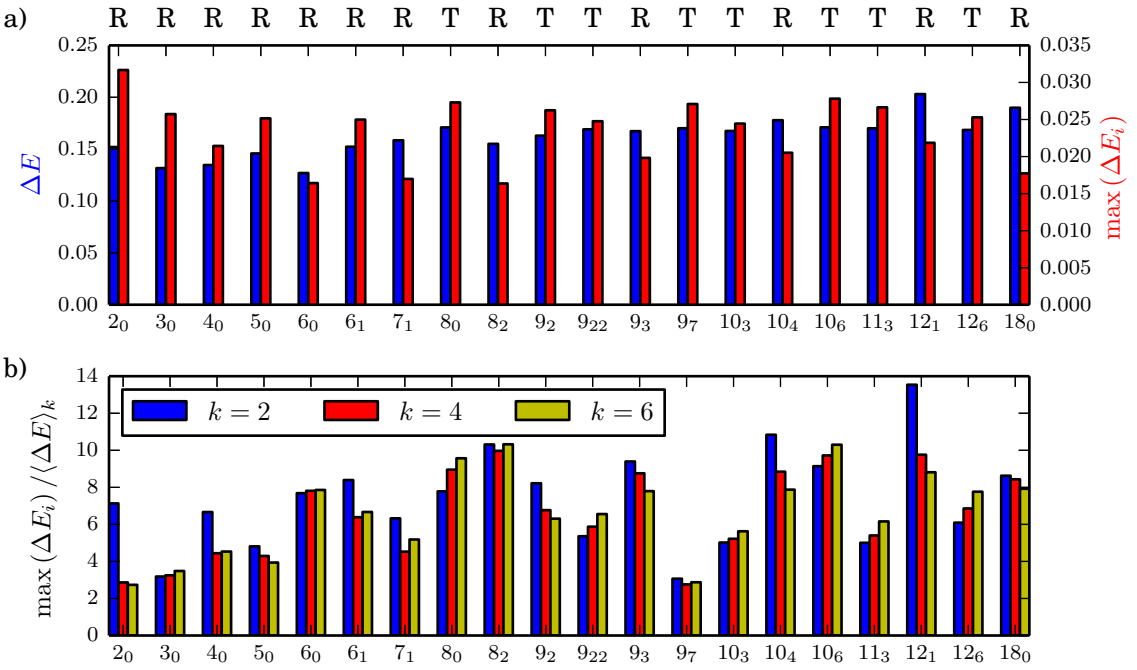

Figure 6.9: Energy barriers of the localized transition states. The characters at the top indicate whether a transition is a rotation (R) or a two-step process (T). In (a), the absolute energy barrier (blue, scale on the left) and largest per-particle barrier (red, scale on the right) are shown. In general, the absolute barrier grows with the number of particles exchanging their positions whereas the per-particle barrier shows no regular pattern. In (b) we relate the per-particle barriers to the weighted averages of the absolute barrier $\langle \Delta E \rangle_k$ (eqn. (5.7)).

barriers.

However, those quantities tell us little about how evenly the energy barrier is distributed among the particles. To this end, we consider the ratio of the maximum per-particle barriers to the average per-particle barriers, shown in figure 6.9(b). The average barriers are computed as weighted averages, eqn. (5.7), and we considered $k = 2$, 4, and 6, indicated as blue, red, and yellow columns. The higher the localization order k, the fewer particles are considered in the average, analogous to the participation numbers. At first glance, it is noteworthy that transition states of the same type and with similar energy barriers show very different distributions of the potential energy. This can be exemplified on transitions 10_6 and 11_3. Both involve two-step transitions, and both the absolute and maximum per-particle barrier are similar in magnitude. Nevertheless, in the eleven-particle exchange the excess energy is distributed more evenly among the particles. Moreover, we make two fundamentally different general observations, depending on whether we look at a rotational or a two-step transition.

For the rotational transition states we find that the ratio decreases with localization order, i.e. the average energy grows. The cause is the barrier energy being localized in the deformation, so that the mean increases when fewer particles are considered in the average.

The only exceptions are the three-particle, six-particle and eight-particle transitions (3_0, 6_0, and 8_2), where we observe a constant ratio or a very slight increase. This hints at an evenly distributed barrier.

For the two-step processes on the other hand, we find an increase of the ratio, i.e. the average energy decreases with the localization order. The reason is simply the nature of the transitions: At the transition state the potential energy of all exchanging particles increases due to relative displacements. At the same time, only half of them have been displaced considerably in reference to their minimum positions whereas the other half have remained fixed. The latter only contribute to the lower-order averages, and hence $\langle \Delta E_i \rangle_k$ decreases with k. The only real exception is the nine-particle exchange 9_2, figure 6.2(d). It shows a considerable decrease of the ratio, caused by a weak two-step behavior: All except of two particles are displaced substantially at the transition state.

6.2.4 Transition rates

Energy barriers do not determine the occurrences of particle exchanges alone, as transition state theory tells us. Another important aspect are the frequencies at which the system visits the different transition states. They determine the maximum attainable rates, which in turn are weighted by a Boltzmann factor of the respective energy barrier in relation to the system temperature. Therefore, in the following we will compute the rates at which each transition is expected to occur. We use the rate description of harmonic transition state theory, eqn. (4.8), and, since we investigate a system at low temperatures, the Kramers rate, eqn. (4.10), which also takes into account the unstable mode at the transition state. A short overview of the theory is given in chapter 4.1. Both descriptions have in common that they rely on the computation of the energy barrier and an effective attempt frequency,

$$\omega_{\text{eff}} = \frac{\prod_{i=1}^{n} \sqrt{-\lambda_i^{(0)}}}{\prod_{i=2}^{n} \sqrt{-\lambda_i^{(*)}}}, \tag{6.1}$$

with λ_i denoting the stable modes of both the minimum and the transition state. While the determination of barrier heights is a simple task, the computation of the effective frequency can be challenging, especially for large systems with $N > 2500$ particles. One might think of reduction methods as described by Brooks et al. (1995). However, they cannot be used for this system as pointed out in appendix A.8, and as a consequence the full spectrum of the $2N$-dimensional system has to be calculated. To this end, we use the Eigen3 package (Guennebaud et al., 2010). Additionally, special care has to be taken when evaluating eqn. (6.1): Both nominator and denominator are a product of $2N$ and $2N - 1$ frequencies. Therefore, in order to avoid canceling effects and preserve accuracy, the quotient has to be computed stepwise. This also prevents us from exploiting the computationally much simpler relation $\prod \lambda_i = \det(\mathbf{H})$.

Multiplicity of transitions

The rates obtained by transition state theory are only valid for one specific transition. On the other hand, our system consists of many identical particles, and so we have to consider

that each transition may take place at any position in the lattice. Moreover, since both minima are only permutations of each other, a transition may take place either in the forward (fw) or backward (bw) direction. Additionally, since the underlying lattice shows several symmetries, the transition can be oriented in different directions. At the same time, we have to correct for multiple counting due to the symmetry of the transition state itself.

Therefore, we classify the symmetry of the transition states by their point groups. In two dimensions, there exist two groups of discrete point symmetries: On the one hand we have the group C_k of cyclic symmetries of order k, and hence its elements are invariant under rotations about $2\pi/k$. The second group is the dihedral group D_k, whose elements are invariant under rotations about $2\pi/k$ and, additionally, under reflections of these images across one axis. The number of possible symmetry operations s is given by $s(C_k) = k$ and $s(D_k) = 2k$, respectively. For instance, a completely unsymmetrical state is of C_1 symmetry, i.e. it is invariant under rotations about 2π which map it onto itself. The hexagonal lattice, on the other hand, is of D_6 symmetry, corresponding to six rotations and six reflections. Naturally, this is the highest symmetry any configuration embedded in the hexagonal lattice can have.

Thus, we can compute the multiplicity of a transition n_i as follows: At each lattice position, we have $s(D_6) = 12$ possible symmetry operations. Since the transition state itself is invariant under some symmetry operations we have to take them into account, and combined we end up with

$$n_i = \{\mathrm{fw}, \mathrm{bw}\} \cdot \frac{s(\mathrm{crystal})}{s(\mathrm{transition\ state})} \cdot N, \tag{6.2}$$

where we also considered the two possible directions of the transition. The symmetry of the transition state is determined close to the center of deformation so that boundary

Table 6.2: Symmetries of the transitions (T) and transition states (TS), and the resulting multiplicity of the transition states, according to eqn. (6.2). It ranges from $2N$ for perfectly symmetric transitions to $24N$ for completely unsymmetrical ones.

Transition	Symmetry		n_i
	T	TS	
2_0	D_2	D_2	$6N$
3_0	D_3	D_3	$4N$
4_0	D_2	D_2	$6N$
5_0	D_1	D_1	$12N$
6_0	D_6	D_6	$2N$
6_1	C_2	C_2	$12N$
7_1	D_1	D_1	$12N$
8_0	C_2	C_2	$24N$
8_2	D_2	D_2	$12N$
9_2	C_1	C_1	$24N$

Transition	Symmetry		n_i
	T	TS	
9_{22}	C_1	C_1	$24N$
9_3	D_3	D_3	$8N$
9_7	D_1	D_1	$12N$
10_3	D_2	D_2	$12N$
10_4	D_2	D_2	$12N$
10_6	C_2	C_2	$24N$
11_3	C_1	C_1	$24N$
12_1	C_2	C_2	$12N$
12_6	D_2	D_2	$12N$
18_0	D_6	D_6	$4N$

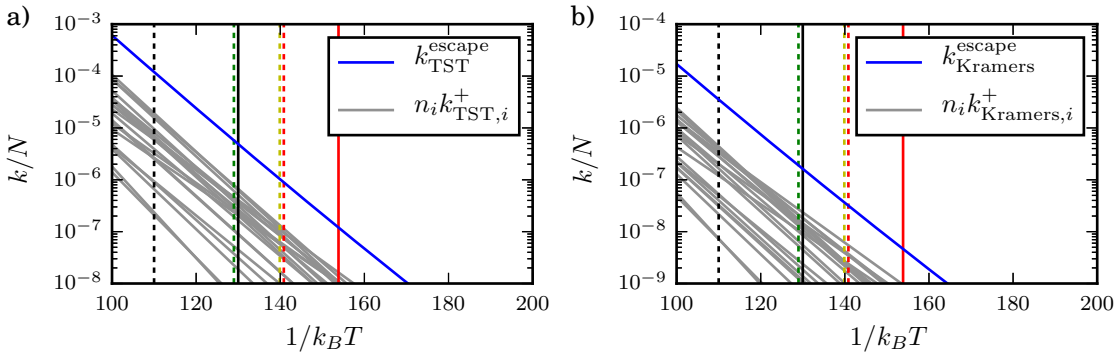

Figure 6.10: Rate at which any event will take place (blue line), according to harmonic transition state theory (a) and Kramers (b). Note that these are the rates per lattice site. The gray lines represent the different transitions. Vertical lines denote temperatures of melting (dashed), and crystallization or emergence of a hexatic phase (solid), determined by Zheng and Earnshaw (1998) (black; solid: crystallization), Hartmann et al. (2005) (yellow), and Vaulina and Koss (2014) (green). Our simulation results are plotted in red. For better comparability, the relative rates are shown in figure 6.11.

effects are neglected. As an example, the transition state of the two-particle swap in figure 5.4 shows a two-fold mirror symmetry D_2 close to the center and hence yields

$$n_2 = 2 \cdot \frac{2 \cdot 6}{2 \cdot 2} N = 6N. \tag{6.3}$$

The multiplicities of the transition states described previously are given in table 6.2, along with their symmetry classifications.

Combined rates

The total rate of escape, or more to the point the rate at which any event will occur, is then given as the sum

$$k_{\text{escape}} = \sum_i n_i k^+_{\text{TST},i}. \tag{6.4}$$

It is shown in figure 6.10 both for transition state theory- and Kramers rates. Additionally, vertical lines denote the critical temperatures of melting and crystallization as reported by Zheng and Earnshaw (1998), Hartmann et al. (2005), and Vaulina and Koss (2014) and as determined in chapter 3. As expected, with the damping taken from the simulations, the rate due to Kramers is over one magnitude smaller, though it depends on the specific damping in the system and might thus be altered. Depending on the reference, the critical rate at which melting occurs is inbetween $10^{-6} < k^{\text{escape}}_{\text{TST}} < 10^{-4}$ and $4\times10^{-8} < k^{\text{escape}}_{\text{Kramers}} < 4\times10^{-6}$, respectively. Rates drop quickly with decreasing temperature and are below 10^{-8} at $k_BT \approx 0.0055$ or $1/k_BT \approx 180$. Also shown in the same figure are the individual rates corresponding to each transition state (gray lines). Naturally, they are considerably lower and lie atop each other. For a given temperature, the rates span approximately two orders of magnitude, thus implying that some processes are more important than others.

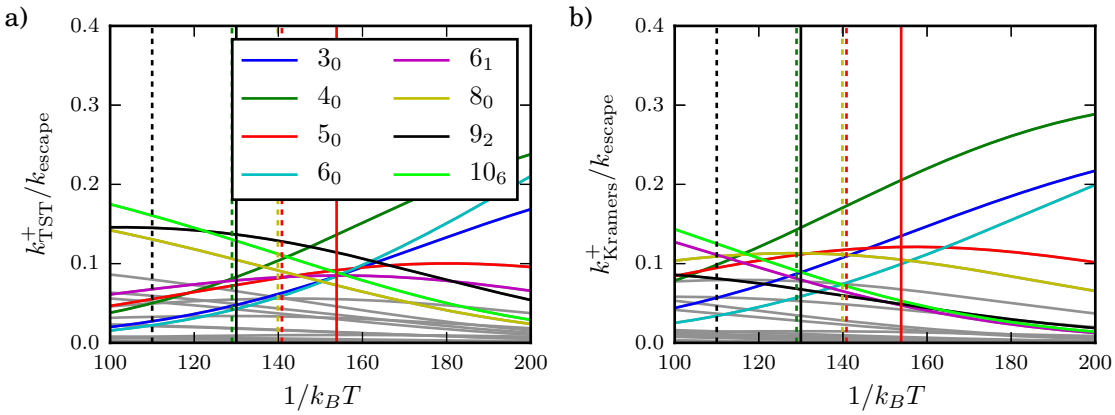

Figure 6.11: Comparison of relative occurrences of different transitions, both for harmonic transition state theory (a) and Kramers (b). Vertical lines denote temperatures of melting (dashed), or crystallization or emergence of a hexatic phase (solid), determined by Zheng and Earnshaw (1998) (black; solid: crystallization), Hartmann et al. (2005) (yellow), and Vaulina and Koss (2014) (green). Our simulation results are plotted in red. Highlighted are those transitions contributing the most. At low temperatures, these are transitions of three to six particles. With increasing temperature, transitions comprising more particles gain in importance.

Therefore, we turn towards the relative occurrences. In the semi-logarithmic representation in figure 6.10 differences are hard to tell, and so we show the relative rates in figure 6.11. Here, transitions with the strongest impact are colored and labeled. At low temperatures, the few-particle transitions comprising three to six particles dominate. Apparently, the two-particle exchange is of no significance. With increasing temperature, this shifts towards more-particle transitions becoming the dominant processes. For both approaches, harmonic transition state theory and Kramers, this crossover occurs in the region where we observe the phase transition, $k_BT \approx 0.007$ or $1/k_BT \approx 140$. Interestingly, at temperatures beyond the melting point transitions contributing the most are two-step processes where at the transition state a vacancy-interstitial pair is formed. For the Kramers rate though, figure 6.11(b), the crossover takes place at slightly higher temperatures. This is due to the unstable mode contributing in eqn. (4.10). It is smaller in magnitude for transitions consisting of more particles, and it is especially low for two-step transitions, cf. table 6.1 the rightmost column. Consequently, those transitions become less important in the Kramers approach, and rotational transitions like the six-particle exchange 6_1 become more frequent. Nevertheless, the effective frequencies of the two-step transitions are still larger so that the crossover is only delayed but not prevented.

6.2.5 Comparison to MD-simulations

In a first attempt to relate the transition states to the critical temperature of melting, we make use of a simple percolation model on a triangular lattice with a critical probability of site percolation $p_c^{\triangle} = 1/2$ (Sykes and Essam, 1964). At each lattice site, we assume

a probability k^+ that an event, namely a transition, will take place. Each transition comprises several particles, and we estimate its area of effect by the average participation number, $\langle \mathrm{PN}_2 \rangle \approx 15$. The timescale on which a transition takes place can be estimated from figure 3.10, $\tau \gtrapprox 300$. Combined, the probability of a lattice site to show substantial displacements is thus given by

$$\begin{aligned} p_{\mathrm{cell}} &= \tau \langle \mathrm{PN}_2 \rangle k^+_{\mathrm{crit}} \\ &\approx 4500 k^+_{\mathrm{crit}} \equiv \frac{1}{2} = p_c^{\triangle}. \end{aligned} \tag{6.5}$$

Hence, the critical rate per lattice site is given by

$$k^+_{\mathrm{crit}} \approx 1 \times 10^{-4}. \tag{6.6}$$

Apparently, when comparing it with figure 6.10, this corresponds to a critical temperature of $k_B T_c \approx 0.009$, or $1/k_B T \approx 110$. While this is still in agreement with Zheng and Earnshaw (1998), our findings and Hartmann et al. (2005) suggest that melting occurs at somewhat lower temperatures and rates. However, it is not too surprising when looking at the simulations: There, we found that melting takes place in the stepwise liquefaction of local patches and not in a singular event comprising the whole domain. Hence, it suffices if particles in an adequately large domain show substantial displacements, and the requirement of a percolating cluster running through the whole domain is not necessary. Moreover, once the lattice is disturbed, more, and more complicated processes occur, increasing the rate k^+_{crit} and consequently accelerating the melting. Finally, it should be noted that we disregarded the interactions between adjacent transition states: The perturbation of the lattice allows for transitions with lower energy barriers. For instance, most transition states show regions where locally the particle density is reduced. Due to the corresponding larger inter-particle distances, less energy is needed to initiate a second transition. Consequently, such secondary transitions have an enhanced probability.

Obviously the localized transition states alone cannot explain the observed melting temperature. Either, one might say that rates are much too low by two orders of magnitude, or that the predicted temperature is slightly too large. Rather, the localized transitions can be regarded as promoters which enable the formation of defects and more complex transitions, consequently disrupting the lattice. Nevertheless, the general dependence on an external parameter, namely the screening parameter μ, should be unaffected and thus reflect the variation of the melting temperature. We will elaborate on this more deeply in section 6.3.

6.2.6 Comparison to the reduced models

Since we have now established the transitions consisting of two and three particles and the corresponding rates in the full system of 2500 particles, we are able to compare them with the results of the reduced models in chapter 4. The key characteristics are summarized in table 6.3. Starting with the two-particle exchange, we consider the transition in the system of two free particles, figure 4.2(a), and the diagonal transition TS^{d} in the three-dimensional reduction of the system comprising three free particles, figure 4.6(a) the upper

right configuration. It closely corresponds to the transition in the full system, whereas in the four-dimensional system the equivalent two-particle exchange proceeds over a co-dimension two point. To characterize the states, we examine the energy barrier, the maximum per-particle energy, the unstable eigenvalue, and the effective frequency of the transition ω_{eff}. Naturally, the per-particle energy at the global minimum is identical for each system. As would be expected, with more particles to be displaced, both the energy barrier and the individual per-particle energy are reduced: With only two particles free to move, they get close to each other, and correspondingly the potential energy shows a large increase. With three free particles, the situation is eased as the distance between particles becomes larger, reducing the potential energy. Finally, with all particles able to make way, each particle gets displaced only by a small amount relative to its direct neighbors, and consequently the potential energy barrier is further reduced. The same holds for the spectrum of the system, which captures the steepness of the gradients close to the transition state. In case of the stable modes, this leads to a considerably larger effective attempt frequency ω_{eff} than in the reduced systems. In the harmonic approximation, the stable frequencies also relate to the accessible area of configuration space, and it is larger the lower the frequencies are. In consequence, the effective frequency ω_{eff} indicates to what extent the accessible configuration space gets reduced at the transition state. Obviously, this reduction is smaller for the 2500-particle system.

As for the three-particle exchange, we consider the transition in the four-dimensional three-particle system, figure 4.5(b). It confirms the aforementioned observations: Whereas energies and the unstable mode are reduced, the effective frequency significantly increases.

Summarized, we can state that, although structurally similar, the dynamical properties of the transition states are quite different in each considered system. Therefore, for a full description of transitions a treatment of the whole system is necessary. Nevertheless, the reduced systems are helpful for a deeper insight into phase space structures.

6.3 Variation with the screening parameter

Up to this point, we mostly neglected the screening parameter and kept it fixed at $\mu = 3$. However, it is an interesting parameter as it intrinsically changes the nature of the particle

Table 6.3: Comparison of the two- and three-particle exchanges of the low dimensional model systems. With more degrees of freedom, the energy barriers and unstable modes decrease whereas the effective frequency increases.

	Two-particle exchange			Three-particle exchange	
	2 free particles	3 free particles TS[d]	full system	3 free particles	full system
ΔE	0.574824	0.426516	0.152002	0.329299	0.131697
$\max(E_i)$	0.371542	0.282708	0.195351	0.251557	0.189404
λ^+	6.75787	2.10460	0.282862	2.27280	0.381573
$\omega_{\text{eff}}/2\pi$	0.0766271	0.0693373	2.84883	0.0573463	1.58772

interaction, ranging from a long-range Coulomb interaction in the limit $\mu \to 0$ to a system of hard spheres for large μ.

In order to obtain the corresponding transition states, we take the ones we found at $\mu = 3$ and track them in μ. To this end, we slightly change the screening length. Naturally, this alters the forces in the system and most likely destroys the force balance of the former transition state. For a small enough step-size though, we can use Newton's method to recover the transition state at the new screening parameter. This procedure works well in a wide range of μ, however for many transition states with increasing screening parameter at some point a second unstable direction emerges. A summary of the intervals in which the different transition states exist is given in table 6.4. Towards the other end of the parameter range below $\mu = 1$, interactions become long-ranged and the algorithm fails due to the imposed cut-off radius. In order to accurately compute the transition states in this region, other methods capturing the long-range character of the potential would have to be implemented, e.g. by using Ewald summations.

6.3.1 Displacement field

While the variation of the screening parameter significantly alters both the potential and the corresponding forces, the basic configurations of the transition states barely change. Close to the center of deformation, the stationary positions qualitatively remain the same, irrespective of the screening length. Correspondingly, the same holds for some of the features of the displacement field. What changes however is the magnitude of displacements, especially for those particles not directly participating in the transition. This can be seen best for the displacement fields shown in figure 6.12. There, we see fields of four different transition states at four different values of the screening parameter each, namely the two-, three-, four-, and five-particle exchanges, and the screening parameter increasing from $\mu = 3$, 6, 9 to 12, corresponding to the potential becoming short ranged.

Qualitatively, the transition states can be classified as one of two types, each of them showing a characteristic behavior with variation of the screening parameter. This also applies to the transition states not depicted in figure 6.12. On the one hand, there are those transition states which already show displacements of up to $d \approx 10^{-2}$ over most of

Table 6.4: Screening parameters for which the different transition states (TS) exist. Beyond the interval, further unstable modes emerge. Below $\mu = 1$, continuation fails due to the long range of the potential.

TS	$\mu_{\min}$	$\mu_{\max}$
2_0	1	12
3_0	1	12
4_0	1	12
5_0	1	12
6_0	1	12
6_1	1	11
7_1	1	7

TS	$\mu_{\min}$	$\mu_{\max}$
8_0	1	3
8_2	1	9
9_2	2	12
9_{22}	1	3
9_3	1	12
9_7	1	9
10_3	1	12

TS	$\mu_{\min}$	$\mu_{\max}$
10_4	1	10
10_6	1	4
11_3	1	9
12_1	1	6
12_6	1	4
18_0	1	11

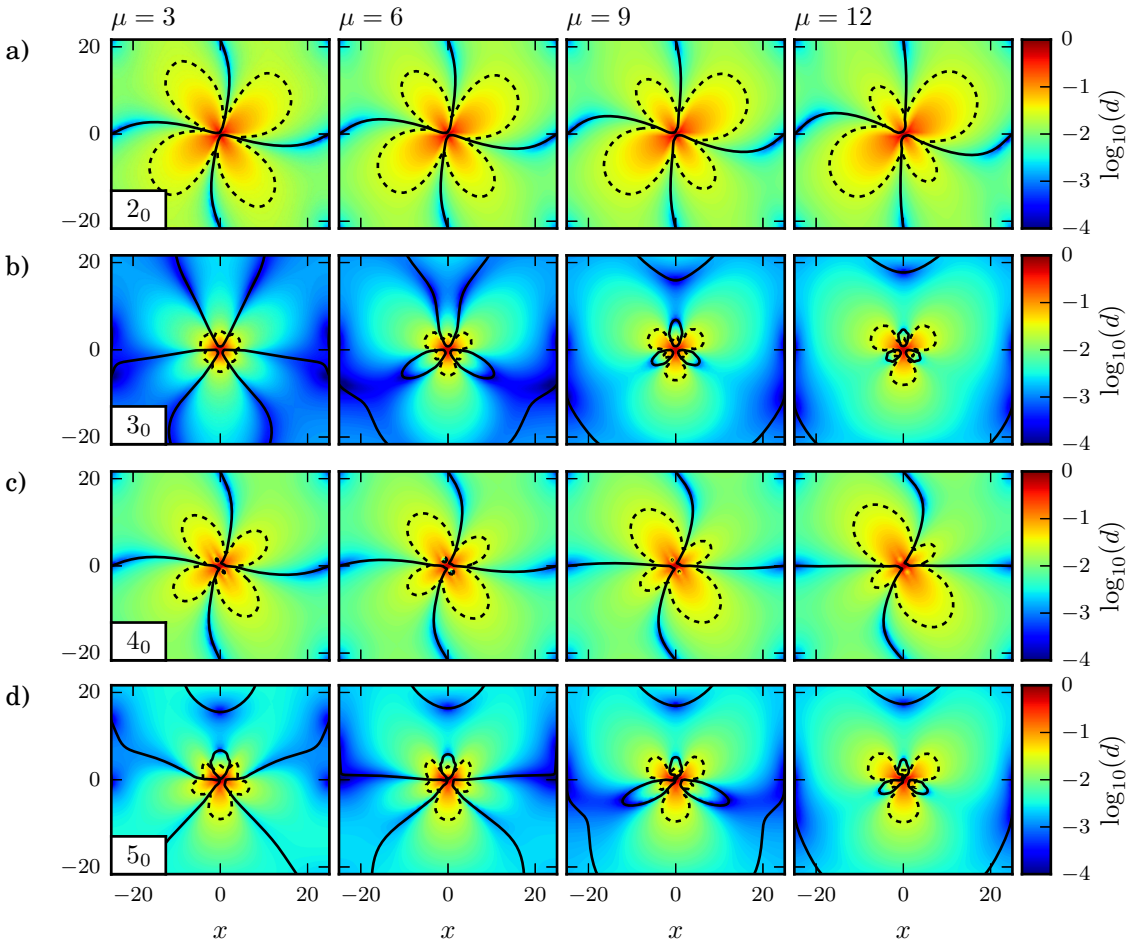

Figure 6.12: Variation of the displacement field of four different transition states, at $\mu = 3$, 6, 9, and 12. Depicted are the two-, three-, four-, and five-particle exchanges, (a)-(d) respectively. Colors represent the displacements on a logarithmic scale. The black lines indicate vanishing radial displacements (solid) and displacements of $d = 0.025$ (dashed).

the domain. Examples are the two- and four-particle exchanges in figure 6.12(a) and (c). Throughout the parameter range, their general appearance hardly changes. However, some details vary with the screening parameter. For instance, for larger μ displacements pointing away from the transition state increase, whereas those pointing inwards decrease. This can be seen in the dashed clubs in figure 6.12 which grow or shrink, respectively. At the same time, the opening angle of particles being pushed outwards increases as can be seen from the black lines indicating vanishing radial displacements. On the other hand, there are states which are well localized for $\mu = 3$, with displacements dropping below $d < 10^{-3}$. Examples are the three- and five-particle exchange, shown in figure 6.12(b) and (d). Here, the general appearance changes. At $\mu = 3$, areas where particles are pulled inwards extent up to the boundaries of the domain, indicated by the lines of vanishing radial

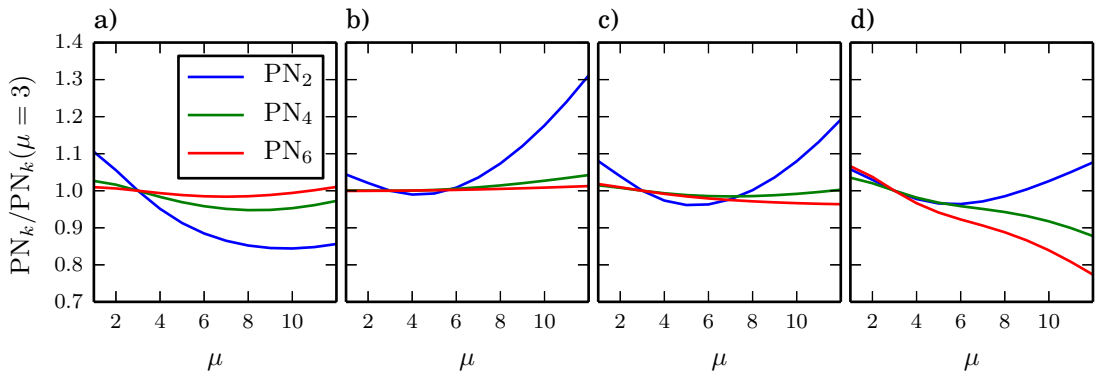

Figure 6.13: Variation of the participation numbers PN_2, PN_4, and PN_6, corresponding to the transition states depicted in figure 6.12(a)-(d). Whereas the strongest displacements show only little variation, PN_2 changes considerably along with μ. As expected, PN_2 and PN_4 show very similar behavior.

displacement extending to the boundaries. When increasing the screening parameter, isolated clubs emerge and particles are almost exclusively pushed outwards. Additionally, outwards pointing displacements increase in magnitude, until at $\mu = 12$ they drop below 10^{-3} only close to the boundaries of the domain.

These effects can be understood by taking a closer look at the potential. With increasing screening parameter μ the interaction becomes short ranged. The potential is very flat close to the equilibrium positions but very steep on close distances. Hence, particles can be displaced farther before an effect of the neighbors becomes noticeable. This has two consequences. First, when pushing a particle towards another, larger displacements are possible before restoring forces build up which are strong enough to counter the motion. Thus, displacements pointing away from the transition state are enhanced. Second, when pulling a particle away from another one, the change of the potential for the second particle is marginal so that it will hardly follow the motion. This results in the reduction of displacements pointing towards the transition state.

While the displacements and in the case of the five-particle exchange even the general shape of the displacement field change, the symmetry of the transition states is preserved throughout the whole parameter range. Therefore, the multiplicity of the transition states remains unaffected.

6.3.2 Localization

In order to quantify changes of the localization, we again look at the participation numbers. They are shown in figure 6.13 in relation to the participation number at $\mu = 3$, with panels (a)-(d) corresponding to the respective displacement fields in figure 6.12. We observe that in general PN_4 and PN_6 barely change with the screening parameter. Since these quantities are a measure of the strongest displacements, this is in agreement with the behavior of the center of the transition states which qualitatively remain the same irrespective of μ. An exception is the five-particle exchange in d) which apparently becomes more localized as it changes its shape with increasing screening parameter. The participation number PN_2

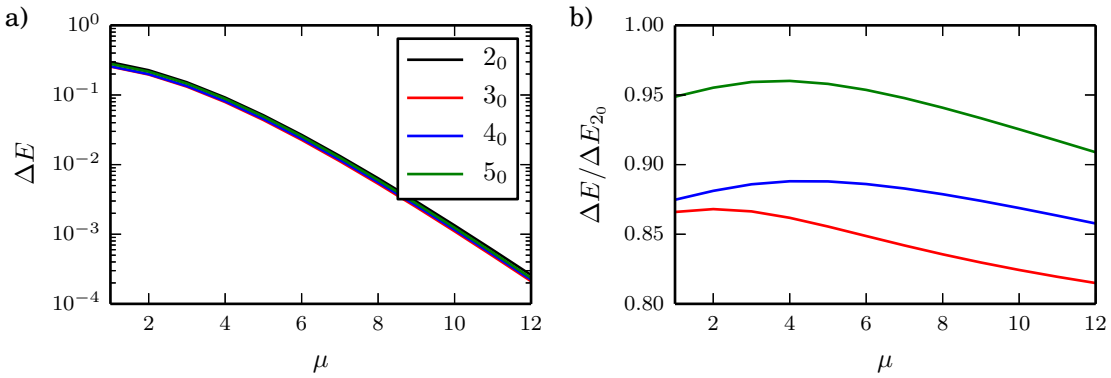

Figure 6.14: Variation of the energy barriers with the screening parameter for the four transitions in figure 6.12, absolute (a) and relative (b). All energy barriers show the same qualitative behavior, and only slight relative variations ($< 0.05\Delta E_{2_0}$) are observed.

on the other hand shows more variation. Since it also captures the smaller displacements, this is no surprise. However, we do not see a general behavior. For instance, for the two-particle exchange PN_2 drops off with increasing μ, which is mainly caused by a reduction of the inward displacements due to the flattening potential. For the other three transition states it grows as the interaction becomes short ranged, reflecting the enhancement of outward displacements also seen in figure 6.12.

Upon shifting towards a long range potential, $\mu < 3$, each participation number increases. This corresponds to an enhancement of the inward displacements while outward displacements remain constant. In effect, this increases the number of participating particles, especially of those showing small displacements.

6.3.3 Energy barriers

Before turning towards the transition rates, we inspect the behavior of the energy barriers in figure 6.14(a). When considering the hexagonal lattice and only next neighbors, we would expect the potential energy to show an exponential dependence, $\Phi_i \approx 3\exp(-\mu)$. Correspondingly, in the range $1 < \mu < 12$ the energy should vary over more than four orders of magnitude. Therefore it is not surprising that the energy barriers vary over three orders of magnitude, though they do not show an exponential dependence. Apparently, all transition states show the same general behavior, with lines lying close to each other in figure 6.14(a).

To unravel this, in figure 6.14(b) the energy barriers are plotted in relation to the one of the two-particle exchange, ΔE_{2_0}. They show only little variation, with relative deviations below approximately $0.05\Delta E_{2_0}$. The energy barriers are mostly constituted by particles showing strong relative displacements. However, the region close to the center of deformation remains mainly unaffected by the change of the screening parameter, irrespective of the individual transition. In consequence, all energy barriers should roughly show the same behavior. Hence, the minor fluctuations are caused by changes in the localization of less displaced particles, and the different next-neighbor distances. Since the screening is

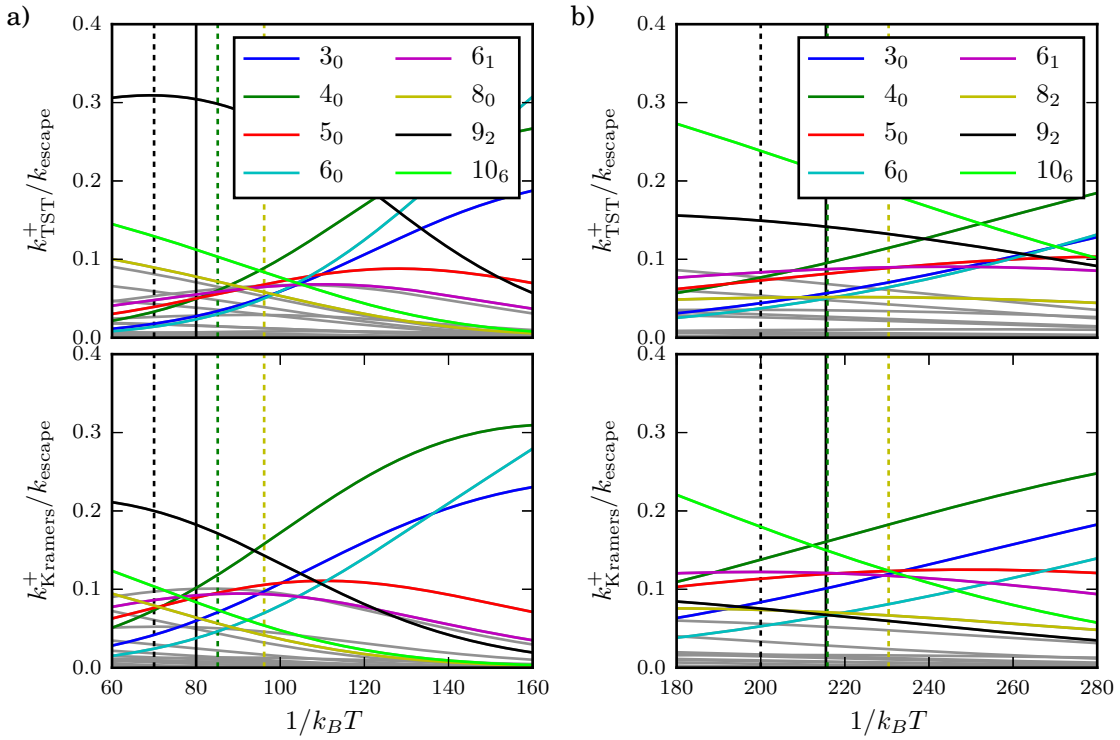

Figure 6.15: Comparison of relative occurrences of different transitions at $\mu = 2$ (a) and $\mu = 4$ (b), both for harmonic transition state theory (top) and Kramers rates (bottom). Vertical lines denote temperatures of melting (dashed), or crystallization (solid), determined by Zheng and Earnshaw (1998) (black), Hartmann et al. (2005) (yellow), and Vaulina and Koss (2014) (green). Similar to the case of $\mu = 3$, in the temperature range of melting we see a crossover from few-particle to many-particle transitions.

not just a prefactor in the potential, the latter result in different dependencies on μ.

6.3.4 Variation of transition rates

In a first step, we consider transition rates at $\mu = 2$ and $\mu = 4$. We restrict our analysis to these two values for two reasons. First, not all transition states can be tracked in the whole range of the screening parameter μ. For several of them, bifurcations occur where a second eigenvalue becomes unstable. The second reason is that we have estimates of the melting temperature for $\mu = 2$ and 4 from three different publications (Zheng and Earnshaw, 1998; Hartmann et al., 2005; Vaulina and Koss, 2014), and hence rates can be compared with them.

The critical overall rate at which melting takes place in either case is in the range $k^{\mathrm{escape}}_{\mathrm{TST}} \approx 10^{-6} \ldots 10^{-3}$ for transition state theory, and $k^{\mathrm{escape}}_{\mathrm{Kramers}} \approx 10^{-7} \ldots 10^{-4}$ in the case of Kramers rates. This is similar to the rates obtained for a screening parameter of $\mu = 3$ in figure 6.10.

Therefore, we turn to the relative rates, shown in figure 6.15 for $\mu = 2$ and 4. Similar to the case of $\mu = 3$, we observe a change in the dominating transitions: Below the melting temperature, $1/k_BT > 100$ and $1/k_BT > 230$ for $\mu = 2$ and 4, respectively, configurational changes are mainly due to rotational few-particle transitions of three to six particles. In the vicinity of the temperature of melting, they are replaced by transitions which temporarily generate pairs of vacancies and interstitials and comprise more particles, typically eight to ten. They dominate the process at higher temperatures.

The order of precedence of the transitions not only changes when increasing the temperature, but also varies when shifting the screening parameter from $\mu = 2$ to 4. For instance, the transition 9_2, which is by far the most active one for $\mu = 2$ and at higher temperatures, gets suppressed at $\mu = 4$. Instead, the ten-particle exchange 10_6 becomes the most active transition. The same applies to the six-particle ring exchange 6_0 in the limit of lower temperatures where it is superseded by the three-particle exchange.

6.3.5 Comparison to simulations and the Lindemann criterion

In this final section we compare predictions of the melting temperature by means of the rate-approach with otherwise determined results in a wider range of the screening parameter. Besides simulation results, we also consider predictions using the Lindemann criterion of melting, which is described in chapter 3.2.4. Whereas both Lindemann (1910) and Gilvarry (1956) aimed at the estimation of natural frequencies, we can readily go the other way round and estimate the critical temperature of melting. To this end, we make use of the equipartition theorem,

$$\tfrac{1}{2}\omega_E^2\gamma_{\mathrm{L}}r_0^2 = \tfrac{1}{2}k_BT, \tag{6.7}$$

which relates the vibrational energy of the system to its thermal energy. Here, ω_E is the Einstein frequency associated with the system, eqn. (3.8), and we already plugged in the Lindemann parameter, $\langle u^2\rangle = \gamma_{\mathrm{L}}r_0^2$.

With the critical temperatures obtained in the MD-simulations and $\omega_E^2(\mu = 3) = 2.098$, we can compute Lindemann parameters of

$$\gamma_E^{\text{crystal}\to\text{hexatic}} \approx 3.1 \times 10^{-3} \quad \text{and} \quad \gamma_E^{\text{hexatic}\to\text{liquid}} \approx 3.3 \times 10^{-3} \tag{6.8}$$

or, correspondingly, average per particle displacements of

$$\delta_E^{\text{crystal}\to\text{hexatic}} \approx 5.6 \times 10^{-2} \quad \text{and} \quad \delta_E^{\text{hexatic}\to\text{liquid}} \approx 5.8 \times 10^{-2}. \tag{6.9}$$

These results are considerably lower than the critical Lindemann parameter obtained from the analysis in chapter 3.2.4, with per-particle displacements roughly half as large as expected from the Lindemann parameter of the local lattice, γ_6.

Intrinsically, the Lindemann criterion is an indicator of the solid-to-hexatic transition. However, most data is for the hexatic-to-liquid transition (or solid-to-hexatic, if the hexatic phase is not discerned). For now, we assume that the melting temperatures of both transitions show the same dependence on the screening parameter. Additionally, since we are only interested in this dependence, the actual value of the Lindemann parameter is

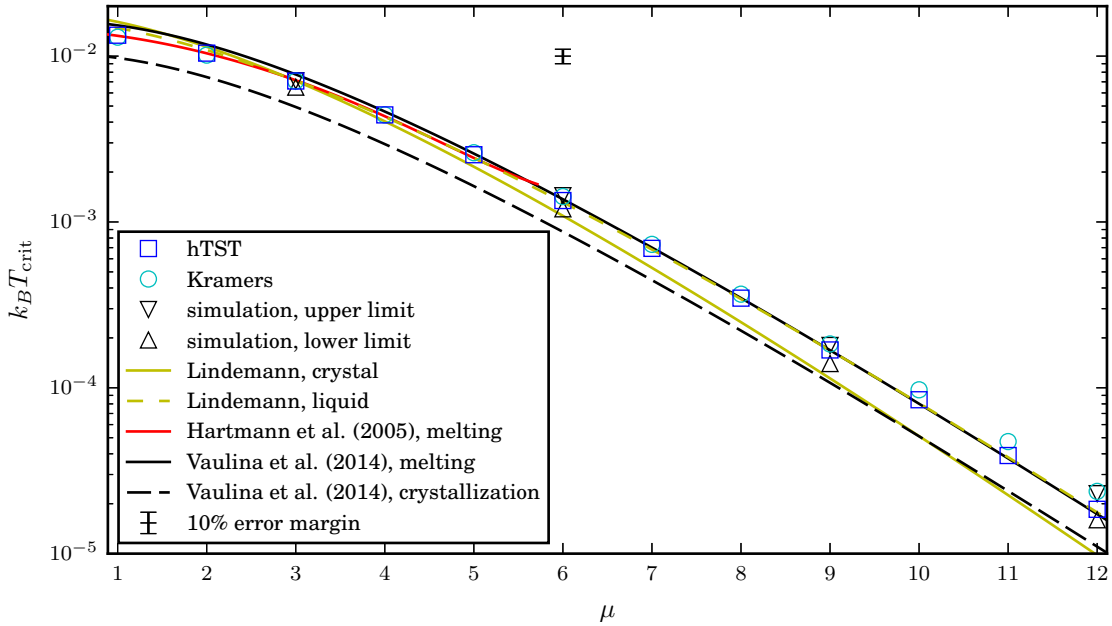

Figure 6.16: Comparison of anticipated melting temperatures, obtained from harmonic transition state theory (□, hTST) and Kramers rates (○), the Lindemann criterion (yellow lines) and various simulations. Triangles indicate estimates of the phase transitions at $\mu = 3, 6, 9$, and 12 obtained from MD-simulations. Vaulina and Koss (2014) (black lines) use a scaling relation based on the Lindemann criterion. In the range $1 \leq \mu \leq 6$, we see that our approach using transition rates closely follows the simulation results of Hartmann et al. (2005) (red line). For reference, a 10% error scale is given.

of minor concern. Since various studies suggest that the critical Lindemann parameter is mostly independent of the potential, we consider $\gamma_{\mathrm{L}} = \gamma_E^{\mathrm{hexatic}\to\mathrm{liquid}}$ so that the criterion matches the melting temperature at $\mu = 3$.

Comparison

We compare our results from rate theory with the predictions of the Lindemann criterion and the simulation results of Vaulina and Koss (2014), Hartmann et al. (2005), and our own simulations in figure 6.16. In the range $1 \leq \mu \leq 12$, we compute the event rate, eqn. (6.4), both for harmonic transition state theory and Kramers rates. Taking the results of $\mu = 3$ in figure 6.10 as reference, we assume a constant critical rate at the melting temperature of $k_{\mathrm{TST}}^{\mathrm{crit}} = 1 \times 10^{-6}$ and $k_{\mathrm{Kramers}}^{\mathrm{crit}} = 3 \times 10^{-8}$ throughout the parameter range. The resulting critical temperatures are indicated as colored open symbols in the figure. As anticipated from the dependence of the energy barriers, the critical temperature spans three orders of magnitude. With increasing screening parameter, the predictions of both approaches slightly separate, with the Kramers theory giving larger melting temperatures.

In a first step, we compare the predictions with results from our simulations, performed

at $\mu = 3$, 6, 9, and 12. Except for $\mu = 3$, those results can only be seen as rough approximations since both the resolution in k_BT is low and integration times are too short to determine the exact temperatures of the transitions. Therefore, we only consider the upper and lower limit, in which cases the system is either in the liquid or solid phase, with the intermediate hexatic phase being located in the temperature range in between. When performing the simulations more accurately, the upper and lower could slightly change. For each considered value of the screening parameter the upper limit is close to the critical temperatures as predicted by rate theory and matches the results of the Kramers rates very well. Moreover, similar to the predicted values, the temperature range specified by the upper and lower limit grows with increasing screening parameter. Interestingly, when prescribing the critical rates needed for our predictions by values corresponding to the solid-to-hexatic transition, $k^{\text{crit}}_{\text{TST}} = 1 \times 10^{-7}$ and $k^{\text{crit}}_{\text{Kramers}} = 5 \times 10^{-9}$, the critical temperatures due to harmonic transition state theory closely follow the lower limit.

The simulation results of Hartmann et al. (2005) are shown in the figure as red line. They found an empirical scaling relation by fitting their results to a polynomial,

$$k_BT = f(\mu)k_BT^* \tag{6.10a}$$

$$f(\mu) = 1 - 0.107\mu^2 + 0.0200\mu^3 - 0.00105\mu^4. \tag{6.10b}$$

Here, k_BT^* is the generalized melting temperature, and since they used the Wigner-Seitz radius as natural length-scale, units have been rescaled to the lattice constant r_0. The corresponding generalized melting temperature is $1/k_BT^* \approx 69$. However, since data was obtained only for $\mu < 6$, this approach inevitably fails at larger screening parameters. A comparison with our results in figure 6.16 reveals that the rate approach closely follows the simulation results throughout the whole range $1 < \mu < 6$.

The simulation results from Vaulina and Koss (2014) are shown as black lines, indicating the hexatic-to-liquid (solid) and solid-to-hexatic transitions (dashed). They use a semi-empirical scaling relation to predict the critical temperature in the whole parameter range (Vaulina and Khrapak, 2000). It is based on the Einstein frequency in a 1-dimensional lattice in combination with the Lindemann criterion similar to eqn. (6.7), resulting in

$$k_BT_p = \tfrac{3}{2}\left(1 + \mu_p + \mu_p^2/2\right) e^{-\mu_p} k_BT_p^*, \tag{6.11}$$

where $k_BT_p^*$ again is the generalized melting temperature. In contrast to the Lindemann criterion where the crystal lattice r_0 sets the length scale, they rescale their quantities by the average particle distance $r_p = \sqrt{\rho^{-1}}$. Hence, their description is more in view of a liquid than of a solid. Accordingly, parameters have to be rescaled using eqn. (3.16). They report a generalized melting temperature of $1/k_BT^*_{p,m} \approx 98$. We observe that their anticipated melting temperature roughly agrees with our predictions in the range $\mu > 6$. However, the slope is slightly too steep, and their estimates are lower than ours for short-range interactions. For long-range interactions, $\mu \leq 4$, the opposite is observed and they predict too large temperatures. This is particularly noticeable when compared with the good agreement of our results with Hartmann et al. (2005). Vaulina and Koss also observed a solid to hexatic transition at lower temperatures, corresponding to $k_BT_C \approx 0.005$ for $\mu = 3$, which is much lower than our simulations suggest, and has already been addressed in chapter 3.

In a final step, we compare our predictions with those of the Lindemann criterion. The Lindemann approach (yellow line) roughly spans the same range in temperature, though it shows a noticeably steeper slope even than the results of Vaulina and Koss. Correspondingly, it predicts higher melting temperatures for long-range interactions ($\mu < 3$) and lower temperatures for short-range interactions. However, we might consider a second approach, similar to the one of Vaulina and Khrapak. To this end, we assume that at the melting temperature the system is still in a crystalline state, but with the lattice spacing given by the average particle distance r_p instead of r_0. Admittedly, such a description is quite contradictory as a perfect lattice with spacing r_p would by no means fit into the computational domain. The resulting critical temperature is shown as a dashed yellow line in figure 6.16. Surprisingly, it gives similar results as those of Vaulina and Koss for $\mu > 6$, and fits better in the range $\mu < 6$. In between $3 < \mu < 6$, it even fits the results of Hartmann et al. quite well.

6.4 Summary

In this chapter, we extended the search for localized transition states and investigated transitions of up to 18 particles exchanging their positions. We were able to identify two characteristic types of transitions. On the one hand, there are rotations of a small patch of the crystal accompanied by the formation of grain boundaries. They are mostly found for transitions comprising only a few particles. The second kind of transition involves the formation of a vacancy-interstitial pair at the transition state and typically comprises more particles. In general, the potential barrier rises with the number of participating particles. Unsurprisingly, the barriers of the two-step transitions roughly equal the excess energy of the observed defect pairs.

We investigated the transition rates and found that few-particle transitions dominate at low temperatures whereas the two-step transitions take precedence at higher temperatures. The crossover between the two regimes falls close to the previously determined melting temperature. However, the rates are too low to explain the onset of melting. Instead, they can be considered as promoters of more complex processes, giving rise to the formation of defects and enabling secondary transitions.

The relevance of the localized transition states is emphasized when investigating their dependence on the screening parameter μ. First of all, the structure of the transition states remains intact, although several of them become unstable when tuning the interaction towards a shorter range of the potential by increasing μ. What is striking though is that the critical temperature of melting, determined by a prescribed critical rate, nicely matches simulation results in the range $1 \leq \mu \leq 6$ and gives better results than predictions based on the Lindemann criterion.

7

Conclusion

In this work, we aimed at a broader understanding of the general transition form order to chaos, be it in the context of a periodically sheared system which evolves from a reversible to an irreversible dynamic, or in the context of the liquefaction of a crystal, which progresses from the ordered, solid state to the liquid phase.

In the first part, we investigated a simplified system, breaking down the complex interactions of particles in a sheared fluid to a pairwise repelling potential and an affine shear. We found that even then the characteristic transition from a reversible to an irreversible behavior could be reproduced. We were able to extract a critical shear rate above which the system inevitably crosses to the irreversible regime. Both regimes are characterized by their diffusivity, which becomes non-zero in the irreversible regime. The critical shear rate can be directly linked to the loss of stability of sheared lattice configurations. As is typical for sheared systems, we observed a strong anisotropy in diffusivities parallel and perpendicular to the shearing force. However, it could be explained only partially by the well known mechanism of advection-diffusion coupling. Interestingly, even far beyond the critical point at very strong shear rates, spatial correlations in the distributions of particles could be revealed, that is phase informations and anisotropies in the length scales. The latter help to understand the abnormal anisotropy of the diffusivities.

Close to the critical point, we observed an interval of the shear rate where a coexistence of both reversible and chaotic motion could be possible. In order to verify this conjecture, further investigations are necessary. With regards to the success of the application of the edge tracking algorithm on the screened Coulomb system in chapters 5 and 6, it seems promising to adopt the algorithm to the sheared system, and search for the transition state connecting these two fundamentally different states of the system. In this setting of an externally driven system, the specialized algorithms introduced in appendix A.4 are not applicable.

In the remaining chapters and the main part of the thesis, we investigated a more commonly known transition, the melting of a crystal into the liquid phase in a two-dimensional system. Here, the main focus has been put on the microscopic processes which lead to a liquefaction. In a first step, we investigated the melting temperatures with the help of MD-simulations. We were able to closely examine the system trajectories at the melting transition. We found that in a first transition an intermediate phase emerges, characterized by a non-vanishing diffusion coefficient. In this phase, mostly localized exchanges of only a few particles occur, each transition contributing to the diffusivity. At higher temperatures, those exchanges lead to secondary transitions and the formation of defects, which disrupt the lattice structure and drive the system towards the liquid phase. This happens not in

one quick global transition, but in a stepwise process where small liquefied clusters emerge, which gradually grow until finally the whole domain is in the liquid phase. Hence, as has already been observed in previous studies (Tang et al., 1989; Radzvilavičius, 2012), the melting process appears to be more complex than anticipated by theories, both KTHNY and grain-boundary. Nevertheless, we found evidence of the KTHNY-mechanism: At both melting temperatures, the number of defects that are associated with the respective transitions by KTHNY-theory increases noticeably.

Apparently, localized transitions are of some significance for the melting transition. Moreover, they only occur in considerable numbers above a certain temperature, similar to e.g. chemical reactions where a certain excess energy is required to trigger an event. This allows for an interpretation of the melting transition in terms of a rate activated process, with localized transition states as building blocks.

In a simplified model system of only a few free particles, we were able to get a first idea of the nature of few-particle exchanges and establish some basic concepts, such as the importance of transition states and the separating nature of their stable manifolds. In a large system, we then systematically searched for possible particle exchanges. In order to locate the corresponding transition states, we adapted the technique of edge tracking. We were able to identify localized transition states comprising up to 18 particles, and analyzed their configurational and dynamical properties.

We identified two different kinds of transitions, a rotation of a small patch of particles and a temporary formation of a vacancy-interstitial pair. In the latter case, a string of particles gets shifted, so that at one location in the crystal a vacancy forms out, whereas at the other end of the string an interstitial emerges. This is in contrast to the common illustration of defect formation where a single particle moves in the otherwise static lattice, and greatly reduces the barrier heights associated with the defect generation. Some of those transitions have been described earlier (Fisher et al., 1979), though their relevance has not been investigated in much detail. At low temperatures, the rotational transitions dominate the exchange processes. At larger temperatures, on the other hand, transitions involving the formation of vacancy-interstitial pairs become more frequent. Additionally, the latter occur on longer timescales, thus giving the defects time to diffuse and eventually disrupt the lattice. Therefore, it is not too surprising that the crossover between the two regimes takes place close to the temperature of melting. However, the localized transitions alone are insufficient to explain the melting temperature. This is supported by results of a simple percolation model. Each transition state appears with a specific rate and disturbs the lattice around it. The combined rate which would be required so that a critical fraction of particles in the system shows substantial displacements is much larger than the rate computed at the melting temperature. However, with the help of secondary transitions and the formation of defects, lower rates could be sufficient to start the melting process, especially since observations suggest a stepwise melting. In this case, as soon as a sufficiently large patch of the crystal becomes liquid, it will stay liquid. Hence, the condition of the percolation model that particles throughout the entire domain have to be displaced must not be fulfilled.

The strong localization of the displacements inspired us to draw a connection between the displacement field of the individual particles and continuum elasticity theory. This description certainly holds farther away from the center of deformation, where locally the

crystalline structure is preserved. Indeed, we can approximate the displacement field induced by a transition state, at least outside the center of deformation. This is achieved by choosing appropriate singular forces acting on a continuous elastic body with the corresponding elastic properties. This approach can be applied to more complex structures as well, and in principle the reverse procedure, where transition states are deduced from their displacement fields, should be possible as well. Yet, most transition states show very similar displacement fields, and their exact shapes strongly depend on the boundary conditions. This is aggravated as soon as the fields of several transition states are superimposed, so that this approach seems unpromising.

The importance of the localized transition states has been emphasized in the final step, where we investigated the implications of a variation of the screening parameter μ. It alters the potential, from long-range Coulombic to a short-range interaction of solid disks. The general configurations of the transition states remain unaffected. However, as the elastic properties of the system change, so do the displacement fields. With increasing screening parameter, displacements away from the transition state are enhanced, whereas opposite displacements diminish. Nevertheless, we still observe the crossover between the two kinds of transitions close to the temperature of melting. We take the event rate at the melting temperature for $\mu = 3$ as reference, and by keeping it fixed we extract a predicted melting temperature for the range $1 < \mu < 12$. This parameter-free approach shows very good agreement with simulation results of Hartmann et al. (2005) in the range $\mu < 6$, fitting the dependence on the screening much better than other approaches based on the Lindemann criterion. For short ranged interactions, $\mu > 6$, all estimates of the melting temperature lie close to each other and capture its dependence, as could be verified by our own simulations.

Since many transition states were lost when increasing the screening parameter, one future goal would be to repeat the search for transition states, for example at $\mu = 12$ where most of the transition states forming vacancy-interstitial pairs have become unstable. However, for such a parameter value the potential is very flat at the minimum configuration and at the same time very steep for short inter-particle distances. Hence, the system has two very different time scales, and the computational effort increases. The same applies to complementing MD-simulations, where longer times for equilibration are needed, as well as shorter time steps in order to capture the strong forces as soon as particles approach each other.

The identified transition states might also help to understand the relaxation of internal stresses in a crystal. There, the very same rearrangements were observed (van der Meer et al., 2014). In this setting, the activation of a transition state will primarily not occur due to thermal fluctuations, but due to the imposed stresses and the deposited energy. Hence, the particle configuration at the transition state, the associated energy barrier, and the path to the next minimum are the important characteristics to look at.

In this work, we only focused on identical particles. However, the described framework should also be applicable on other systems, such as amorphous systems consisting of particles of different sizes or varying interactions. In such systems no long-range order of any kind is observed, and consequently a characterization of the phase transition by a change in the correlations breaks down. A first step in this direction could be to look into particles on the surface of a sphere (e.g. Bausch et al., 2003). There, the hexagonal lattice

cannot be realized and we observe a mixture of hexagonal and pentagonal structures.

Overall, we were able to add a new facet to the problem of how melting of a solid proceeds. It appears that local transitions play an important role. They are among the first processes to occur as temperature is increased, and give rise to temporary disruptions of the lattice. Moreover, they provide a mechanism to generate defects, be it directly by formation of vancancy-interstitial pairs, or indirectly by lowering the energy barriers for secondary, more complex transitions.

A

Appendix

A.1 Thermalization

When performing MD-simulations, one has to take care that the system at hand is in thermal equilibrium. Only then it is possible to make statements about e.g. kinetic temperatures or phase transitions. In the latter case, this becomes even more important since close to a phase transition transients may become very long. In our case, we considered three different indicators.

Velocity distribution

In thermal equilibrium, the velocity distribution of the particles is expected to follow a Maxwell-Boltzmann distribution,

$$f(v_i) = \sqrt{\frac{m_i}{2\pi k_B T}} \exp\left(-\frac{m_i v_i^2}{2k_B T}\right), \tag{A.1}$$

with the width being determined by the temperature. This criterion is often considered a sufficient one for thermal equilibration (Rapaport, 1997). In figure A.1 we show the velocity distribution at $k_B T = 0.0071$. We take configurations at three different points of the simulation, namely during the heating process (red diamonds), and after 20000 and

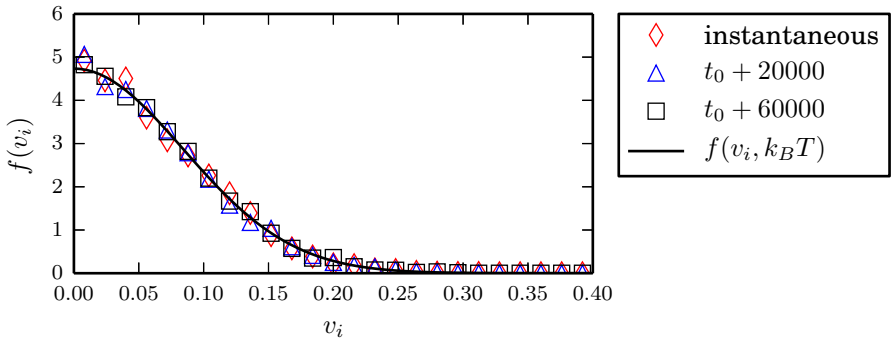

Figure A.1: Velocity distribution at $k_B T = 0.0071$ during heating (diamonds), and after equilibration at constant temperature for 20000 and 60000 time units (triangles and squares, respectively). The solid line represents the anticipated Maxwell-Boltzmann distribution, which is matched perfectly in all three cases.

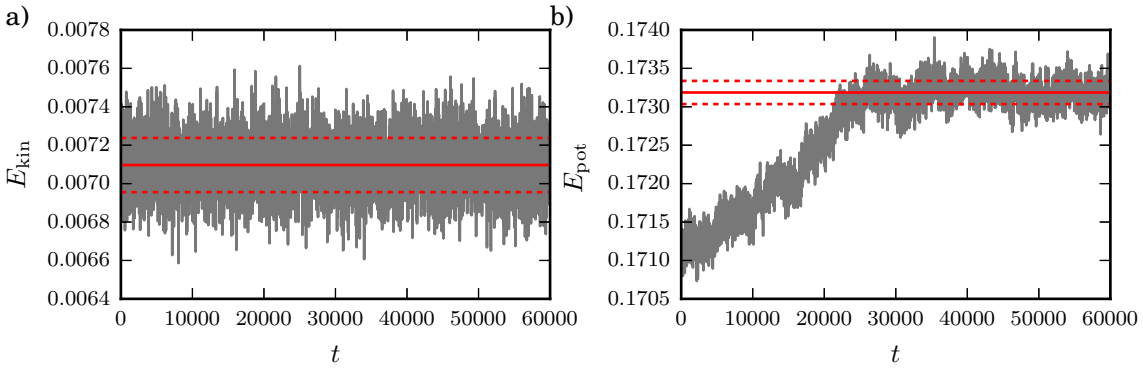

Figure A.2: Relaxation of (a) kinetic and (b) potential energy. The solid red lines indicate the mean values, averaged over the last 10000 time units, whereas the dashed lines represent the standard deviations.

60000 time units at fixed temperature (blue triangles and black squares, respectively). The black line indicates the expected Maxwell-Boltzmann distribution, which is matched perfectly in all three cases. Thus, velocities are equilibrated almost instantaneously. Further investigations show that the results are independent of the prescribed temperature.

Relaxation of energies

Next, we investigate the relaxation of both kinetic and potential energy. The former is also an indicator of the temperature of the ensemble, since both are closely related by the equipartition theorem. In figure A.2, we show the average energies per particle as function of time at constant temperature $k_B T = 0.0071$. The initial conditions are taken from the heated ensemble. In (a), we see the kinetic energy fluctuating around its mean value $\langle E_{\mathrm{kin}}/N \rangle \approx 0.0071$, indicated as solid red line. Apparently, the asymptotic value is reached very quickly since a relaxation is not visible. The dashed red lines represent the standard deviation, which is approximately 2% of the mean. Moreover, the fluctuations are proportional to the temperature as an inspection at different temperatures reveals, and would be expected from the fluctuation dissipation theorem. In order to reduce fluctuations, one would have to consider a larger system. In the right panel (b), we show the potential energy. At the considered temperature, which is slightly above the melting point, it takes the system a long time to reach equilibrium: Compared to the kinetic energy, the potential energy only slowly approaches its final value, reaching it after about 30000 time units.

Obviously, as already reported by Likhachev et al. (2009) and Derzsi et al. (2014), the velocity distribution alone is not a sufficient criterion for thermalization, though it is a necessary one. Even the kinetic energy, which takes longer to approach its equilibrium value, is not an adequate indicator. It is the relaxation of the potential energy which sets the time scale of equilibration. As Likhachev et al. pointed out, at low temperatures this is mainly due to long-wavelength modes which take long times to relax. Accordingly, Derzsi et al. found that long range correlations take very long to break down. In our system, this corresponds to a full disintegration of the lattice structures towards an isotropic

configuration of particles, which in turn leads to a noticeable increase in the potential energy.

Admittedly, at temperatures slightly below the melting point it can take the system even longer to reach equilibrium. However, due to the fluctuations in temperature this might also be caused by the system locally hopping back and forth between the two phases.

A.2 Reformulations of the rate equation

Restricted partition functions

For now, consider a dynamical system with n positions and n velocities. Its Hamiltonian is given as $H(\boldsymbol{v},\boldsymbol{x}) = \sum v_i^2/2 + \Phi(\boldsymbol{x})$. The rate at which transitions across a transition state take place is given by eqn. (4.5),

$$k^+_{\mathrm{TST}} = \frac{\left\langle \chi^S_*(\boldsymbol{x})\hat{\boldsymbol{n}}\cdot\boldsymbol{v}\Theta\left[\hat{\boldsymbol{n}}\cdot\boldsymbol{v}\right]\right\rangle}{\left\langle \chi^V_0(\boldsymbol{x})\right\rangle}. \tag{A.2}$$

We can rewrite the denominator of eqn. (4.5) by defining a restricted partition function

$$\begin{aligned} Z_0 &= \iint_{\mathbb{R}^n\times\mathbb{R}^n} \chi^V_0(\boldsymbol{x}) e^{-\beta H}\mathrm{d}\boldsymbol{x}\mathrm{d}\boldsymbol{v} \\ &= \iint_{\mathbb{R}^n\times V_0} e^{-\beta H}\mathrm{d}\boldsymbol{x}\mathrm{d}\boldsymbol{v} = Z\big\langle \chi^V_0(\boldsymbol{x})\big\rangle. \end{aligned} \tag{A.3}$$

Here, spatial integration is restricted to the volume around the minimum, defined by χ^V_0. Similarly, the numerator of eqn. (4.5) requires the spatial integration on the dividing surface of the transition state. Additionally, we have to average over velocity components normal to the surface, corresponding to trajectories piercing the surface and thus leaving the area of attraction of the minimum. Since the velocity distribution is independent of space, we can integrate out this component,

$$\begin{aligned} Z\left\langle \chi^S_*(\boldsymbol{x})\ \hat{\boldsymbol{n}}\cdot\boldsymbol{v}\Theta\left[\hat{\boldsymbol{n}}\cdot\boldsymbol{v}\right]\right\rangle &= \iint_{\mathbb{R}^n\times\mathbb{R}^n} \chi^S_*(\boldsymbol{x})\hat{\boldsymbol{n}}\cdot\boldsymbol{v}\Theta\left[\hat{\boldsymbol{n}}\cdot\boldsymbol{v}\right] e^{-\beta H}\mathrm{d}\boldsymbol{x}\mathrm{d}\boldsymbol{v} \\ &= \int_{S_*}\int_0^\infty v e^{-\beta v^2/2}\mathrm{d}v \int_{\mathbb{R}^{n-1}} e^{-\beta\sum v^2/2}\mathrm{d}\boldsymbol{v} e^{-\beta\Phi(\boldsymbol{x})}\mathrm{d}\boldsymbol{x} \\ &= \frac{1}{\beta}\iint_{\mathbb{R}^{n-1}\times S_*} e^{-\beta H}\mathrm{d}\boldsymbol{x}\mathrm{d}\boldsymbol{v} \equiv k_B T Z_*. \end{aligned} \tag{A.4}$$

Note that both integrations in space and velocity are effectively $(n-1)$-dimensional integrals which motivates the definition of the restricted partition function Z_*. Combined, this yields eqn. (4.7)[1], $k^+_{\mathrm{TST}} = k_B T\frac{Z_*}{Z_0}$.

[1] Throughout literature (e.g. Eyring, 1935b; Hänggi et al., 1990), transition rates k^+_{TST} are written as $k^+_{\mathrm{TST}} = \frac{k_B T}{h}\frac{Z_*}{Z_0}e^{-\Delta E/k_B T}$. The factor of $1/h$ is due to a different definition of the partition function. The exponential though appears to be an honest mistake: Integrating out the delta-function along the reaction coordinate fixes a single degree of freedom. Consequently, the exponential of the barrier energy only comes up in the harmonic approximation, as is shown further below.

Harmonic approximation

We are interested in the partition function of the harmonic approximation $H(\boldsymbol{x}, \boldsymbol{v}) = E_0 + \sum H_i(x_i, v_i) = E_0 + \sum v_i^2/2 + \omega_i^{(0)2} x_i^2/2$, where E_0 is the potential energy at the minimum and the sum extends over all n dimensions. Plugging this into the restricted partition function we find

$$\begin{aligned}
Z_0 &= \iint \exp\left(-\beta H\right) \mathrm{d}\boldsymbol{x}\mathrm{d}\boldsymbol{v} \\
&= \prod_i^n \left(\iint \exp\left(-\beta H_i\right) \mathrm{d}v_i \mathrm{d}x_i \right) \exp\left(-\frac{E_0}{k_B T}\right) \\
&= \prod_i^n \left(\int \exp\left(-\beta \frac{v_i^2}{2}\right) \mathrm{d}v_i \int \exp\left(-\beta \frac{\omega_i^{(0)2} v_i^2}{2}\right) \mathrm{d}x_i \right) \exp\left(-\frac{E_0}{k_B T}\right) \\
&= \prod_i^n \left(\sqrt{\frac{2\pi}{\beta}} \sqrt{\frac{2\pi}{\beta \omega_i^{(0)2}}} \right) \exp\left(-\frac{E_0}{k_B T}\right) \\
&= \prod_i^n \left(\frac{2\pi k_B T}{\omega_i^{(0)}} \right) \exp\left(-\frac{E_0}{k_B T}\right). \qquad \text{(A.5)}
\end{aligned}$$

The same calculation can be done at the transition state in a constricted subspace spanned by the stable modes, yielding

$$Z_* = \prod_i^{n-1} \left(\frac{2\pi k_B T}{\omega_i^*} \right) \exp\left(-\frac{E_*}{k_B T}\right). \qquad \text{(A.6)}$$

Here, we had to take into account that in the harmonic approximation χ_*^S corresponds to a delta function along the unstable direction. Plugging this into eqn. (4.7), we can rewrite the rate equation in terms of the frequencies, giving us eqn. (4.8),

$$k_{\mathrm{TST}}^+ = k_B T \frac{Z_*}{Z_0} = \frac{1}{2\pi} \frac{\prod_{i=1}^n \omega_i^{(0)}}{\prod_{i=2}^n \omega_i^*} \exp\left(\frac{-\Delta E}{k_B T}\right). \qquad \text{(A.7)}$$

A.3 Computing invariant manifolds

Considering an autonomous ordinary differential equation

$$\dot{\boldsymbol{x}} = \boldsymbol{F}(\boldsymbol{x}), \qquad \text{(A.8)}$$

the flow of the vector field $\boldsymbol{F}$ is defined by (Guckenheimer and Holmes, 2002)

$$\frac{\mathrm{d}}{\mathrm{d}t} \boldsymbol{\phi}(\boldsymbol{x}, t)|_{t=\tau} = \boldsymbol{F}(\boldsymbol{\phi}(\boldsymbol{x}, \tau)). \qquad \text{(A.9)}$$

For fixed $\boldsymbol{x}(0) = \boldsymbol{x}_0$ and solution $\boldsymbol{\phi}(\boldsymbol{x}_0, 0) = \boldsymbol{x}_0$, $\boldsymbol{\phi}(\boldsymbol{x}_0, t)$ defines a trajectory.

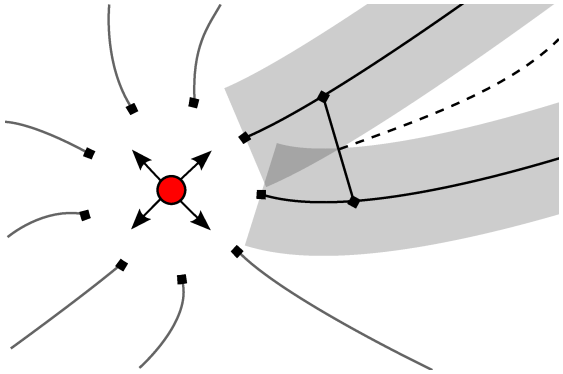

Figure A.3: Computing the unstable manifold using 'fat trajectories'. Depicted is a fixed point with two unstable directions (red). Trajectories are computed, starting at points in the unstable eigenspace (black squares). As soon as two neighboring trajectories (solid black lines, with the associated covered area in gray) separate beyond a threshold, a new initial condition is generated in between, along with the corresponding trajectory (black dotted line). Successively, the whole manifold gets covered by this procedure.

For a fixed point $\boldsymbol{x}^*$ of eqn. (A.8), we can define two invariant sets, the stable and the unstable manifold. The stable manifold comprises all points belonging to trajectories which will end up at $\boldsymbol{x}^*$. Correspondingly, the unstable manifold covers all points which are reached by trajectories that start in $\boldsymbol{x}^*$. Obviously, since $\boldsymbol{x}^*$ is a stationary point it cannot be reached by any trajectory, and both definitions only hold in the limit of infinite integration times,

$$W^s(\boldsymbol{x}^*) = \{\boldsymbol{x} | \boldsymbol{\phi}_t(\boldsymbol{x}) \to \boldsymbol{x}^* \text{ as } t \to \infty\}\,, \tag{A.10a}$$

$$W^u(\boldsymbol{x}^*) = \{\boldsymbol{x} | \boldsymbol{\phi}_t(\boldsymbol{x}) \to \boldsymbol{x}^* \text{ as } t \to -\infty\}\,. \tag{A.10b}$$

The manifolds structure phase space, e.g. the stable manifold of a stationary state of co-dimension one is of one less dimension than the configuration space. By definition, trajectories next to the manifold are repelled and hence it separates volumes of phase space. At the stationary point, the manifolds are tangent to the corresponding stable and unstable eigenspaces.

While it is very straightforward to compute the unstable manifold of a transition state with only one unstable direction by just integrating eqn. (A.8) from starting points lying ε-close in the unstable direction, this becomes a more challenging question when addressing higher-order manifolds, e.g. of co-dimension two points. One might get an idea of the most unstable direction by integrating a trajectory starting in this direction. This quickly gets unreliable when investigating less unstable modes: As soon as the trajectory leaves the area where the harmonic approximation is valid, it is strongly influenced by the more unstable directions and thus deflected. This could be attenuated by stabilizing the most unstable direction.

Though many elaborate methods to determine invariant manifolds exist, we implement a simplification of the method presented by Henderson (2005). The basic idea is to start a

bundle of trajectories lying in the manifold. Since in the case of unstable manifolds of hyperbolic fixed points the manifold itself is attracting, this can easily be achieved by starting at points in the tangential space spanned by the unstable eigenvectors of the stationary point, as illustrated in figure A.3. Next, the distance between two neighboring trajectories is monitored, for example at equidistant times. As soon as a threshold is exceeded, a new starting point is generated in between the two relevant positions. The resulting trajectory is then inserted in the list of all trajectories, and the process is recursively repeated. Thus, successively the whole manifold gets covered by trajectories - or points, which can then be used to approximate the surface, e.g. by triangulation. Due to the fact that we associate a finite surface section with an object of one less dimension, this approach is also called 'fat trajectories'.

In contrast to Henderson (2005), we use some simplifications. First, he uses a tessellation with polyhedra in order to optimize the position of new starting points whereas we take the midpoint of the connecting line. Furthermore, with a tessellation it would be possible to exclude converging trajectories and remove irrelevant data points. We ignore this and consider all trajectories up to a previously specified maximum integration time.

By inverting the equations of motion with respect to time, we can investigate stable manifolds in the same manner as well. A complication arises due to singularities of the potential where integration has to be stopped at an appropriate distance.

A.4 Algorithms to locate transition states

Sampling algorithms

The most primitive way to determine transition states would be to systematically sample configuration space point by point. However, by definition transition states are metastable points in configuration space. Therefore, they cannot be obtained by a minimization of the potential energy, and more advanced optimization techniques such as Newton's algorithm have to be used. While the latter may stop on any stationary state, we are only interested in those with exactly one unstable direction so that many unnecessary computations have to be done.

A better approach is to take advantage of the vanishing of the forces at the transition state and define an auxiliary function (Stillinger and Weber, 1984b)

$$\Psi = (\boldsymbol{\nabla}\Phi)^2 = \|\boldsymbol{F}\|^2. \tag{A.11}$$

Hence, any point in the potential energy landscape with vanishing force is a minimum of Ψ, thus replacing the task of finding the transition state with the much easier problem of finding local minima. However, there are two serious drawbacks: First, the minimization will end on any minimum of Ψ, which may either be higher order equilibria or even inflection points of the potential, i.e. local minima in $\|\boldsymbol{F}\|$. Typically, transition states represent only a small subset thereof, and many excess computations have to be done. To identify the desired states, in a second step the spectrum of the minimum configuration has to be inspected. Another issue is that during the minimization second derivatives have to be evaluated, which may be computationally expensive.

An approach inspired by the separating nature of the transition state was proposed by Berry et al. (1988). The idea is, in a first step to generate a path connecting the minima, e.g. by MD-simulations. Thereafter, initial conditions are sampled randomly in the vicinity of the configuration with maximum potential energy, which presumably should be close to the transition state. For each initial condition, a steepest descent quench is performed. Close to a transition state, forces become very small and the minimization algorithm stays in its vicinity for several iterations. Thus, by stopping the algorithm at moderate forces $\|\boldsymbol{F}\|$, quenches can be interrupted close to the transition state before they relax towards a minimum. By sampling several initial points, chances to hit the transition state during the minimization are increased. In contrast to the previous method, the algorithm will not stop at local force minima. However, the co-dimension of the point still has to be determined since the algorithm will terminate at any force equilibrium. Furthermore, due to its unsystematic approach, the algorithm cannot guarantee to find the transition state corresponding to the transition in question.

Ridge algorithm

An algorithm which is conceptually close to the edge tracking algorithm was proposed by Ionova and Carter (1993). Here, we start with two sets of initial conditions, one on either side of the transition state. Hence, the potential energy has a maximum on the line connecting the two configurations. Instead of computing the complete trajectories, each configuration is shifted in the downhill direction, such that the energy maximum on the line connecting the two resulting configurations is lower than the previous maximum. In the next step, two new initial conditions for the next iteration are determined, each one situated on the connecting line and in a distance p from the maximum. Since they are on different sides of a maximum, they evolve towards two different minima. Thereafter, the algorithm repeats itself, gradually approaching the transition state, which by definition has the lowest maximum energy. The algorithm does not check the minima corresponding to the intermediate initial conditions. Thus, when investigating a transition between two minima consisting of a chain of several transitions and intermediate minima, the algorithm will end up on any one of the transition states. Therefore, the algorithm is not suitable for a systematic search for transition paths.

Step and slide algorithm

Similar to the ridge algorithm, the step and slide method (Miron and Fichthorn, 2001) considers two replicas of the system as well. The algorithm incorporates two steps. It starts with a configuration close to each minimum, set to a potential energy Φ_{trial}. In the *slide* phase, both configurations are displaced along their equipotential lines such that the distance between the ensembles is minimized. Thereafter, in the *step* phase, both configurations are shifted towards a higher potential energy level, and the algorithm repeats itself. In case that the new level was set too high and both ensembles collide, an intermediate value of Φ_{trial} is tested. Unlike other algorithms, it thereby brackets the potential energy of the transition state both from below and above. However, it is unsuitable to determine a chain of several subsequent transitions connecting two minima:

The potential energy levels will be increased until only the energetically highest transition state is obtained, ignoring all intermediate transitions.

Nudged elastic band method

In the *Nudged Elastic Band* (NEB) method (Jónsson et al., 1998), not only one or two but many copies of the system are considered, spaced between e.g. two minimum configurations. Each for itself will relax towards the closest minimum, giving no additional information. To prevent this, the copies are connected with each other, forming a band of configurations in the potential energy landscape. Along the connecting lines, spring forces are invoked so that neighboring copies will stay close together. The forces constituted by the potential are then projected on the direction perpendicular to the band, whereas the spring forces are projected on the tangent. In consequence, the copies will form an elastic string, connecting minima via transition states and approximating the minimum energy path. A slight modification is made in the *Climbing Image Nudged Elastic Band* (CI-NEB) algorithm (Henkelman et al., 2000). In the last step, in order to pin the transition state the copy with the largest potential energy is allowed to move uphill. To this end, forces along the line connecting it to its neighbors are inverted. Another modification is the *Doubly Nudged Elastic Band* (DNEB) method, which allows for spring forces perpendicular to the band, as long as they are perpendicular to the potential forces as well (Trygubenko and Wales, 2004). It speeds up convergence, but also leads to deviations from the minimum energy path as it cuts corners in the potential energy landscape. A broad overview over the different realizations of the NEB-algorithm can be found in Sheppard et al. (2008).

An algorithm which is conceptually closely related to the NEB-method is the string method (E et al., 2002). The difference is that the spacing between copies of the system is set explicitly at each iteration, and not determined implicitly by spring forces. More recently, this method has been improved by the application of splines to interpolate between images (E et al., 2007).

All those methods are very efficient. Since the system has to be duplicated several times, memory demand increases likewise, and the implementation is less straightforward as for example of edge tracking. A downside of the NEB algorithms is that with only few images taken into account, the methods may lead to deviations from the optimum path or, more severely, fail to converge.

Activation-relaxation technique & eigenvector following

Another variety of algorithms use a bottom-up approach: They start at a minimum and use different types of hill climbing procedures to find the transition state. The second minimum is obtained by a subsequent minimization.

The activation-relaxation technique (ART) (Barkema and Mousseau, 1996; Mousseau and Barkema, 1998; Barkema and Mousseau, 2001) implements the hill climbing by inverting the force component parallel to the displacement from the starting minimum $\Delta\boldsymbol{x} = \boldsymbol{x} - \boldsymbol{x}_0$,

$$\boldsymbol{g} = \boldsymbol{f} - (1+\alpha)\langle \boldsymbol{F}, \boldsymbol{e}_{\Delta\boldsymbol{x}}\rangle \boldsymbol{e}_{\Delta\boldsymbol{x}}. \tag{A.12}$$

Here, $\boldsymbol{g}$ is the adjusted force, α is a parameter which determines the strength of the inverted force, and $\boldsymbol{e}_{\Delta\boldsymbol{x}}$ is the unit vector of $\Delta\boldsymbol{x}$. Thus, the system will be minimized in all but one direction, at the same time driving it away from the minimum towards a saddle point. At the transition state, the overlap $\langle \boldsymbol{F}, \boldsymbol{e}_{\Delta\boldsymbol{x}} \rangle$ will reverse its sign, thus providing a stopping criterion.

It is crucial to define $\Delta\boldsymbol{x}$ properly. If all particles are considered in $\Delta\boldsymbol{x}$, the method is likely to fail, as the displacement quickly spreads across all particles such that the few particles to exchange their positions fall back upon their initial coordinates. However, when restricting $\Delta\boldsymbol{x}$ to only a few particles, for example to those which should exchange their positions, this method gives a good approximation of the transition state, i.e. the force is non-zero, and the associated energy and unstable eigenvalue are slightly off.

Obviously, this method is only able to detect a single transition at a time. Thereafter, the next minimum has to be determined, and the process can be restarted. However, in a chain of several transitions, it is a non-trivial task to identify the next search direction. Moreover, it becomes unreliable the more particles are considered in $\Delta\boldsymbol{x}$.

A more involved method is the eigenvector following (Wales, 1994; Munro and Wales, 1999). As the name suggests, the direction of the least stable mode is evaluated, and the system is then displaced uphill along this direction and optimized in the perpendicular space. Just as ART, it is a single ended method, less suitable for finding prescribed connections between minima.

Dimer method

A method which can be seen as closely related to both the band methods and eigenvector following is the dimer-method (Henkelman and Jónsson, 1999). It uses two copies of the system, with the distance between them kept fixed. This dimer is then rotated such that its orientation is parallel to the direction of lowest curvature. In the picture of an energy landscape, it is oriented along a valley. This is equivalent to a minimization of the combined potential energy of the constituting particles, while keeping the center of mass fixed. Thereby, potentially expensive evaluations of second derivatives are avoided. Afterwards, the potential force is applied, where the force component parallel to the orientation of the dimer is inverted, subsequently pushing the dimer uphill towards a transition state. This last step is conceptually the same in the eigenvector following, where the direction is directly derived from the spectrum. This method is especially interesting for systems where the evaluation of the spectrum is computationally expensive. The crucial point is an effective way to implement the rotation of the dimer.

A.5 Analytical solution for the singular force in an infinite 2d-solid

To solve the problem of the singular force in an infinite two-dimensional solid, several analytical approaches exist. One possibility is to use a potential formulation with Airy stress functions, where in polar coordinates the general solution is given by the Michell solution (Michell, 1899).

Here, we follow the calculations of (Landau and Lifschitz, 1966) who derived the solution for the three-dimensional problem. Starting from eqn. (5.16b) and a singular force $\boldsymbol{F} = \boldsymbol{F}\delta(r)$, we note that when writing the displacements as a sum

$$\boldsymbol{u} = \boldsymbol{u}^{(0)} + \boldsymbol{u}^{(1)}, \tag{A.13}$$

we can recast the elastostatic equation as two separate ones, a Poisson-equation and an inhomogeneous part, namely

$$\Delta \boldsymbol{u}^{(0)} = -\frac{1}{\mu_L}\boldsymbol{F}\delta(r) \tag{A.14a}$$

$$\text{grad div } \boldsymbol{u}^{(1)} + \frac{\mu_L}{\lambda_L + \mu_L}\Delta \boldsymbol{u}^{(1)} = -\text{grad div } \boldsymbol{u}^{(0)}. \tag{A.14b}$$

The Poisson-equation is solved by

$$\boldsymbol{u}^{(0)} = -\frac{\boldsymbol{F}}{2\pi\mu_L}\log(\sqrt{x^2+y^2}) = -\frac{\boldsymbol{F}}{2\pi\mu_L}\log(r). \tag{A.15}$$

Taking the curl of eqn. (A.14b), we find

$$\text{curl grad div } \boldsymbol{u}^{(1)} + \frac{\mu_L}{\lambda_L + \mu_L}\text{curl } \Delta \boldsymbol{u}^{(1)} = -\text{curl grad div } \boldsymbol{u}^{(0)} \tag{A.16a}$$

$$0 + \frac{\mu_L}{\lambda_L + \mu_L}\Delta\text{curl } \boldsymbol{u}^{(1)} = 0. \tag{A.16b}$$

Hence, and because curl $\boldsymbol{u}^{(1)}$ has to vanish at infinity, it follows that it has to vanish at any distance, i.e. $\boldsymbol{u}^{(1)}$ can be described by a potential, $\boldsymbol{u}^{(1)} = \text{grad } \phi$. We can thus rewrite eqn. (A.14b) as

$$\text{grad } \left(\text{div grad } \phi + \frac{\mu_L}{\lambda_L + \mu_L}\Delta\phi + \text{div } \boldsymbol{u}^{(0)}\right) = 0. \tag{A.17}$$

Therefore, the part in brackets has to be constant, and since it vanishes at $r \to \infty$, we have

$$\Delta\phi = \frac{\mu_L + \lambda_L}{2\mu_L + \lambda_L}\frac{1}{2\pi\mu_L}\left(F_x\partial_x + F_y\partial_y\right)\log(\sqrt{x^2+y^2}). \tag{A.18}$$

Taking Ψ such that $\Delta\Psi = \log(r)$, we end up with

$$\Psi = \frac{1}{4}r^2\left(\log(r) - 1\right) \tag{A.19}$$

$$\begin{aligned}\phi &= \frac{\mu_L + \lambda_L}{2\mu_L + \lambda_L}\frac{1}{2\pi\mu_L}\boldsymbol{F}\text{grad } \Psi \\ &= \frac{\mu_L + \lambda_L}{2\mu_L + \lambda_L}\frac{1}{2\pi\mu_L}\left[F_x x(\frac{1}{2}(\log(r) - \frac{1}{2})) + F_y y(\frac{1}{2}(\log(r) - \frac{1}{2}))\right].\end{aligned} \tag{A.20}$$

This finally leads to

$$\boldsymbol{u}^{(1)} = \frac{\mu_L + \lambda_L}{2\mu_L + \lambda_L}\frac{1}{4\pi\mu_L}\begin{pmatrix} F_x\left(\log(r) - \frac{1}{2}\right) + \left(F_x x + F_y y\right)\frac{x}{r^2} \\ F_y\left(\log(r) - \frac{1}{2}\right) + \left(F_x x + F_y y\right)\frac{y}{r^2}\end{pmatrix}. \tag{A.21}$$

Considering a singular force $\boldsymbol{F}(r) = F_x\delta(r)\boldsymbol{e}_x$, we obtain eqn. (5.30).

A.6 Discretization on a hexagonal lattice

Since the global minimum of our two-dimensional system shows a hexagonal lattice structure, it is appealing to discretize the Navier-Cauchy equation on this lattice as well. To this end, we first have to derive the corresponding differential operators, the following idea being borrowed from Sun et al. (2003). We start by introducing three lattice vectors of unit length,

$$\boldsymbol{r} = \begin{pmatrix} -1/2 \\ \sqrt{3}/2 \end{pmatrix}, \qquad \boldsymbol{s} = \begin{pmatrix} -1/2 \\ -\sqrt{3}/2 \end{pmatrix}, \qquad \boldsymbol{t} = \begin{pmatrix} 1 \\ 0 \end{pmatrix}. \tag{A.22}$$

Derivatives along these principal directions are given by the directional derivatives and read

$$\partial_r u = (\boldsymbol{\nabla} u)\,\boldsymbol{r} = -\tfrac{1}{2}\partial_x u + \tfrac{\sqrt{3}}{2}\partial_y u \tag{A.23a}$$
$$\partial_s u = -\tfrac{1}{2}\partial_x u - \tfrac{\sqrt{3}}{2}\partial_y u \tag{A.23b}$$
$$\partial_t u = \partial_x u \tag{A.23c}$$
$$\partial_{rr} u = \tfrac{1}{4}\partial_{xx} u - \tfrac{\sqrt{3}}{2}\partial_{xy} u + \tfrac{3}{4}\partial_{yy} u \tag{A.23d}$$
$$\partial_{ss} u = \tfrac{1}{4}\partial_{xx} u + \tfrac{\sqrt{3}}{2}\partial_{xy} u + \tfrac{3}{4}\partial_{yy} u \tag{A.23e}$$
$$\partial_{tt} u = \partial_{xx} u. \tag{A.23f}$$

By forming the appropriate sums we can now identify expressions for the differential operators in eqn. (5.16c):

$$\partial_{xx} u = \partial_{tt} u \tag{A.24a}$$
$$\partial_{yy} u = \tfrac{2}{3}\left(\partial_{rr} + \partial_{ss} - \tfrac{1}{2}\partial_{tt}\right) u \tag{A.24b}$$
$$\partial_{xy} u = \tfrac{1}{\sqrt{3}}\left(\partial_{ss} - \partial_{rr}\right) u. \tag{A.24c}$$

Thus, all differential operators can be recast using second order directional derivatives along the three lattice directions. We can now rewrite eqn. (5.16c) as

$$\left[\partial_{rr}\mathbf{R} + \partial_{ss}\mathbf{S} + \partial_{tt}\mathbf{T}\right] \begin{pmatrix} u_x \\ u_y \end{pmatrix} + \begin{pmatrix} F_x \\ F_y \end{pmatrix} = \begin{pmatrix} 0 \\ 0 \end{pmatrix}, \tag{A.25}$$

with

$$\mathbf{R} = \begin{pmatrix} \frac{2}{3}\mu & -\frac{1}{\sqrt{3}}(\mu+\lambda) \\ -\frac{1}{\sqrt{3}}(\mu+\lambda) & \frac{2}{3}(2\mu+\lambda) \end{pmatrix} \tag{A.26a}$$
$$\mathbf{S} = \begin{pmatrix} \frac{2\mu}{3} & \frac{1}{\sqrt{3}}(\mu+\lambda) \\ \frac{1}{\sqrt{3}}(\mu+\lambda) & \frac{2}{3}(2\mu+\lambda) \end{pmatrix} \tag{A.26b}$$
$$\mathbf{T} = \begin{pmatrix} \frac{5}{3}\mu+\lambda & 0 \\ 0 & \frac{1}{3}(\mu-\lambda) \end{pmatrix}. \tag{A.26c}$$

Each of the derivatives can be discretized by a 3-point central difference scheme,

$$\partial_{kk} u_i = \left(u_{(i+h\boldsymbol{k})} + u_{(i-h\boldsymbol{k})} - 2u_i\right)/h^2, \tag{A.27}$$

with $k \in \{r, s, t\}$. Plugging this into eqn. (A.25), we end up with a linear system of equations for the displacements, discretized on a hexagonal lattice:

$$\mathbf{A}\boldsymbol{u} + \boldsymbol{F} = \mathbf{0}. \tag{A.28}$$

At the i-th site, the corresponding matrix reads

$$\begin{array}{c|ccccccc} & \leftarrow & \nwarrow & \nearrow & u_x\ u_y & \swarrow & \searrow & \rightarrow \\ \begin{matrix} u_x \\ u_y \end{matrix} & \mathbf{T}/h^2 & \mathbf{R}/h^2 & \mathbf{S}/h^2 & -\boldsymbol{\Sigma}/h^2 & \mathbf{S}/h^2 & \mathbf{R}/h^2 & \mathbf{T}/h^2 \end{array} \tag{A.29}$$

where arrows point to the neighbor in question. The diagonal elements are given by

$$\boldsymbol{\Sigma} = 2\left(\mathbf{R} + \mathbf{S} + \mathbf{T}\right) = \begin{pmatrix} 2\left(3\mu + \lambda\right) & 0 \\ 0 & 2\left(3\mu + \lambda\right) \end{pmatrix}, \tag{A.30}$$

and all other entries are zero. For a very short interaction radius such that only the next neighbors are considered, the matrix $\mathbf{A}$ corresponds to the Jacobian of the Yukawa-system.

Direct correspondence

In dynamical equilibrium, the linearization of the Yukawa-system around its lattice configuration reads

$$\mathbf{0} + \mathbf{H}\boldsymbol{u} = \mathbf{0}, \tag{A.31}$$

where $\boldsymbol{u}$ are the displacements from the equilibrium position. When choosing a cut-off radius $r_{\text{cut}} < \sqrt{3}$, both matrices $\mathbf{A}$ (eqn. (A.28)) and $\mathbf{H}$ show the same structure, i.e. only next-neighbor relations are taken into account. Moreover, a closer inspection reveals that both matrices match exactly for an appropriate set of Lamé coefficients. For example, in the case of $\mu = 10.0$ and $r_{\text{cut}} = 1.5$ with $h = r_{ij} = 1.0$, we obtain

$$\lambda_L = 3.013 \times 10^{-3} \qquad \mu_L = 1.515 \times 10^{-3}. \tag{A.32}$$

This correspondence can be seen when rewriting the matrices $\mathbf{R}$, $\mathbf{S}$ and $\mathbf{T}$,

$$\mathbf{T} = \begin{pmatrix} \frac{5}{3}\mu + \lambda & 0 \\ 0 & \frac{1}{3}(\mu - \lambda) \end{pmatrix} = \frac{1}{3}\left(\mu_L - \lambda_L\right)\mathbb{I} + \frac{4}{3}\left(\mu_L + \lambda_L\right)\boldsymbol{t} \otimes \boldsymbol{t} \tag{A.33a}$$

$$\mathbf{R} = \frac{1}{3}\left(\mu_L - \lambda_L\right)\mathbb{I} + \frac{4}{3}\left(\mu_L + \lambda_L\right)\boldsymbol{r} \otimes \boldsymbol{r} \tag{A.33b}$$

$$\mathbf{S} = \frac{1}{3}\left(\mu_L - \lambda_L\right)\mathbb{I} + \frac{4}{3}\left(\mu_L + \lambda_L\right)\boldsymbol{s} \otimes \boldsymbol{s}. \tag{A.33c}$$

A Comparison with the Jacobian eqn. (3.7) and the finite difference scheme eqn. (A.29) reveals the exact same structure, which is inherent for any conservative potential. As a consequence, small perturbations of the Yukawa-system can be described by linear elasticity theory, at least in the limit of small cut-off radii. Obviously, this correspondence is unapparent when considering the rectangular lattice where the Yukawa-system is unstable.

A.7 Displacement fields of superimposed singular forces

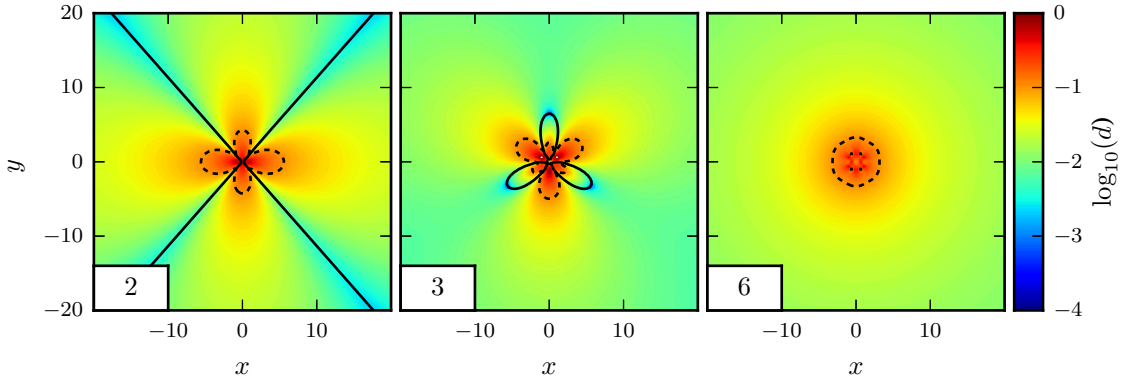

Figure A.4: Superposition of displacement fields of singular forces in an infinite solid, eqn. (5.30). Combined are - from left to right - 2, 3, and 6 singular forces. They are placed on a unit circle, pointing outwards with $\|\boldsymbol{F}\| = 1$. The elastic constants are those of the particle system at $\mu = 3$. Solid lines represent vanishing radial displacements, dashed lines mark $d = 0.1$. The displacement fields show qualitative agreement with those of the two-particle, three-particle and hexagonal six-particle exchanges, 2_0, 3_0 and 6_0 shown in figure 5.5(a) and figure 6.1(a),(d). Due to the missing periodic boundaries, displacements drop off considerably slower. In order to match the displacement fields of the transition state more accurately, boundary conditions as well as position and strength of the forces would have to be adjusted.

A.8 Spectrum reductions

The calculation of the spectrum turns out to be computationally expensive for large systems since we have to solve a (sparse) eigenvalue problem in $3N$ or $2N$ dimensions. We follow an approach by Brooks et al. (1995) and perform a reduced basis normal mode analysis. The principal idea is to remove less important degrees of freedom from the Jacobian of the system. To achieve this, the Jacobian is partitioned into two parts which, ideally, would form two separate blocks. The method was developed for molecules where this holds in many cases, for example when separating local vibrations from global motions. However, since part of the system is neglected despite a (possible) coupling, an unfortunate choice of the basis set can lead to wrong predictions. The algorithm itself goes as follows:

- Unwanted motions are detected and a set $\{\Psi_i\}$ of orthonormal vectors is produced using Gram-Schmidt orthonormalization.
- The m relevant degrees of freedom are defined and a set $\{\Phi_i\}$ of orthonormal vectors is produced. They are orthogonalized with respect to $\{\Psi_i\}$.
- The reduced Jacobian is computed, $\tilde{\mathbf{H}} = \mathbf{\Phi}^\dagger \mathbf{H} \mathbf{\Phi}$. $\tilde{\mathbf{H}}$ is now a $m \times m$ matrix.

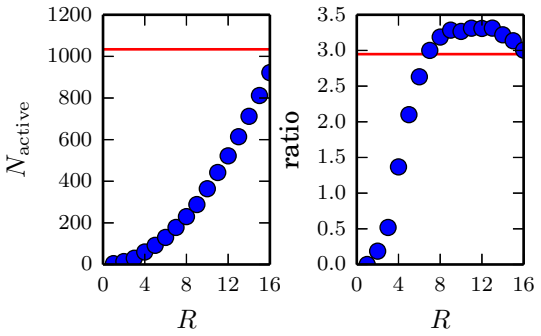

Figure A.5: Ratio eqn. (A.34) as function of active particles. Particles are considered active inside a circle of radius R around the center of deformation. Deviation decreases with the number of active particles but reaches the ratio of the full system only for $R \to R_{\text{fix}}$.

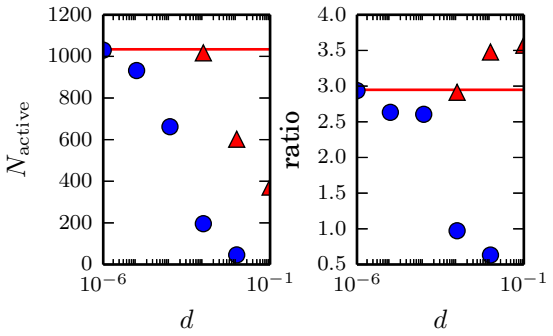

Figure A.6: Ratio eqn. (A.34) as function of active particles. Particles are considered active if displaced from their minimum positions by a threshold d (blue circles) or if additionally they are interacting with such particles (red triangles).

- $\tilde{\mathbf{H}}$ is diagonalized, $\mathbf{U}^{\dagger}\tilde{\mathbf{H}}\mathbf{U} = \mathbf{\Lambda}$ where $\mathbf{U}$ is a unitary matrix (essentially, its columns are the eigenvectors). Its eigenvalues are bounded by the eigenvalues of $\mathbf{H}$.

- The normal modes of the full problem are given by $y_a = \sum \Phi_j U_{ja}$.

The crucial step is to determine which motions to take into account, especially when considering long-range interactions. Here, we only considered single particles and no coordinated motions of groups of particles. The Φ_i are thus given by the cartesian basis vectors of active particles, e.g. $\Phi_1 = \boldsymbol{e}_{0,x}$, $\Phi_2 = \boldsymbol{e}_{0,y}$, $\Phi_3 = \boldsymbol{e}_{0,z}$, and so on. This essentially breaks down to algorithm to eliminating rows and columns of the Jacobian.

In a first attempt, we set inactive rows and columns to zero. We then solve the eigenvalue problem using an Arnoldi algorithm (Lehoucq et al., 1998), aiming for eigenvalues with largest magnitude. For $N_{\text{active}} > 10$ and when starting with a random vector, this gives a good approximation, i.e. no neutral modes corresponding to inactive particles are computed.

We tested several approaches. First, we put a sphere of radius R around the center of deformation. All particles inside are considered active. In a second approach, we determine the displacement of each particle at the transition state. When a certain threshold is exceeded, the particle is marked as active. This is motivated by the idea that for inactive particles, relative displacements hardly change and thus the Jacobian locally should be similar for both configurations. However, existing interactions with the active particles are neglected as well and will alter the results. This is addressed an a third approach, where we consider the same threshold, but also take into account all particles directly interacting with the identified ones.

We compare the ratio

$$\frac{1}{2\pi}\frac{\prod_{i=1}^{N}\sqrt{-\lambda_i^0}}{\prod_{i=2}^{N}\sqrt{-\lambda_i^*}} \tag{A.34}$$

obtained with those approaches for various parameters with the ratio of the full system with $N = 2500$ particles, the results shown in figures A.5 & A.6. In order to eliminate effects from periodic boundary conditions and symmetry restrictions, we fix particles beyond a distance to the center of deformation of $R_{\text{fix}} = L_y/2 - 4.75$ at their positions, thus preventing interactions across the periodic boundary. Irrespective of the approach we choose, a good agreement with the ratio of the full system is only achieved in the limit of $N_{\text{active}} \to N_{\text{system}}$.

Bibliography

Barber, C. B., Dobkin, D. P., and Huhdanpaa, H. (1996). The quickhull algorithm for convex hulls. *ACM Trans. Math. Softw.*, 22(4):469–483.

Barkema, G. T. and Mousseau, N. (1996). Event-Based Relaxation of Continuous Disordered Systems. *Phys. Rev. Lett.*, 77(21):4358–4361.

Barkema, G. T. and Mousseau, N. (2001). The activation–relaxation technique: an efficient algorithm for sampling energy landscapes. *Comput. Mater. Sci.*, 20(3-4):285–292.

Bausch, A. R., Bowick, M. J., Cacciuto, A., Dinsmore, A. D., Hsu, M. F., Nelson, D. R., Nikolaides, M. G., Travesset, A., and Weitz, D. A. (2003). Grain boundary scars and spherical crystallography. *Science*, 299(5613):1716–8.

Bedanov, V. M., Gadiyak, G. V., and Lozovik, Y. E. (1985a). Melting of two-dimensional crystals. *Zh. Éksp. Teor. Fiz*, 88:1622.

Bedanov, V. M., Gadiyak, G. V., and Lozovik, Y. E. (1985b). On a modified Lindemann-like criterion for 2D melting. *Phys. Lett. A*, 109(6):289–291.

Bell, R. J. and Dean, P. (1970). Atomic vibrations in vitreous silica. *Discuss. Faraday Soc.*, 50:55.

Berry, R. S. (1990). Introductory lecture. Clusters, melting, freezing and phase transitions. *J. Chem. Soc. Faraday Trans.*, 86(13):2343.

Berry, R. S. (1993). Potential surfaces and dynamics: what clusters tell us. *Chem. Rev.*, 93(7):2379–2394.

Berry, R. S., Davis, H. L., and Beck, T. L. (1988). Finding saddles on multidimensional potential surfaces. *Chem. Phys. Lett.*, 147(1):13–17.

Berry, R. S. and Wales, D. J. (1989). Freezing, melting, spinodals, and clusters. *Phys. Rev. Lett.*, 63(11):1156–1159.

Binder, K., Sengupta, S., and Nielaba, P. (2002). The liquid-solid transition of hard discs: first-order transition or Kosterlitz-Thouless-Halperin-Nelson-Young scenario? *J. Phys. Condens. Matter*, 14(9):2323–2333.

Boltzmann, L. (1877). Bemerkungen über einige Probleme der mechanischen Wärmetheorie. *Sitzungsber. Kais. Akad. Wiss. Wien*, 75:62 – 100.

Brooks, B. R., Janežič, D., and Karplus, M. (1995). Harmonic analysis of large systems. I. Methodology. *J. Comput. Chem.*, 16(12):1522–1542.

Carr, H. Y. and Purcell, E. M. (1954). Effects of Diffusion on Free Precession in Nuclear Magnetic Resonance Experiments. *Phys. Rev.*, 94(3):630–638.

Casati, G., Chirikov, B. V., Guarneri, I., and Shepelyansky, D. L. (1986). Dynamical Stability of Quantum "Chaotic" Motion in a Hydrogen Atom. *Phys. Rev. Lett.*, 56(23):2437–2440.

Cassak, P. A., Drake, J. F., Shay, M. A., and Eckhardt, B. (2007). Onset of Fast Magnetic Reconnection. *Phys. Rev. Lett.*, 98(21):215001.

Chaiken, J., Chevray, R., Tabor, M., and Tan, Q. M. (1986). Experimental Study of Lagrangian Turbulence in a Stokes Flow. *Proc. R. Soc. A*, 408(1834):165–174.

Chicone, C. (2006). *Ordinary Differential Equations with Applications*, volume 34 of *Texts in Applied Mathematics*. Springer New York, ISBN: 978-0-387-30769-5.

Chu, J. H. and I, L. (1994). Direct observation of Coulomb crystals and liquids in strongly coupled rf dusty plasmas. *Phys. Rev. Lett.*, 72(25):4009–4012.

Chui, S. T. (1982). Grain-Boundary Theory of Melting in Two Dimensions. *Phys. Rev. Lett.*, 48(14):933–935.

Chui, S. T. (1983). Grain-boundary theory of melting in two dimensions. *Phys. Rev. B*, 28(1):178–194.

Corté, L., Chaikin, P. M., Gollub, J. P., and Pine, D. J. (2008). Random organization in periodically driven systems. *Nat. Phys.*, 4(5):420–424.

Corté, L., Gerbode, S. J., Man, W., and Pine, D. J. (2009). Self-Organized Criticality in Sheared Suspensions. *Phys. Rev. Lett.*, 103(24):248301.

Dasgupta, R., Hentschel, H. G. E., and Procaccia, I. (2012). Microscopic Mechanism of Shear Bands in Amorphous Solids. *Phys. Rev. Lett.*, 109(25):255502.

Dasgupta, R., Hentschel, H. G. E., and Procaccia, I. (2013). Yield strain in shear banding amorphous solids. *Phys. Rev. E*, 87(2):022810.

Dash, J. G. (1999). History of the search for continuous melting. *Rev. Mod. Phys.*, 71(5):1737–1743.

DaSilva, L. C., Cândido, L., da F. Costa, L., and Oliveira, O. N. (2007). Formation energy and interaction of point defects in two-dimensional colloidal crystals. *Phys. Rev. B*, 76(3):035441.

Derzsi, A., Kovács, A. Z., Donkó, Z., and Hartmann, P. (2014). On the metastability of the hexatic phase during the melting of two-dimensional charged particle solids. *Phys. Plasmas*, 21(2):023706.

Deutschländer, S., Horn, T., Löwen, H., Maret, G., and Keim, P. (2013). Two-Dimensional Melting under Quenched Disorder. *Phys. Rev. Lett.*, 111(9):098301.

Dillmann, P., Maret, G., and Keim, P. (2012). Comparison of 2D melting criteria in a colloidal system. *J. Phys. Condens. Matter*, 24(46):464118.

Düring, G., Bartolo, D., and Kurchan, J. (2009). Irreversibility and self-organization in hydrodynamic echo experiments. *Phys. Rev. E*, 79(3):030101.

E, W., Ren, W., and Vanden-Eijnden, E. (2002). String method for the study of rare events. *Phys. Rev. B*, 66(5):052301.

E, W., Ren, W., and Vanden-Eijnden, E. (2007). Simplified and improved string method for computing the minimum energy paths in barrier-crossing events. *J. Chem. Phys.*, 126(16):164103.

Eckhardt, B. (2003). Echoes in classical dynamical systems. *J. Phys. A*, 36(2):371–380.

Eckmann, J.-P. and Ruelle, D. (1985). Ergodic theory of chaos and strange attractors. *Rev. Mod. Phys.*, 57(3):617–656.

Eyring, H. (1935a). The Activated Complex and the Absolute Rate of Chemical Reactions. *Chem. Rev.*, 17(1):65–77.

Eyring, H. (1935b). The Activated Complex in Chemical Reactions. *J. Chem. Phys.*, 3(2):107.

Fiocco, D., Foffi, G., and Sastry, S. (2013). Oscillatory athermal quasistatic deformation of a model glass. *Phys. Rev. E*, 88(2):020301.

Fiocco, D., Foffi, G., and Sastry, S. (2014). Encoding of Memory in Sheared Amorphous Solids. *Phys. Rev. Lett.*, 112(2):025702.

Fisher, D. S., Halperin, B. I., and Morf, R. (1979). Defects in the two-dimensional electron solid and implications for melting. *Phys. Rev. B*, 20(11):4692–4712.

Franceschini, A., Filippidi, E., Guazzelli, E., and Pine, D. J. (2011). Transverse Alignment of Fibers in a Periodically Sheared Suspension: An Absorbing Phase Transition with a Slowly Varying Control Parameter. *Phys. Rev. Lett.*, 107(25):250603.

Franceschini, A., Filippidi, E., Guazzelli, E., and Pine, D. J. (2014). Dynamics of non-Brownian fiber suspensions under periodic shear. *Soft Matter*, 10(35):6722–31.

Frenkel, J. (1946). *Kinetic Theory of Liquids*. Oxford University Press.

Galassi et al., M. (2010). *GNU Scientific Library Reference Manual - Third Edition*. Network Theory Ltd., ISBN: 0954612078. Library available online at http://www.gnu.org/software/gsl/.

Gilvarry, J. J. (1956). The Lindemann and Grüneisen Laws. *Phys. Rev.*, 102(2):308–316.

Grimvall, G. and Sjödin, S. (1974). Correlation of Properties of Materials to Debye and Melting Temperatures. *Phys. Scr.*, 10(6):340–352.

Guasto, J. S., Ross, A. S., and Gollub, J. P. (2010). Hydrodynamic irreversibility in particle suspensions with nonuniform strain. *Phys. Rev. E*, 81(6):061401.

Guckenheimer, J. and Holmes, P. (2002). *Nonlinear Oscillations, Dynamical Systems, and Bifurcation Theory*. Springer-Verlag New York Berlin Heidelberg, 7th edition, ISBN: 978-0-387-90819-9.

Guennebaud, G., Jacob, B., and Others (2010). Eigen v3. http://eigen.tuxfamily.org.

Gupta, R. P. and Sharma, P. K. (1968). Test of a Melting Criterion for Cubic Metals. *J. Chem. Phys.*, 48(6):2451.

Hahn, E. L. (1950). Spin Echoes. *Phys. Rev.*, 80(4):580–594.

Halperin, B. I. and Nelson, D. R. (1978). Theory of Two-Dimensional Melting. *Phys. Rev. Lett.*, 41(2):121–124.

Hänggi, P., Talkner, P., and Borkovec, M. (1990). Reaction-rate theory: fifty years after Kramers. *Rev. Mod. Phys.*, 62(2):251–341.

Hartmann, P., Donkó, Z., Bakshi, P. M., Kalman, G. J., and Kyrkos, S. (2007). Molecular Dynamics Studies of Solid–Liquid Phase Transition in 2-D Yukawa Systems. *IEEE Trans. Plasma Sci.*, 35(2):332–336.

Hartmann, P., Kalman, G. J., Donkó, Z., and Kutasi, K. (2005). Equilibrium properties and phase diagram of two-dimensional Yukawa systems. *Phys. Rev. E*, 72(2):026409.

Hartmann, P., Sándor, M. C., Kovács, A., and Donkó, Z. (2011). Static and dynamic shear viscosity of a single-layer complex plasma. *Phys. Rev. E*, 84(1):016404.

Henderson, M. E. (2005). Computing Invariant Manifolds by Integrating Fat Trajectories. *SIAM J. Appl. Dyn. Syst.*, 4(4):832–882.

Henkelman, G. and Jónsson, H. (1999). A dimer method for finding saddle points on high dimensional potential surfaces using only first derivatives. *J. Chem. Phys.*, 111(15):7010.

Henkelman, G., Uberuaga, B. P., and Jónsson, H. (2000). A climbing image nudged elastic band method for finding saddle points and minimum energy paths. *J. Chem. Phys.*, 113(22):9901.

Homsy, G. M., editor (2008). *Multimedia Fluid Dynamics*. Cambridge University Press, 2nd edition, ISBN: 978052172169.

Ionova, I. V. and Carter, E. A. (1993). Ridge method for finding saddle points on potential energy surfaces. *J. Chem. Phys.*, 98(8):6377.

Jain, S. and Nelson, D. R. (2000). Statistical mechanics of vacancy and interstitial strings in hexagonal columnar crystals. *Phys. Rev. E*, 61(2):1599–1615.

Jeanneret, R. and Bartolo, D. (2014). Geometrically protected reversibility in hydrodynamic Loschmidt-echo experiments. *Nat. Commun.*, 5:3474.

Jin, Z. H., Gumbsch, P., Lu, K., and Ma, E. (2001). Melting Mechanisms at the Limit of Superheating. *Phys. Rev. Lett.*, 87(5):055703.

Jónsson, H., Mills, G., and Jacobsen, K. W. (1998). Nudged elastic band method for finding minimum energy paths of transitions. In Berne, B., Ciccotti, G., and Coker, D., editors, *Class. Quantum Dyn. Condens. Phase Simulations - Proc. Int. Sch. Phys.*, pages 385–404, Singapore. World Scientific Publishing Co. Pte. Ltd.

Kapfer, S. C. and Krauth, W. (2015). Two-Dimensional Melting: From Liquid-Hexatic Coexistence to Continuous Transitions. *Phys. Rev. Lett.*, 114(3):035702.

Keim, N. C. and Arratia, P. E. (2013). Yielding and microstructure in a 2D jammed material under shear deformation. *Soft Matter*, 9(27):6222.

Keim, N. C. and Arratia, P. E. (2014). Mechanical and Microscopic Properties of the Reversible Plastic Regime in a 2D Jammed Material. *Phys. Rev. Lett.*, 112(2):028302.

Keim, N. C. and Nagel, S. R. (2011). Generic Transient Memory Formation in Disordered Systems with Noise. *Phys. Rev. Lett.*, 107(1):010603.

Keim, N. C., Paulsen, J. D., and Nagel, S. R. (2013). Multiple transient memories in sheared suspensions: Robustness, structure, and routes to plasticity. *Phys. Rev. E*, 88(3):032306.

Keim, P., Maret, G., and von Grünberg, H. H. (2007). Frank's constant in the hexatic phase. *Phys. Rev. E*, 75(3):031402.

Kleinert, H. (1989). Test of new melting criterion. Angular stiffness and order of 2D melting in Lennard-Jones and Wigner lattices. *Phys. Lett. A*, 136(9):468–471.

Knapek, C. (2010). *Phase Transitions in Two-Dimensional Complex Plasmas*. PhD thesis, Ludwig-Maximilians-Universität München.

Knapek, C. A., Samsonov, D., Zhdanov, S., Konopka, U., and Morfill, G. E. (2007). Recrystallization of a 2D Plasma Crystal. *Phys. Rev. Lett.*, 98(1):015004.

Konopka, U., Morfill, G. E., and Ratke, L. (2000). Measurement of the Interaction Potential of Microspheres in the Sheath of a rf Discharge. *Phys. Rev. Lett.*, 84(5):891–894.

Kosterlitz, J. M. and Thouless, D. J. (1973). Ordering, metastability and phase transitions in two-dimensional systems. *J. Phys. C: Solid State Phys.*, 6(7):1181–1203.

Kramers, H. A. (1940). Brownian motion in a field of force and the diffusion model of chemical reactions. *Physica*, 7(4):284–304.

Landau, L. D. and Lifschitz, E. M. (1966). *Lehrbuch der theoretischen Physik VII - Elastizitätstheorie*. Akademie Verlag Berlin, 2. edition.

Lees, A. W. and Edwards, S. F. (1972). The computer study of transport processes under extreme conditions. *J. Phys. C: Solid State Phys.*, 5(15):1921–1928.

Lehoucq, R. R. B., Sorensen, D. D. C., and Yang, C.-C. (1998). *Arpack User's Guide: Solution of Large-Scale Eigenvalue Problems With Implicityly Restarted Arnoldi Methods*. Siam, 6 edition, ISBN: 978-0-89871-407-4. Library available online at http://www.caam.rice.edu/software/ARPACK/.

Libál, A., Reichhardt, C., and Olsen Reichhardt, C. J. (2007). Point-defect dynamics in two-dimensional colloidal crystals. *Phys. Rev. E*, 75(1):011403.

Likhachev, V. N., Astakhova, T. Y., Ebeling, W., and Vinogradov, G. A. (2009). Equilibrium thermodynamics and thermodynamic processes in nonlinear systems. *Eur. Phys. J. B*, 72(2):247–256.

Lindemann, F. A. (1910). Ueber die Berechnung molekularer Eigenfrequenzen. *Phys Z.*, 11(14):609–612.

Loschmidt, J. (1876). Über den Zustand des Wärmegleichgewichts eines Systems von Körpern mit Rücksicht auf die Schwerkraft. *Sitzungsber. Kais. Akad. Wiss. Wien*, 73:128 – 142.

Löwen, H. (1992). Structure and Brownian dynamics of the two-dimensional Yukawa fluid. *J. Phys. Condens. Matter*, 4(50):10105–10116.

Löwen, H., Allahyarov, E., Likos, C. N., Blaak, R., Dzubiella, J., Jusufi, A., Hoffmann, N., and Harreis, H. M. (2003). Charged colloids, polyelectrolytes and biomolecules viewed as strongly coupled Coulomb systems. *J. Phys. A*, 36(22):5827–5834.

Lozovik, Y. E. and Farztdinov, V. M. (1985). Oscillation spectra and phase diagram of two-dimensional electron crystal: "New" (3+4)-self-consistent approximation. *Solid State Commun.*, 54(8):725–728.

Mangan, N., Reichhardt, C., and Olson Reichhardt, C. J. (2008). Reversible to Irreversible Flow Transition in Periodically Driven Vortices. *Phys. Rev. Lett.*, 100(18):187002.

Meissner, G., Namaizawa, H., and Voss, M. (1976). Stability and image-potential-induced screening of electron vibrational excitations in a three-layer structure. *Phys. Rev. B*, 13(4):1370–1376.

Melzer, A., Homann, A., and Piel, A. (1996a). Experimental investigation of the melting transition of the plasma crystal. *Phys. Rev. E*, 53(3):2757–2766.

Melzer, A., Schweigert, V. A., Schweigert, I. V., Homann, A., Peters, S., and Piel, A. (1996b). Structure and stability of the plasma crystal. *Phys. Rev. E*, 54(1):R46–R49.

Menon, G. I. and Ramaswamy, S. (2009). Universality class of the reversible-irreversible transition in sheared suspensions. *Phys. Rev. E*, 79(6):061108.

Merlino, R. L. and Goree, J. A. (2004). Dusty plasmas in the laboratory, industry, and space. *Phys. Today*, 57(7):32–38.

Mermin, N. D. (1968). Crystalline Order in Two Dimensions. *Phys. Rev.*, 176(1):250–254.

Metzger, B. and Butler, J. E. (2010). Irreversibility and chaos: Role of long-range hydrodynamic interactions in sheared suspensions. *Phys. Rev. E*, 82(5):051406.

Metzger, B. and Butler, J. E. (2012). Clouds of particles in a periodic shear flow. *Phys. Fluids*, 24(2):021703.

Michell, J. H. (1899). On the Direct Determination of Stress in an Elastic Solid, with application to the Theory of Plates. *Proc. London Math. Soc.*, s1-31(1):100–124.

Miron, R. A. and Fichthorn, K. A. (2001). The Step and Slide method for finding saddle points on multidimensional potential surfaces. *J. Chem. Phys.*, 115(19):8742.

Mohan, L., Pellet, C., Cloitre, M., and Bonnecaze, R. (2013). Local mobility and microstructure in periodically sheared soft particle glasses and their connection to macroscopic rheology. *J. Rheol.*, 57(3):1023–1046.

Motohashi, A. and Okuma, S. (2011). Plastic depinning in superconducting vortices. *J. Phys. Conf. Ser.*, 302:012029.

Mousseau, N. and Barkema, G. T. (1998). Traveling through potential energy landscapes of disordered materials: The activation-relaxation technique. *Phys. Rev. E*, 57(2):2419–2424.

Munro, L. J. and Wales, D. J. (1999). Defect migration in crystalline silicon. *Phys. Rev. B*, 59(6):3969–3980.

Murray, C. A. and Van Winkle, D. H. (1987). Experimental observation of two-stage melting in a classical two-dimensional screened Coulomb system. *Phys. Rev. Lett.*, 58(12):1200–1203.

Murrell, J. N. and Laidler, K. J. (1968). Symmetries of activated complexes. *Trans. Faraday Soc.*, 64:371.

Naidoo, K. J. and Schnitker, J. (1994). Melting of two-dimensional colloidal crystals: A simulation study of the Yukawa system. *J. Chem. Phys.*, 100(4):3114.

Nelson, D. R. and Halperin, B. I. (1979). Dislocation-mediated melting in two dimensions. *Phys. Rev. B*, 19(5):2457–2484.

Nosenko, V., Goree, J., and Piel, A. (2006). Laser method of heating monolayer dusty plasmas. *Phys. Plasmas*, 13(3):032106.

Nosenko, V., Zhdanov, S. K., Ivlev, A. V., Knapek, C. A., and Morfill, G. E. (2009). 2D Melting of Plasma Crystals: Equilibrium and Nonequilibrium Regimes. *Phys. Rev. Lett.*, 103(1):015001.

Okuma, S., Suzuki, Y., and Tsugawa, Y. (2010). Reversible to irreversible flow transition in driven vortices. *Phys. C*, 470:S842–S843.

Okuma, S., Tsugawa, Y., and Motohashi, A. (2011). Transition from reversible to irreversible flow: Absorbing and depinning transitions in a sheared-vortex system. *Phys. Rev. B*, 83(1):012503.

Oswald, P. (2009). *Rheophysics*. Cambridge University Press, ISBN: 978-0-521-88362-7.

Ott, T., Stanley, M., and Bonitz, M. (2011). Non-invasive determination of the parameters of strongly coupled 2D Yukawa liquids. *Phys. Plasmas*, 18(6):063701.

Pastawski, H. M., Levstein, P. R., and Usaj, G. (1995). Quantum Dynamical Echoes in the Spin Diffusion in Mesoscopic Systems. *Phys. Rev. Lett.*, 75(23):4310–4313.

Peierls, R. (1934). Bemerkungen über Umwandlungstemperaturen. *Helv. Phys. Acta*, 7:81–83.

Peierls, R. (1935). Quelques propriétés typiques des corps solides. *Ann. Inst. Henri Poincaré*, 5(3):177–222.

Penner, S. S. (1948). Melting and Evaporation as Rate Processes. *J. Phys. Colloid Chem.*, 52(6):949–954.

Pine, D. J., Gollub, J. P., Brady, J. F., and Leshansky, A. M. (2005). Chaos and threshold for irreversibility in sheared suspensions. *Nature*, 438(7070):997–1000.

Plimpton, S. (1995). Fast Parallel Algorithms for Short-Range Molecular Dynamics. *J. Comput. Phys.*, 117(1):1–19.

Politi, A. (2013). Lyapunov exponent. *Scholarpedia*, 8(3):2722.

Price, R. and Platzman, P. M. (1991). Defect configurations in a two-dimensional classical Wigner crystal. *Phys. Rev. B*, 44(5):2356–2357.

Qi, W.-K., Qin, S.-M., Zhao, X.-Y., and Chen, Y. (2008). Coexistence of hexatic and isotropic phases in two-dimensional Yukawa systems. *J. Phys. Condens. Matter*, 20(24):245102.

Qi, W.-K., Wang, Z., Han, Y., and Chen, Y. (2010). Melting in two-dimensional Yukawa systems: A Brownian dynamics simulation. *J. Chem. Phys.*, 133(23):234508.

Quinn, R. A. and Goree, J. (2001). Experimental test of two-dimensional melting through disclination unbinding. *Phys. Rev. E*, 64(5):051404.

Radzvilavičius, A. (2012). Geometrical defects in two-dimensional melting of many-particle Yukawa systems. *Phys. Rev. E*, 86(5):051111.

Rapaport, D. C. (1997). *The art of molecular dynamics simulation*. Cambridge University Press, ISBN: 0-521-59942-3.

Regev, I., Lookman, T., and Reichhardt, C. (2013). Onset of irreversibility and chaos in amorphous solids under periodic shear. *Phys. Rev. E*, 88(6):062401.

Roberts, J. A. G. and Quispel, G. R. W. (1992). Chaos and time-reversal symmetry. Order and chaos in reversible dynamical systems. *Phys. Rep.*, 216(2-3):63–177.

Rousse, A., Rischel, C., Fourmaux, S., Uschmann, I., Sebban, S., Grillon, G., Balcou, P., Förster, E., Geindre, J. P., Audebert, P., Gauthier, J. C., and Hulin, D. (2001). Non-thermal melting in semiconductors measured at femtosecond resolution. *Nature*, 410(6824):65–8.

Royer, J. R. and Chaikin, P. M. (2014). Precisely cyclic sand: Self-organization of periodically sheared frictional grains. *Proc. Natl. Acad. Sci.*, 112(1):49–53.

Schneider, T. and Stoll, E. (1978). Dynamics of the Sine-Gordon Chain. *Phys. Rev. Lett.*, 41(21):1429–1432.

Schneider, T. M., Eckhardt, B., and Yorke, J. A. (2007). Turbulence Transition and the Edge of Chaos in Pipe Flow. *Phys. Rev. Lett.*, 99(3):034502.

Schneider, T. M., Gibson, J. F., Lagha, M., De Lillo, F., and Eckhardt, B. (2008). Laminar-turbulent boundary in plane Couette flow. *Phys. Rev. E*, 78(3):037301.

Schreck, C. F., Hoy, R. S., Shattuck, M. D., and O'Hern, C. S. (2013). Particle-scale reversibility in athermal particulate media below jamming. *Phys. Rev. E*, 88(5):052205.

Schweigert, V. A., Schweigert, I. V., Melzer, A., Homann, A., and Piel, A. (1998). Plasma Crystal Melting: A Nonequilibrium Phase Transition. *Phys. Rev. Lett.*, 80(24):5345–5348.

Sheppard, D., Terrell, R., and Henkelman, G. (2008). Optimization methods for finding minimum energy paths. *J. Chem. Phys.*, 128(13):134106.

Siders, C. W., Cavalleri, A., Sokolowski-Tinten, K., Tóth, C., Guo, T., Kammler, M., Horn von Hoegen, M., Wilson, K. R., von der Linde, D., and Barty, C. P. J. (1999). Detection of Nonthermal Melting by Ultrafast X-ray Diffraction. *Science*, 286:1340–1342.

Skufca, J. D., Yorke, J. A., and Eckhardt, B. (2006). Edge of Chaos in a Parallel Shear Flow. *Phys. Rev. Lett.*, 96(17):174101.

Slawinski, M. A. (2010). *Waves and Rays in Elastic Continua*. World Scientific Publishing Co. Pte. Ltd, 2nd edition, ISBN: 978-9814289009.

Slotterback, S., Mailman, M., Ronaszegi, K., van Hecke, M., Girvan, M., and Losert, W. (2012). Onset of irreversibility in cyclic shear of granular packings. *Phys. Rev. E*, 85(2):021309.

Stillinger, F. H. and Weber, T. A. (1982). Hidden structure in liquids. *Phys. Rev. A*, 25(2):978–989.

Stillinger, F. H. and Weber, T. A. (1984a). Packing structures and transitions in liquids and solids. *Science*, 225(4666):983–9.

Stillinger, F. H. and Weber, T. A. (1984b). Point defects in bcc crystals: Structures, transition kinetics, and melting implications. *J. Chem. Phys.*, 81(11):5095.

Strandburg, K. J. (1988). Two-dimensional melting. *Rev. Mod. Phys.*, 60(1):161–207.

Sun, H., Kang, N., Zhang, J., and Carlson, E. S. (2003). A fourth-order compact difference scheme on face centered cubic grids with multigrid method for solving 2D convection diffusion equation. *Math. Comput. Simul.*, 63(6):651–661.

Swayamjyoti, S., Löffler, J. F., and Derlet, P. M. (2014). Local structural excitations in model glasses. *Phys. Rev. B*, 89(22):224201.

Sykes, M. F. and Essam, J. W. (1964). Exact Critical Percolation Probabilities for Site and Bond Problems in Two Dimensions. *J. Math. Phys.*, 5(8):1117.

Tang, Y., Armstrong, A. J., Mockler, R. C., and O'Sullivan, W. J. (1989). Free-expansion melting of a colloidal monolayer. *Phys. Rev. Lett.*, 62(20):2401–2404.

Taylor, G. I. (1960). Low Reynolds Number Flow. Published in Homsy (2008).

Thomas, H., Morfill, G. E., Demmel, V., Goree, J., Feuerbacher, B., and Möhlmann, D. (1994). Plasma Crystal: Coulomb Crystallization in a Dusty Plasma. *Phys. Rev. Lett.*, 73(5):652–655.

Thomas, H. M. and Morfill, G. E. (1996). Melting dynamics of a plasma crystal. *Nature*, 379(6568):806–809.

Tobochnik, J. and Chester, G. V. (1982). Monte Carlo study of melting in two dimensions. *Phys. Rev. B*, 25(11):6778–6798.

Toh, S. and Itano, T. (2003). A periodic-like solution in channel flow. *J. Fluid Mech.*, 481:67–76.

Trygubenko, S. A. and Wales, D. J. (2004). A doubly nudged elastic band method for finding transition states. *J. Chem. Phys.*, 120(5):2082–94.

van der Meer, B., Qi, W., Fokkink, R. G., van der Gucht, J., Dijkstra, M., and Sprakel, J. (2014). Highly cooperative stress relaxation in two-dimensional soft colloidal crystals. *Proc. Natl. Acad. Sci. U. S. A.*, 111(43):15356–61.

Van Winkle, D. H. and Murray, C. A. (1986). Layering transitions in colloidal crystals as observed by diffraction and direct-lattice imaging. *Phys. Rev. A*, 34(1):562–573.

Vanden-Eijnden, E. and Tal, F. A. (2005). Transition state theory: variational formulation, dynamical corrections, and error estimates. *J. Chem. Phys.*, 123(18):184103.

Vaulina, O. S. and Khrapak, S. A. (2000). Scaling law for the fluid-solid phase transition in Yukawa systems (dusty plasmas). *J. Exp. Theor. Phys.*, 90(2):287–289.

Vaulina, O. S. and Koss, X. G. (2014). Thermodynamics and phase transitions in two-dimensional Yukawa systems. *Phys. Lett. A*, 378(46):3475–3479.

Vaulina, O. S. and Vasilieva, E. V. (2014). Orientational order and topological defects in two-dimensional Yukawa systems. *Phys. Lett. A*, 378(9):719–722.

Vineyard, G. H. (1957). Frequency factors and isotope effects in solid state rate processes. *J. Phys. Chem. Solids*, 3(1-2):121–127.

Wales, D. J. (1994). Rearrangements of 55-atom Lennard-Jones and (C60)55 clusters. *J. Chem. Phys.*, 101(5):3750.

Wales, D. J. and Berry, R. S. (1990). Melting and freezing of small argon clusters. *J. Chem. Phys.*, 92(7):4283.

Weinberger, C., Cai, W., and Barnett, D. (2005). Lecture Notes–Elasticity of Microscopic Structures. http://micro.stanford.edu/˜caiwei/me340b/content/me340b-notes_v01.pdf.

Wigner, E. (1934). On the Interaction of Electrons in Metals. *Phys. Rev.*, 46(11):1002–1011.

Young, A. P. (1979). Melting and the vector Coulomb gas in two dimensions. *Phys. Rev. B*, 19(4):1855–1866.

Young, W. R., Rhines, P. B., and Garrett, C. J. R. (1982). Shear-Flow Dispersion, Internal Waves and Horizontal Mixing in the Ocean. *J. Phys. Oceanogr.*, 12(6):515–527.

Zahn, K., Lenke, R., and Maret, G. (1999). Two-Stage Melting of Paramagnetic Colloidal Crystals in Two Dimensions. *Phys. Rev. Lett.*, 82(13):2721–2724.

Zahn, K. and Maret, G. (2000). Dynamic Criteria for Melting in Two Dimensions. *Phys. Rev. Lett.*, 85(17):3656–3659.

Zhang, W., Zhou, W., and Luo, M. (2010). Irreversibility of two-dimensional vortex systems with random pinning. *Phys. Lett. A*, 374(35):3666–3670.

Zheng, X. H. and Earnshaw, J. C. (1998). On the Lindemann criterion in 2D. *Europhys. Lett.*, 41(6):635–640.

Wissenschaftlicher Werdegang

seit 05/2011	Wissenschaftlicher Mitarbeiter in der AG Komplexe Systeme Philipps-Universität Marburg Doktorand bei Prof. Dr. Eckhardt
04/2011	Diplom Physik Diplomarbeit in der Arbeitsgruppe Komplexe Systeme bei Prof. Dr. Eckhardt *Motion of Inertial Particles in a Cellular Flow Field*
10/2007	Vordiplom Physik
10/2005 - 04/2011	Studium Physik (Diplom) Philipps-Universität Marburg

Danksagung

Zum Abschluss dieser Arbeit möchte ich noch allen danken, die direkt oder indirekt zu ihrer Entstehung beigetragen haben.

Allen voran möchte ich mich bei Prof. Bruno Eckhardt bedanken, für die Betreuung dieser Arbeit sowie insbesondere für die inspirierenden Diskussionen und die fortwährende Unterstützung. Herrn Prof. Waalkens danke ich, dass er sich bereit erklärt hat das Zweitgutachten zu erstellen.

Ganz herzlich bedanken möchte ich mich auch bei meinen Kollegen in der Arbeitsgruppe *Komplexe Systeme*, für die angenehme Atmosphäre und zahlreiche Diskussionen auch abseits der Arbeit. Besonders hervorzuheben sind dabei Felix, Hannes und Tobias, die den IT-Support gestemmt haben. Vielen Dank auch an Thomas Gebhardt und das Support-Team von MaRC2, die immer schnell und kompetent auf Probleme reagiert haben.

Ohne die Hilfe eifriger Leser wären in dieser Arbeit noch weit mehr Fehler versteckt. Vielen Dank fürs Korrekturlesen und die vielen Anmerkungen an Felix, Hannes, Marina, Stefan und Stefanie.

Ganz besonderer Dank gilt natürlich meiner Lebensgefährtin Stefanie, die mich durch alle Höhen und Tiefen dieser Arbeit begleitet hat.